Enriching the understanding of synaptic architecture from single synapses to networks with advanced imaging techniques

Dissertation zur Erlangung des naturwissenschaftlichen Doktorgrades der Julius-Maximilians-Universität Würzburg

vorgelegt von

Sebastian Matthias Markert

geboren in Mellrichstadt

Würzburg, 2019

Eingereicht am: 27. Juni 2019

Mitglieder der Promotionskommission:

Vorsitzende: Prof. Dr. Charlotte Förster

Gutachter: Prof. Dr. Christian Stigloher

Gutachter: Prof. Dr. Philip Kollmannsberger

Tag des Promotionskolloquiums: 09. Oktober 2019

Doktorurkunde ausgehändigt am: .....

Zusammenfassung

Das Nervensystem ist ein definierendes Merkmal aller Tiere, unter anderem verantwortlich für Sinneswahrnehmung, Bewegung und „höhere“ Hirnfunktionen. Wegen dessen Komplexität und Feingliedrigkeit stellt das Erforschen des Nervensystems oft eine Herausforderung dar. Jedoch ist der kleine Fadenwurm *Caenorhabditis elegans* als Modellsystem für neurobiologische Grundlagenforschung gut etabliert. Er besitzt eines der kleinsten und unveränderlichsten bekannten Nervensysteme. *C. elegans* ist auch das einzige Modell, für das ein annähernd vollständiges Konnektom vorliegt, eine durch Elektronenmikroskopie erstellte Karte der synaptischen Verbindungen eines gesamten Organismus, die Einblicke in die Funktionsweise des Nervensystems als Ganzes erlaubt. Allerdings ist die Anzahl der verfügbaren Datensätze gering und das Konnektom enthält Fehler und Lücken. Davon sind beispielsweise elektrische Synapsen betroffen. Elektrische Synapsen werden von Gap Junctions gebildet und sind auf Grund ihrer oft uneindeutigen Morphologie in elektronenmikroskopischen Aufnahmen schwierig zu kartieren, was dazu führt, dass einige falsch klassifiziert oder übersehen werden. Chemische Synapsen sind dagegen einfacher zu kartieren, aber viele Aspekte ihrer Funktionsweise sind schwer zu erfassen und ihre Rolle im Konnektom von *C. elegans* ist daher zu vereinfacht dargestellt. Ein umfassendes Verständnis der Signaltransduktion von Neuronen untereinander und zu anderen Zellen wird Voraussetzung für ein vollständiges Erfassen des Nervensystems sein. In der vorliegenden Arbeit gehe ich diese Herausforderungen mithilfe einer Kombination aus modernsten licht- und elektronenmikroskopischen Verfahren an.

Zunächst beschreibt diese Arbeit eine Strategie, um die synaptische Spezifität in der Konnektomik zu erhöhen, indem ich Gap Junctions mit einem hohen Maß an Genauigkeit klassifiziere. Um dies zu erreichen, nutzte ich *array tomography* (AT), eine Technik, die Licht- und Elektronenmikrokopie miteinander korreliert. In dieser Arbeit wird AT adaptiert für Hochdruckgefrierung, um die Strukturerhaltung zu optimieren, sowie für ultrahochauflösende Lichtmikroskopie; so wird die Kluft zwischen den Auflösungsbereichen von Licht- und Elektronenmikroskopie überbrückt. Diese Adaption nenne ich *super-resolution array tomography* (srAT). Der srAT-Ansatz machte es möglich, Gap Junctions mit hoher Präzision und Genauigkeit

klar zu identifizieren. Für diese Arbeit konzentrierte ich mich dabei auf Gap Junctions des retrovesikulären Ganglions von *C. elegans*. Die Ergebnisse dieser Studie veranschaulichen, wie es möglich wäre, elektrische Synapsen systematisch in Konnektome aufzunehmen. Nachfolgende Studien haben srAT auch auf andere Modelle und Fragestellungen angewandt.

Wie bereits erwähnt, leidet das Konnektom-Modell von *C. elegans* darunter, dass die Anzahl der verfügbaren Datensätze sehr limitiert ist. Hinzu kommt, dass das bestehende Konnektom aus Teilen von verschiedenen adulten Hermaphroditen zusammengesetzt wurde. Unter anderem von dem speziellen Dauerlarven-Stadium fehlen Konnektom-Daten bisher vollständig. Um das erste partielle Konnektom der Dauerlarve von *C. elegans* zu generieren, haben wir *focused ion-beam scanning electron microscopy* (FIB-SEM) eingesetzt. Diese Technik bietet eine ausgezeichnete axiale Auflösung und eignet sich für das Aufnehmen großer Volumina für die Konnektomik. Im Zuge dessen entwickelte ich ein Verfahren für das Einbetten von Dauerlarven-Proben in minimalen Mengen von Harz, sodass die Würmer im Mikroskop unmittelbar gefunden und evaluiert werden konnten. Zusammen mit unseren Kollaborationspartnern nahmen wir mehrere Datensätze auf, die es ermöglichen die Konnektivitlät des Dauer-Nervensystems zu untersuchen und damit wertvolle Einblicke in die Plastizität bzw. Variabilität des Konnektoms erlauben.

Chemische Synapsen sind im Vergleich zu elektrischen relativ einfach zu kartieren, aber die Signaltransduktion mittels chemischer Transmitter setzt voraus, dass eine große Anzahl verschiedener Proteine und molekularer Prozesse auf engstem Raum zusammenwirken. Die Funktionen vieler dieser synaptischen Proteine sind zur Zeit noch unbekannt, was dazu führt, dass bestimmte Aspekte der synaptischen Transmission wenig verstanden sind. Die Synapse befindet sich auf einer äußerst kleinen räumlichen Skala, weshalb eine sehr hohe Auflösung für die Untersuchung der Proteinfunktionen benötigt wird. In dieser Arbeit bediente ich mich daher der Elektronentomographie. Diese Methode bietet eine sehr viel höhere laterale Auflösung als FIB-SEM, bei ähnlicher axialer Auflösung. Allerdings ist Elektronentomographie nur für kleine Volumina geeignet, da es viel Zeit erfordert die Proben anzufertigen, aufzunehmen und zu verarbeiten. Ich analysierte Elektronentomogramme einer Wurmlinie mit einem mutierten synaptischen Protein, der Serin/Threonin-Kinase SAD-1, und fand bemerkenswerte Veränderungen bei mehreren strukturellen Merkmalen. Meine Ergebnisse bestätigen vorherige Erkenntnisse und stellen diese in

einen neuen Kontext. Sie bieten außerdem neue Einsichten in die Funktionen dieses Proteins an der chemischen Synapse.

Schließlich untersuchte ich mit einem Modell für amyotrophische Lateralsklerose (ALS) die Wirksamkeit unserer Methoden an krankhaft veränderten Synapsen. In der mutmaßlichen Synapsenerkrankung ALS sind die Mechanismen des Absterbens von Motorneuronen größtenteils unbekannt. Mutationen in dem Gen *FUS* (*Fused in Sarcoma*) sind aber ein bekannter Auslöser der Erkrankung. Es stellt jedoch eine große Herausforderung dar, die Effekte von FUS-Mutationen auf Motorneuronen zu untersuchen, oder zu klären, wie solche Mutationen zum Absterben von Zellen führen können. Allerdings wurde kürzlich gezeigt, dass die Expression von mutiertem humanen FUS in *C. elegans* ALS-artige Phänotypen im Wurm auslöst, was *C. elegans* zu einem attraktiven Krankheitsmodell für ALS macht. Zusammen mit unseren Kollaborationspartnern wandte ich sowohl srAT, als auch Elektronentomographie auf „ALS-Würmer“ an und wir fanden heraus, dass das Docking von Vesikeln verändert ist. Diese Erkenntnisse helfen dabei, elektrophysiologische Messungen in ALS-Würmern zu erklären, die im Vergleich zu Kontrollen eine Verringerung der Frequenz von exzitatorischen Miniatur-Synapsenströmen zeigen, jedoch keine Veränderung der Amplitude. Des Weiteren waren synaptische Endosomen in unseren Tomogrammen größer und enthielten elektronendichte faserartige Strukturen. Diese Ergebnisse stärken die Hypothese, dass mutiertes FUS Vesikel-Docking behindert, und bieten außerdem neue Erkenntnisse über weitere molekulare Mechanismen der Krankheitsentwicklung bei FUS-vermittelter ALS. Darüber hinaus zeigen wir die breite Einsetzbarkeit unserer Methoden, indem wir sie erfolgreich auf kultivierte Motorneuronen der Maus anwenden.

Insgesamt hilft diese Arbeit dabei, mithilfe von *C. elegans* als Modell und einer Kombination aus licht- und elektronenmikroskopischen Methoden, den Aufbau und die Funktion von neuronalen Synapsen aufzuklären; mit dem Ziel, ein umfassendes Modell des Nervensystems zu erlangen.

Table of contents

Abstract

The nervous system is a defining feature of all animals, responsible for sensory perception, motion, and "higher" brain functions. Because of its complexity and intricacy, studying the nervous system is often challenging. Fortunately, the small nematode roundworm *Caenorhabditis elegans* is well established as a model system for basic neurobiological research and possesses one of the smallest and most invariable nervous systems. The *C. elegans* model is also the only organism with a supposedly complete connectome, an organism-wide map of synaptic connectivity resolved by electron microscopy, which provides some understanding of how the nervous system works as a whole. However, the number of available data-sets is small and the connectome contains errors and gaps. One example of this concerns electrical synapses. Electrical synapses are formed by gap junctions and difficult to map due to their often ambiguous morphology in electron micrographs, leading to misclassification or omission. On the other hand, chemical synapses are more easily mapped, but many aspects of their mode of operation remain elusive and their role in the *C. elegans* connectome is oversimplified. A comprehensive understanding of signal transduction of neurons between each other and other cells will be indispensable for a comprehensive understanding of the nervous system. In this thesis, I approach these challenges with a combination of advanced light and electron microscopy techniques.

First, this thesis describes a strategy to increase synaptic specificity in connectomics. Specifically, I classify gap junctions with a high degree of confidence. To achieve this, I utilized array tomography (AT), a correlative light and electron microscopy (CLEM) technique. In this thesis, AT is adapted for high-pressure freezing to optimize for structure preservation and for super-resolution light microscopy; in this manner, I aim to bridge the gap between light and electron microscopy resolutions. I call this adaptation super-resolution array tomography (srAT). The srAT approach made it possible to clearly identify and map gap junctions with high precision and accuracy. For this thesis, I focused on gap junctions in the retrovesicular ganglion of *C. elegans*. The results from this study showcased the feasibility of incorporating

electrical synapses into connectomes in a systematic manner, and subsequent studies have used srAT for other models and questions.

As mentioned above, the *C. elegans* connectomic model suffers from a shortage of datasets. Also, the existing connectome was pieced together from parts of several adult hermaphrodite worms. For most larval stages, including the special *dauer* larval stage, connectome data is completely missing up to now. To obtain the first partial connectome data-set of the *C. elegans dauer* larva, we used focused ion-beam scanning electron microscopy (FIB-SEM). This technique offers an excellent axial resolution and is useful for acquiring large volumes for connectomics. In the process, I developed a protocol for embedding the *dauer* samples in minimal resin so the worms could be targeted and evaluated in the microscope immediately. Together with our collaborators, I then acquired several data-sets which enable the analysis of *dauer* stage-specific "re-wiring" of the nervous system and thus offer valuable insights into connectome plasticity/variability.

While chemical synapses are easy to map relative to electrical synapses, signal transduction via chemical transmitters requires a large number of different proteins and molecular processes acting in conjunction in a highly constricted space. The functions of many synaptic proteins are currently unknown, and thus, certain aspects of synaptic transmission are poorly understood. Because of the small spatial scale of the synapse, investigating protein function requires very high resolution. In this thesis, I thus employed electron tomography. This method offers far higher resolution in the lateral dimensions than FIB-SEM while maintaining similar axial resolution. However, it is only practical for small volumes because of the time required to prepare, image, and process samples. I analyzed electron tomograms of a worm-line with a mutant synaptic protein, the serine/threonine kinase SAD-1, and found remarkable alterations in several architectural features. My results confirm and re-contextualize previous findings and provide new insight into the functions of this protein at the chemical synapse.

Finally, I investigated the effectiveness of our methods on "malfunctioning," synapses, using an amyotrophic lateral sclerosis (ALS) model. In the putative synaptopathy ALS, the mechanisms of motor neuron death are mostly unknown. However, mutations in the gene *FUS* (Fused in Sarcoma) are one known cause of the disease. Unfortunately, it remains challenging to study the effects of FUS mutation on motor neurons or how the mutation leads to cell death. Nevertheless, the expression

of the mutated human FUS in *C. elegans* was recently shown to produce an ALS-like phenotype in the worms, rendering *C. elegans* an attractive disease model for ALS. Together with our collaboration partners, I applied both srAT and electron tomography methods to "ALS worms" and found effects on vesicle docking. These findings help to explain electrophysiological recordings that revealed a decrease in frequency of mini excitatory synaptic currents, but not amplitudes, in ALS worms compared to controls. In addition, synaptic endosomes appeared larger and contained electron-dense filaments in our tomograms. These results substantiate the idea that mutated FUS impairs vesicle docking and also offer new insights into further molecular mechanisms of disease development in FUS-dependent ALS. Furthermore, we demonstrated the broader applicability of our methods by successfully using them on cultured mouse motor neurons.

Overall, using the *C. elegans* model and a combination of light and electron microscopy methods, this thesis helps to elucidate the structure and function of neuronal synapses, towards the aim of obtaining a comprehensive model of the nervous system.

Glossary

3D ART VeSElecT	3D automated reconstruction tool for vesicle structures of electron tomograms
ADA	ring interneuron in *C. elegans*
ADE	anterior deirid, mechanosensory neuron in *C. elegans*
ADF	amphid sensory neuron in *C. elegans*
AFD	amphid finger sensory neuron in *C. elegans*
AIB	amphid interneuron in *C. elegans*
ALS	amyotrophic lateral sclerosis
AT	array tomography
ATUM	automated tape-collecting ultramicrotome
AVA	ventral cord interneuron in *C. elegans*
AVK	ring and ventral cord interneuron in *C. elegans*
AWA	amphid wing sensory neuron in *C. elegans*
AWB	amphid wing sensory neuron in *C. elegans*
AWC	amphid wing sensory neuron in *C. elegans*
BSA	bovine serum albumin
CCV	clear core vesicle
CEP	cephalic neuron in *C. elegans*, mechnosensory
CLEM	correlative light and electron microscopy
DA9	ventral motor neuron in *C. elegans*, innervates dorsal muscles
DAPI	4',6-diamidino-2-phenylindole
DCV	dense core vesicle
ddH_2O	double-destilled water
DNC	dorsal nerve cord

dSTORM ..... direct stochastic optical reconstruction microscopy

FIB-SEM ..... focused ion-beam scanning electron microscopy

FISH ..... fluorescence in situ hybridization

FLP ..... sensory neuron in *C. elegans*, polymodal nociceptive for mechanosensation and thermosensation

FS ..... freeze-substitution

FUS ..... fused in sarcoma (human protein)

GABA ..... γ-aminobutyric acid (neurotransmitter)

GFP ..... green fluorescent protein

HA-tag ..... human influenza hemagglutinin tag

HPF ..... high-pressure freezing

HPF/FS ..... high-pressure freezing followed by freeze-substitution

IF ..... immunofluorescence

LB ..... lysogeny broth

LR White ..... methacrylate resin manufactured by London Resin

MAD ..... median absolute deviation

MRSA ..... methicillin-resistant *Staphylococcus aureus*

N2 ..... strain of *C. elegans* considered as wild-type

NGM ..... nematode growth medium

NMJ ..... neuromuscular junction

NR ..... nerve ring

OLQ ..... mechanosensory neuron and interneuron in *C. elegans*

PALM ..... photo-activated localization microscopy

PAR-1 ..... abnormal embryonic PARtitioning of cytoplasm (*C. elegans* protein)

PBS ..... phosphate-buffered saline

PDMS ..... polydimethylsiloxane

PTL-1 ..... Protein with Tau-Like repeats (*C. elegans* protein)

RIG ..... ring interneuron in *C. elegans*

RIH ..... ring interneuron in *C. elegans*

RIM ..... ring interneuron in *C. elegans*

RIS ..... ring interneuron in *C. elegans*

RNP ..... ribonucleoprotein

RT ..... room temperature

RVG ..... retrovesicular ganglion

SAD-1 ..... Synapses of Amphids Defective (*C. elegans* innexin protein)

SBF-SEM ..... serial block-face scanning electron microscopy

SDS ..... sodium dodecyl sulfate

SEM ..... scanning electron microscopy

SIM ..... structured illumination microscopy

SMBD ..... ring motor neuron/interneuron in *C. elegans*

srAT ..... super-resolution array tomography

TEM ..... transmission electron microscopy

TWK-40 ..... TWiK family of potassium channels (*C. elegans* poassium leak channel)

UNC-7 ..... UNCoordinated (*C. elegans* innexin protein)

UNC-9 ..... UNCoordinated (*C. elegans* innexin protein)

UV ..... ultraviolet

VNC ..... ventral nerve cord

wt ..... wild-type

List of figures

List of tables

1. Introduction

1.1. The nematode *C. elegans* and its (very) tractable nervous system

Communication between neurons is key to nearly all their capabilities. This intercellular communication is realized by synaptic connections and volume transmission of messenger molecules. A comprehensive understanding of signal transduction of neurons between each other and other cells will be indispensable for a comprehensive understanding of the nervous system. However, due to the sheer complexity and intricacy of synapses, this task remains challenging. The *Caenorhabditis elegans* model reduces the number of intercellular connections and synaptic complexity as much as possible such that the entire system is experimentally much more tractable. This is one of the reasons *C. elegans* was suggested as a model organism by Sydney Brenner in his seminal publication from 1974 [Brenner 1974] and why it is now firmly established [Sulston and Horvitz 1977; White et al. 1986; Chalfie et al. 1994; Fire et al. 1998; Girard et al. 2007]. The nematode possesses 302 neurons as adult hermaphrodite and has a eutelic cell lineage, i. e., any adult hermaphrodite wild-type worm has exactly the same number of somatic cells, including neurons [Sulston and Horvitz 1977]. A small and invariant nervous system offers a starting point to understanding a nervous system comprehensively.

Nematodes are an extremely successful taxon. They can be found all over the globe with some 25,000 described species so far [Zhang 2013]. Many nematode species are parasites and affect humans substantially. They were responsible for the projected loss of 12.3 % of worldwide crop yield, causing much more damage than insect pests [Singh et al. 2015], and they are a huge problem for tropical and subtropical regions livestock [Waller 1997]. In humans, they are responsible for diseases like ascariasis, trichuriasis, hookworm, enterobiasis, strongyloidiasis, filariasis, and trichinosis [Wright 1979; Liu and Weller 1993; Grencis and Cooper 1996; Hotez et al. 2004; Taylor et al. 2010; Knopp et al. 2012]. These diseases devastate health and are

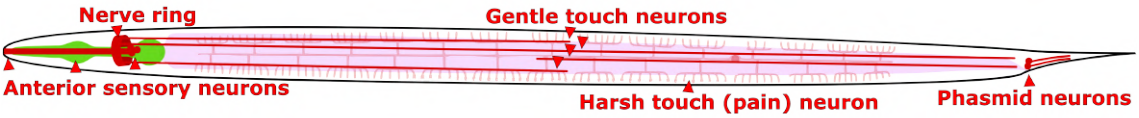

Figure 1.1.: **Schematic representation of the *C. elegans* sensory nervous system.** The anterior sensory system includes the ampid neurons, cephalic neurons, inner and outer labials, and the anterior deirid neurons. The posterior deirids project along the whole midbody (not shown). Pharynx is indicated in green and intestine in pink.

difficult to treat. Nematodes therefore represent a serious socio-economic burden. Thus, *C. elegans* research is relevant for a basic understanding of animal biology, socio-economic protection, and human health. Insights into *C. elegans* neurobiology will assist the search for anti-parasitic drug targets, for example.

While small, the *C. elegans* nervous system is still fully capable of performing the diverse tasks necessary for their survival and success. For instance, they perceive their environment via an array of sensory neurons (Figure 1.1). *C. elegans* is able to perceive chemicals [Bargmann and Mori 1997; Mori 1999], temperature [Hedgecock and Russell 1975; Bargmann and Mori 1997; Mori 1999], light [Burr 1985], touch [Chalfie et al. 1985; O'Hagan and Chalfie 2005], shape [Sawin et al. 2000], pain [Tobin and Bargmann 2004], and possibly even magnetic fields [Vidal-Gadea et al. 2015]. These capabilities are owed to the efficient processing center called the "nerve ring", a circular ganglion around the pharynx that could be regarded the "brain" of the worm [White et al. 1986]. From the nerve ring, the retrovesicular ganglion branches off and transitions into the ventral nerve cord (Figure 1.2). Somata of the motor neurons line this ventral cord and enervate the body wall muscles. Some motor neurons project to the dorsal side and form the dorsal nerve cord. In fact, the dorsal nerve cord does not contain any motor neuron somata [White et al. 1986]. In both nerve cords, as is typical for nematodes, muscles form muscle arms and reach towards the motor neurons to form neuromuscular junctions [Stretton 1976; White et al. 1986; Dixon and Roy 2005]. The propagating waves of activity between these two nerve cords enable sinusoidal movement of the longitudinal body wall. Musculature for more complex movements is mostly restricted to the anterior head part. The pharynx possesses its own small, nearly independent, nervous system including a pacemaker for rhythmical pumping movement [Albertson and Thompson

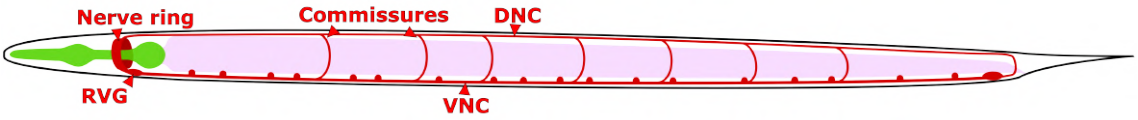

Figure 1.2.: **Schematic representation of the *C. elegans* motor nervous system.** RVG: retrovesicular ganglion, DNC: dorsal nerve cord, VNC: ventral nerve cord. Only the VNC contains somata of motor neurons (circles). Commissures project from VNC to DNC. Pharynx is indicated in green and intestine in pink.

1976]. Males possess additional neurons related to reproductive behavior [Jarrell et al. 2012].

All neurons in *C. elegans* were named by John Sulston and Rober Horvitz in the 1977 publication that included a complete cell-lineage [Sulston and Horvitz 1977]. As a next step, Sydney Brenner and his colleagues mapped all connections, the synapses between neurons, to obtain a complete "circuitry map" of the worm.

1.2. Connectomics is concerned with circuit maps of nervous systems

Since *C. elegans* has such a small and well-defined nervous system, Sydney Brenner thought it feasible to acquire a map of all neurons and their synapses [White et al. 1986; Emmons 2015]. For such a map eventually the term "connectome" was coined and the field of connectomics was born [Sporns et al. 2005].

Similarly to the genome, the connectome represents a foundational resource [Sporns et al. 2005; Lichtman and Sanes 2008]. It allows the formulation of mechanistic hypotheses based on structural connectivity. These hypotheses can then be tested with ablation experiments and by genetic analysis of behavioral mutants. Thus, the connectome informs the study of the specific as well as the general roles of individual neurons [Schafer 2018]. But, moreover, the connectome is hoped to give insight into systemic properties and functions that will allow us to obtain a mechanistic basis for behavior and even for mental phenomena like cognition in more complex brains [Lichtman and Sanes 2008; Schafer 2018]. This approach holds great promise and extensive efforts are currently undertaken to obtain connectome data-sets of mice

[Helmstaedter et al. 2013] and even humans [van Essen et al. 2013] in the hope to comprehend how thoughts arise from the vast tangle of neurons firing in a human brain in the future.

While the mammalian connectome is in development, the *C. elegans* connectome has been available for many years now, thanks to the heroic efforts of Sydney Brenner and his colleagues [White et al. 1986]. Way ahead of the times, they achieved what nowadays no-one would dare without advanced imaging techniques and image analysis software [Emmons 2015]. With that said, insights into "the mind of a worm" [White et al. 1986] remain limited. Predicting behavior from circuitry remains challenging even with the connectome at hand [Bentley et al. 2016; Schafer 2018]. Is the premise that the connectome contains the "mind" false? What else is missing? These questions are difficult to answer. In fact, the connectome is not complete. Indeed, it contains many gaps [Bargmann and Marder 2013]. Inclusion of neuromodulation has only recently started to emerge [Bentley et al. 2016]. Further, synapses are largely mapped based on morphology only, with functional validation or quantification of connection strength being restricted to specific sub-networks in specialized studies [Weimer et al. 2003; Klassen and Shen 2007]. Also, the *C. elegans* connectome is based on a very limited number of data-sets, none of which contains a whole animal. All available data-sets are of adult worms, so the connectome lacks developmental information. To gain insight into variability and development of connectomes, more data-sets are required, but producing more of these data-sets remains time-consuming. Last but not least, many electrical synapses formed by gap junctions are probably missing from the connectome, since many new gap junctions have been added to the connectome [cf. the WormWiring database of the Scott Emmons laboratory; http://wormwiring.org/] since White et al. [1986] and new ones are still being described [Ramirez-Suarez et al. 2019].

1.3. Gap junctions are essential components of connectomes, but are challenging to map

Gap junctions electrically couple cells directly with each other. This is the reason gap junctions are also called electrical synapses. Each cell presents a hemi-channel formed from six subunits of connexins in chordates [Gilula et al. 1972] or innexins in invertebrates [Phelan et al. 1998] on the plasma membrane. Hemichannels from

two cells can then combine to form a channel between the two cells. Ions and small molecules can freely diffuse through the resulting pore (Figure 1.3A). This means that if one cell is depolarized, the other is too [Söhl et al. 2005]. It could be argued that they represent "hardwiring" of connections between cells and between neurons

In contrast to chemical synapses, electrical synapses transmit neuronal signals immediately and directly to synaptic partners. They have a strong impact on neuronal circuits, thus they are very important elements of connectomes. However, in the field of vertebrate connectomics, gap junctions are less studied than chemical synapses [Denk and Horstmann 2004; Kasthuri et al. 2015]. In *C. elegans*, gap junctions have been mapped [White et al. 1986; Varshney et al. 2011], but it is uncertain how many are still missing, because the structure of electrical synapses is harder to identify than the one of chemical synapses. The latter are readily distinguishable by vesicle pools and pre- or postsynaptic densities, which appear dark in electron micrographs [Denk and Horstmann 2004; Kasthuri et al. 2015]. In contrast, gap junctions appear just as tightly connected membrane portions with electron-dense material located in a 2-4 nm gap (Figure 1.3) [Goodenough and Paul 2009]. Good resolution and an orthogonal cutting angle are required to detect a gap junction with some degree of confidence. Data-sets for connectomics are typically acquired at lower resolution to obtain large fields of view. This reduces image acquisition time, but gap junctions are easily overlooked in such data-sets [Denk and Horstmann 2004; Kasthuri et al. 2015]. In order to reliably map gap junctions, a technique which correlates immunofluorescence and electron microscopy is needed, such as array tomography [Micheva and Smith 2007].

1.4. Array tomography combines the specificity and versatility of immunofluorescence microscopy with the ultrastructural resolution of electron microscopy

For many biological questions, it is desirable to localize proteins or other molecules of interest in their full ultrastructural context. For example, the relative location of the protein with regard to membranes, organelles, cytoskeleton elements, and so

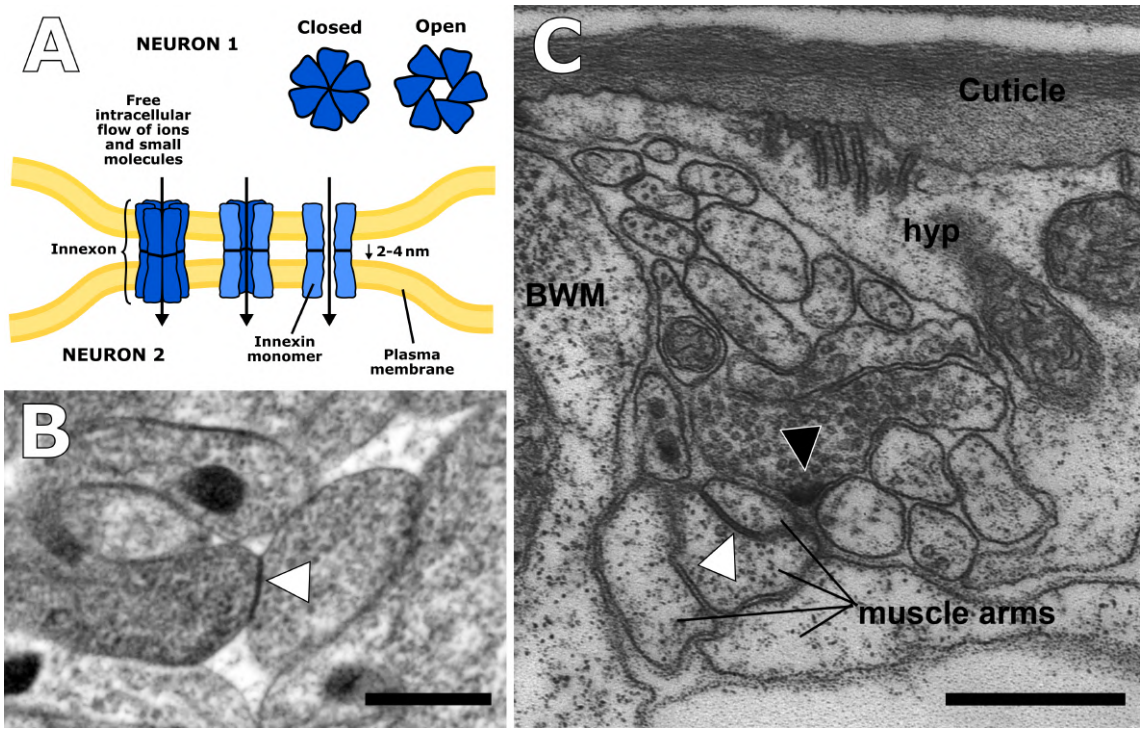

Figure 1.3.: **Electrical synapses are formed by gap junctions. A** Schematic representation of gap junction channels coupling two neurons. **B** Scanning electron micrograph of an electrical synapse (arrowhead) in the retrovesicular ganglion of *C. elegans*. **C** Transmission electron micrograph of a *C. elegans* ventral nerve cord. Image modified from WormAtlas[a]. The gap junction (white arrowhead) is much more challenging to identify than the chemical synapse, which is clearly defined by its vesicle pool and the presynaptic dense projection (black arrowhead). BWM: body wall muscle, hyp: hypodermal cell. Scale bars: 500 nm.

[a] https://www.wormatlas.org/hermaphrodite/gapjunctions/mainframe.htm last accessed: May 23rd 2019

on. Electron microscopy is currently still the standard imaging modality to resolve and depict the ultrastructure of biological samples. If the sample is fixed and processed with appropriate, gentle protocols, epitopes are preserved and proteins can be stained with antibodies. However, electron microscopy has some considerable disadvantages compared to immunofluorescence labeling. First, electron microscopy is incompatible with fluorochrome-labeled antibodies and thus secondary antibodies or antibody-binding proteins conjugated with gold nanoparticles of 1-15 nm are commonly used. Second, labeling density is much lower, probably due to steric inhibition of the gold-conjugated antibodies or proteins [Horisberger 1981; Stierhof and Schwarz 1989; Humbel et al. 1995; Kurth et al. 1996], so only a fraction of available epitopes is labeled. Thus, proteins with lower copy-numbers can be challenging to localize. The use of ultra-small gold particles can increase labeling density, but requires additional silver-enhancement to visualize the particles [Humbel et al. 1995]. Third, labeling is more challenging to detect. Visualizing gold particles in electron micrographs requires high magnifications and low contrasting of the section. Consequently, it can be very time-consuming to scan an ultrathin section for gold particles; stereology might be necessary [Lucocq 1994, 2008]. With fluorescence, all labeled areas become apparent immediately. Fourth and last, multiple labeling is limited. Reasonably, three epitopes at once can be labeled by using gold particles of different sizes. However, this means using bigger particles as well, which exhibit low labeling densities (see above). Also, multiple labeling is incompatible with ultra-small gold particles, because the necessary silver-enhancement results in particles of varying sizes [Humbel et al. 1995].

To overcome these drawbacks, it is desirable to combine electron microscopy with immunofluorescence instead of immunogold techniques. Since light and electron microscopy have fundamentally different requirements in sample preparation, combining the two imaging modalities is challenging. Nevertheless, more and more techniques are currently developed. Whenever light and electron microscopy are combined, this is called correlative light and electron microscopy (CLEM). In recent years, many CLEM techniques have been published, using very different approaches. Post-embedding on-section labeling with fluorophores actually has a long history and several studies used this technique since the 1980s [Herken et al. 1988; Ojeda et al. 1989; Albrecht et al. 1990; Fialka et al. 1996; Kurth et al. 1996; Haraguchi and Yokota 2002; Schwarz and Humbel 2014]. Micheva and Smith built on these techniques and developed an approach utilizing arrays of serial sections they call “array

tomography" [Micheva and Smith 2007; Micheva et al. 2010b, a; Collman et al. 2015; Smith 2018].

In array tomography, samples are processed for electron microscopy, but fixation and embedding resin are chosen to preserve protein epitopes. While structure preservation can suffer, it can be a good compromise for many applications. In general, ultrathin serial sections of 50-200 nm are cut with a diamond knife and collected on glass slides, instead of collecting them on grids for classical electron microscopy. Then, the sections can be stained with adapted immunofluorescence protocols. Since many epitopes are still intact and have been exposed by sectioning, they can be labeled on the surface of the section. After image acquisition with standard fluorescence microscopy, sections are processed for electron microscopy, i. e., they are contrasted with heavy metals and coated with a thin layer of carbon to improve conductivity. Then, the very same sections can be imaged with scanning electron microscopy directly on the glass slides. Thus, it is possible to obtain a fluorescence image as well as an electron micrograph from each region of interest on the very same section. The resulting images can be correlated and this puts the specific protein signal in its full ultrastructural context. Since serial sections are collected and analyzed, regions of interest can also be followed in axial direction and 3D representations can be generated.

Array tomography can be very powerful for many questions. For example, it is possible to determine which neurotransmitter occurs in a specific neuron [Collman et al. 2015]. Drawbacks of the technique are the compromised structure preservation and the differences in resolution between fluorescence and electron modalities. Protein signals cannot be localized very precisely, since the signal itself is diffraction limited. This also limits the precision of the correlation itself. To alleviate these drawbacks, I advanced array tomography within the scope of my thesis by introducing super-resolution light microscopy and new correlation work-flows [Markert et al. 2016, 2017]. Using this *super-resolution* array tomography (srAT), I was able to map gap junctions with high precision and accuracy. Since I imaged ultrastructure at high resolution while preserving antigenicity as much as possible, appropriate sample preparation was key. For *C. elegans* samples high-pressure freezing followed by freeze-substitution is the technique of choice.

1.5. High-pressure freezing followed by freeze-substitution offers near-to-native structure preservation for most electron microscopy applications

Biological samples for classical electron microscopy need to be dehydrated to be able to withstand the low pressure in the column of the microscope. Prior to dehydration, biological samples are stabilized and fixed to avoid loss of structural integrity. However, these two steps, fixation and dehydration, produce damage and artifacts to the structure itself [Ebersold et al. 1981]. Because of this, high-pressure freezing followed by freeze-substitution (HPF/FS) [Moor 1987; Rostaing et al. 2004; Weimer 2006] has become widespread in the electron microscopy community. This technique stabilizes samples via rapid cryo-immobilization at very high pressure. This results in so-called vitrification of the water in the sample. That means the water molecules are unable to form ice crystals that would destroy the ultrastructure, but transition directly from liquid into an amorphous, glass-like state. This way, all molecules in a living cell are stabilized in the position they were in during the freezing, thus creating a "snapshot" of the living cells. They can be stored in liquid nitrogen and processed via freeze-substitution for chemical fixation and dehydration. Since the chemical fixation and dehydration typically take place at -90 °C, while the sample is still stabilized, freeze-substitution is more gentle to the structure than classical fixation methods. Moreover, it is of particular relevance for this thesis that classical fixation methods induce fusion of synaptic vesicles [Rostaing et al. 2006] and thus impede analyses of vesicle pool sizes, vesicle docking, etc. With HPF/FS, however, structure preservation is near-native, comparable to pure cryo-electron microscopy protocols, where chemical fixation and dehydration are avoided altogether, which has drawbacks in other ways, e. g., in sample stability and contrast [Lučić et al. 2013]. I adapted and established HPF/FS protocols for *C. elegans* samples for different applications. Due to the superior preservation [Rostaing et al. 2004], all samples used in this thesis were processed via HPF/FS. This technique makes it possible to study effects of mutations in synaptic proteins on synaptic ultra-architecture via electron tomography and to obtain high quality imaging data via focused ion-beam scanning electron microscopy.

1.6. Acquisition of large isotropic volumes of *C. elegans dauer* larvae with focused ion-beam scanning electron microscopy

Reconstructions of connectomes are based on huge volumes of electron microscopy imaging data. White and colleagues acquired these data for the adult *C. elegans* hermaphrodite via serial transmission electron microscopy [White et al. 1986]. This approach is technically extremely demanding, both on skill and time, and the only attempt published since was of the posterior connectome of the adult male [Jarrell et al. 2012]. New data-sets are essential to gain insights into variability between individuals and development of the connectome through the larval stages. Fortunately, modern automated serial imaging techniques are now available. One such technique is called focused ion-beam scanning electron microscopy (FIB-SEM) [Narayan and Subramaniam 2015]. FIB-SEM uses a focused beam of ions to vaporize a few nanometers off the block-face. The block-face is then scanned by the electron beam, and the process is iterated. FIB-SEM can generate a high-volume data-set of the ultrastructure that is near-isotropic, i.e., the resolution is the same in all three axial dimensions.

We need connectomes of larval stages if we want to gain insight into the development of the nervous system. There is an ongoing effort to map the larval connectomes of L1, L2, and L3 larvae. A combination of serial transmission electron microscopy (TEM) and serial block-face scanning electron microscopy (SBF-SEM) [Titze and Genoud 2016] is used to obtain these data-sets. However, so far there was no ongoing community effort to map the the so-called *dauer* stage (from German *Dauer*: endurance), although it is arguably highly interesting: The *dauer* larva is an alternative L3 stage with specialized survival and dispersal adaptations for harsh conditions [Cassada and Russell 1975; Albert and Riddle 1983; Golden and Riddle 1984]. Among other adaptations, they feature an especially thick cuticle and a closed mouth [Cox et al. 1981; Albert and Riddle 1983]. This way, they are able to withstand desiccation and also toxins [Erkut et al. 2013]. Due to metabolic adaptations, their life span is greatly increased although they do not feed and thus *dauers* are a valuable model for research of aging and energy conservation [Burnell et al. 2005; Russell and Kahn 2007; Kenyon Cynthia 2011; Houthoofd et al. 2002]. Moreover, they feature many anatomical and molecular similarities to dispersal stages of parasitic nematodes and represent a pre-adaptation of parasitism within their phylum

[Crook 2014]. For this reason, studying *dauer* neurobiology could aid the search for novel anti-parasitic drug targets and thus address the substantial socio-economic burden caused by nematode parasites.

Together with our collaborators,[1] I established a protocol for FIB-SEM imaging of *C. elegans dauer* larvae and generated high-volume isotropic data-sets of parts of several individuals with an effective voxel size of 5 nm.

While FIB-SEM is the technique of choice for larger volumes of tissue, it is less suitable for analysis of synaptic ultra-architecture. For localization and characterization of individual synaptic vesicles and protein complexes, I used electron tomography. This technique allows for 3D reconstruction of synapses with nanometer resolution and is thus suitable for analyzing more subtle effects of genetic mutations on synaptic architecture.

1.7. Electron tomography allows for 3D analysis of synaptic architecture on a nanometer scale

The field of connectomics focuses mostly on connectivity, i. e., the existence and number of connections between cells, and not the quality of the individual connections. In contrast to gap junctions, chemical synapses are relatively easy to map from electron micrographs due to their unique features like vesicle pools and dense projections (Figure 1.5). However, chemical synapses possess intricate machinery that has been researched for decades but is still not completely understood [Südhof 2004; Gan and Watanabe 2018]. To obtain accurate connectomes, these intricacies and the qualities of connections need to be taken into account [Haueis and Slaby 2017]. For example, chemical synapses can be either excitatory or inhibitory, and this crucial information can often not be derived from their ultrastructure. Also, to obtain the actual "strength" of a synapse, the rate of neurotransmitter release, electrophysiological studies are necessary. A comprehensive understanding of the mechanisms of synaptic transmission would surely support a more differentiated implementation of chemical synapses into connectomes. This will aid in the biological interpretation

[1] Dr. Yannick Schwab and Dr. Anna Steyer, EMBL, Heidelberg, Germany
Prof. Mei Zhen, Lunenfeld-Tanenbaum Research Institute, Mount Sinai Hospital, Toronto, Canada and Departments of Physiology and Molecular Genetics, University of Toronto, Toronto, Canada.

Figure 1.4.: **Schematic representation of the electron tomography work-flow.** Worms are embedded in resin, sectioned, and TEM tilt series of sections containing synapses are acquired. These are the basis for computational reconstruction of 3D tomograms. See section "Materials and methods" for details.

of connectomes as well as in *in silico* modeling approaches. The process is not simple; the presynaptic machinery alone is made up of dozens of proteins that work in conjunction in a spatially and temporally highly constricted manner [Südhof 2004; Takamori et al. 2006; Südhof 2013]. To reach a fundamental understanding of chemical synapses, we need to understand the interplay of the parts first, i. e., synaptic proteins in particular. There are many such proteins with poorly understood functions [Südhof 2004, 2013]. However, with HPF/FS and electron tomography, the study of effects of mutations in these proteins on synapse architecture and vesicle configuration is made possible at high spatial accuracy and very close to the native state. Electron tomography is based on the acquisition of tilt series of regions of interest via TEM. This way, a region of interest is imaged systematically from a series of angles. The resulting images can be back-projected by suitable software to create the electron tomograms (Figure 1.4) [Kremer et al. 1996]. I used this technique to describe chemical synapses on the ultrastuctural level at nanometer 3D-resolution to help complete our understanding of synaptic architecture and function. I chose a forward genetics approach and decided to investigate protein mutations that show synaptic phenotypes. In a comprehensive literature search I looked for such synaptic proteins with poorly understood functions on the molecular level. The kinase SAD-1 was one of the most interesting candidates. Though it has been shown that SAD-1 is involved in proper synaptic development and maintenance, one important piece of missing information is the architectural role of SAD-1 at the chemical synapse. Thus, I analyzed the ultra-architecture of chemical synapses in *sad-1* mutants with electron tomography and compared it to wild-type synapses.

1.7.1. The structure and composition of chemical synapses

Chemical synapses can exhibit many different shapes and sizes and specializations. I used the neuromuscular junction (NMJ) as model synapse in *C. elegans*. Figure 1.5 shows a schematic representation of a typical excitatory NMJ synapse. The axons of motor neurons run along the ventral or dorsal nerve cords (cf. Figure 1.2) and form *en passant* synapses. Body wall muscles extend muscle arms towards the nerve cords to establish the NMJs [White et al. 1976]. Synapses are usually dyadic or triadic, i. e., one presynapse connects to two or three postsynapses. Postsynapses can be muscle arms or inhibitory neurons that project to the opposite side of the worm body to inhibit muscles there [White et al. 1976].

All chemical synapses have in common that they release neurotransmitter from synaptic vesicles. In excitatory NMJs of *C. elegans*, this transmitter is acetylcholine. These synapses are therefore referred to as cholinergic synapses. Inhibitory NMJs use γ-aminobutyric acid (GABA) as transmitter and these synapses are thus called GABAergic. Neurotransmitter is released by fusion of the so-called clear core vesicles (CCV) with the plasma membrane. Transmitter molecules then diffuse freely and are detected by receptors in the postsynaptic membrane. The second type of synaptic vesicle is called dense core vesicle (DCV). They have an electron-dense core and typically contain neuropeptides and other signaling molecules [Njus et al. 1986; Richmond and Broadie 2002; Michael et al. 2006; Salio et al. 2006]. CCVs fuse at specialized regions of the plasma membrane, the active zones [Couteaux and Pécot-Dechavassine 1970; Südhof 2012]. In *C. elegans*, active zones in NMJs are marked by presynaptic electron-dense filamentous structures called dense projections (see Figure 1.5). Most vesicle membrane docking and fusion happens close to the dense projections. Further, the presynapse often features mitochondria, endosomes, and endoplasmic reticulum. Microtubules run along axons and synapses and offer structural support and "railtracks" for cellular transport. They are usually located distally to the active zone at the periphery or outside of the vesicle cloud.

The proper function of the chemical synapse is dependent upon an intricate machinery consisting of more than 100 different proteins. The vesicle membrane alone contains more than 80 proteins [Takamori et al. 2006]. For extensive reviews on the synaptic vesicle cycle see Südhof [2004, 2013].

1.7.2. The serine/threonine kinase SAD-1 is a regulator of synapse organization and neuron polarity

Crump et al. [2001] first described *sad-1* after they found the gene in a screen for regulators of synaptic development. They derived its name from "synapses of amphids defective," since they discovered the mutant from a defect in presynaptic vesicle clustering in ASI chemosensory neurons. It is a serine/threonine kinase (Figure 1.6). Their study revealed that SAD-1 is localized to synapse-rich regions of axons, promotes vesicle clustering in GABAergic motor neurons, and regulates axonal branching and termination. Furthermore, it was found that SAD-1 is involved in regulating neuronal polarity through a distinct mechanism [Hung et al. 2007] and it is also involved in regulating vesicle transport of both CCVs [Edwards et al. 2015]

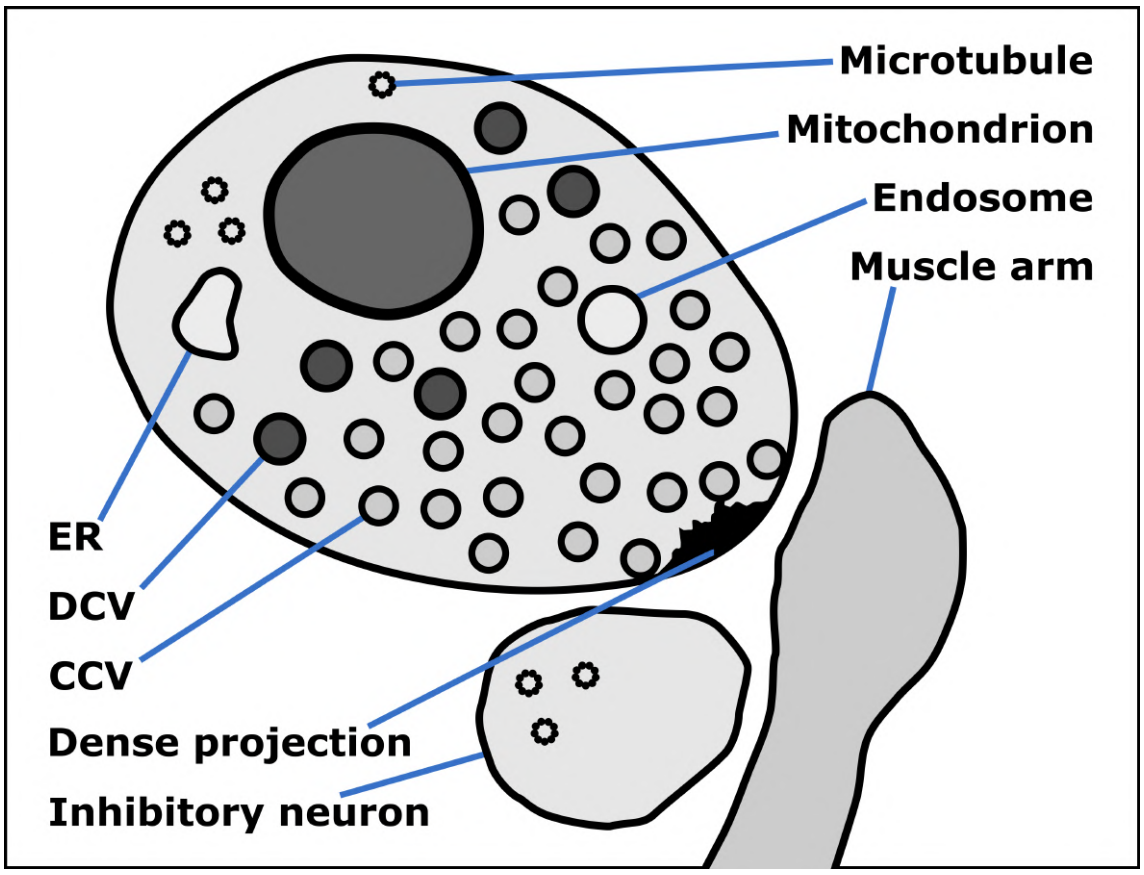

Figure 1.5.: **Schematic illustration of an excitatory NMJ synapse in *C. elegans*.** Typical structure of an excitatory cholinergic synapse of a motor neuron. Inhibitory neurons project to the opposite side of the body and relax muscles there. ER: endoplasmic reticulum, DCV: dense core vesicle, CCV: clear core vesicle.

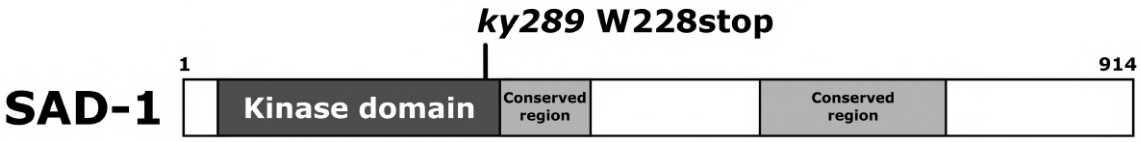

Figure 1.6.: **The domain structure of SAD-1.** SAD-1 contains a highly conserved kinase domain and two conserved regions. The *ky289* allele used in this thesis features a stop codon within the kinase domain and is considered a null allele [Crump et al. 2001]. Modified from Crump et al. [2001].

and DCVs [Morrison et al. 2018]. Knock-out of *sad-1* causes a distinct behavioral phenotype: The amplitude of the sinusoidal movement is reduced [Pekar 2013]. Crump et al. [2001] discuss a model where SAD-1 might regulate the transition from axon growth to synapse formation.

All these findings make it clear that SAD-1 is an important part of the synaptic machinery. Crump et al. [2001] and Hung et al. [2007] based that conclusion on thorough studies with mutant worm lines expressing transgenic fluorescent reporters and genetic analyses. Crump et al. [2001] also analyzed transmission electron micrographs of ultrathin plastic sections of glutaraldehyde-fixed worms and found that general synapse morphology seems intact but observed a decrease in vesicle pool density. Since chemical fixation with glutaraldehyde does not preserve the vesicle pool in a physiological state [Rostaing et al. 2006], I re-examined this observation with samples fixed via HPF/FS and electron tomography to increase resolution, especially in the axial dimension. As a result, I discovered distinct ultrastructural alterations in *sad-1* worms that helped in refining the model of SAD-1 function.

I studied normal synaptic functionality in *C. elegans* both in wild-type synapses and with the help of mutant lines. A deeper understanding of synaptic architecture and function can not only be derived from mutant analysis (from forward genetic screens) but also from studying dysfunction due to genetic diseases with impact on the nervous system. This is becoming increasingly relevant, as more and more neurological diseases are (re)classified as synaptopathies [Li et al. 2003; Forero et al. 2006; Brose et al. 2010; Schmitt et al. 2011; Won et al. 2013].

1.8. *C. elegans* expressing mutated human FUS protein as a model for amyotrophic lateral sclerosis

Amytrophic lateral sclerosis (ALS) is a severe disease of the locomotor system [Hardiman et al. 2017]. ALS is hypothesized to be a synaptopathy [Fogarty 2019], because the disease usually starts with dysfunction and degeneration of synapses, before axons and dendrites become dystrophic and the neurons undergo cell death [Chou 1992]. In ALS patients, motor neurons progressively degenerate which causes muscles to atrophy. One cause of the disease is a set of mutations in the Fused in Sarcoma (FUS) protein (Figure 1.7) [Kwiatkowski et al. 2009; Vance et al. 2009; López-Erauskin et al. 2018]. Wild-type FUS is located in the nucleus and is involved in DNA repair and many other processes involving DNA and RNA [Andersson et al. 2008; Lagier-Tourenne et al. 2010; Ratti and Buratti 2016]. Currently, the mechanisms that lead the mutated protein to cause motor neuron degeneration are still largely enigmatic. A few years ago, Murakami et al. [2012] expressed several human variants of disease-causing mutated FUS proteins in *C. elegans*. Notably, the worms showed ALS-like phenotypes. They died prematurely and locomotion decreased severely with age, pointing to a degeneration of the locomotor system by a dominant gain-of-function mechanism. The strength of the phenotype was correlated with the severity of the disease caused in humans by the same mutation variants. Thus it seems that the effect of mutated FUS on motor neurons is functionally conserved between humans and nematodes to a considerable extent. Also, the worm is genetically very tractable and motor neurons are readily accessible for imaging, e. g., via electron tomography and srAT. These features make *C. elegans* an attractive model for studying FUS disease mechanisms. Up to now, a HPF/FS electron tomography analysis is crucially missing. For this thesis, I investigated the ultrastructure of ALS-worm motor neurons, offered insights into disease mechanisms, and provided tools and hypotheses for future investigations.

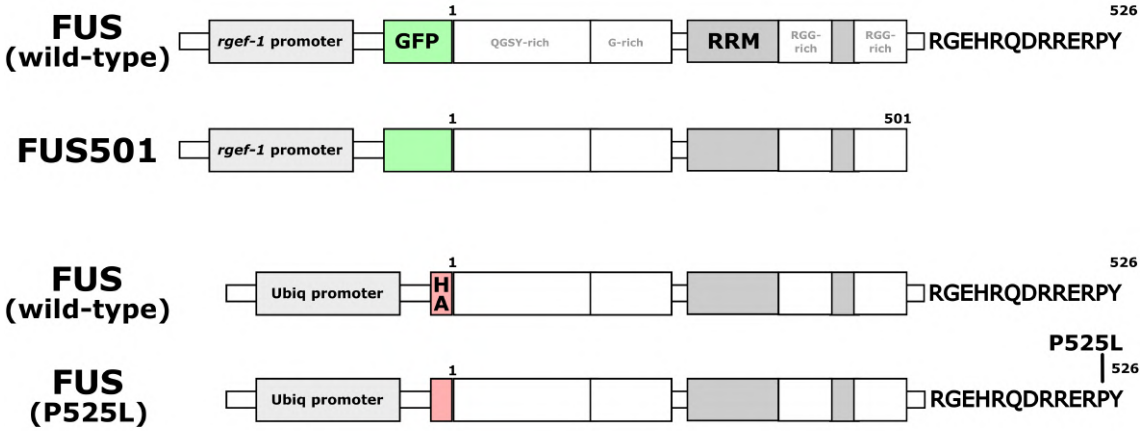

Figure 1.7.: **The alleles of FUS used in this thesis.** Wild-type human FUS contains regions enriched with certain amino acids (one-letter code given), a RNA recognition motif (RRM) and a nuclear targeting signal at the C-terminus. The FUS allele FUS(P525L) shows a point mutation in the C-terminus. The FUS allele FUS501 is truncated and 25 amino acids from the C-terminus are missing. The constructs featuring a GFP-tag and a pan-neuronal *rgef-1* promoter were expressed in *C. elegans*, the constructs featuring HA-tags and Ubiquitin promoters were introduced via lentiviral transduction in cultured primary mouse motor neurons. Modified from Murakami et al. [2012].

2. Materials and methods

2.1. Worm strains

Unless stated otherwise, all *C. elegans* worms were maintained according to standard methods [Brenner 1974]. The N2 Bristol strain was considered wild-type.

For gap junction analyses, the *C. elegans* strain ZM1158 was used, because this strain contains an out-crossed integrated array, where the innexin UNC-7S is fused to GFP and is expressed from an endogenous *unc-7* promoter: *lwIs48*[*Punc-7*::UNC-7S::GFP] [Starich et al. 2009; Yeh et al. 2009; Markert et al. 2016]. UNC-7S appears to be the dominant isoform of UNC-7 [Starich et al. 2009]. For simplicity, this isoform is shortened to UNC-7 in the following.

For the *sad-1* analysis, the strain CX5156 was used. The mutation allele in this strain is *sad-1(ky289)* [Crump et al. 2001] (Figure 1.6).

For the FUS analysis, three strains were used. ZM9566 expresses FUS501 and ZM5838 expresses wild-type FUS under control of a pan-neuronal *rgef-1* promoter [Murakami et al. 2012] (Figure 1.7). Additionally, the strain ZM9569 was used as N2 control in the FUS experiments only. This strain was used for creating ZM9566 and for outcrossing.

2.2. High-pressure freezing

High-pressure freezing is a technique for immobilizing biological samples for electron microscopy. The samples are subjected to >2100 bars of pressure and cooling rates of >20,000 K/s. These conditions facilitate the vitrification of the water within the sample. Vitrification means the water assumes an amorphous, glass-like state. This way, damaging ice crystals are avoided and ultrastructural features are preserved and stabilized in a near-native state.

Table 2.1.: **The cryoprotectants used in this thesis.**

Cryoprotectant	Sample type	Notes
E. coli OP50 bacteria paste	*C. elegans*, all stages	Results in dense, stable pellet. Best structure preservation, but individual worms can be hard to isolate
10-20 % bovine serum albumin in M9	*C. elegans*, especially *dauer* larvae	Results in somewhat stable pellet. Structure preservation for non-*dauers* not always ideal, but individual worms are easier to isolate, especially with lower concentrations of albumin
Hexadecene	Cultured neurons on sapphire discs	Hexadecene does not cross-link and gets removed during freeze-substitution

2.2.1. High-pressure freezing of *C. elegans*

All samples used in this thesis were cryo-immobilized using a EM HPM100 (Leica Microsystems) high-pressure freezing machine. For *C. elegans*, the standard procedure was to use freezing platelets (Leica Microsystems) with 100 µm recesses. They were slightly overfilled with an appropriate freeze protectant (see Table 2.1) and then worms were transferred into the platelet. A second platelet with a flat surface was placed on top as a lid. Some freeze protectant should spill out, indicating the volume is completely filled with no remaining air bubbles. Air bubbles collapse during the freezing process and compromise vitrification. The sample is processed by the machine and then stored in liquid nitrogen until freeze-substitution.

2.2.2. *E. coli* OP50 bacteria paste

A 100 ml volume of *E. coli* OP50 overnight culture was pelleted at 1,500 ×g, washed with 400 µl 20 % bovine serum albumin (BSA) in M9 [Stiernagle 2006] (3.0 g KH_2PO_4,

6.0 g Na_2HPO_4, 0.5 g NaCl, 1 ml 1 M $MgSO_4$, H_2O to 1 l; sterilize by autoclaving), spun down again, and carefully re-suspended in 20 µl 20 % BSA in M9.

2.2.3. High-pressure freezing of motor neurons

Primary motor neurons from mouse embryos were cultured by Michael Skoruppa[2] exactly according to Wiese et al. [2010] on 6 mm sapphire discs for six days prior to HPF/FS. Culture medium was removed and cells were immediately covered with hexadecene (see Table 2.1) and high-pressure frozen.

2.3. Freeze-substitution and resin embedding

Freeze-substitution is a process to fix and dehydrate cryo-immobilized samples for electron microscopy. Compared to classical fixation methods, fixation and dehydration take place at much lower temperatures, which results in significantly improved structure preservation in many tissues, including *C. elegans* [Rostaing et al. 2004]. Depending on specific needs, different freeze-substitution protocols have been used in this thesis.

2.3.1. Morphology protocol optimized for structure preservation

The protocol is originally based on Weimer [2006]. Table 2.2 gives an overview of the exact protocol used here. A description of the individual steps of the freeze-substitution and resin embedding can be found in Stigloher et al. [2011].

The morphology protocol uses glutaraldehyde for fixation and osmium tetroxide for fixation and staining. After substitution, samples are embedded in Epon or other epoxy resins, which are very hydrophobic and form covalent bonds with the sample, further stabilizing it and facilitating ultramicrotomy. The protocol produces richly stained membranes and preserves proteins, nuclei, and cytoplasm (cf. Figure 3.17). Unfortunately, epitopes are not preserved in this preparation, and the hydrophobicity of Epon repels antibodies from the specimen's surface. Thus, this protocol

[2] then in the group of Prof. Michael Sendtner, Institute of Clinical Neurobiology, University Hospital Würzburg, Würzburg, Germany

Table 2.2.: **Overview of the freeze-substitution and embedding protocol for optimized structure preservation.** At each step the indicated solution or chemical is added to the samples for the time and at the temperature given. RT: room temperature.

Step	Time	Temperature
0.1 % tannic acid and 0.5 % glutaraldehyde in acetone	24 h	-90 °C
0.1 % tannic acid and 0.5 % glutaraldehyde in acetone	72 h	-90 °C
4 washes with acetone	4 h	-90 °C
2 % osmium tetroxide in acetone	28 h	-90 °C
2 % osmium tetroxide in acetone	14 h	-90 °C to -20 °C
2 % osmium tetroxide in acetone	16 h	-20 °C
2 % osmium tetroxide in acetone	4 h	-20 °C to 4 °C
4 washes with acetone	2 h	4 °C
Acetone	1 h	4 °C to 20 °C
50 % Epon in acetone	5 h	RT
90 % Epon in acetone	16 h	4 °C
100 % Epon	3 h	RT
100 % Epon	3 h	RT
100 % Epon	3 h	RT
Embedding in 100 % Epon and curing	72 h	60 °C

is unsuitable for super-resolution array tomography (srAT) and immunostainings in general.

2.3.2. Immuno protocol for retention of antigenicity

Again, the protocol is originally based on Weimer [2006]. Table 2.3 gives an overview of the exact protocol used here. We published a detailed description of the individual steps of the freeze-substitution and resin embedding in Markert et al. [2017].

The immuno protocol uses potassium permanganate alone as fixative. After substitution, samples are embedded in LR White resin (Medium Grade Acrylic Resin,

Table 2.3.: **Overview of the freeze-substitution and embedding protocol for retention of antigenicity.** At each step the indicated solution or chemical is added to the samples for the time and at the temperature given. At the last two steps, samples are either kept at 4 °C and cured with UV light, or embedded at room temperature (RT) and cured at 52 °C.

Step	Time	Temperature
0.1 % potassium permanganate in acetone	24 h	-90 °C
0.1 % potassium permanganate in acetone	72 h	-90 °C
0.1 % potassium permanganate in acetone	11 h	-90 °C to -45 °C
4 washes with acetone	3 h	-45 °C
2/3 acetone and 1/3 ethanol	30 min	-45 °C
1/3 acetone and 2/3 ethanol	30 min	-45 °C
2 washes with ethanol	1 h	-45 °C
Ethanol	16 h	-45 °C to 4 °C
2 washes with ethanol	1 h	4 °C
50 % LR White in ethanol	16 h	4 °C
100 % LR White	1 h	4 °C
100 % LR White	4 h	4 °C
100 % LR White	16 h	4 °C
100 % LR White	3 h	4 °C or RT
Embedding in 100 % LR White and curing	96 h	4 °C UV or 52 °C

London Resin Company Ltd.). This methacrylate resin is less hydrophobic than epoxy resins like Epon and does not form covalent chemical bonds with the sample. These features render ultramicrotomy a bit more challenging, but epitopes remain accessible for antibodies. Thus, this protocol was used for all srAT applications.

2.3.3. Preparation of *C. elegans* larvae for FIB-SEM

To generate *dauer* larvae, 12 cm NGM lite plates with OP50 "lawn" were seeded with chunks from well-fed (i. e., non-starved) plates and incubated for one week at 20 °C. On the day of high-pressure freezing, the worms would have reached a

starved state and all worms were washed off with M9. The worms were incubated in 1 % SDS solution for 10 min to poison all non-*dauers*, then they were washed by centrifugation at 2000 ×g and re-suspended in M9 buffer. This washing step was repeated five times. The resulting pellet contains live *dauers* and dead worms of other stages. The pellet was poured onto the periphery of an unseeded NGM lite plate, and live *dauers* crawled out off the debris and spread on the plate as soon as the residual M9 evaporated enough for them to move on the agar surface. After 1-2 hours, the residual debris was removed by excising a chunk of agar using a spatula. The rest of the plate containing the *dauers* was washed off with M9. The *dauers* were centrifuged as before, and the pellet was re-suspended in 20 % BSA solution in M9. This suspension was directly pipetted into the HPF carriers. At least 20 worms were placed in each carrier. If the worm concentration was too low, pipetting from the bottom of the tube or re-centrifugation and re-suspension in a smaller volume was helpful.

After HPF/FS according to the standard protocol for morphology (see section 2.3.1), the worms were separated from the BSA pellets as soon as the first 100 % resin step was reached. Instead of Epon, the epoxy resin Durcupan was used here. Durcupan is more stable in the focused-ion beam and leads to more even milling of the sample [Hayworth et al. 2015].

To separate *dauers* from the pellet, the blackened pellet was carefully poked in between worms (if visible). This way, the BSA matrix tended to break around the worms and they fell out intact. Though most worms broke in the process, usually 2-5 intact worms per pellet could be obtained. If only the anterior or posterior part was necessary for an experiment, broken worms were usable. Individual worms were then moved with very thin and sharp needles held by forceps. The specimens were transferred to fresh Durcupan twice for 1 h and finally transferred to an Aclar film. To remove most of the resin from the worms, a needle or a toothpick was used to move the worms from the drop of resin across the plastic surface until they appeared dry. It was possible to remove almost all resin this way. This was very useful for SEM of surface structures, but for FIB-SEM, a little bit of support was crucial so that the sample did not fly off as soon as the point of contact with the surface is severed by milling. If it became apparent that too much resin had been removed, more resin was added to the worms to increase support. The minimally embedded worms were then cured at 60 °C for at least 48 h before processing them for FIB-SEM.

2.3.4. Embedding of cultured motor neurons

Sapphire discs with cultured neurons were processed either with the morphology protocol or immuno protocol (see above) and subsequently embedded in Epon or LR White. For curing, the discs were placed in 1.5 ml Eppendorff tubes and, in the case of using LR White, tightly sealed. The samples were otherwise processed exactly as worm samples.

2.4. Ultramicrotomy

Ultramicrotomy is a technique used to cut resin blocks with embedded biological (or other) samples in ultrathin sections <100 nm. This is absolutely necessary for transmission electron microscopy, since the electron beam must penetrate the section to create an image. For srAT, the surfaces of the sections are imaged by scanning electron microscopy. Here, section thickness determines the resolution in the axial dimension, both for electron micrographs and the immunostaining.

2.4.1. Ultramicrotomy for srAT

Preparation of the block
When preparing a block for srAT, several important points have to be considered. First, LR White and other methacrylate resins are quite brittle. Thus, care was taken when trimming the block with a razor blade. Second, block-faces were generally left quite large. This results in larger sections, which are easier to handle, easier to find under the microscope, and seem to better stick to the slide due to the adhesive surface. Usually, *C. elegans* samples were cured standing upright in gelatin capsules. Because of this, worms were orientated horizontally at the bottom of the capsule. To achieve cross sections of the worms, the bottom of the capsule was sawed off and glued to the side of an empty block of cured Epon using super glue or Epon. This way, the worms could be oriented and cross sectioned (Figure 2.1).

Considerations for section thickness
In general it is desirable to cut the sections as thin as possible, since section thickness determines the axial resolution of both the electron microscopy images and

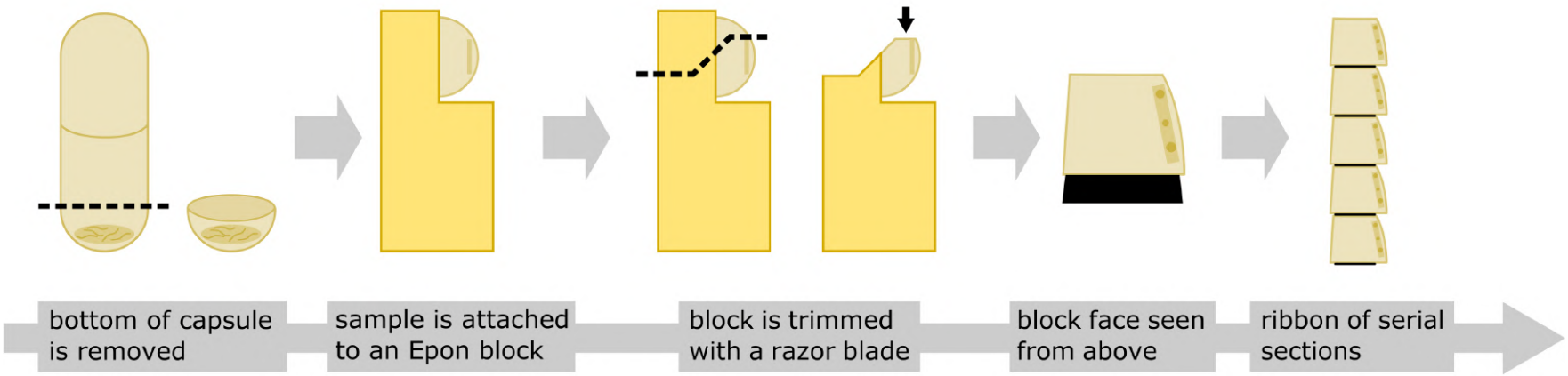

Figure 2.1.: **Preparation of LR White blocks for srAT.** Pellets with worms are cured in gelatin capsules. Using a fine fret saw, the bottom of the capsule containing the sample is cut off, the gelatin is removed, and the sample is glued to an Epon block with super glue or Epon. In the latter case, the sample was cured overnight at 60 °C without noticeable negative effects on antigenicity for the antibodies used here. The resulting block is trimmed with a razor blade to form a pyramid. The arrow points at the block-face, which is depicted as seen from above in the next pictograph. Darker circles indicate cross-sectioned worms embedded in the pellet created during HPF/FS. Glue (black area) is applied to the lower edge of the block-face prior to serial sectioning. It is recommended to add black pigment to the glue to facilitate localization of sections with a light microscope (cf. Markert et al. [2017]).

the immunofluorescence images. However, thinner sections are more challenging to cut and reliable serial sectioning might be impossible. Moreover, the contrast can suffer during scanning electron microscopy. This happens presumably because the electrons hit the glass surface underneath the sections when they are too thin. With my samples and our scanning electron microscope, 100 nm proved to be the best overall compromise. Sections cut for srAT in this thesis are at 100 nm, unless stated otherwise.

Serial sectioning

Methacrylate resins like LR White are more hydrophilic than epoxy resins. For this reason they hardly form section ribbons on their own. It was necessary to add glue to the block to achieve proper ribboning. A drop of contact adhesive (Pattex Gel Compact) was thinned out with xylene roughly 1:1 in a small dish using two toothpicks. I found the best performance, when the glue was barely stringy, i. e., when removing a toothpick from the mixture, a string formed but snapped almost immediately. The glue was applied to the lower edge of the pyramid of the block. Glue spilled on top of the block-face only compromised the first section. If ribboning was inconsistent, glue was applied to the opposite edge of the pyramid as well. Glue on the lateral sides negatively affected sectioning.

Transferring sections to glass slides

Individual sections or short ribbons floating in the knife's boat were retrieved with a wire loop and directly transferred to a glass slide. Slides coated with poly-L-lysine (Polysine, Thermo Fisher) were used to improve adhesion of the sections to the slides. I found the best method to transfer sections from loop to slide was to lower the loop, sections up, on the slide, gently blowing on the sections, and lifting up the loop to make the water film rupture. The sections then floated on a drop of water. They were left to dry in a dust-free place at room temperature before staining. For most srAT experiments, long ribbons with dozens or even hundreds of sections were desired. In this case, a special diamond knife with a boat large enough to accommodate glass slides (histo Jumbo diamond knife, DiATOME) was used. Slides were submerged in the boat before sectioning. Then the desired number of sections was cut without interruption. If necessary, a long ribbon was carefully divided into smaller ribbons using two mounted eyelashes. Sub-ribbons were then placed next to each other on the same slide or on separate slides. To transfer a ribbon to the slides, the ribbon was carefully moved towards the edge of the water film on the slide with a mounted eyelash. The lower edge of the first section was

attached to the dry glass. At this point, the slide could be slowly lifted out of the boat. The ribbon stayed on the slide while the water drained. Alternatively, if the ribbon was unstable, the water was removed from the boat with a syringe to make the sections attach to the slide.

2.4.2. Ultramicrotomy for electron tomography

Preparation of the block
Epoxy resins like Epon can be readily trimmed with razor blades. For electron tomography, it is usually desirable to have many sections per grid and also to obtain as much stability as possible, as the grid is continually imaged via tilt series. To achieve this, blocks were trimmed as indicated in Figure 2.2. This way, many sections fitted on a slotted grid and the sections overlapped on both sides with the grid.

Considerations for section thickness
In electron tomography, sections are generally thicker to obtain larger volumes of regions of interest. However, resolution does suffer if sections are too thick. For imaging with a 200 kV TEM, I used sections up to 250 nm with good results. Sections between 150 and 200 nm in thickness were favored.

Serial sectioning and transfer to slotted grids
Serial tomograms can be made from serial sections. Several hundred nanometers of a continuous structure or series of cells can be reconstructed in 3D this way. For this, Epon sections are used as described above, because they ribbon well on their own. In rare cases, glue was added to the block to facilitate ribboning (cf. Figure 2.1). To minimize loss of sections, the desired final number of sections was cut in one long ribbon. Then, the ribbon was subdivided into chunks using two mounted eyelashes. Two sections were poked with the eyelashes and pulled apart. The chunks were attached to a hair fixed to the knife's boat with tape. This way, they did not float away, which might confuse the sequence. The hair was even more helpful when picking up the ribbons with a slotted grid. It was much easier to properly align the grid with the ribbon, since it does not move away from the grid (Figure 2.2). As mentioned earlier, the sections were intentionally broader than the slot of the grid so that they overlapped with the grid for improved stability.

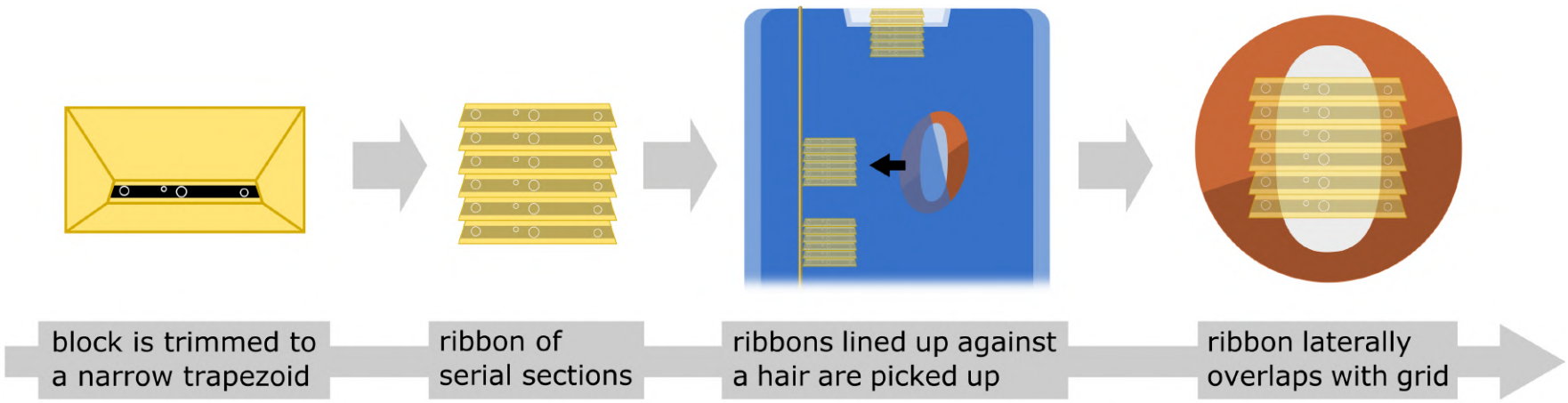

Figure 2.2.: **Ultramicrotomy strategies for electron tomography.** Pellets with worms are embedded in Epon to achieve a desired orientation. After curing, the block is trimmed to a pyramid with a very narrow trapezoid block-face. Serial sections with a thickness of up to 250 nm are cut to a ribbon. Using two eyelashes (not depicted), the ribbon can be divided into sizable chunks and lined up against a hair that has been attached to the knife's boat with tape. This way, picking up sections with a slotted grid is greatly facilitated. In the end, the sections overlapped with the grid on both sides to achieve high stability during imaging.

Table 2.4.: **Overview of the immunostaining protocol for LR White sections on glass slides.**

Step	Time
Blocking with 0.1 % BSA and 0.05 % Tween 20 in Tris-buffer	5 min
Primary antibody in blocking solution	1 h
4 washes with Tris-buffer	20 min
Secondary antibody in blocking solution	30 min
4 washes with Tris-buffer	20 min
DNA stain with Hoechst or propidium iodide at 1 µg/ml in Tris-buffer	10 min
2 washes with Tris-buffer	2 min
dSTORM imaging or mounting in Mowiol for SIM imaging	

2.4.3. Ultramicrotomy of cultured motor neurons

The following applies to samples embedded in Epon and LR White equally. To remove the samples from the 1.5 ml plastic tubes, the tips of the tubes were removed with a saw or razor blade and the block pushed out. The block was then briefly submerged in liquid nitrogen and warmed up again. This procedure was repeated, until the sapphire disc came off from both sides of the block. With a stereo microscope and oblique lighting, the block containing the cells was determined. On the correct side, the neurons were visible, whereas the other side was smooth. Using a fret saw, the block was split in fourths or eights, since the whole surface was much too large for sectioning. The smaller pieces were either mounted directly for sectioning or glued to an empty resin block first. Then they were trimmed and sectioned as usual and described above. Special care was taken to align the knife's edge with the block face, since the very first section already contained cell material.

2.5. Immunostaining

Ultrathin sections of LR White-embedded tissue were immunostained for srAT. Ultramicrotomy exposed epitopes at the section surface. Thus, sections could be

Table 2.5.: **Primary antibodies used in this thesis.**

Antibody (type)	Dilution	Species	Source
FUS (polyclonal)	1:1000	Rabbit	Bethyl #A300-293A
GFP (polyclonal)	1:500	Chicken	Abcam #ab13970
HA-tag (monoclonal)	1:100	Rat	Roche #11867431001
α-Tubulin (monoclonal)	1:1000	Mouse	Sigma #T5168
β-Actin (monoclonal)	1:200	Mouse	GeneTex #GTX26276

stained, even though antibodies do generally not penetrate the resin [Stierhof et al. 1991].

Table 2.4 gives an overview of the immunostaining protocol. The detailed protocol has been published in Markert et al. [2017]. In brief, sections were placed in a humid chamber, and blocking buffer was applied to the sections prior to staining with primary and secondary antibodies. They were washed with buffer and then stained with a DNA stain, where applicable. Lastly, sections were mounted with Mowiol and stored at 4 °C for up to a week before fluorescence imaging.

Table 2.5 shows the list of primary antibodies and Table 2.6 the list of secondary antibodies used in this thesis.

2.6. Imaging for srAT

For srAT plastic sections were imaged first by super-resolution light microscopy, then by scanning electron microscopy. Two things were kept in mind during imaging. First, orientation must be set and maintained. The section and region of interest were noted at all times so that they could be found again in the next imaging modality. Second, processing for SEM is an irreversible process. All potential regions of interest were imaged and the data was saved in at least two separate locations before SEM imaging. The following workflow of srAT imaging has been published in detail [Markert et al. 2016, 2017]. The general workflow and some unpublished rationale, information, and techniques are given.

Table 2.6.: **Secondary antibodies used in this thesis.** Excitation gives the exact wavelength of the laser used during imaging in nm. All secondary antibodies were used at a dilution of 1:500.

Antibody	Excitation	Used for	Manufacturer
Alexa Fluor 488 anti-mouse	488 nm	SIM	Thermo Fisher Scientific
Alexa Fluor 488 anti-mouse	488 nm	SIM	Jackson ImmunoResearch
Alexa Fluor 488 anti-chicken	488 nm	SIM	Thermo Fisher Scientific
Alexa Fluor 488 anti-rat	488 nm	SIM	Jackson ImmunoResearch
Alexa Fluor 594 anti-rabbit	561 nm	SIM	Jackson ImmunoResearch
Alexa Fluor 647 anti-chicken	640 nm	dSTORM	Thermo Fisher Scientific
Alexa Fluor 647 anti-mouse	640 nm	dSTORM	Thermo Fisher Scientific
Alexa Fluor 647 anti-rabbit	642 nm	SIM	Thermo Fisher Scientific
Cy5 anti-mouse	642 nm	SIM	Jackson ImmunoResearch
Texas Red anti-mouse	561 nm	SIM	Jackson ImmunoResearch

2.6.1. Structured Illumination Microscopy (SIM)

Since the sections are very thin and transparent, it can be challenging to locate them in the microscope. Depending on the sample, it can be easier to locate the sections by fluorescence or by transmitted light. Black glue (see 2.1) [Markert et al. 2017] can help a lot with finding the sections in the latter case, but the glue is fluorescent, so it was also suitable for searching in this modality. The sections were also marked with a pen on the glass slide. This greatly decreased the search area.

In general, the staining faded very quickly, since only the surface of the section was stained. To minimize fading, illumination outside of image acquisition was kept at a minimum. The rule-of-thumb for imaging time was that about one hour is needed for imaging 10 sections.

2.6.2. Direct stochastic optical reconstruction microscopy (dSTORM)

Imaging by dSTORM is more involved than imaging by SIM and was performed in collaboration with Dr. Sven Proppert.[3] The detailed description of how we performed dSTORM imaging and image reconstruction can be found in Markert et al. [2016]. Our setup using PDMS chambers attached to high-precision cover slips allowed for imaging of at least three regions of interest before the buffer needed to be replaced.

2.6.3. Contrasting and carbon coating

Contrasting was achieved by incubation of the sections in 2.5 % uranyl acetate in ethanol for 15 min and 50 % Reynolds' lead citrate [Reynolds 1963] in ddH_2O for 10 min. The glass slides were reduced in size before contrasting, so less reagent was used and more samples could be processed at once. The published protocol was since adjusted such that the glass pieces were put section-down on drops of the contrasting reagents. This resulted in more reliable contrasting. During incubations, samples were covered to minimize evaporation. While incubating in lead citrate, sodium hydroxide pellets were placed around the samples to decrease local carbon dioxide

[3] then in the group of Prof. Markus Sauer, Department of Biotechnology and Biophysics, Biocenter, University of Würzburg, Würzburg, Germany

concentration, as carbon dioxide forms a precipitate with lead citrate. In between contrasting steps, the slides were washed first in ethanol, then in 50 % ethanol in ddH_2O, and finally in ddH_2O. After contrasting, they were thoroughly washed in ddH_2O and dried with pressurized air.

Carbon coating was usually performed right after contrasting. Based on the shadow cast on a piece of white filter paper, I estimated the thickness of the carbon layer necessary to quench charging to be about 10 nm. If in doubt, a thin carbon layer was tested first. In case there was charging, the samples were coated again until it ceased. If the carbon layer was too thick, SEM imaging resolution was negatively affected.

2.6.4. Scanning electron microscopy (SEM)

All scanning electron microscopy was performed with a field emission scanning electron microscope JSM-7500F (JEOL, Japan) with LABE detector (for back scattered electron imaging at extremely low acceleration voltages). The acceleration voltage was kept at 5 kV at all times, the probe current was kept at 0.3 nA. Imaging was generally performed at 10 µA beam current or lower. The resulting working distance was 6-8 mm.

Samples for srAT were generally stable and stored at normal atmosphere in a dust-free container; they could be imaged many times. Some samples showed significant burning of the imaged region, especially at higher magnifications. Worm samples were typically stable, whereas sections of brain tissues of insects and zebrafish were often very susceptible to beam damage, for unknown reasons. In some cases, the burning happened so quickly that the sections formed bubbles and the tissue was destroyed before it could be imaged. It proved effective to slowly accustom the section to the electron beam. This was achieved by scanning the sections first at much lower beam currents for a few times before switching to the beam current that is optimal for imaging contrast (10 µA).

2.6.5. Correlation

Correlation strategies and procedures are described in detail in Markert et al. [2017]. Briefly, there were two main strategies used: manual and semi-automatic. Manual

correlation was performed with Inkscape (version 0.91; http://www.inkscape.org). For semi-automatic correlation, the eC-CLEM plugin [Paul-Gilloteaux et al. 2017] for the software Icy [de Chaumont et al. 2012] was used. Here, a small number of markers are placed on structures visible in both imaging modalities. The images are then superimposed automatically on the basis of these manually placed markers.

2.7. FIB-SEM Imaging

FIB-SEM imaging was performed in collaboration with Dr. Anna Steyer.[4] How we processed the samples and acquired images with FIB-SEM is described in detail in Schieber et al. [2017]. Briefly, a piece of Aclar film containing a worm was cut out with a scalpel, mounted on a specimen holder and surrounded with conductive silver paint. The samples were sputter-coated with gold prior to imaging. After a region of interest was identified in SEM mode, a trench was milled with the FIB to gain access to the ultrastructure. We then acquired images in between 8 nm milling steps.

2.8. Preparation of sections and imaging for electron tomography

Electron tomography was used in cases where smaller volumes of samples needed to be imaged at nanometer resolution. Imaging with the SerialEM [Mastronarde 2005] and IMOD [Kremer et al. 1996] software packages is semi-automatic and typically several tomograms could be reconstructed in a day of work. A 200 kV JEM-2100 (JEOL) electron microscope equipped with a TemCam F416 4k×4k camera (Tietz Video and Imaging Processing Systems) was used for all TEM imaging and electron tomography.

[4] then in the group of Dr. Yannick Schwab, EMBL, Heidelberg, Germany; now Department of Neurogenetics, Max Planck Institute of Experimental Medicine, Göttingen, Germany; Electron Microscopy Core Unit, Max Planck Institute of Experimental Medicine, Göttingen, Germany; Center for Nanoscale Microscopy and Molecular Physiology of the Brain, Göttingen, Germany

2.8.1. Contrasting

Contrasting was achieved by floating the grids sections down on drops of 2.5 % uranyl acetate in ethanol for 15 min and 50 % Reynolds' lead citrate [Reynolds 1963] in ddH_2O for 10 min. During incubation, samples were covered to minimize evaporation. During incubation in lead citrate, sodium hydroxide pellets were placed around the samples to decrease local carbon dioxide concentration. Carbon dioxide forms precipitates with lead citrate. In between contrasting steps, the grids were washed first in ethanol, then in 50 % ethanol in ddH_2O, and finally in ddH_2O. After contrasting, they were thoroughly washed in ddH_2O and blotted dry with filter paper.

2.8.2. Carbon coating and placement of gold fiducials

Grids used for electron tomography were coated with a thin layer of carbon to prevent charging during imaging at high tilt angles. The carbon layer had an approximate thickness of 3 nm.

Gold fiducials were used to facilitate tomogram reconstruction (see section 2.8.4). To achieve fiducial placement, an antibody conjugated with 10 nm gold particles was used. Many different antibodies from different species were used with no apparent differences in performance. The antibody was diluted 1:10 with ddH_2O and 50 µl of this dilution were pipetted on a piece of clean parafilm. The carbon-coated grids were then floated on the drop for 10 min on each side, with a single wash in ddH_2O in between and at the end. A single wash meant that the grid was submerged in water for one second and then immediately dried with a filter paper. The gold fiducial placement was always performed right after carbon coating or at most a few hours after. For unknown reasons, longer delays caused very pronounced electron-dense precipitation on the sections, making them unsuitable for imaging in extreme cases.

2.8.3. Acquisition of tilt series

In theory, higher tilt angles result in more complete reconstructions. However, in practice tilt angles greater than 70 ° in either direction were never used. Effective section thickness increases at higher angles and focusing the image is harder.

Thus, images taken at high angles are blurry and dark and do not contribute many ultrastructural features. When tilt angles from 60 ° to -60 ° were used, loss in reconstruction quality at these angles compared to 70 ° to -70 ° was imperceptible. Tilt series for this thesis were acquired either from 60 ° to -60 ° or from 70 ° to -70 °.

Double tilts were performed where appropriate and possible, i. e., tilt series from a region of interest were acquired in two orthogonal tilt axes. This was achieved by manually rotating the grid by about 90 ° in the sample holder. Double tilts improved tomogram quality significantly. They were not performed when the tomogram of a single axis was sufficient to answer the specific questions or if it was just not possible due to loss of the section, typically because of grid damage. To make it easier to rotate the grids by 90 °, it was always made sure that the slotted grids were placed either in vertical or horizontal orientation in the holder.

In the course of the thesis work, different settings and approaches for imaging with the serial EM software were used. In the end, a best practice approach was reached that is time efficient without compromising quality. This best practice is described in the appendix (section A.3).

2.8.4. Tomogram reconstruction

All tomograms were reconstructed with the eTomo software from the IMOD package [Kremer et al. 1996]. Gold fiducials were always included to improve the alignment of the tilt series. For the step of tomogram positioning, the option “find boundary model automatically” was used. Manual adjustments of the boundary model were almost never necessary. Tomograms were always created using the “Back Projection” algorithm.

2.8.5. Segmentation and 3D reconstruction

Segmentation and 3D reconstruction were performed with the 3dmod software from the IMOD package [Kremer et al. 1996]. All structures except for the vesicles were segmented as closed objects using the “sculpt” tool. Clear core and dense core vesicles were annotated as perfect spheres by creating a point in the center of a vesicle using the “normal” drawing tool. This point was then resized with the mouse wheel to match the outer dimensions of the given vesicle. Global quality of

points was set to 4 to achieve smooth spheres and the "drawing style" of points was set to "fill" to obtain closed surfaces. All other objects except the dense projections were meshed to obtain closed surfaces here as well. Dense projections were left with the default drawing style "lines". The "interpolator" tool was used whenever appropriate. For large structures like the plasma membranes, gaps of 20 virtual sections or more were linearly interpolated. For mitochondria and microtubules typically gaps of 10 sections were interpolated. Larger spherical structures like endosomes were interpolated with the "spherical" option. Dense projections were not interpolated.

2.9. Quantitative vesicle analyses

In the FUS and SAD-1 projects, electron tomograms were used to reconstruct and classify synaptic vesicles. This was performed manually or in an automated manner.

2.9.1. Automated vesicle reconstruction and classification

Automatic vesicle reconstruction from electron tomograms was performed via macros for the open source image processing software Fiji [Schindelin et al. 2012] as described in Kaltdorf et al. [2017]. They were then automatically classified into clear core and dense core vesicles according to Kaltdorf et al. [2018]. Manual adjustments of the outcomes were not performed. However, if overall classification results for a given tomogram were not satisfactory, this tomogram was excluded from analysis.

The active zone was determined manually for the classification macro. A point on the plasma membrane that is closest to the center of gravity of the dense projection seen in a given tomogram was set as the center of the active zone. The center of gravity of the dense projection was chosen by visual judgment of the user during the macro workflow.

2.9.2. Manual vesicle reconstruction and classification

Manual vesicle reconstruction from electron tomograms was performed via 3dmod from the software package IMOD [Kremer et al. 1996]. The center points of vesicles

were set by the user's judgment and set as centers of spheres with the approximate outer diameter of the vesicles.

The dense projections were segmented manually and their center of gravity was determined with the "imodinfo" function of IMOD. The center of the active zone was defined as the intersection of the inner plasma membrane and an orthogonal line through the center of gravity of the dense projection. Linear distances of vesicles to the active zone were measured with the "measure" tool in 3dmod from the centers of the vesicles to the center of the active zone.

2.10. Statistical analyses

Statistical analyses and their representations were performed with R [R Core Team 2019]. The Mann-Whitney-Wilcoxon test was used to determine statistical significance. The following significance levels were applied: * $p<0.05$, ** $p<0.01$, *** $p<0.001$.

Variability of quantitative data samples was measured via median absolute deviation (MAD). The MAD is more robust against outliers and suitable for non-parametric data, i. e., data that does not show normal distribution [Pham-Gia and Hung 2001]. It is defined as the median of the absolute deviations of the data's median:

$$MAD = median(|x_i - \bar{x}|)$$

for an univariate data-set $x_1, x_2, ..., x_n$ where $\bar{x}$ is the median of the data: $\bar{x} = median(x)$.

3. Results

3.1. Super-resolution array tomography enables mapping of gap junctions at the *C. elegans* connectome

Electrical synapses formed by gap junctions play an important role in the nervous system and are crucial components of the connectome. However, mapping of gap junctions is difficult. Their ultrastructural features are subtle, so it can be challenging to identify them in electron micrographs. With light microscopy, specific staining of gap junction proteins is possible, but without the ultrastructural context, signals cannot be assigned to specific cells in most cases. I developed an approach combining electron microscopy with fluorescence light microscopy and was able to map gap junctions with high precision and accuracy. Notably, this was possible while also retaining the molecular identity of gap junction proteins. My approach is based on array tomography [Micheva and Smith 2007]. I advanced this technique by implementing super-resolution light microscopy and offer new strategies for immunostaining, correlation, and structure preservation. I therefore call this approach super-resolution array tomography (srAT). Figure 3.1 gives the schematic overview of the srAT work-flow. Most of the results shown here have been published in Markert et al. [2016]. A detailed protocol with more application examples was later published as a book chapter [Markert et al. 2017]. The srAT approach is very flexible in its application and has successfully been applied beyond neuroscience, e.g. for the analysis of uncultivable symbiotic bacteria in host environment [Jahn et al. 2016] or localization of lipid rafts in MRSA [García-Fernández et al. 2017].

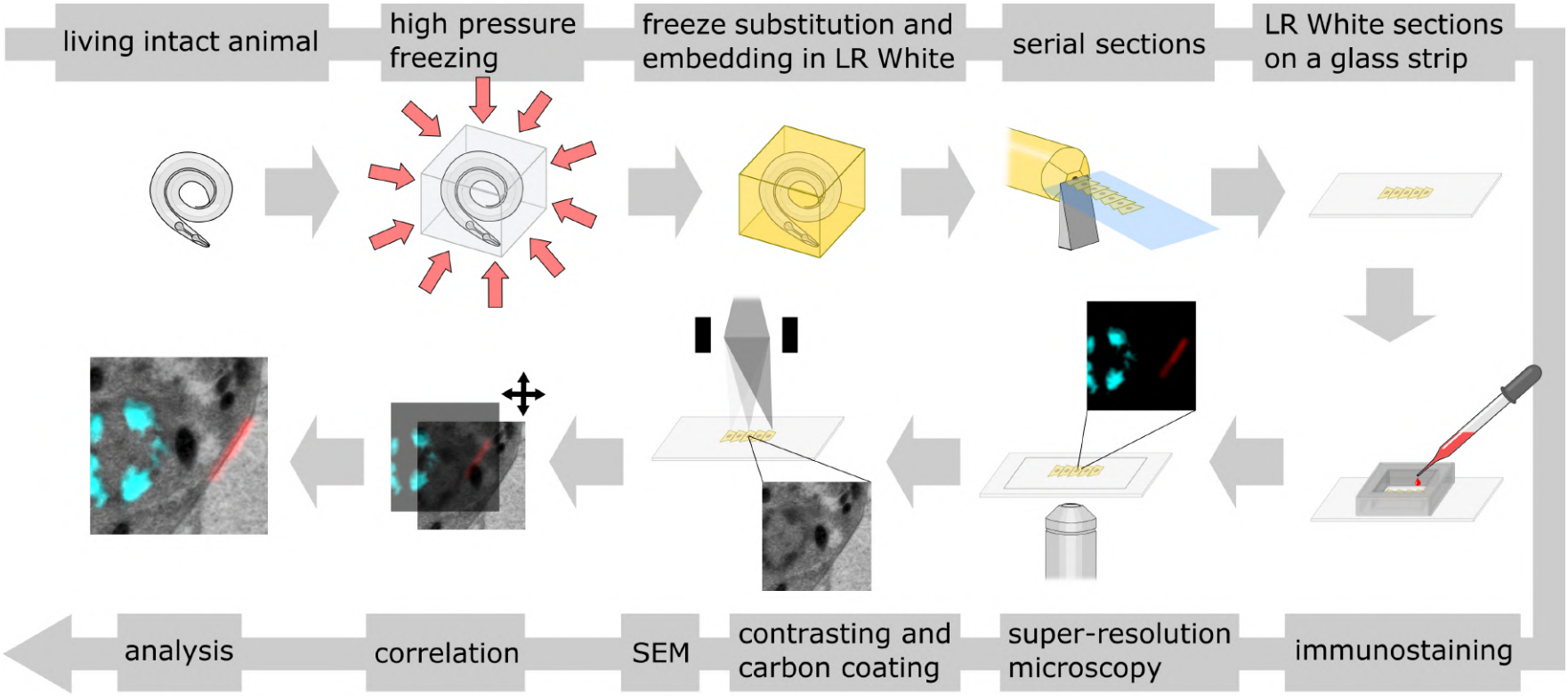

Figure 3.1.: **Schematic overview of the srAT workflow.** Samples are processed via high-pressure freezing and freeze-substitution and embedded in LR White. Serial ultrathin sections are stained and imaged with super-resolution light microscopy. After processing for electron microscopy, the sections are imaged again with scanning electron microscopy. The resulting images of any given region of interest are correlated with each other. Thus, specific signals can be analyzed in their full ultrastructural context. See section "Materials and methods" for details. Modified from Markert et al. [2016].

3.1.1. Gap junctions of the retrovesicular ganglion mapped with srAT

To showcase the mapping of gap junctions in *C. elegans*, I chose the retrovesicular ganglion (see Figure 3.4A). This ganglion connects the nerve ring with the ventral nerve cord and has a well-defined anatomy. This makes it easier to identify specific cells.

We used a worm line that over-expresses the innexin UNC-7 tagged with GFP in an *unc-7* mutant background. UNC-7 is widely expressed throughout the nervous system and mutant studies have shown that it is important for proper locomotion and movement [Lewis and Hodgkin 1977; Yeh et al. 2009; Yemini et al. 2013]. The GFP-tag makes it possible to observe UNC-7 distribution *in vivo* and offers a good target for stainings. Further, good antibodies against GFP are commercially available and well-characterized. Thin sections (100 nm) of the retrovesicular ganglion in a young adult hermaphrodite worm were collected on glass slides. After staining against GFP, the samples were imaged with structured illumination microscopy (SIM) [Gustafsson 2000]. This technique offers significantly higher resolution than diffraction-limited fluorescence microscopy (Figure 3.2). After completing SIM imaging, samples were processed and imaged via scanning electron microscopy (SEM). SIM and SEM images of the same regions of interest were correlated and superimposed using intrinsic independent landmarks for registration (Figure 3.3).

Figure 3.4 shows a typical result for one section. In the SIM image, nuclei (Hoechst), microtubules, and UNC-7 (via GFP) are stained. Neither the SIM nor SEM image alone is sufficient to identify gap junctions. With SIM, the ultrastructural context is missing completely, whereas with SEM gap junctions cannot be localized without specific staining at this resolution. However, the correlated image made it possible to identify and characterize the gap junction stained here. Identification of neurons was performed by Daniel Witvliet (Mei Zhen group[5]) on 30 consecutive sections. To distinguish real signal from background noise, a gap junction staining was only counted as such, if it could be found on at least two consecutive sections at the same location. Some signals were clearly intracellular and very likely stained UNC-7 located in endoplasmic reticulum (Figure 3.5). This shows how srAT makes it possible to differentiate between true gap junction signal and instances of UNC-7 trafficking

[5]Lunenfeld-Tanenbaum Research Institute, Mount Sinai Hospital, Toronto, Canada and Departments of Physiology and Molecular Genetics, University of Toronto, Toronto, Canada

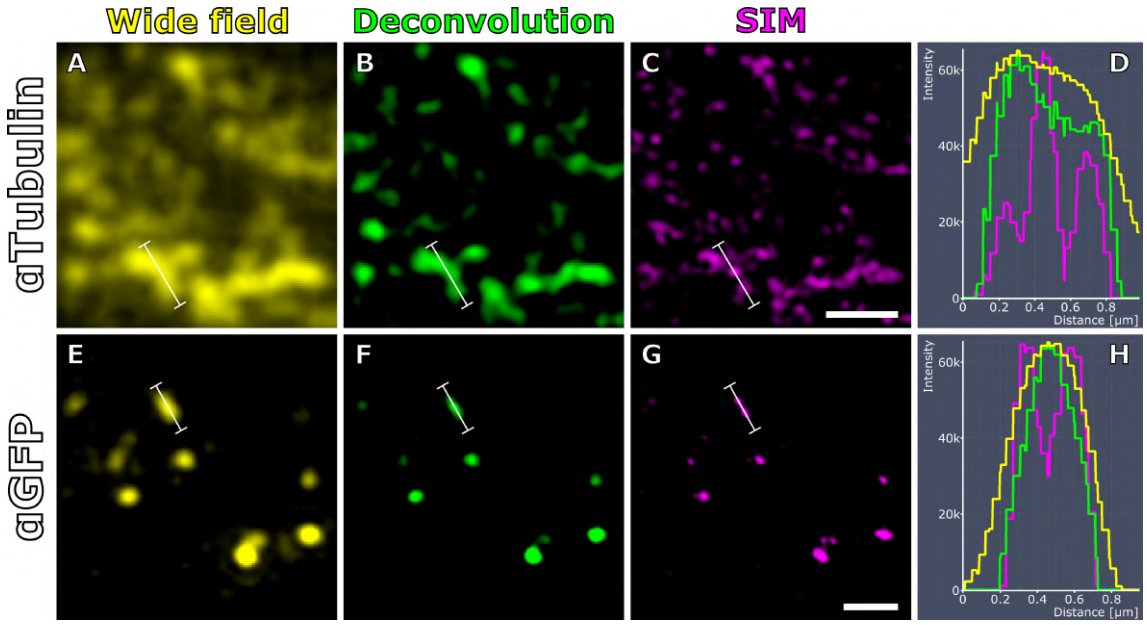

Figure 3.2.: **Structured Illumination Microscopy increases resolution beyond the diffraction limit.** **A** Anti-Tubulin staining on a 100 nm-LR White section through nervous tissue of *C. elegans* as it appears with standard wide field fluorescence microscopy. **B** Deconvolution algorithm on raw data in **A** partially improves lateral resolution by removing out-of-focus signals. This result is comparable to results obtained with confocal laser scanning microscopy. **C** Same raw signal data as in **A** after application of the structured illumination algorithm. Compared to deconvolution, the resolution is significantly increased. **D** The intensity profile along the line depicted in **A-C** reveals three clearly distinct signal peaks that could not be resolved by deconvolution. **E-H** A second example corresponding to **A-D**, but depicting an anti-UNC-7::GFP staining in a different region of the same section. Scale bars: 1 µm. From Markert et al. [2016].

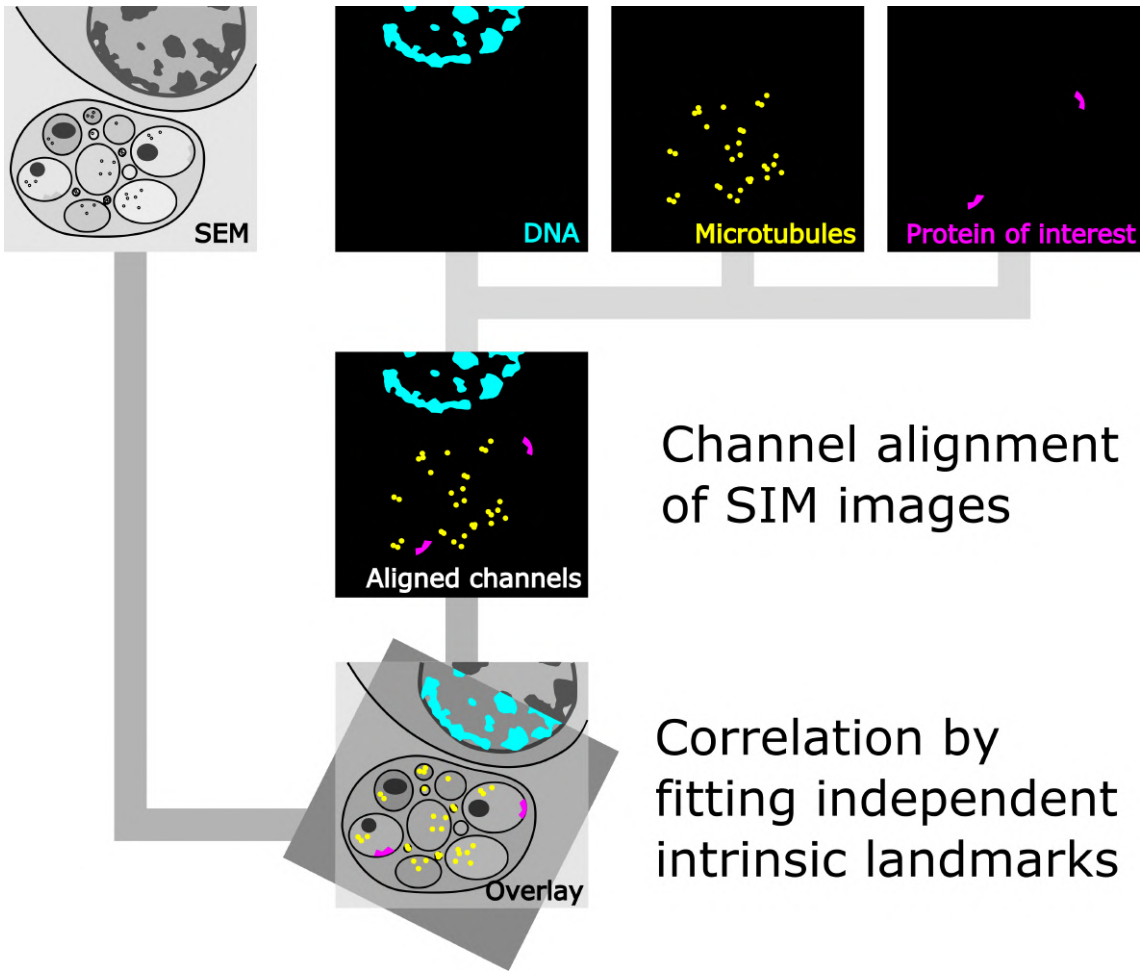

Figure 3.3.: **Schematic illustration of correlation by fitting independent intrinsic landmarks.** SIM channels are aligned and then correlated with the SEM image using landmarks independent of the protein of interest. DNA or other proteins (here: microtubules) can be stained, depending on required correlation precision and feasibility. Modified from Markert et al. [2016].

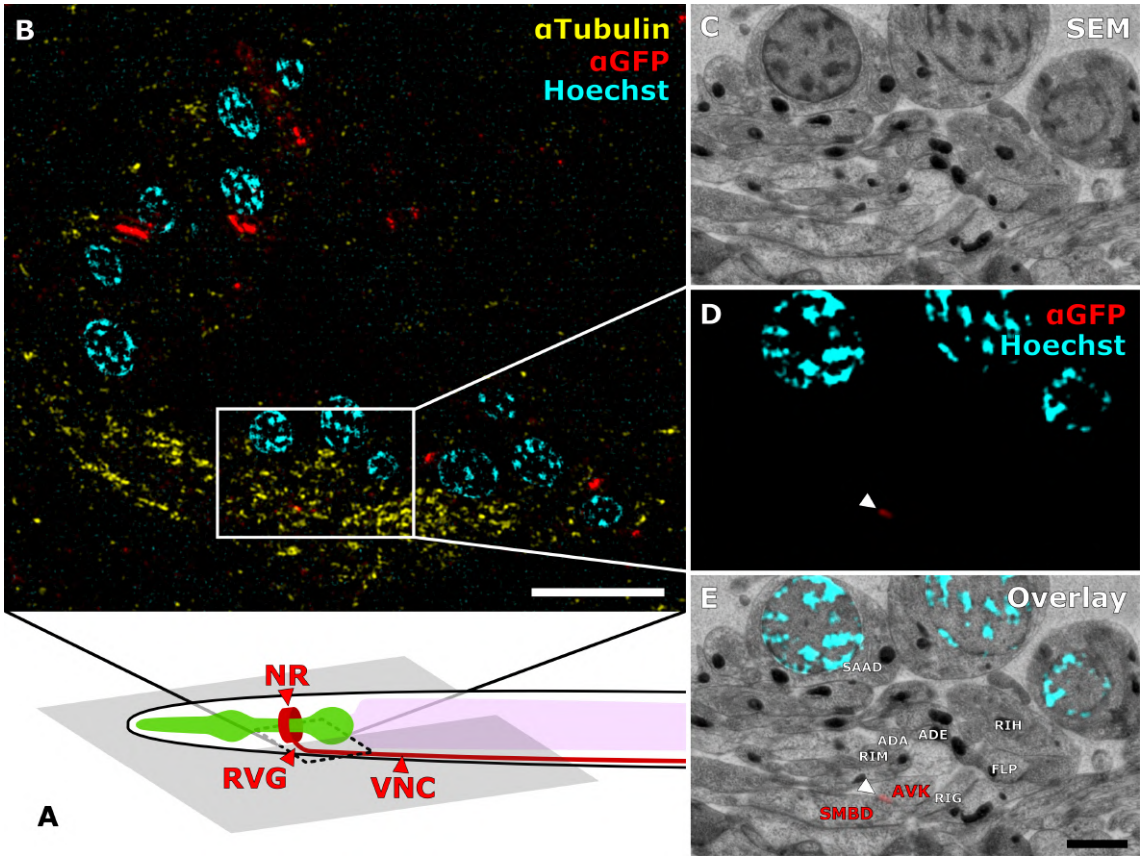

Figure 3.4.: **Examination of an example section reveals how the data-set was generated.** **A** Schematic representation of the cutting plane in relation to the worm. NR: nerve ring, RVG: retrovesicular ganglion, VNC: ventral nerve cord. **B** SIM image of an example section through the RVG, as indicated by a dashed square in **A**. Nuclei are revealed by Hoechst DNA stain, neuropil tissue by anti-Tubulin stain, and UNC-7::GFP by anti-GFP stain. Scale bar: 5 µm. **C** Scanning electron micrograph of a region of interest in the RVG reveals ultrastructural features, but the locations of gap junctions are not obvious. **D** The same region of interest as in **C** shown for two SIM channels. Three nuclei and a putative anti-GFP signal (arrowhead) are visible. Without ultrastructure, it is impossible to discern if the signal is indeed a gap junction, UNC-7::GFP in another compartment (cf. Figure 3.5), or random background staining. **E** Overlay of the correlated **C** and **D**. The combination of molecular identity and ultrastructure reveals the anti-GFP signal as a gap junction. By analyzing several consecutive sections, some of the neurons here could be identified by Daniel Witvliet. The gap junction can thus be further characterized as being between the neurons SMBD and AVK. Scale bar: 1 µm. From Markert et al. [2016]

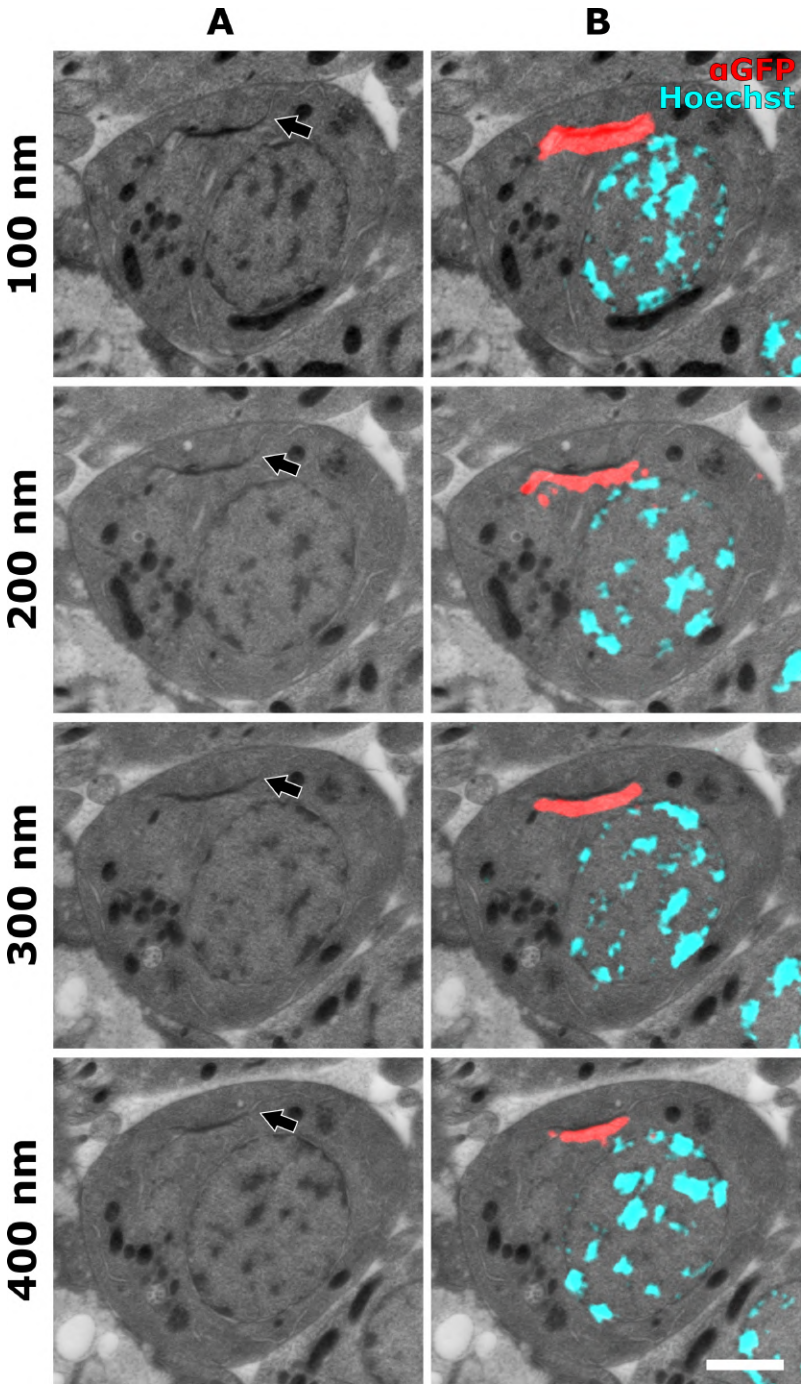

Figure 3.5.: **Intracellular conglomerates of gap junction proteins revealed by srAT. A** Series of sections through a neuronal cell body. Endoplasmic reticulum is clearly visible and contains electron dense material (arrow). **B** Overlay with SIM signals indicates UNC-7::GFP accumulation in the endoplasmic reticulum. Without ultrastructural context, this accumulation of UNC-7::GFP could not be differentiated from a real gap junction. Scale bar: 1 µm.

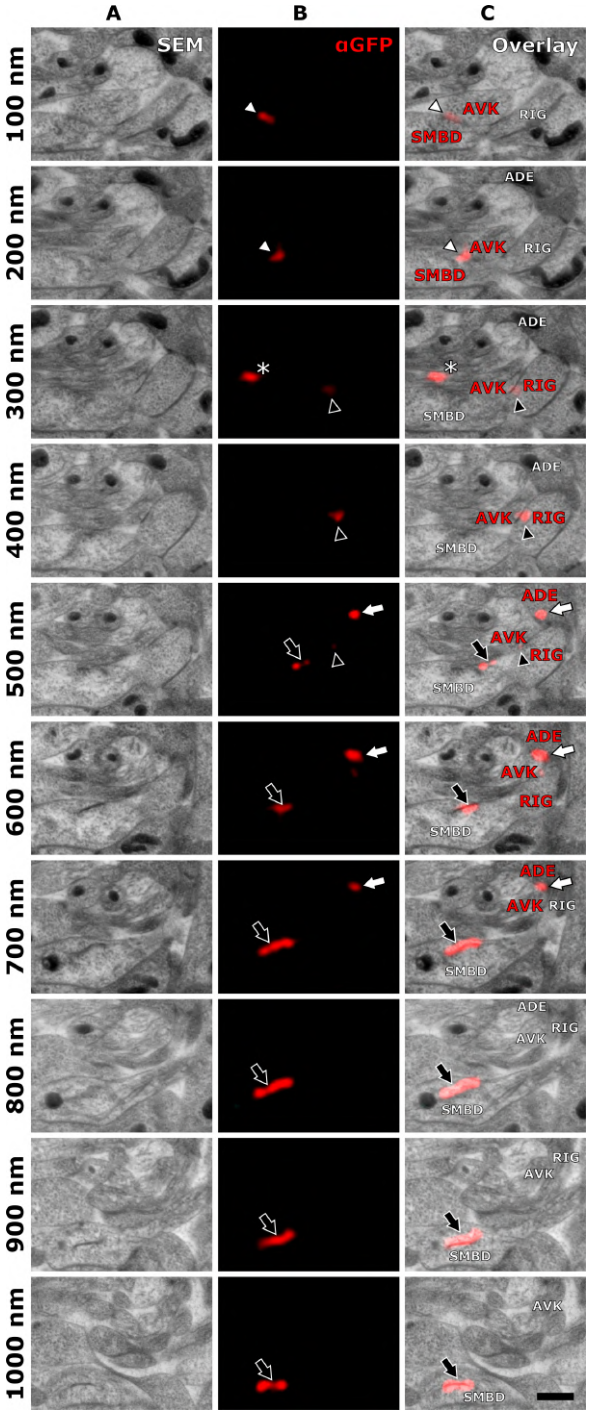

Figure 3.6.: **Consecutive sections reveal spatial map of UNC-7::GFP expression.** **A** Region of interest imaged by scanning electron microscopy in 10 consecutive 100 nm-sections through the RVG. **B** Same region as in **A** imaged with SIM reveals anti-GFP signals. **C** Overlay of **A** and **B**. Identified neurons and gap junctions are labeled. White arrowhead: gap junction between AVK and SMBD. Black arrowhead: gap junctions between AVK and RIG. White arrow: gap junctions between ADE and AVK. Black arrow: anti-GFP signal located in endoplasmic reticulum (cf. Figure 3.5). Asterisk: signal that occurs on a single section only is deemed random background labeling. Scale bar: 500 nm. From Markert et al. [2016]

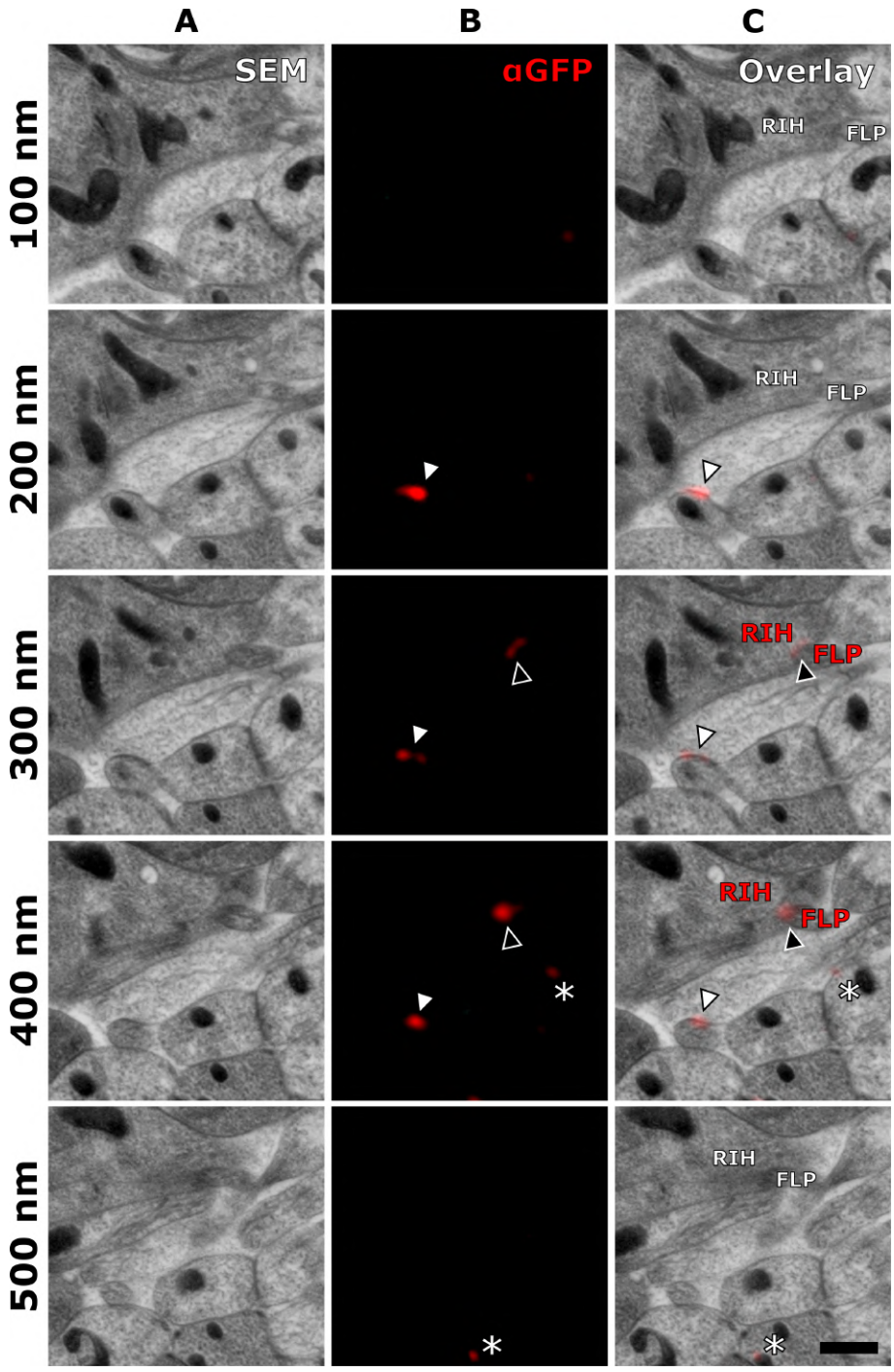

Figure 3.7.: **A second example of consecutive sections that reveal gap junctions. A** Region of interest imaged by scanning electron microscopy in 5 consecutive 100 nm-sections through the RVG. **B** Same region as in **A** imaged with SIM reveals anti-GFP signals. **C** Overlay of **A** and **B**. Identified neurons and gap junctions are labeled. White arrowhead: gap junction between unidentified neurons. Black arrowhead: gap junction between FLP and RIH. Asterisk: signal that occurs on a single section only is deemed random background labeling. Scale bar: 500 nm.

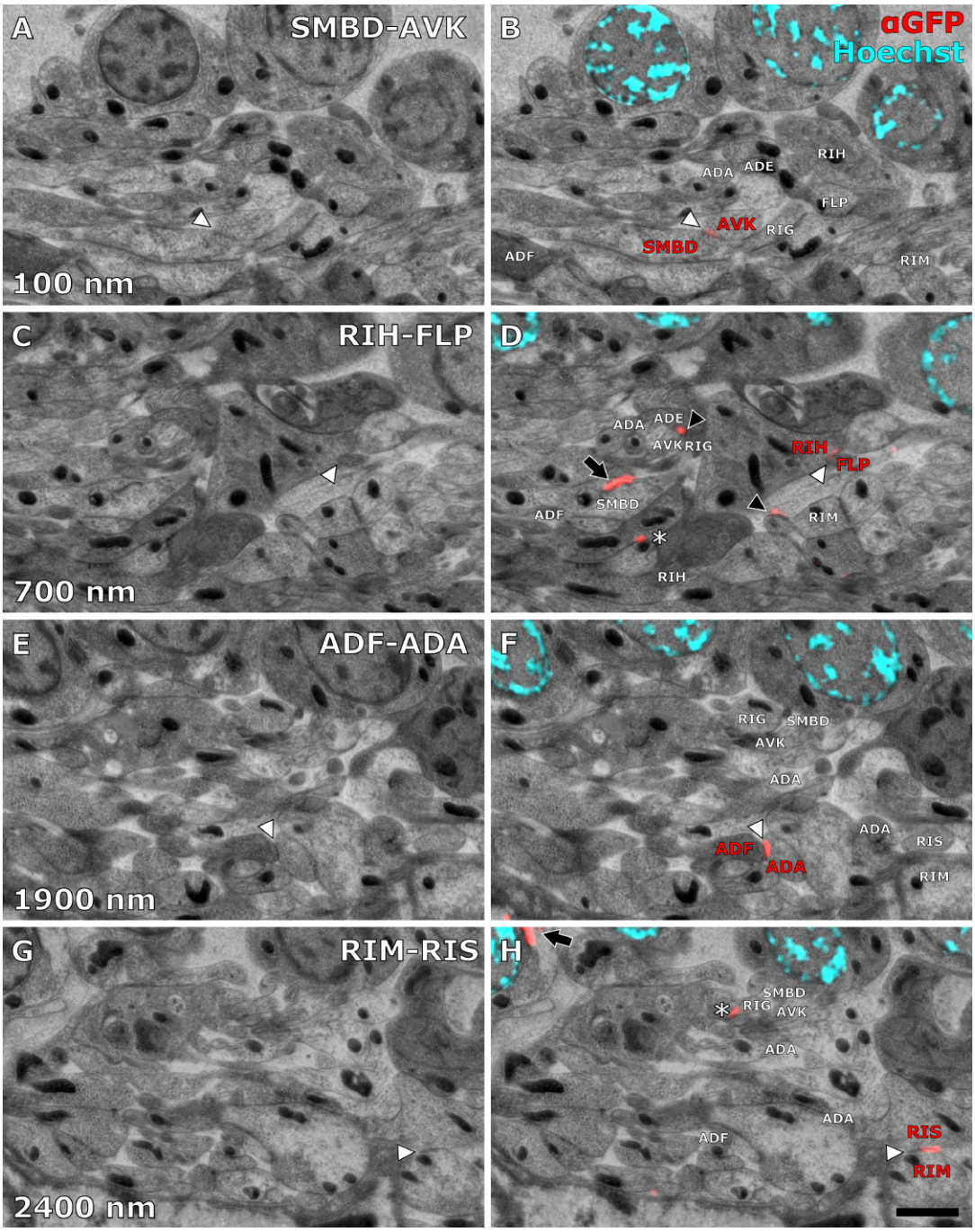

Figure 3.8.: **Identified gap junctions in our RVG data-set.** **A** Gap junction between SMBD and AVK (white arrowhead). **C** Gap junction between RIH and FLP (white arrowhead). **E** Gap junction between ADF and ADA (white arrowhead). **G** Gap junction between RIM and RIS (white arrowhead). Relative section positions in the data-set are given in lower left corners. **B**, **D**, **F**, **H** Corresponding images with SIM images overlaid. Hoechst: DNA staining, anti-GFP: UNC-7::GFP staining. Some identified neurons are labeled. Black arrowheads point to additional gap junctions, black arrows point to anti-GFP signal in endoplasmic reticulum. Asterisks mark signals deemed random background staining. Scale bars: 500 nm. From Markert et al. [2016]

or processing within the cell. These cases are very challenging to differentiate via light microscopy alone.

Figures 3.6, 3.7, and 3.8 show regions of interest within the RVG as it develops from section to section. UNC-7::GFP identifies gap junctions clearly while also labeling portions of the endoplasmic reticulum. In Figure 3.7, a single gap junction remained of unknown identity. However, most gap junctions found in our data-set could be identified, as in Figure 3.8. These synapses have been previously characterized in published work [Yeh et al. 2009; Starich et al. 2009], thus the literature validated our findings. In one case, the gap junction between ADA and ADF was known but not the type of innexin it is made of. Since srAT also offers specific molecular identity, I can report that at least one of the two involved cells expresses UNC-7. In other parts of the nervous system, especially the nerve ring, neuronal processes are not typically parallel nor sectioned transversally, as is the case with our RVG data-set. This makes identification of gap junctions much harder and thus mapping of gap junctions via srAT is bound to reveal new junctions in these parts.

Since srAT is based on consecutive sections, images can be compiled into 3D volume stacks. 3D reconstruction of such data-sets can help understanding the spatial architecture of the neurons and their connections with each other (Figure 3.9).

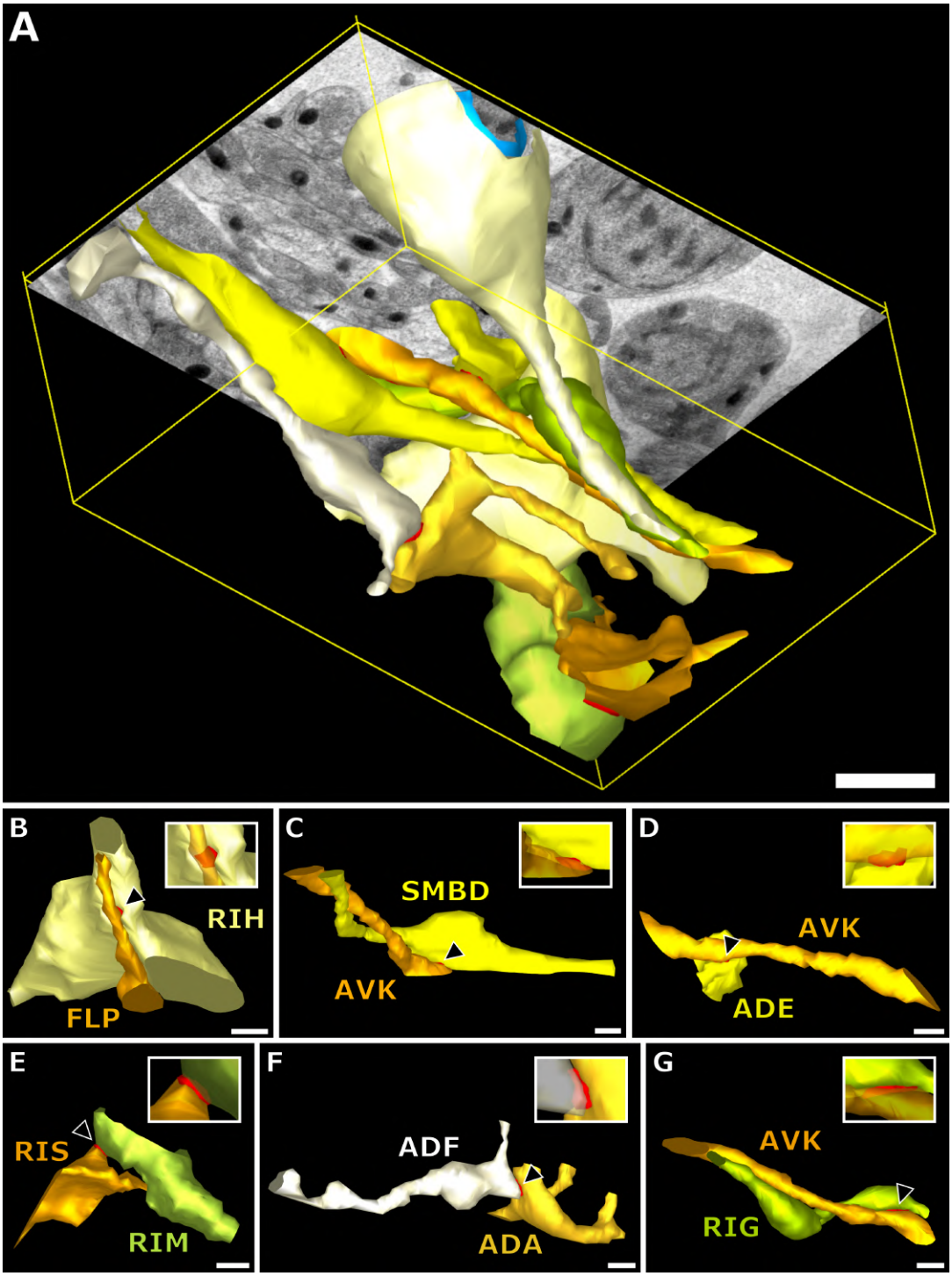

Figure 3.9.: **3D models illustrate spatial arrangements of neurons and gap junctions. A** Overview of all modelled neurons and gap junctions in a 3 µm dataset. Neurons are given in yellowish colors, gap junctions in red, and a nucleus is shown in blue for context. Scale bar: 1 µm. **B-G** Detailed views of neurons paired by gap junctions. Arrow heads mark the gap junctions. Insets show gap junctions in greater detail with partially transparent neurons. Scale bars: 500 nm. From Markert et al. [2016]

3.1.2. Increasing resolution of fluorescence microscopy in srAT even more by implementation of dSTORM

When correlating light and electron microscopy, the difference in resolution is often a challenge. I used super-resolution fluorescence microscopy to narrow this gap in resolution, as these methods resolve items below light resolution limit. For my gap junction analysis, SIM provided sufficient resolution to correlate the light signal with ultrastructure. Also, I tested the compatibility of srAT with direct stochastic optical reconstruction microscopy (dSTORM) [Heilemann et al. 2008; van de Linde et al. 2011; Löschberger et al. 2014]. dSTORM achieves the highest light resolution currently possible, tied with photo-activated localization microscopy (PALM) [Betzig et al. 2006]. Together with Dr. Sven Proppert[6] I performed dSTORM recordings directly on stained sections and was able to correlate microtubules in the *C. elegans* ventral nerve cord with very high precision (Figure 3.10). This showcases how srAT can be used for precise localizations of proteins. With 2-color-dSTORM, one channel could be used for the independent intrinsic landmark, and the other one for the protein of interest.

3.1.3. Embedding and curing LR White at low temperature preserves *C. elegans* structure better than thermal curing

Nearly all CLEM techniques require some degree of compromise. Since light and electron microscopy demand very different protocols for sample preparation, it is difficult to optimize for both techniques at the same time. For srAT, it is crucial to maintain antigenicity. This calls for gentle fixation and contrasting, which can negatively affect preservation of ultrastructure. Different combinations of fixation and resin embedding protocols were tested, their structure preservation and antigenicity were compared. The overall best fixation protocol turned out to be freeze-substitution with potassium permanganate in acetone. This resulted in high preservation of antigenicity and acceptable structure.

The embedding protocol had significant effect on structure preservation. Embedding and curing in LR White resin at low temperature (4 °C) under UV light overall preserved nervous tissue in *C. elegans* better than thermal curing at 52 °C. At low

[6] then in the group of Prof. Markus Sauer, Department of Biotechnology and Biophysics, Biocenter, University of Würzburg, Würzburg, Germany

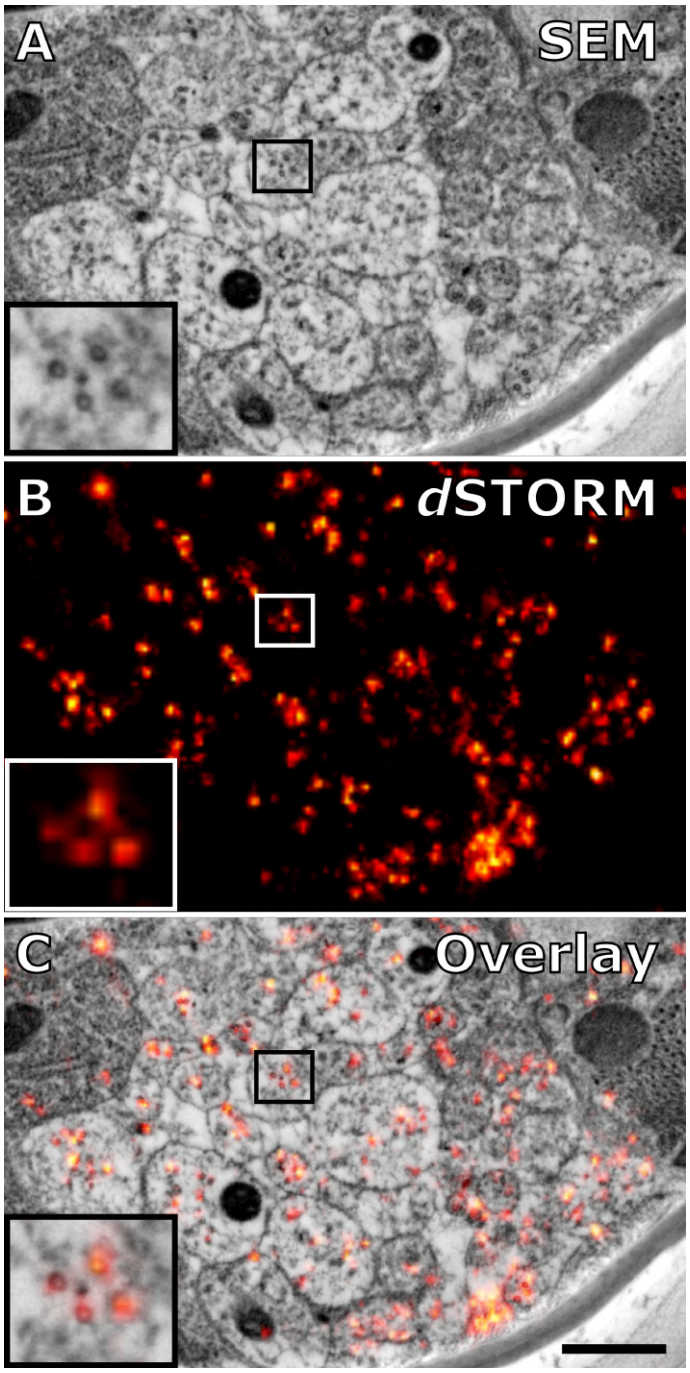

Figure 3.10.: **Super-resolution imaging via dSTROM for increased correlation precision in srAT. A** SEM image of a ventral nerve cord of a *C. elegans* young adult hermaphrodite, embedded in LR White and thermally cured at 52 °C. **B** Reconstructed *d*STROM image of the same section and region as in **A**. Microtubules were stained via immunohistochemistry. **C** Overlay of **A** and **B**. Microtubules are visible in the electron micrograph and labeled via dSTORM. Insets focus on four microtubules that are close together yet still distinguishable by dSTORM. Scale bars: 500 nm. From Markert et al. [2016].

temperatures, synaptic vesicles and dense projections could be observed (cf. Figure 3.8), whereas thermal curing extracted these structures (cf. Figure 3.10). On the other hand, thermal curing also has some advantages. Depending on the question, more extraction might even be desirable and was actually useful for the dSTORM experiment, as microtubules were easier to distinguish there (cf. Figure 3.10). Also, thermal curing is easier to implement, because it is possible to process samples at room temperature without UV lamp. Low temperature curing was less consistent than thermal curing. In low temperature, samples were not properly cured in some cases, which compromised structure and ultramicrotomy.

Choice of resin is important as well. For this thesis, I used LR White, as in the original array tomography publication [Micheva and Smith 2007]. While other methacrylate resins, like the Lowicryls HM20 and K11M, can be cured at even lower temperatures (down to -40 °C), LR White always yielded better results for *C. elegans* tissues, in my experiments.

3.1.4. Considerations and strategies for correlation

Mapping gap junctions reliably requires high precision and accuracy of correlation. Some studies used fiducial markers [Nisman et al. 2004; Kukulski et al. 2011], which have downsides in ease of handling and consistency of results. Instead, we established a protocol for correlation that makes use of independent intrinsic landmarks. Potential landmarks are all structures in the tissue or cell that can be fluorescently labeled and are also distinguishable in electron micrographs. Furthermore, these landmarks should be as independent as possible from the protein or structure of interest. For my study of synaptic proteins, I used mostly nuclei as landmarks. They can be conveniently stained on-section by common DNA stains like DAPI, Hoechst, propidium iodide, and methyl green (Veronika Perschin, personal communication). These stains predominantly label the heterochromatin pattern, which is also readily visible in electron micrographs. The intricate patterns are ideal for precise correlations. By correlating only the independent landmarks without taking signals from the protein of interest into account, correlation is unbiased. Other potential landmarks include mitochondria, microtubules, membranes, and large protein complexes. I used two main methods of correlation: Manual correlation using the software Inkscape (http://www.inkscape.org), and semi-automatic correlation using the eC-CLEM plugin for the software package Icy [Heiligenstein

et al. 2017; Paul-Gilloteaux et al. 2017] (http://icy.bioimageanalysis.org/plugin/ec-CLEM#documentation). Both options use only freely available software. See "Materials and methods" section 2.6.5 for details.

3.1.5. Feasibility of adding gap junctions to the connectome with srAT

This thesis showcases how srAT can be used to map gap junctions at the *C. elegans* connectome. Although the retrovesicular ganglion mapped here is only a small part of the full nervous system, srAT makes it feasible to re-annotate the entire connectome for gap junctions. Furthermore, the connectome can be enriched with the molecular identity of the gap junction proteins. These will be important steps towards a truly complete and comprehensive connectome in *C. elegans*, even if this final destination might never be reached [Haueis and Slaby 2017].

3.2. Focused ion-beam scanning electron microscopy of *C. elegans dauer* larvae for connectomics

Via srAT, reliable mapping of gap junctions is feasible. Re-evaluation of chemical synapses will also be a crucial step towards a comprehensive connectome. Connectomes up to now are mostly crafted by meticulous manual mapping of synapses across huge numbers of electron micrographs. This is a very challenging and time-consuming task and also relies on excellent sample preparation and image acquisition; any error could lead to disaster with every artifact/gap potentially being fatal for tracing consistency. Because of this challenge, the *C. elegans* connectome is based on a very limited number of data-sets; none feature a complete worm [White et al. 1986; Hall and Russell 1991]. Clearly, an easier, faster, and more reliable method for connectome data acquisition is needed to increase the number of data-sets and obtain coherent data-sets.

Moving forward, connectomes of the larval stages of *C. elegans* are necessary to understand the development of connectomes. There are some community efforts to obtain connectomes of larval stages, but the so-called *dauer* stage has not been tackled up to now. This dispersal stage is only formed in adverse conditions and

features a thick cuticle and a closed mouth to shield it against the environment. Because of these properties, we feared that high-pressure freezing of *dauers* could turn out to be challenging. We expected tissue infiltration issues during freeze-substitution and/or resin embedding. Surprisingly, the structure preservation was as good as any we had ever seen for *C. elegans* samples. This result gave us confidence to attempt the acquisition of *dauer* data-sets that are suitable for connectomics.

Focused ion-beam scanning electron microscopy (FIB-SEM) offers relatively fast automated image acquisition and coherent, near-isotropic data-sets. These qualities make FIB-SEM the perfect choice for our aim of acquiring high-volume data-sets of *C. elegans dauer* larvae at high resolution in all axial directions. We collaborated with the laboratories of Dr. Yannick Schwab[7] and Prof. Mei Zhen[8] and successfully acquired several data-sets with FIB-SEM.

3.2.1. *Dauer* larvae are especially suitable for FIB-SEM imaging

During image acquisition with FIB-SEM, the ion-beam and electron-beam alternate. These two modes must be tuned to each other to achieve stable and even acquisition. This requirement limits the physical size of the acquisition window, because larger windows take too much time for acquisition, leading to poor stability and resolution. In practice, the acquisition window is limited to $50 \times 50\,\mu m$ with the machine we used. *Dauer* larvae have a diameter of 15-20 µm and fit nicely in this window. Adult worms are about 80 µm in diameter. Another advantage of using *dauer* larvae for FIB-SEM is that they are consistently well preserved with HPF/FS, and, therefore, intact worms can be prepared for FIB-SEM in great numbers, if desired.

3.2.2. Minimal resin embedding enables precise targeting of regions of interest

Since it is impossible to discern samples within a block of resin with SEM, areas of interest are challenging to identify. Even marking them on the block surface by laser etching is problematic, since this gives no information about the z-position of the region of interest. Ideally, the sample is surrounded by only a minimal amount

[7] EMBL, Heidelberg, Germany
[8] Lunenfeld-Tanenbaum Research Institute, Mount Sinai Hospital, Toronto, Canada and Departments of Physiology and Molecular Genetics, University of Toronto, Toronto, Canada

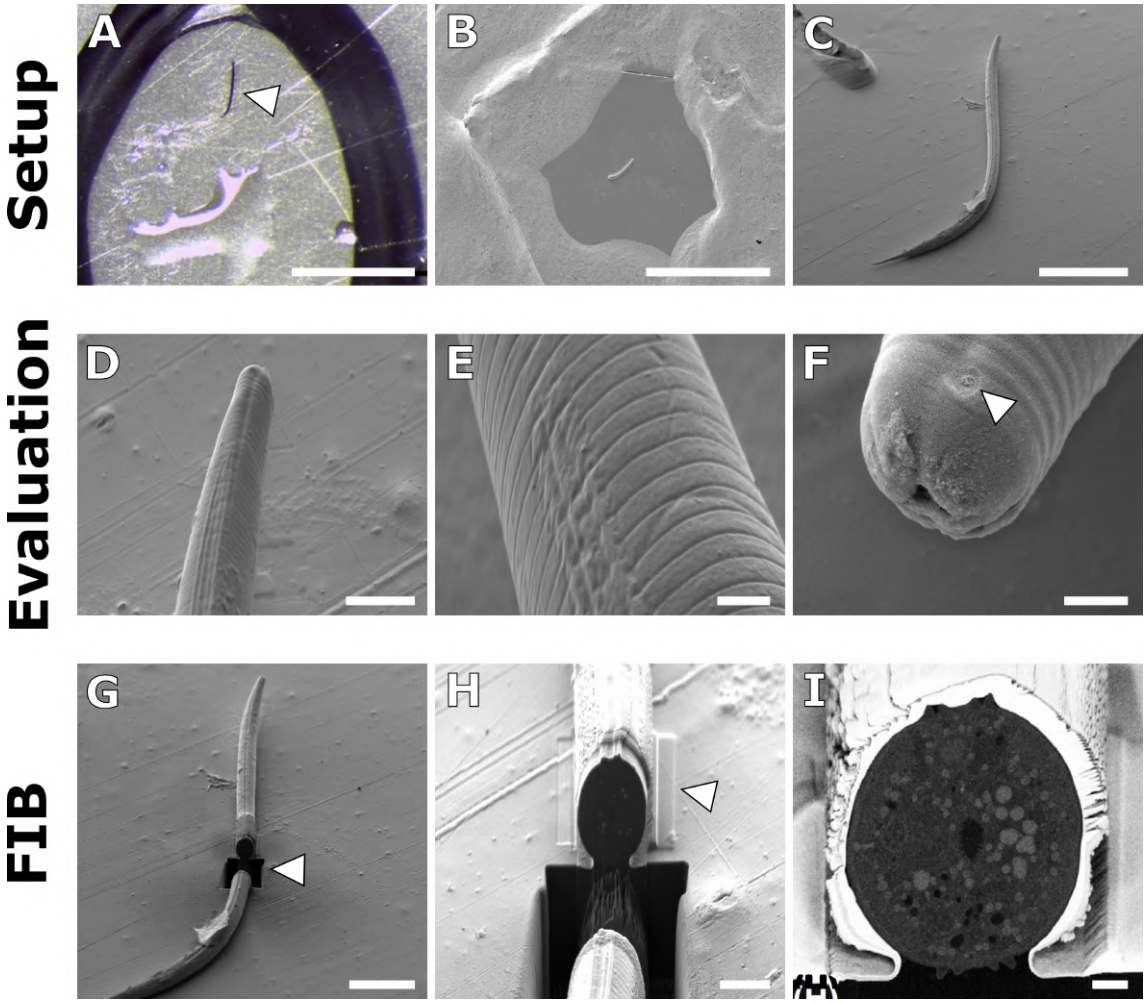

Figure 3.11.: **The principle steps of FIB-SEM imaging of *C. elegans dauer* larvae. A** Minimal resin embedding. The fully infiltrated larva (arrowhead) was pushed out of a drop of resin across a dry plastic surface prior to curing. Scale bar: 1 mm. **B** Plastic piece containing the worm is visible via SEM. It was surrounded with conductive silver paint and coated with gold. Scale bar: 1 mm. **C** Due to minimal resin embedding, individual worms can be easily targeted for evaluation. Scale bar: 100 µm. **D-E** External features of the worm aid in evaluating quality of preservation and target selection. Hypodermal ridges, alae, and amphid opening (arrowhead in **F**) are visible. Scale bars: **D**: 20 µm, **E, F**: 2 µm. **G** The initial trench for access has been established via FIB (arrowhead). Scale bar: 50 µm. **H** The area of interest was locally coated with platinum to reduce charging (arrowhead). Scale bar: 10 µm. **I** Cross section of the worm right before image acquisition. Ultrastructural features and white platinum coat are visible. Scale bar: 2 µm.

of resin that allows for discerning its contours with SEM. However, trimming away most of the resin after embedding is extremely challenging, especially for intricate samples like thin worms. For this reason, Dr. Anna Steyer[9] and I developed a method for minimal resin embedding of *dauers*. This technique is based on similar ideas for embedding zebrafish and *Platynereis* larvae. Typically, excess resin is drained from the samples, but this does not work for *dauer* larvae, because they are too small. In the end, moving the worms from a drop of resin across a dry plastic surface worked best (cf. Figure 3.11A). In result, the worms had no visible resin remaining on the outside, while the inside remained completely infiltrated with resin. With this technique, we could target areas of interest with maximum precision and reduce the time needed to set up FIB-SEM acquisition to a minimum (Figure 3.11). Furthermore, this made it possible to pre-evaluate if worms were completely intact, i. e, free of cracks, and suitable for acquisition of coherent data-sets. We published the minimal resin technique as a book chapter [Schieber et al. 2017].

3.2.3. Acquisition of high-volume data-sets with 5 nm isotropic resolution

Thanks to minimal resin embedding and the high quality of structure preservation with the HPF/FS protocol established in our laboratory [Helmprobst et al. 2015; Kaltdorf et al. 2017, 2018], we were able to acquire *dauer* FIB-SEM data-sets with high stability and resolution, resulting in a voxel size of 5 nm in isotropic data-sets.

The largest data-set extends from just posterior to the nerve ring all the way to the anterior tip of the worm and spans a length of 80 µm. Figures 3.12, 3.13, 3.14, and 3.15 showcase the overall image quality and resolution in this data-set by means of ultrastructural features. The morphology of the sensory system can be observed (Figures 3.12, 3.13) and even very intricate structures like microtubules (Figures 3.12B and 3.13C), Golgi apparatuses (Figure 3.15B), dense projections (Figure 3.15C), and endoplasmic reticulum (Figure 3.15D) can clearly be discerned.

Of the anterior sensory system, two data-sets have been acquired as well as an additional nerve ring data-set (data not shown). These will be important for judging inter-individual variability of *dauer* larvae.

[9] then in the group of Yannick Schwab, EMBL, Heidelberg, Germany; now Department of Neurogenetics, Max Planck Institute of Experimental Medicine, Göttingen, Germany; Electron Microscopy Core Unit, Max Planck Institute of Experimental Medicine, Göttingen, Germany; Center for Nanoscale Microscopy and Molecular Physiology of the Brain, Göttingen, Germany

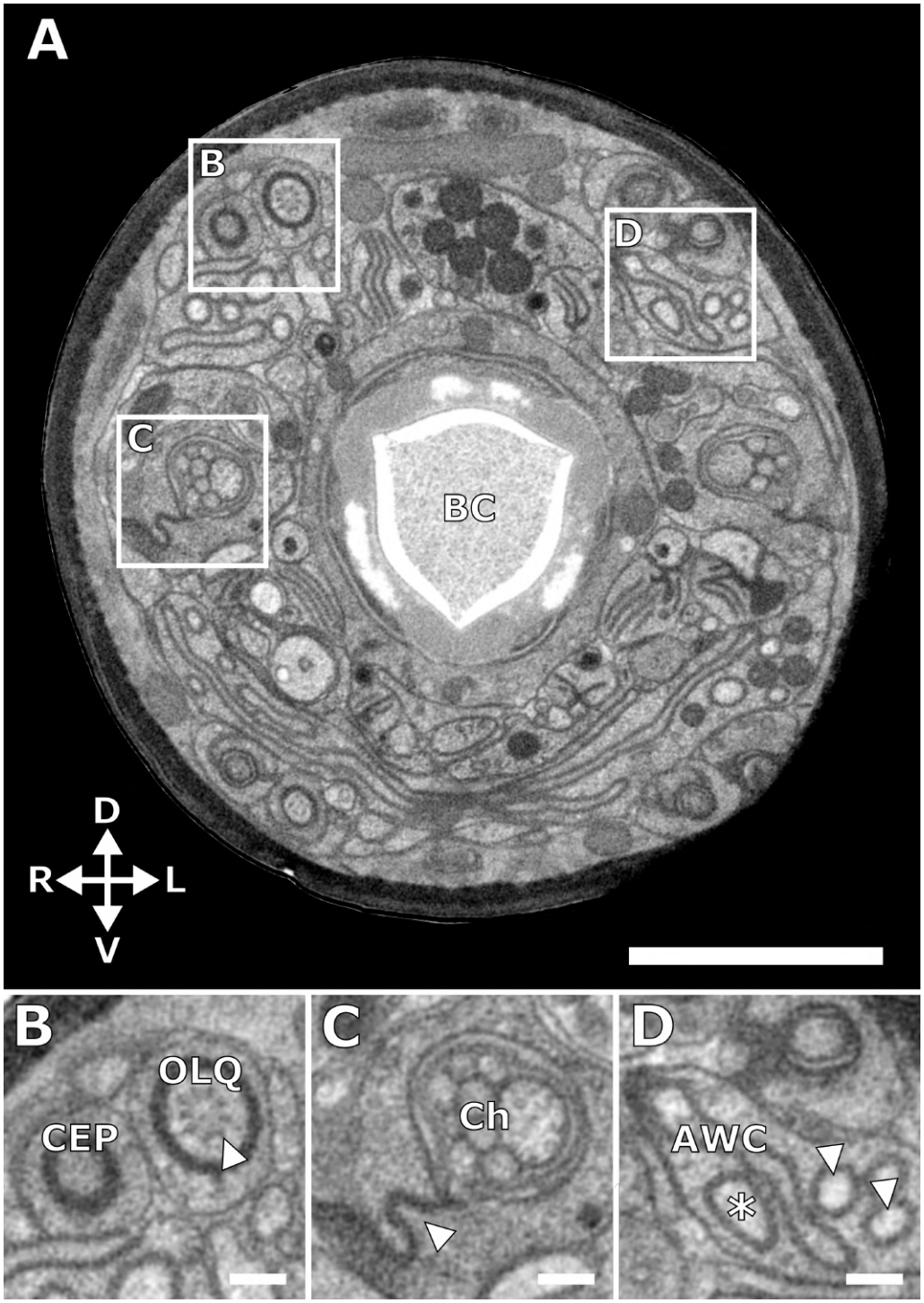

Figure 3.12.: **Ultrastructural features of the anterior tip of a *dauer* larva revealed by FIB-SEM. A** Cross section approximately 4 µm deep from the tip of the worm. BC: buccal cavity. **B** The neurons CEP and OLQ are visible. In OLQ microtubules can be discerned (arrowhead). **C** Amphid channel containing channel cilia (Ch). The seam of the glial amphid sheath is visible (arrowhead). **D** The amphid neurons AWA (arrowheads), AWB (asterisk), and AWC. Scale bars: **A**: 2 µm. **B, C, D**: 100 nm.

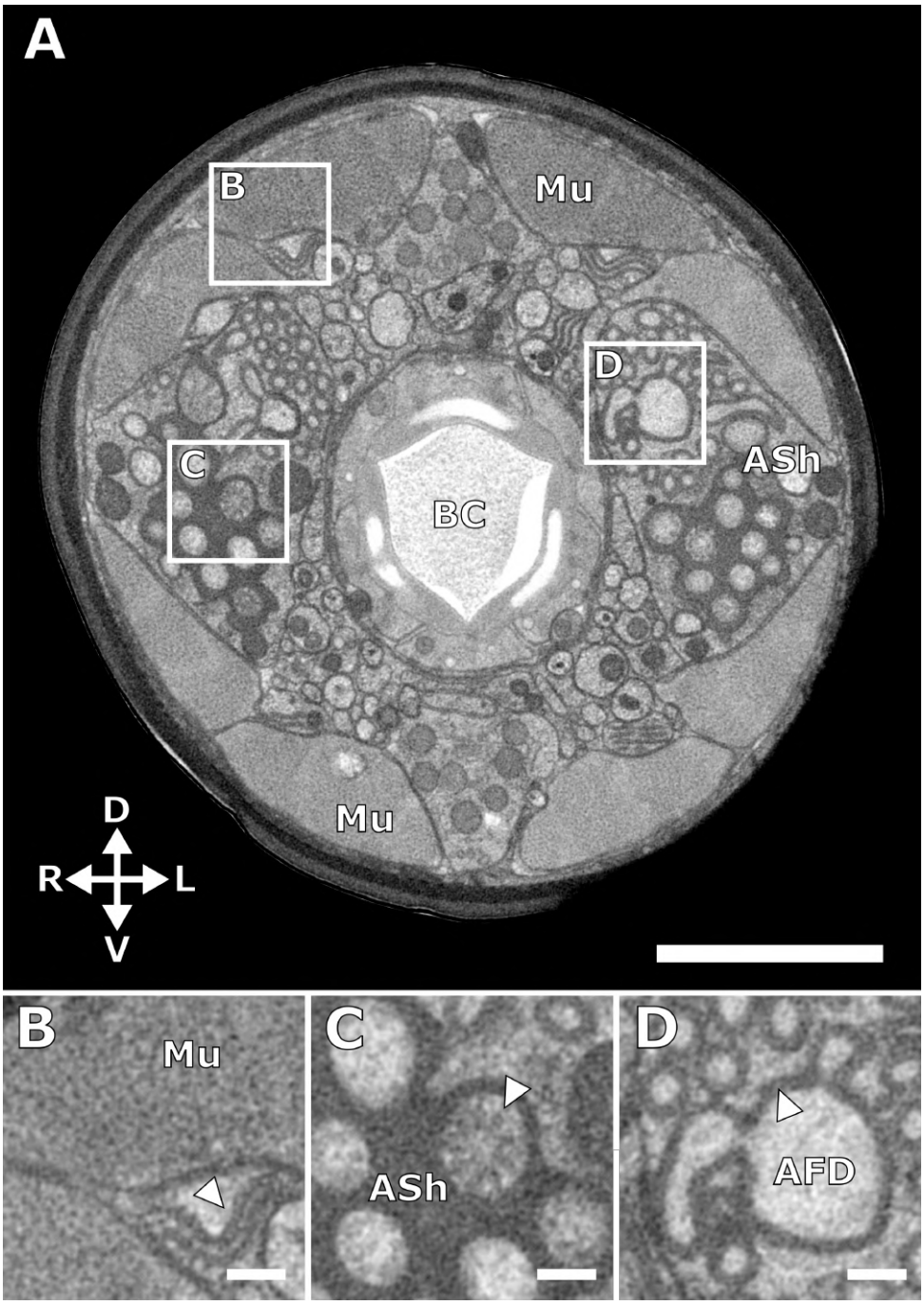

Figure 3.13.: **Ultrastructural features of the anterior tip of a *dauer* larva revealed by FIB-SEM. A** Cross section approximately 8 µm deep from the tip of the worm. BC: buccal cavity, Mu: muscle, ASh: amphid sheath. **B** Detailed view of muscle (Mu) and a membrane stack (arrowhead). **C** Amphid channel cilia and amphid sheath (ASh). The cilia are encased in electron-dense material. Microtubules are visible (arrowhead). **D** The amphid neuron AFD. The amphid sheath encases all "fingers" of AFD, thus creating a double membrane that appears thick and electron-dense (arrowhead). Scale bars: **A**: 2 µm. **B, C, D**: 100 nm.

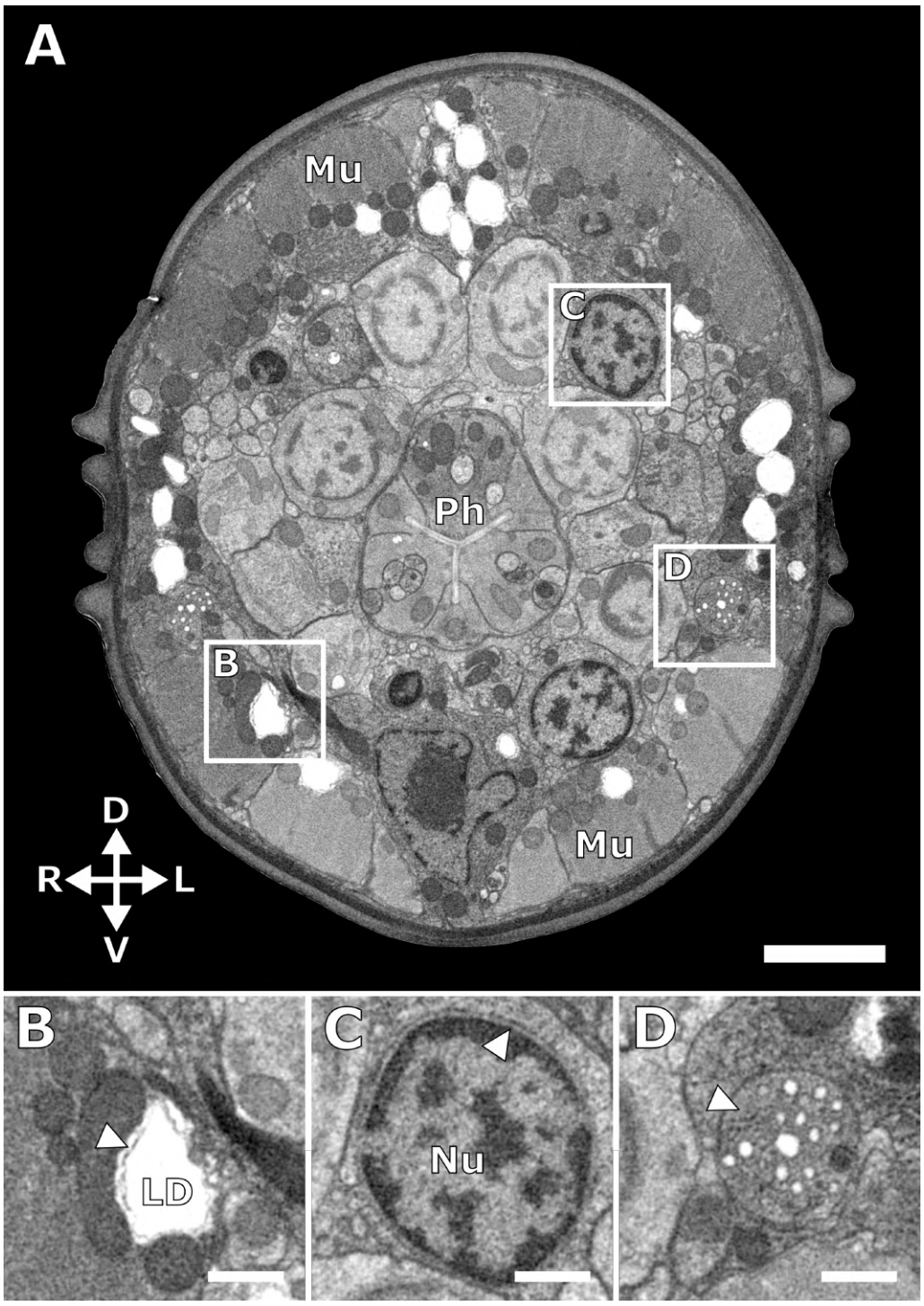

Figure 3.14.: **Ultrastructural features anterior to the nerve ring of a *dauer* larva revealed by FIB-SEM. A** Cross section approximately 65 µm deep from the tip of the worm. Ph: pharynx, Mu: muscle. **B** Detailed view of a lipid droplet (LD). Smooth endoplasmic reticulum is visible (arrowhead). **C** Nucleus of a neuron (Nu). The nuclear envelope is clearly discernible (arrowhead). **D** H-cell (arrowhead) with characteristic vesicles. Scale bars: **A**: 2 µm. **B, C, D**: 500 nm.

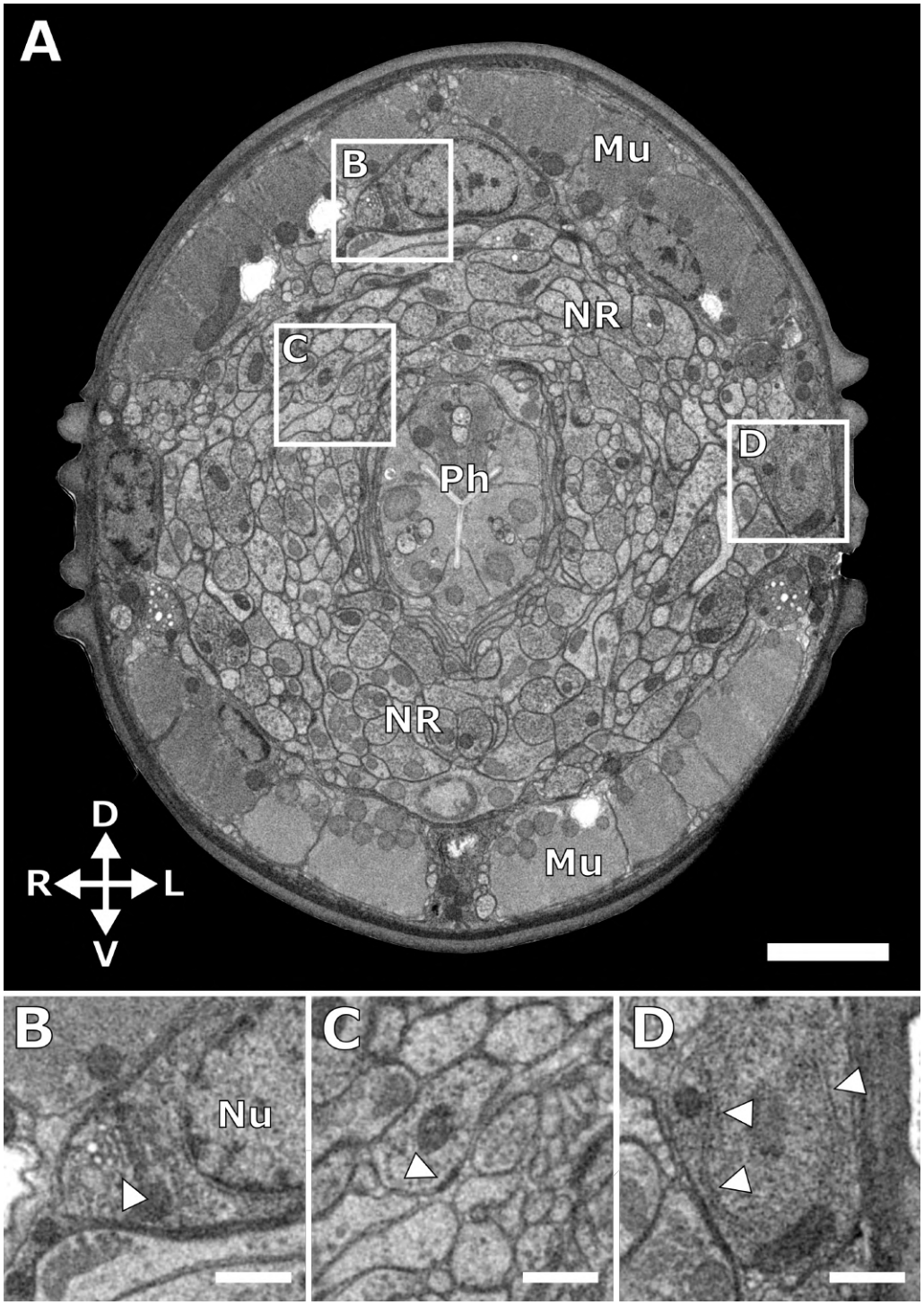

Figure 3.15.: **Ultrastructural features at the nerve ring of a *dauer* larva revealed by FIB-SEM. A** Cross section approximately 72 µm deep from the tip of the worm. Ph: pharynx, Mu: muscle, NR: nerve ring. **B** Detailed view of a cell soma including a Golgi apparatus (arrowhead) and a nucleus (Nu). **C** Neuropil tissue in the nerve ring. A synapse with dense projection (arrowhead) is visible. **D** Cell soma including rough endoplasmic reticulum (arrowheads). Scale bars: **A**: 2 µm. **B, C, D**: 500 nm.

In the mid-body range, four data-sets have been acquired. They focus on the ventral portion of the worm and include the ventral nerve cord. Figures 3.16 and 3.17 showcase overall image quality and resolution in these data-sets, which are comparable to the other data-sets shown.

3.2.4. The limits of FIB-SEM: Electron tomography is more appropriate for sub-synaptic analyses

FIB-SEM is suitable for analyzing large volumes of the nervous system but not necessarily for the molecular machinery of individual synapses. For this purpose, electron tomography is more appropriate. For example, the FIB-SEM data-sets suggested that synpases contained more dense core vesicles (DCVs) in our *dauer* larvae than in adult worms. While the number of vesicles could be counted by FIB-SEM, morphology could not be adequately analyzed. To investigate differences in vesicle morphology in an automated large-scale approach, I used the automated vesicle reconstruction tool published by Kaltdorf et al. [2017]. We collaborated with Prof. Philip Kollmannsberger,[10] Prof. Thomas Dandekar,[11] Prof. Mei Zhen,[12] Maria Theiss,[10,11] and Dr. Kristin Kaltdorf[10,11,13] They developed a software tool that builds on the previous macro [Kaltdorf et al. 2017] and classifies synaptic vesicles based on electron tomograms [Kaltdorf et al. 2018]. I directly contributed in Kaltdorf et al. [2018] by providing electron tomograms of *C. elegans* synapses. By using this classification tool, we could show that the fraction of DCVs in *dauers* was significantly increased compared to adult worms [Kaltdorf et al. 2018]. In this thesis, I used electron tomography extensively for studying the chemical synapse and its machinery.

[10]Center for Computational and Theoretical Biology, Biocenter, University of Würzburg, Würzburg, Germany
[11]Department of Bioinformatics, Biocenter, University of Würzburg, Würzburg, Germany
[12]Lunenfeld-Tanenbaum Research Institute, Mount Sinai Hospital, Toronto, Canada and Departments of Physiology and Molecular Genetics, University of Toronto, Toronto, Canada
[13]Imaging Core Facility, Biocenter, University of Würzburg, Würzburg, Germany

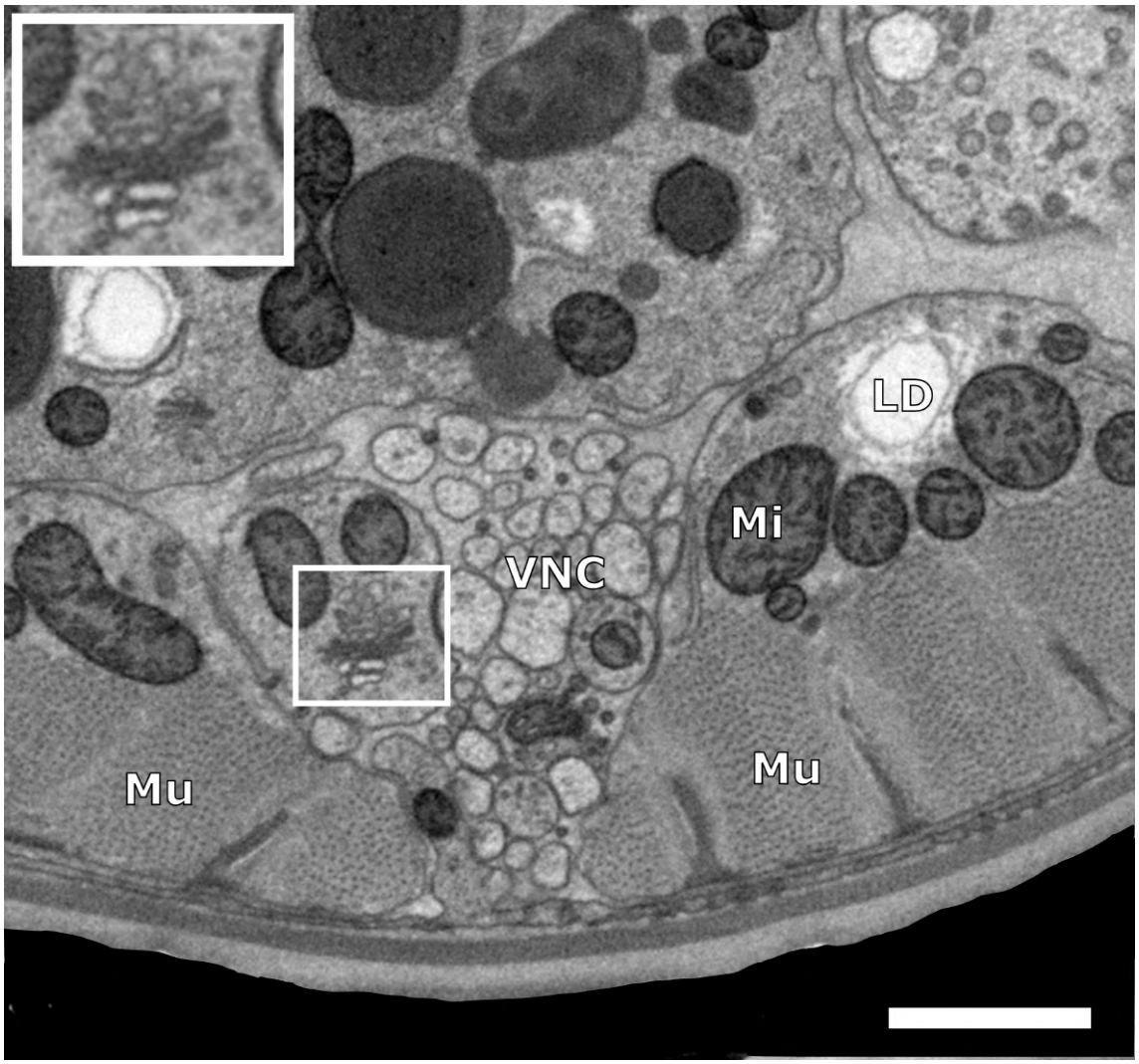

Figure 3.16.: **Ultrastructural features at the ventral nerve cord of a *dauer* larva revealed by FIB-SEM.** Cross section through the mid-body. VNC: ventral nerve cord, Mu: muscle, Mi: mitochondria, LD: lipid droplet. Inset: Golgi apparatus. Scale bar: 2 µm.

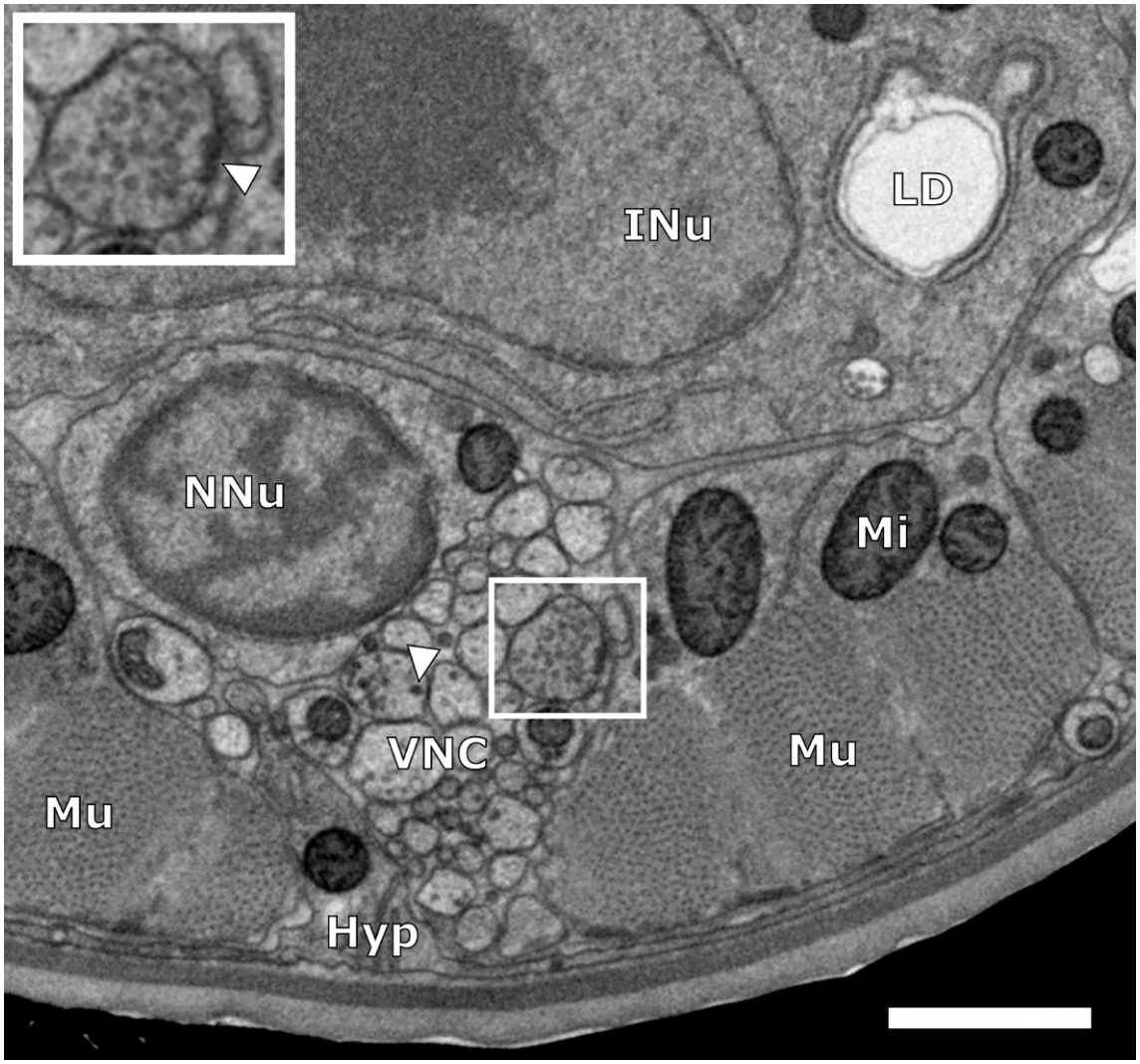

Figure 3.17.: **Ultrastructural features at the ventral nerve cord of a *dauer* larva revealed by FIB-SEM, second example.** Cross section through the mid-body. VNC: ventral nerve cord, Mu: muscle, Mi: mitochondria, LD: lipid droplet, NNu: neuronal nucleus, INu: intestinal nucleus, Hyp: hypodermal cell. Arrowhead: dense core vesicle. Inset: synapse with clear core vesicles and dense projection (arrowhead). Scale bar: 2 µm.

3.3. Nanoscale 3D reconstructions of chemical synapses by electron tomography elucidate parts of the synaptic machinery

A comprehensive understanding of the synaptic machinery will make it possible to implement detailed characterization of chemical synapses into connectomes. This in turn should significantly improve the biological significance of connectomes. I therefore used electron tomography to obtain 3D reconstructions of chemical synapses with nanometer resolution. These reconstructions allowed insights into mechanisms and functions of a selected synaptic protein, the kinase SAD-1.

3.3.1. Lack of the kinase SAD-1 causes "nested synapses" and larger vesicle pools

SAD-1 is a serine/threonine kinase reported to be involved in neuron polarity and synapse organization [Crump et al. 2001]. I investigated the synaptic ultrastructure of *sad-1* null-mutants via electron tomography to further elucidate the functions of SAD-1 at the synapse.

I recorded more than 100 tilt series of the ventral and dorsal nerve cords of *sad-1* worms. I calculated electron tomograms of most of them and analyzed 11 cholinergic excitatory synapses spread over four individual young adult hermaphrodites. I analyzed two instances of "nested synapses" in separate individuals (Figures 3.18, 3.19). The nested synapses are characterized by a protrusion of one synapse into the other. Protrusions contain vesicles in each case, and they seemingly represent extensions of the presynapses and not misguided axon outgrowths. Such a phenotype has not been described for *sad-1* mutants before, but supports the presumptive roles of SAD-1 in the integrity of synaptic structure [Crump et al. 2001; Hung et al. 2007; Kim et al. 2010]. Consistent with such functions, my data qualitatively show that varicosities are more unevenly shaped in *sad-1* worms (Figure 3.20). Finally, microtubule orientation is affected in 8 of 11 synapses analyzed, with microtubules running through vesicle pools and in two cases even perpendicular to the synapse (Figure 3.21); this is atypical for *C. elegans* synaptic architecture.

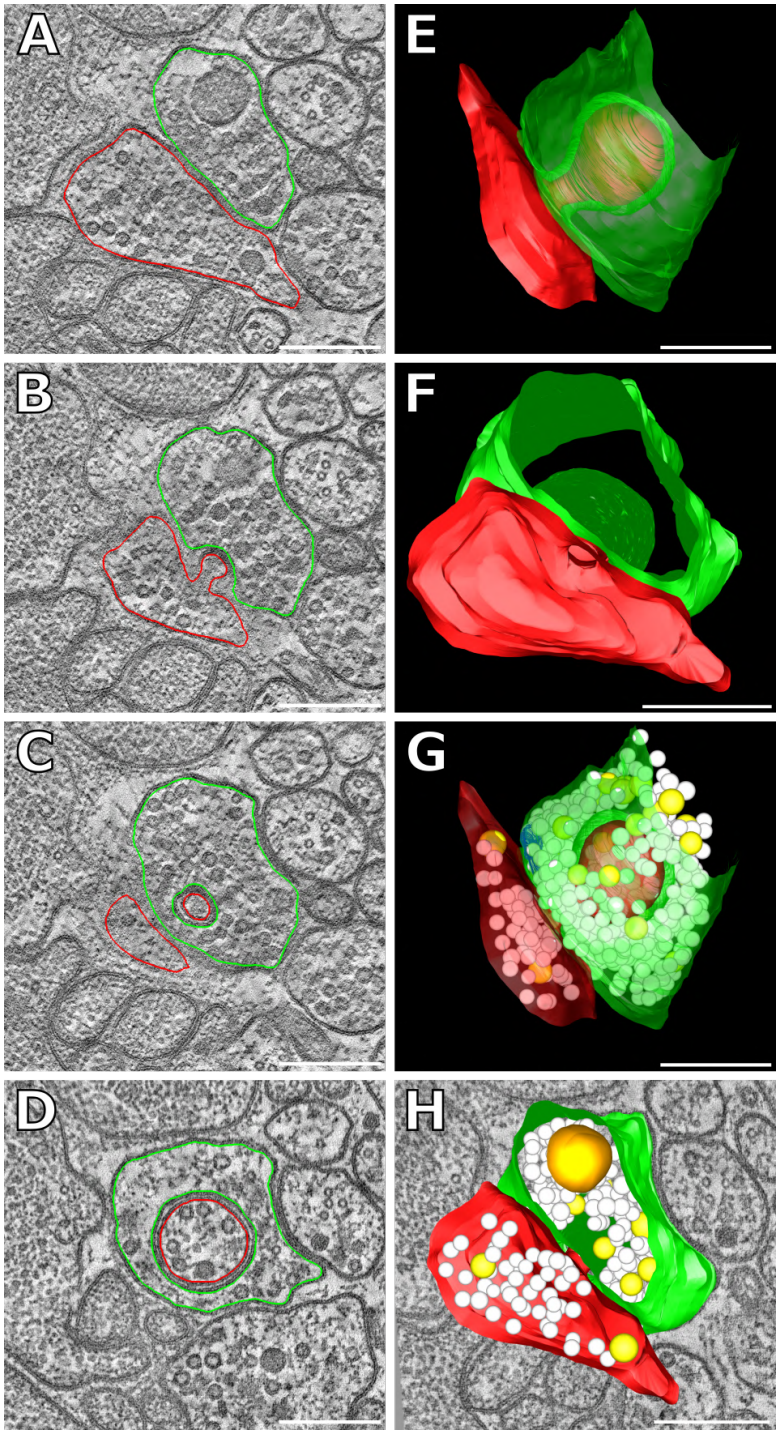

Figure 3.18.: **Loss of function of SAD-1 leads to defects in synapse development.** One axon (membrane shown in red) has grown into the presynapse of another neuron (green). The defective outgrowth contains vesicles. **A-D** Virtual slices of three joined serial tomograms from 200 nm sections reveal one synapse growing into the other. **E-H** 3D reconstruction of the synapses and some of their organelles. Clear core vesicles (white), dense core vesicles (yellow), one dense projection (blue), and one mitochondrion (orange) are shown. Scale bars: 250 nm.

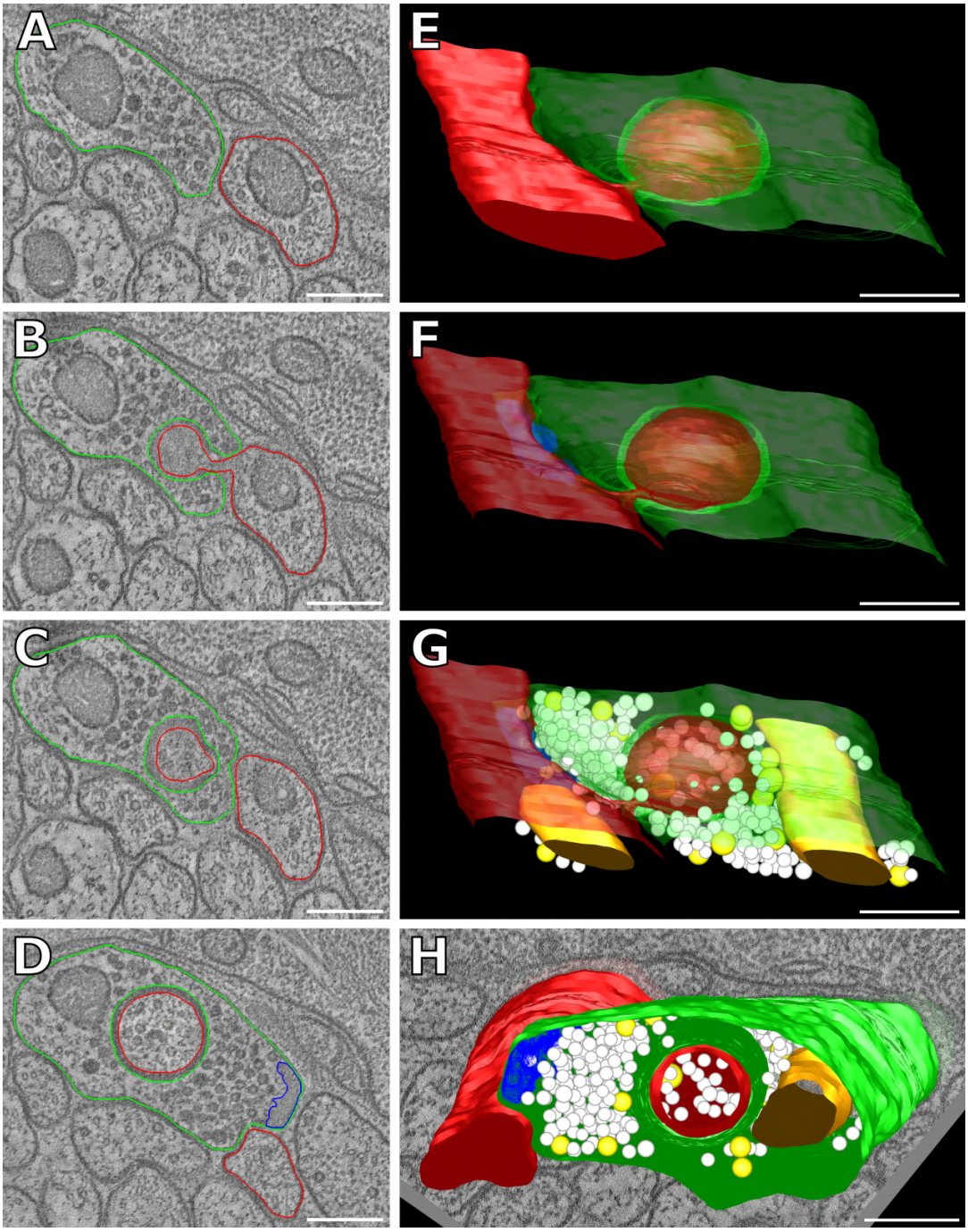

Figure 3.19.: **A second example of defects in synapse development due to SAD-1 loss of function.** One axon (membrane shown in red) has grown into the presynapse of another neuron (green). The defective outgrowth contains vesicles. **A-D** Virtual slices of two joined serial tomograms from 200 nm sections reveal one synapse growing into the other. Dense projection shown in blue. **E-H** 3D reconstruction of the synapses and some of their organelles. Clear core vesicles (white), dense core vesicles (yellow), one dense projection (blue), and mitochondria (orange) are shown. Scale bars: 250 nm.

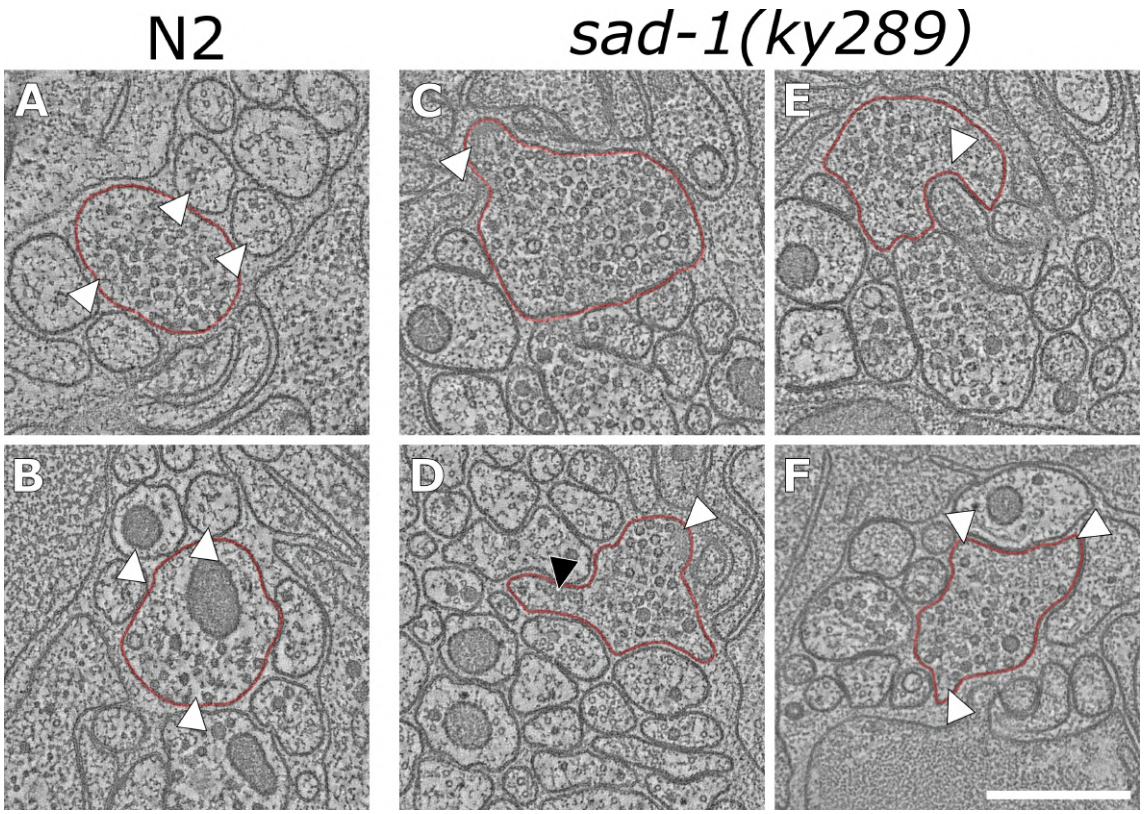

Figure 3.20.: **Lack of SAD-1 affects the shape of synapses.** Virtual slices from tomograms of N2 and *sad-1* nerve cords. **A, B** Two typical N2 examples. Virtual transverse sections of axons and synapses appear rounded and self-consistent (arrowheads). **C-F** Four typical *sad-1* examples. Plasma membrane shows many protrusions (arrowheads). Sometimes, dense projections are located in protrusions (white arrowheads in **C** and **D**). Scale bar: 500 nm.

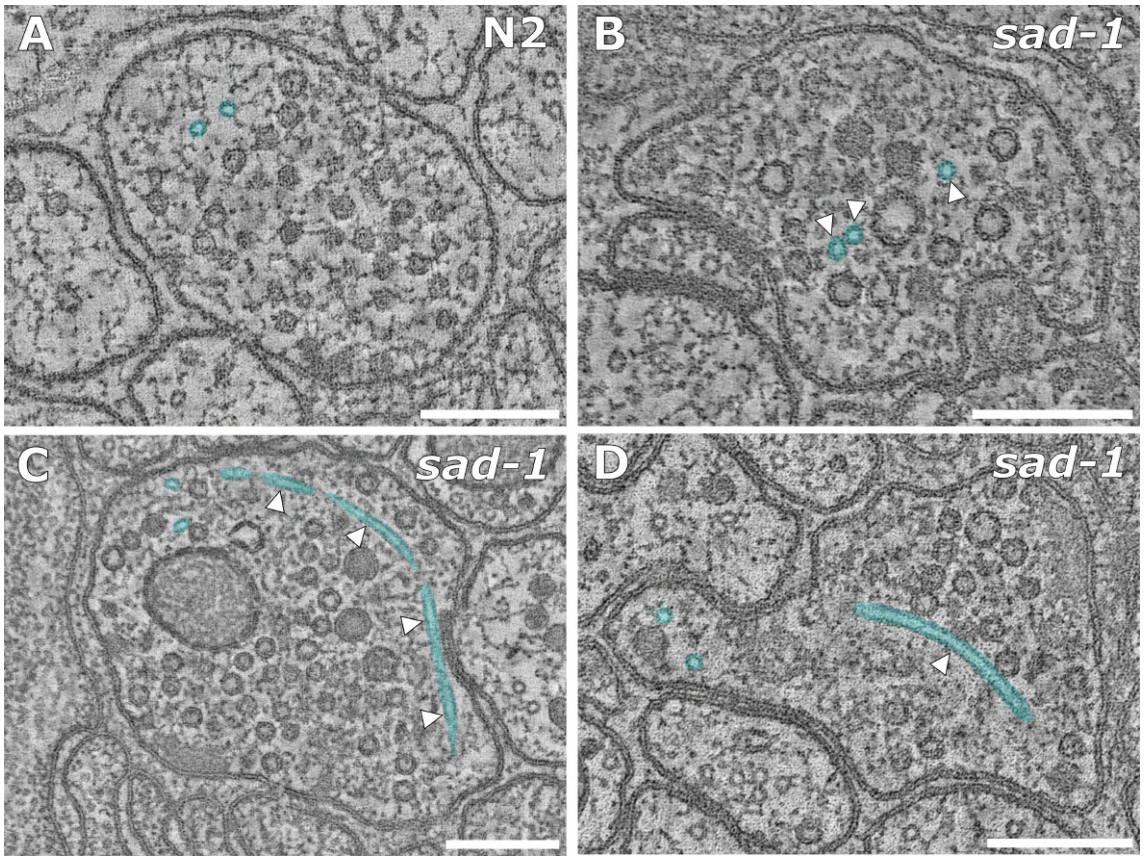

Figure 3.21.: **Lack of SAD-1 affects microtubule position and orientation within the synapse.** Virtual slices from tomograms of N2 (**A**) and *sad-1* (**B-D**) cholinergic synapses. Microtubules within synapses are shaded in cyan. Arrowheads point to microtubules with deviant orientations. **A** Microtubules are typically located in distal synaptic regions, outside of the vesicle pool, and oriented parallel to the axon. **B** Microtubules are located within the vesicle pool. **C, D** Microtubules are located within the vesicle pool and oriented perpendicular to the axon. Scale bars: 200 nm.

To analyze the vesicle pools, I reconstructed and classified the vesicles via automated Fiji macros [Kaltdorf et al. 2017, 2018]. Five double-tilt tomograms of N2 worms and 20 double-tilt tomograms of *sad-1* worms were used for the analysis. Overall, for N2 807 CCVs and 51 DCVs, and for *sad-1* 4507 CCVs and 163 DCVs were reconstructed and classified. The comparison of vesicle sizes between N2 and *sad-1* showed no significant difference for DCVs (median DCV radii: 21.3 nm for *sad-1*, MAD[14]=4.3 nm vs. 20.6 nm for N2, MAD=3.6 nm), but CCVs were significantly larger with a 3.5 % increase in median radius (median CCV radii: 12.4 nm for *sad-1*, MAD=3.1 nm vs. 11.9 nm for N2, MAD=3.2 nm) (Figure 3.22A). This amounts to approximately a 0.9 nm difference in diameter.

The distances of vesicles to the active zone differed only significantly for DCVs, where is was slightly larger for *sad-1* (413 nm for *sad-1*, MAD=132 nm vs. 393 nm for N2, MAD=76 nm). For CCVs, this was just a tendency (p-value = 0.094; 290 nm for *sad-1*, MAD=156 nm vs. 284 nm for N2, MAD=157 nm) (Figure 3.22B). The vesicle pool density was also analyzed. In an analysis of each vesicle's three closest neighbors, there was no significant difference between N2 and *sad-1* when looking at the first closest (31.1 nm for *sad-1*, MAD=8.4 nm vs. 30.9 nm for N2, MAD=9.4 nm), but the second (38.2 nm for *sad-1*, MAD=6.8 nm vs. 38.4 nm for N2, MAD=7.7 nm) and third closest neighbors (42.7 nm for *sad-1*, MAD=6.5 nm vs. 44.0 nm for N2, MAD=7.6 nm) were significantly closer in *sad-1* compared to N2 worms (Figure 3.22C). The vesicle pool density given as number of vesicles per volume of the synapse yielded no significant difference for CCVs, however (105 CCVs per 100 nm^3 for *sad-1*, MAD=20 vs. 83 CCVs per 100 nm^3 for N2, MAD=35). For DCVs the density was slightly decreased (3.0 DCVs per 100 nm^3 for *sad-1*, MAD=1.6 vs. 6.3 DCVs per 100 nm^3 for N2, MAD=2.8), which was weakly significant (p-value = 0.044) (Figure 3.22D). Taken together, these results are consistent with the model that CCV pools are larger in *sad-1* worms, but of normal density. In larger pools, a lower percentage of all vesicles is located at the periphery of the pool (due to the lower surface-volume ratio) and thus the probability of a given vesicle to possess several close neighbors is higher than in smaller pools (cf. Figure 3.22C). Additionally, average distances of vesicles to the active zone should be bigger in larger pools. This was the case for DCVs (see above). CCVs tend towards bigger distances (p-value = 0.094), but this result is probably masked by limitations of the analysis (see Discussion). The fact that DCVs are further from the active zone and display a lower density might indicate that lack of SAD-1 leads to an increase in CCVs, but not

[14]MAD = median absolute deviation, see section 2.10.

DCVs. Indeed, DCVs make up 6 % of total vesicles in N2 but only 3.5 % in *sad-1* tomograms analyzed.

Overall, electron tomography and automated vesicle analysis made it possible to discover new phenotypes of *sad-1* worms on the ultrastructural level. Careful descriptions of mutant phenotypes are often key to understand a protein's function. Thus, analysis of effects of mutated synaptic proteins like SAD-1 are a powerful tool to elucidate molecular mechanisms at the synapse. The end goal is a comprehensive understanding of the synaptic machinery. However, it is not only important to understand healthy synapses but also the mechanisms of synaptopathies.

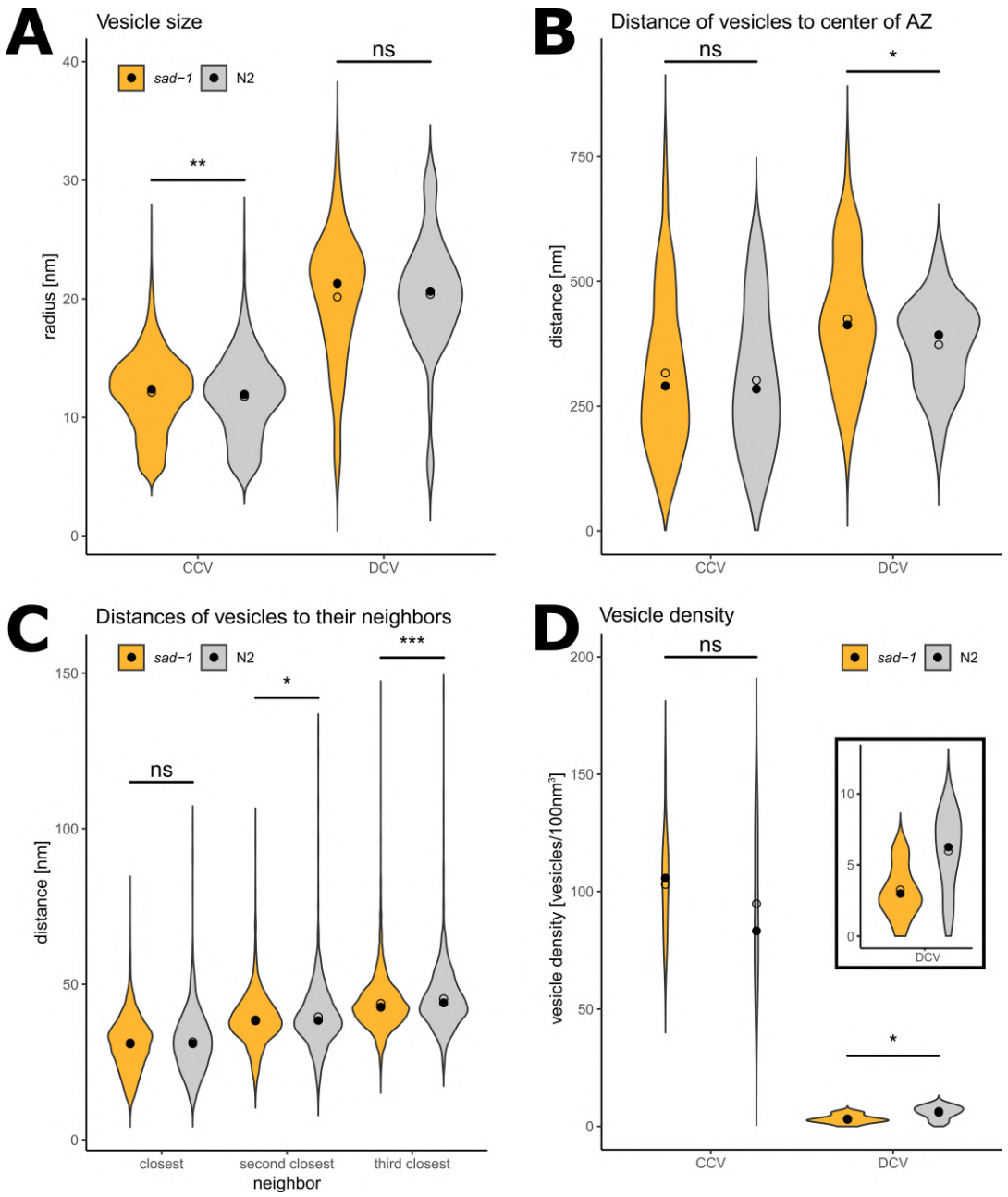

Figure 3.22.: **Quantitative vesicle analysis in *sad-1* worms.** Electron tomograms of NMJs of adult hermaphrodite *sad-1* and N2 worms were used for automated vesicle analysis. Vesicle reconstruction and classification via the 3D ART VeSElecT and automated classification Fiji macros [Kaltdorf et al. 2017, 2018]. Statistical analysis via Mann-Whitney Wilcoxon test. Data are depicted as violin plots. Median (closed circles) and mean (open circles) are given on each plot. **A** Vesicle radii for clear core (CCV) and dense core vesicles (DCV). **B** Linear distances of the center points of all vesicles to the center of the active zone (AZ). **C** Distances of vesicles to their first, second, and third closest neighbor. **D** Vesicle pool density: number of vesicles per volume of the synapse within a given tomogram. The inset shows the plots for DCVs at a different scale.

3.4. The effects of mutated FUS on the ultrastructure of motor neurons

For the FUS project I collaborated with Prof. Mei Zhen,[15] Prof. Shangbang Gao,[16] and Prof. Michael Sendtner.[17] Much of the work has been performed together with Michael Skoruppa from the laboratory of Prof. Sendtner. Prof. Sendtner provided expertise in neurodegeneration, particularly in mammals. Prof. Zhen provided the worm strains. Prof. Gao provided electrophysiological data on FUS worm strains.

Studying the disease mechanisms of FUS-mediated amyotrophic lateral sclerosis (ALS) remains challenging. However, the recent advances in establishing *C. elegans* as a disease model and advanced structure preservation and imaging techniques made the analysis of FUS-affected synapses an attractive model to apply the techniques used or established during this thesis. Indeed, we found an effect of FUS on synaptic ultrastructure in *C. elegans* and we were able to localize FUS via srAT in its ultrastructural context. Furthermore, we analyzed the ultrastructure and FUS localization on cultured mouse primary motor neurons and thus demonstrated the potential of these techniques for future studies.

3.4.1. *C. elegans* expressing mutated FUS show alterations in synaptic ultrastructure

For a comparative analysis, we chose old hermaphrodite worms that pan-neuronally express FUS501 and were six days of age. Initial experiments and the literature [Murakami et al. 2012] have shown that the neurodegenerative phenotype is well-pronounced at this age, while survival is still high. We reasoned that a pathological synaptic phenotype should already be pronounced prior to degeneration causing overwhelming secondary phenotypes that could make analysis more difficult. As controls, we used the N2 wild-type strain that had been used to create the FUS501 line and a line expressing wild-type FUS (FUSwt).

[15] Lunenfeld-Tanenbaum Research Institute, Mount Sinai Hospital, Toronto, Canada and Departments of Physiology and Molecular Genetics, University of Toronto, Toronto, Canada
[16] Key Laboratory of Molecular Biophysics of the Ministry of Education, College of Life Science and Technology, Huazhong University of Science and Technology, Wuhan, China
[17] Institute of Clinical Neurobiology, University Hospital Würzburg, Würzburg, Germany

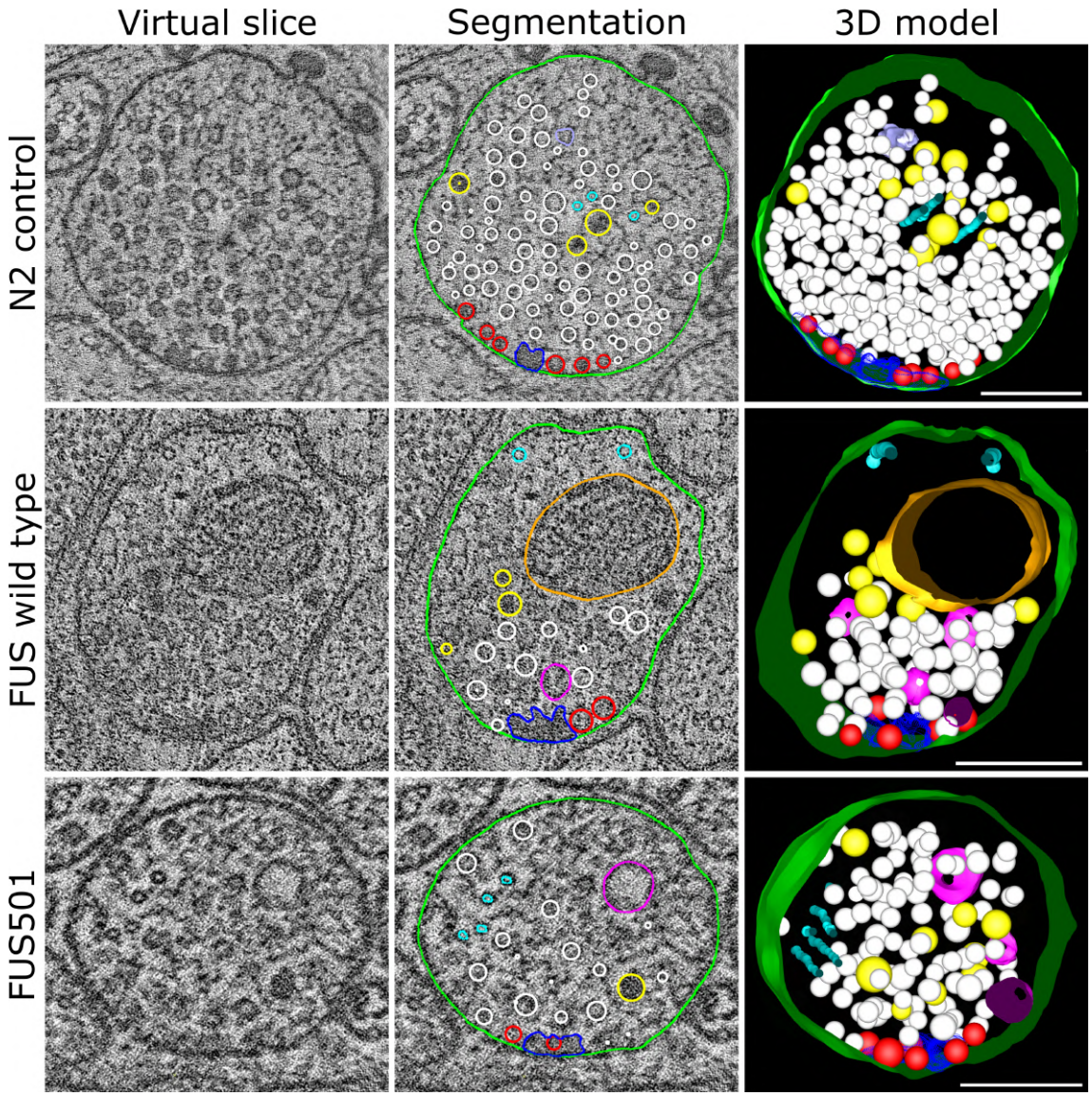

Figure 3.23.: **Mutated FUS affects the synaptic ultrastructure of cholinergic motor neurons.** Shown are virtual ∼1 nm slices from electron tomograms of cholinergic motor neurons, segmentations of these slices, and the 3D models of the whole tomograms. Segmented structures: plasma membrane (green), mitochondria (orange), dense projections (dark blue), microtubules (cyan), endoplasmic reticulum (lavender), dense core vesicles (yellow), clear core vesicles (white), docked clear core vesicles (red), and endosome-like structures (pink). Large, endosome-like structures appear in synapses affected by mutated FUS501, but not in FUSwt and N2 controls. FUSwt controls show smaller structures that presumably represent normal endosomes. Scale bars: 200 nm.

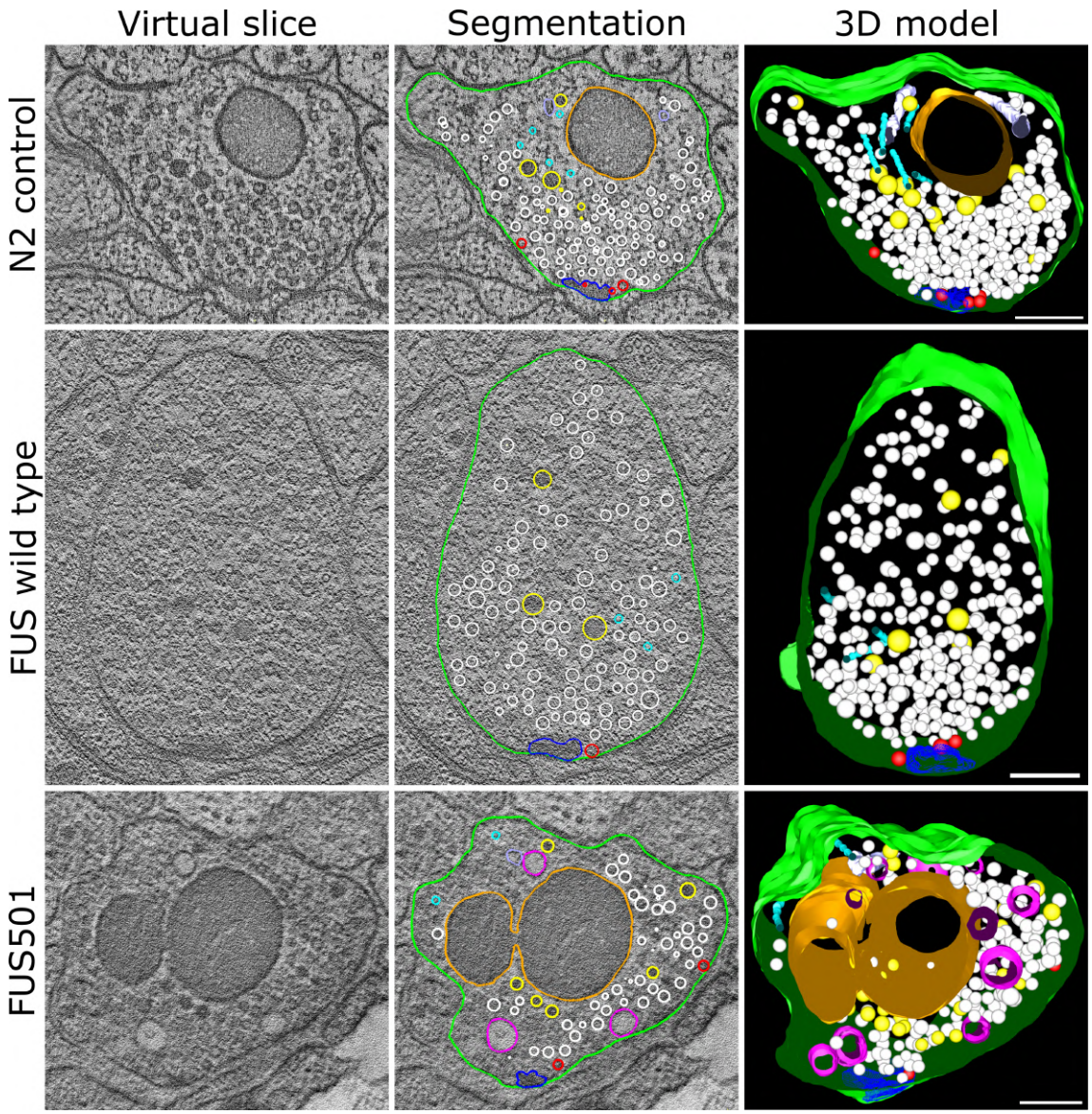

Figure 3.24.: **Mutated FUS affects the synaptic ultrastructure of GABAergic motor neurons.** Shown are virtual ∼1 nm slices from electron tomograms of GABAergic motor neurons, segmentations of these slices, and the 3D models of the whole tomograms. Segmented structures: plasma membrane (green), mitochondria (orange), dense projections (dark blue), microtubules (cyan), endoplasmic reticulum (lavender), dense core vesicles (yellow), clear core vesicles (white), docked clear core vesicles (red), and endosome-like structures (pink). Large, endosome-like structures appear in synapses affected by mutated FUS501, but not in FUSwt and N2 controls. Scale bars: 200 nm.

A total of 196 electron tomograms of FUS501, FUSwt, or N2 synapses of NMJs in the ventral and dorsal nerve cords were reconstructed. Analyses were performed in a genotype-blinded manner. I selected 65 tomograms that contained active zones and were of sufficient quality for reliable vesicle analysis. We analyzed both GABAergic and cholinergic synapses. Indeed, synapses of worms expressing mutated FUS501 showed ultrastructural features rarely seen in controls. Arguably most striking was the presence of large, mostly electron-light endosome-like organelles (see section 4.3.1 for a discussion on the identity of these putative endosomes) that we saw both in cholinergic and GABAergic synapses (Figures 3.23, 3.24). They appeared within the vesicle pool and had mostly spherical shapes, although more complex networks occurred as well (see Figure 3.25D). We observed that many of these endosomes showed filamentous electron-dense inclusions (Figure 3.25). I quantified the outer diameters of all endosomes in tomograms that contained active zones. Average endosome diameters were calculated from the longest and shortest diameter of a given endosome measured manually on the virtual tomogram slice where the endosome appeared largest. A density plot (kernel density estimation) of these diameters shows that endosome populations and sizes are similar in N2 and FUSwt, but that much larger endosomes >100 nm exclusively appear in FUS501 worms (Figure 3.26A). However, a clear distinction of these endosome populations was not apparent. Thus, it was not possible to separate endosomes into "normal" and "FUS501" endosomes based on their sizes alone. Therefore, endosomes were separated into two groups based on the presence of electron-dense filaments in their lumina, namely "clear" endosomes vs. "filled" endosomes. Overall, I found 50 clear endosomes and 35 filled ones in FUS501, 25 clear and 14 filled in FUSwt, and 7 clear and 5 filled ones in N2. When I compared the diameters of the "clear" endosomes, there were no significant differences between FUS501 (53.8 nm, MAD=4.8 nm), FUSwt (52.0 nm, MAD=4.4 nm), and N2 (53.0 nm, MAD=5.2 nm). However, the "filled" endosomes were larger in FUS501 worms (88.5 nm, MAD=35.6 nm) compared to FUSwt (59.3 nm, MAD=14.1 nm) and N2 (74.5 nm, MAD=17.0 nm). The difference was highly significant for FUSwt, but only a tendency for N2 (p-value = 0.098) (Figure 3.26). Since for N2 only a small number of endosomes was analyzed, the small n might explain why statistical significance was not achieved here. Nevertheless, these data suggest that FUS501 expression in *C. elegans* causes the emergence of a population of endosome-like structures in NMJ synapses that have two properties: They are considerably larger than normal endosomes and contain electron-dense filaments.

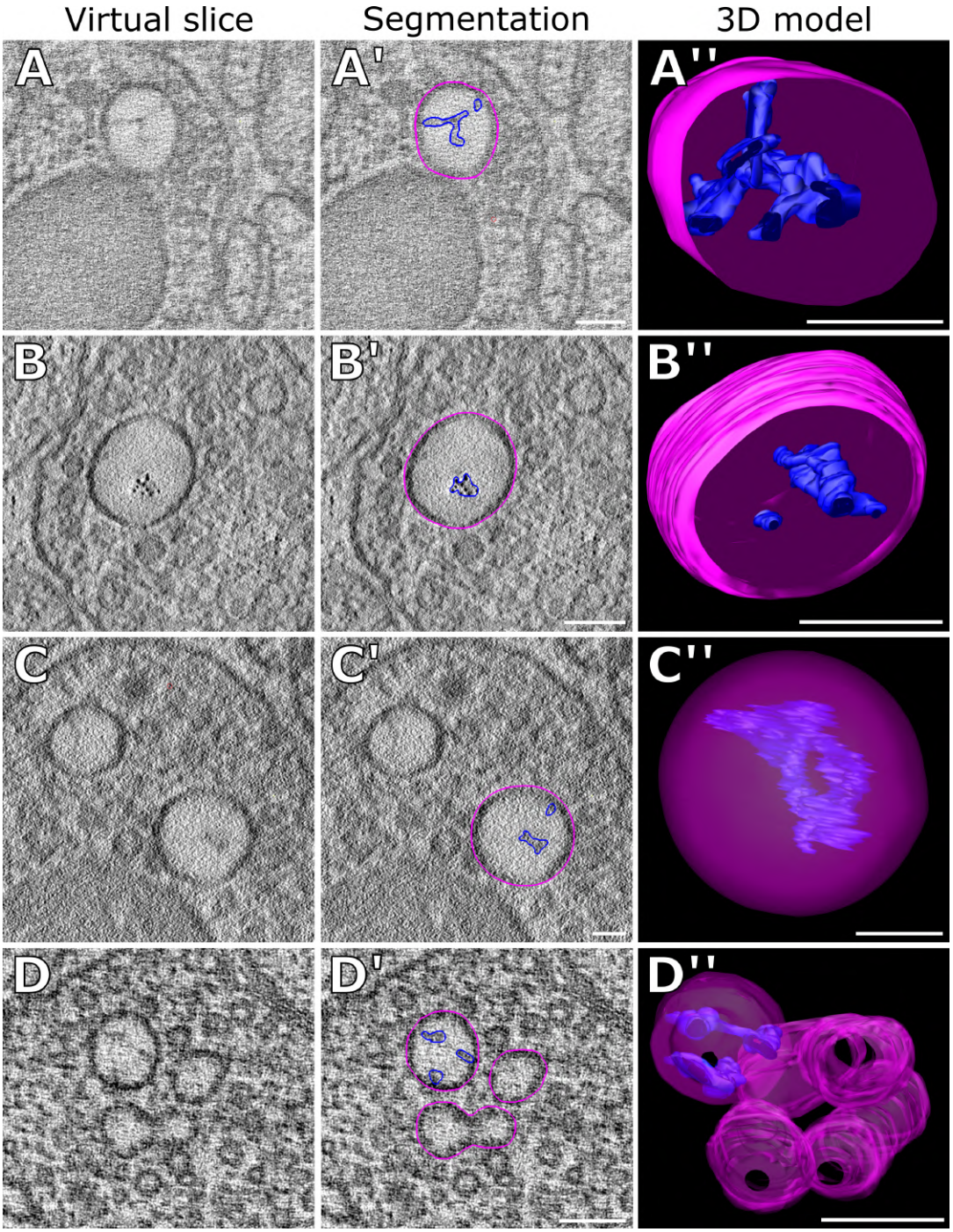

Figure 3.25.: **Morphology of the large endosomes.** Examples of large endosomes (pink) in synapses of NMJs. Only endosomes in tomograms containing a dense projection are shown here. They appear large, with diameters of >80 nm, and often contain some electron-dense material (dark blue). **A** Typical example. The electron-dense content is often branched, as shown. **B** Electron-dense content appears partially in distinct dots. **C** Instance of a complete large endosome. **D** In one instance, large endosomes formed a group and "network" as shown. Scale bars: **A, B, D**: 100 nm, **C**: 50 nm.

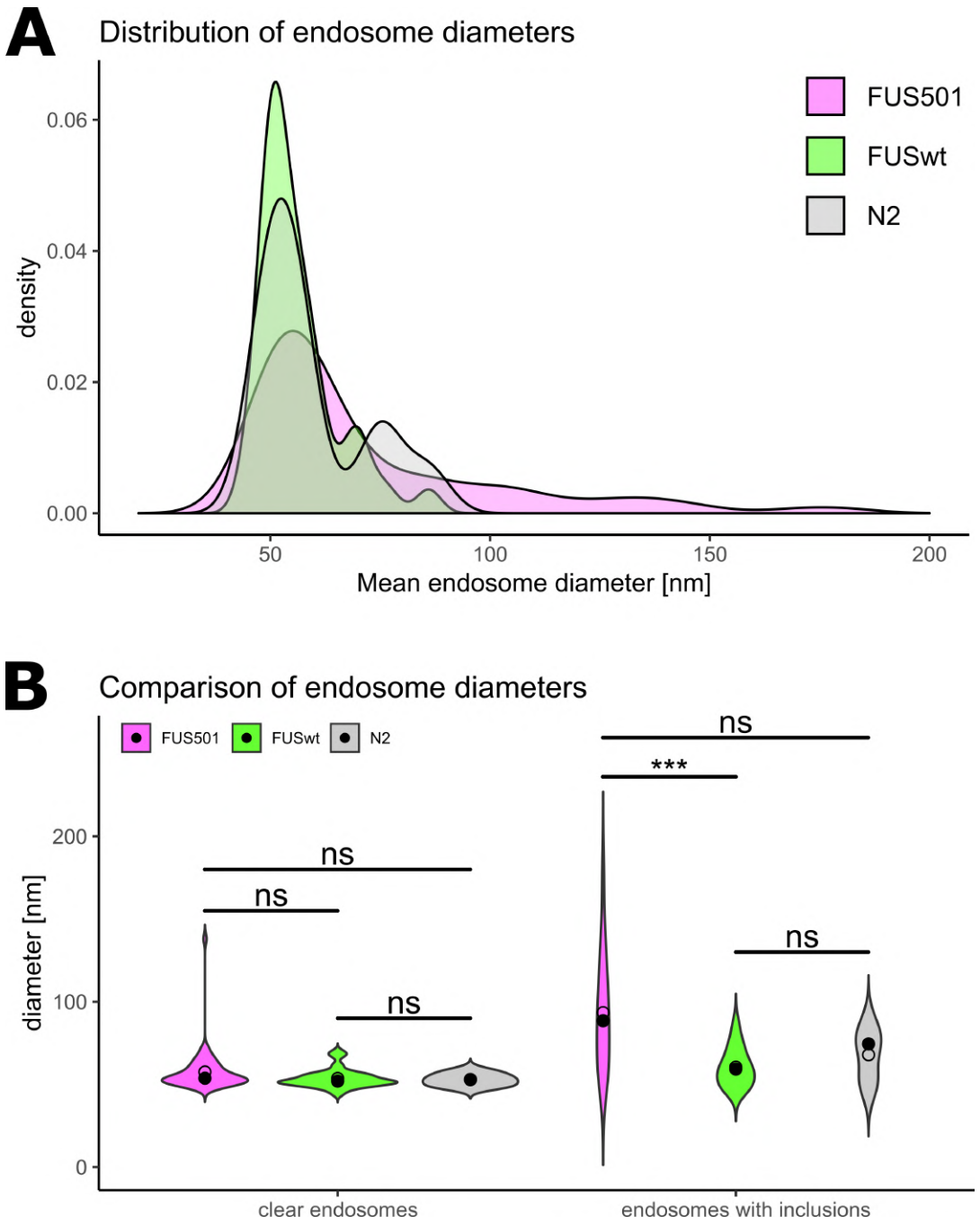

Figure 3.26.: **Larger endosomes that contain electron-dense filaments are caused by FUS501.** Electron tomograms of 6 d old hermaphrodite worms expressing FUS501 or FUSwt, or N2 worms were used to manually measure endosome diameters. For each endosome the average diameter calculated from the longest and shortest measured diameter was used for subsequent analysis. **A** Density plot of endosome diameters. FUS501 worms show populations of especially large endosomes not present in controls (arrows). **B** Comparison of endosome diameters in relation to the presence of electron-dense filaments. Statistical analysis via Mann-Whitney Wilcoxon test. Data are depicted as violin plots. Median (closed circles) and mean (open circles) are given on each plot.

To investigate if the vesicle pool is also affected, I analyzed vesicles with automated reconstruction and classification tools as before (see section 3.3). These tools require high quality tomograms. However, since most tomograms acquired for the FUS project were only single tilt, they were not suitable for this approach and only a subset of 11 tomograms was used for this analysis. Overall, I automatically reconstructed and classified 1,030 vesicles for FUS501, 164 for FUSwt and 2,053 for N2. The quantification was performed on cholinergic synapses only since the number of GABAergic ones was too small for proper quantification. I analyzed the vesicle sizes and found that CCVs had similar sizes between the three genotypes (median vesicle radii: 12.6 nm for FUS501, MAD=3.5 nm vs. 11.3 nm for FUSwt, MAD=4.4 nm vs. 13.2 nm for N2, MAD=3.5 nm) (Figure 3.27A). The differences were significant, however. DCVs had similar sizes in FUSwt and N2 (median DCV radii: 23.5 nm for FUSwt, MAD=5.3 nm vs. 22.8 nm for N2, MAD=5.3 nm), but were significantly different in FUS501 (median DCV radius: 17.8 nm for FUS501, MAD=2.8 nm). DCVs made up 11.4 % of all vesicles in FUS501, 4.9 % in FUSwt, and 4.5 % in N2. Thus, in FUS501 worms synapses contain more than twice as many DCVs in relation to CCVs compared to controls, but DCVs are smaller (Figure 3.27A).

When comparing the distances of CCVs to the center of the active zone, FUS501 and FUSwt both showed smaller distances than N2, but FUS501 showed also larger distances than FUSwt (249 nm for FUS501, MAD=141 nm vs. 208 nm for FUSwt, MAD=116 nm vs. 373 nm for N2, MAD=211 nm). All these differences were highly significant. For DCVs, distances for FUS501 and FUSwt differed weakly significantly from each other (p-value = 0.035) with greater distances for FUS501, but they showed both highly significantly smaller distances compared to N2 (339 nm for FUS501, MAD=85.3 nm vs. 261 nm for FUSwt, MAD=80.7 nm vs. 505 nm for N2, MAD=127 nm) (Figure 3.27B). To sum up, these results show that vesicles are generally a bit smaller in FUS501 and FUSwt and located closer to the active zone.

To evaluate synaptic transmission, I also analyzed docked vesicles. I identified and counted docked vesicles in all tomograms that contained a cholinergic synapse with clearly visible dense projections, which mark the active zone (28 tomograms for FUS501, 16 for FUSwt, and 5 for N2). Interestingly, FUS501 and FUSwt had both significantly less docked vesicles than N2 worms (number of docked vesicles per tomogram normalized to dense projection volume: 2.7 for FUS501, MAD=2.4 vs. 6.2 for FUSwt, MAD=5.9 vs. 10.5 for N2, MAD=3.4) (Figure 3.27C). When

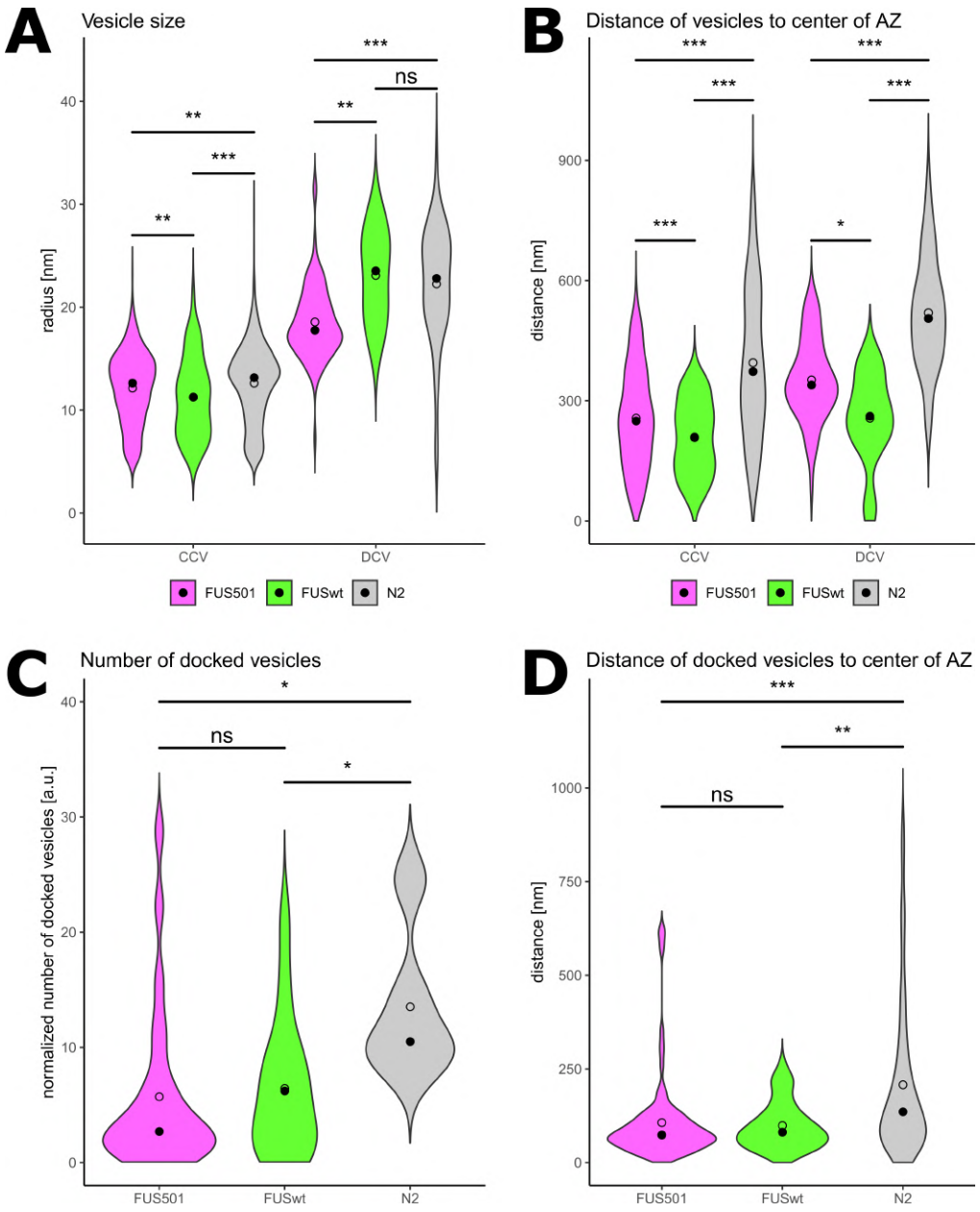

Figure 3.27.: **Quantitative vesicle analysis in FUS worms.** Electron tomograms of 6 d old hermaphrodite worms expressing FUS501 or FUSwt, or N2 worms were used for automated and manual analysis. Only cholinergic synapses were included. Statistical analysis via Mann-Whitney Wilcoxon test. Data are depicted as violin plots. Median (closed circles) and mean (open circles) are given on each plot. **A, B** Vesicle reconstruction and classification via the 3D ART VeSElecT and automated classification Fiji macros [Kaltdorf et al. 2017, 2018]. **A** Linear distances of the center points of all vesicles to the center of the active zone (AZ) as given by the classification macro. **B** Vesicle radii as given by the classifiaction macro. **C, D** Analysis of vesicles docked to the plasma membrane via manual analysis. **C** Numbers of docked vesicles per tomogram normalized to approximate volume of the dense projection in a given tomogram. **D** Linear distances of docked vesicles to the center of the active zone (AZ).

looking at the linear distances of docked vesicles to the center of the active zone, FUS501 and FUSwt showed no significant difference, but again both were significantly different compared to N2, where these distances were greater (73.5 nm for FUS501, MAD=37.8 nm vs. 81.0 nm for FUSwt, MAD=54.9 nm vs. 136 nm for N2, MAD=102 nm) (Figure 3.27D). Thus, in FUS501 and FUSwt less vesicles are docked, but those that are, are located closer to the active zone.

These results indicate that FUS proteins, FUS501 and FUSwt both, affected synaptic ultrastructural features. The larger filament-filled endosomes were almost exclusively found for FUS501, however. The question arose, if FUS501 protein itself might be present in these endosome-like structures. To look at the localization of FUS at the ultrastructural level, we thus decided to employ srAT.

3.4.2. Mutated FUS proteins can be localized on an ultrastructural level to the somatic cytoplasm of motor neurons, but not to their projections

To localize FUS proteins in their ultrastructural context, we used srAT (see section 3.1). We found that mutated FUS501 is localized in clusters in the nucleus and the cytoplasm of motor neurons, but not in the nerve cords (Figure 3.29). In our control worms, FUSwt staining was diffuse and limited to the nucleus (data not shown). We thus can confirm on the ultrastructural level what Murakami et al. [2012] found using fluorescence microscopy alone (see also Figure A.4 in the appendix).

For the FUS analyses, we tried propidium iodide to our knowledge for the first time on LR White sections as a stain for independent landmarks. Propidium iodide stained not only DNA but also RNAs [Suzuki et al. 1997]. Thus, in our sections propidium iodide delineated the shape of the cytoplasm, where RNAs are abundant (Figure 3.28), which made this stain even more useful for correlation than DAPI or Hoechst.

To confirm the results of mutated FUS localization, we repeated the staining. Mutated FUS was consistently localized in clusters in both cytoplasm and nucleus (Figure 3.30). Again, no staining could be observed on the nerve cords. To confirm specificity of our FUS antibody we also performed a co-stain with an antibody against GFP, since the FUS constructs all contain a GFP-tag (see Figure 1.7). Indeed, the FUS and GFP stainings overlapped almost perfectly on three consecutive

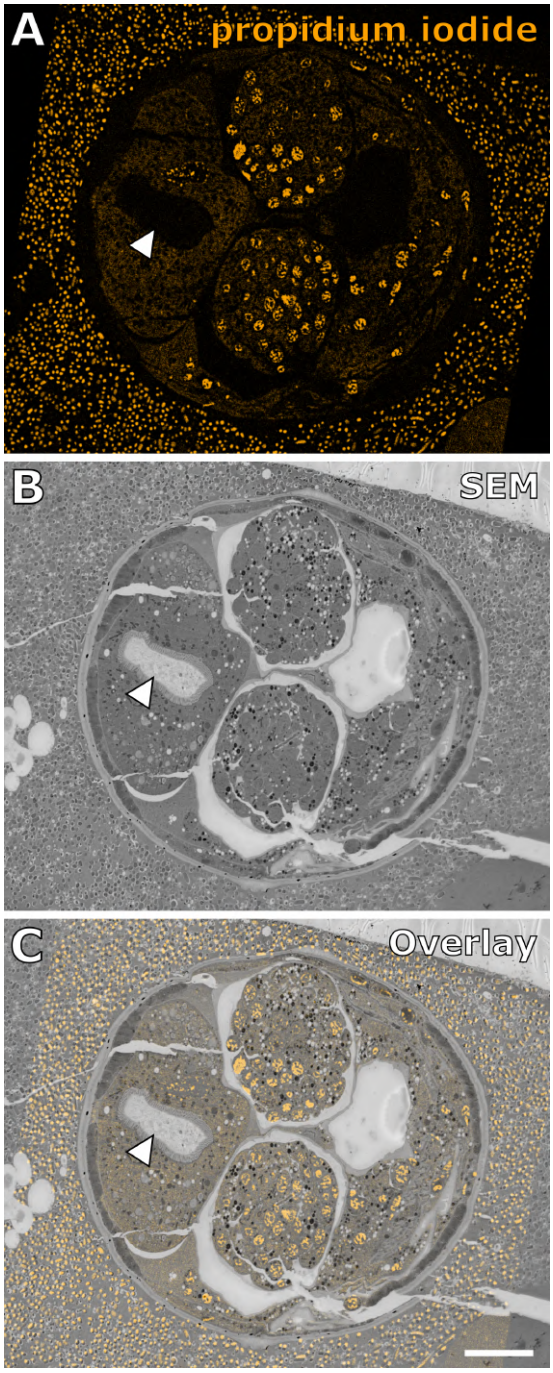

Figure 3.28.: **Propidium iodide is an improved staining of intrinsic landmarks for correlation.** **A** 100 nm LR White section of a *C. elegans* worms surrounded by bacteria. The section was stained with propidium iodide and recorded via SIM. Especially compacted DNA is stained (heterochromatin in the nuclei and bacterial chromatin) but also RNAs in the cytoplasm. Some structures are thus delineated, e. g., the intestinal lumen (arrowhead). **B** Scanning electron micrograph of the same region as in **A**. **C** Overlay of **A** and **B**. Scale bar: 10 µm.

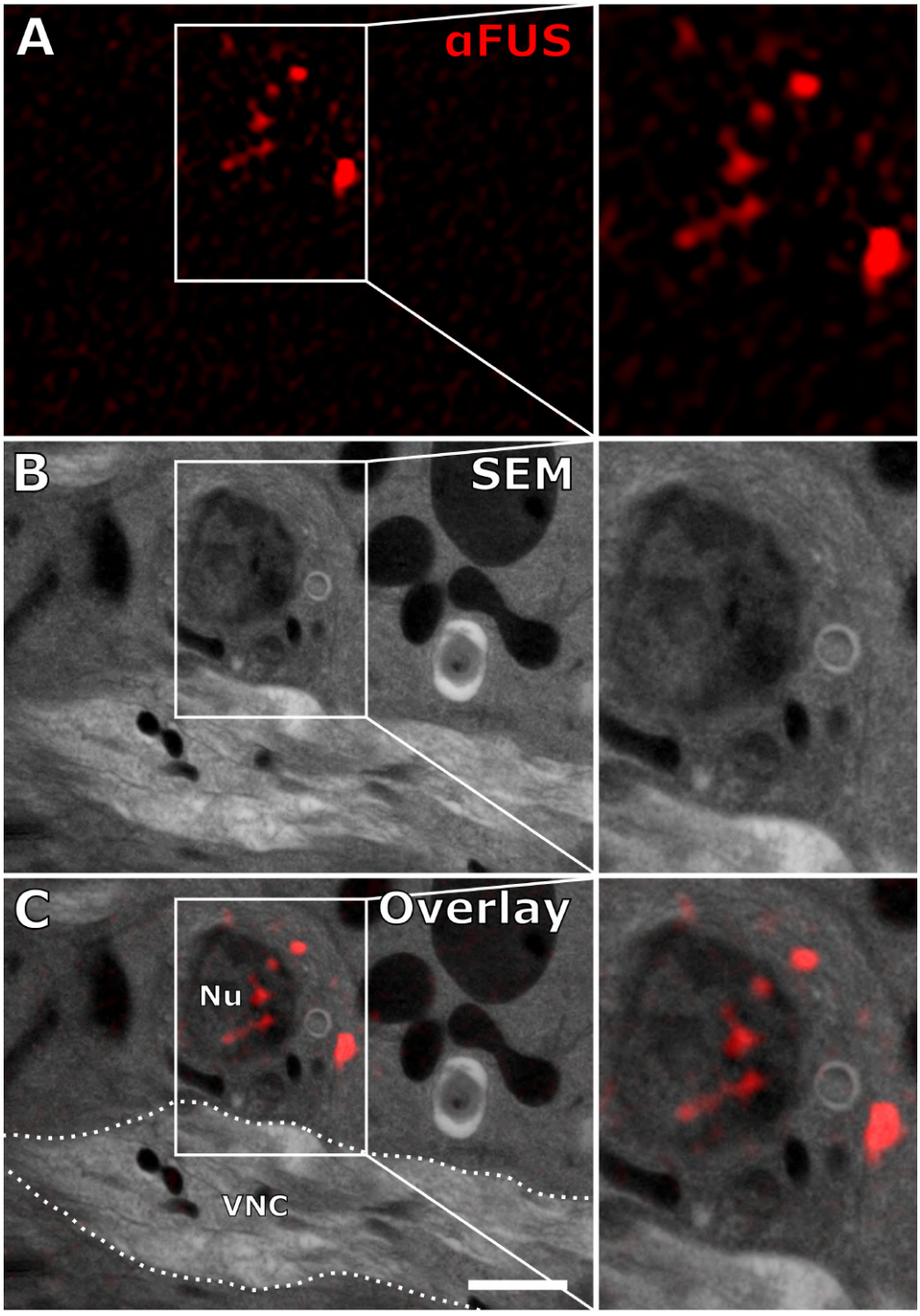

Figure 3.29.: **Mutated FUS is present in nucleus and cytoplasm of motor neurons but not in the nerve cords.** **A** Immunofluorescence staining against mutated FUS acquired by SIM. **B** Scanning electron micrograph of the same region as in **A**. **C** Overlay of **A** and **B** localizes FUS501 signals to the nucleus (Nu) and cytoplasm of a motor neuron, but does not show any signals on the synapses of the ventral nerve cord (VNC). Scale bar: 1 µm.

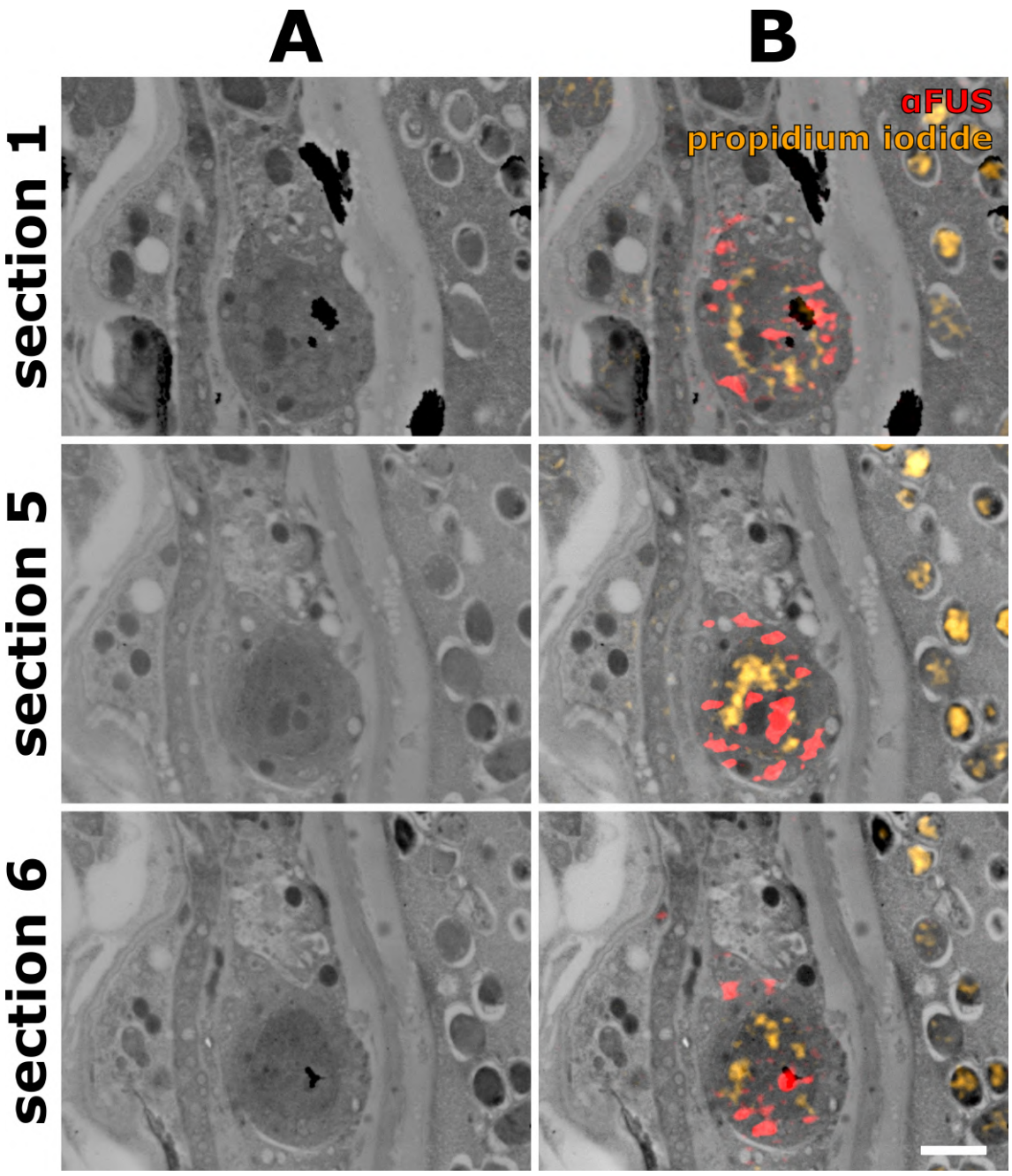

Figure 3.30.: **A selection of sections through a VNC consistently shows localization of mutated FUS in both cytoplasm and nucleus. A** Scanning electron micrographs of the VNC region of an adult hermaphrodite worm expressing mutated FUS. **B** The images of **A** overlaid with their corresponding fluorescent SIM images. Propidium iodide was used for correlation. FUS501 signals are consistently localized to both the nucleus and the cytoplasm of a motor neuron. The patchy staining suggests the presence of FUS accumulations. See supplemental Figure A.1 in the appendix for separate fluorescence channels. Scale bar: 1 µm.

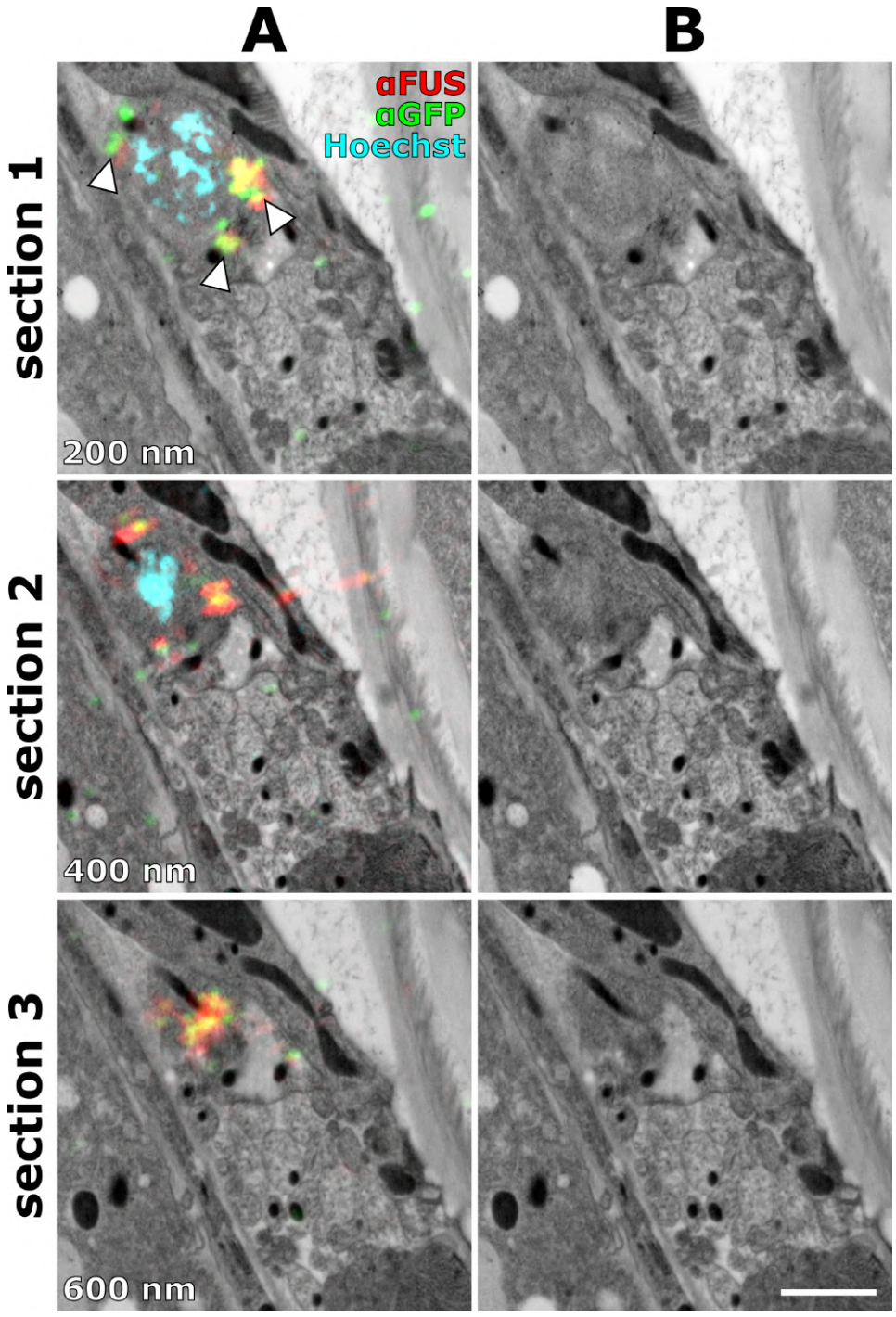

Figure 3.31.: **The FUS immunofluorescence staining is specific. A** Scanning electron micrographs of the VNC region of an adult hermaphrodite worm expressing mutated FUS. Consecutive 200 nm sections were stained. Hoechst was used for correlation. FUS501 was stained via direct antibody (red) and via its GFP-tag (green). Both stainings overlap significantly (arrowheads). **B** Micrographs shown without overlay for reference. See supplemental Figure A.2 in the appendix for separate fluorescence channels. Scale bar: 1 µm.

200 nm sections (Figure 3.31), confirming specificity of the antibodies on LR White sections.

The results of our FUS analyses in the worm consolidate *C. elegans* as a useful disease model for investigating ALS mechanisms. As a second and complementary model, we decided to look at cultured primary motor neurons from mouse. Although less tractable, as a mammalian model it is evolutionarily much closer to humans.

3.4.3. Visualization of cultured mouse primary motor neurons expressing mutated FUS for the first time with near-native preservation of ultrastructure

Michael Skoruppa cultured mouse primary motor neurons on sapphire discs for six days and I processed them with HPF/FS. With the morphology protocol established in our laboratory [Helmprobst et al. 2015; Kaltdorf et al. 2017, 2018], we obtained high-quality structure-preservation as revealed by TEM (Figure 3.32). With the immuno protocol established for srAT, results for morphology were also satisfying, with microtubules being even more clearly discernible (Figure 3.34). It was also possible to follow growth cone structures from the very bottom, i. e., at the surface of the sapphire disc, upwards in consecutive sections. Thus, the 3D ultra-architecture of the growth cones could be judged (Figure 3.33).

Our results demonstrate that this preparation preserves even very thin filopodia of growth cones and the ultrastructural morphology of growth cones and somata can be readily analyzed. Cyto-skeleton structures and organelles are well preserved. Because of these results and the fact that srAT worked very consistently on FUS worms, we also performed srAT on mouse motor neurons.

3.4.4. srAT reveals localization of FUS proteins in cultured mouse primary motor neurons in their ultrastructural context

To investigate the localization of mutated FUS in mouse motor neurons, we performed srAT on cultured primary motor neurons. Since these cells are not proliferative, lentiviruses with very high transduction rate were used to transfect them with

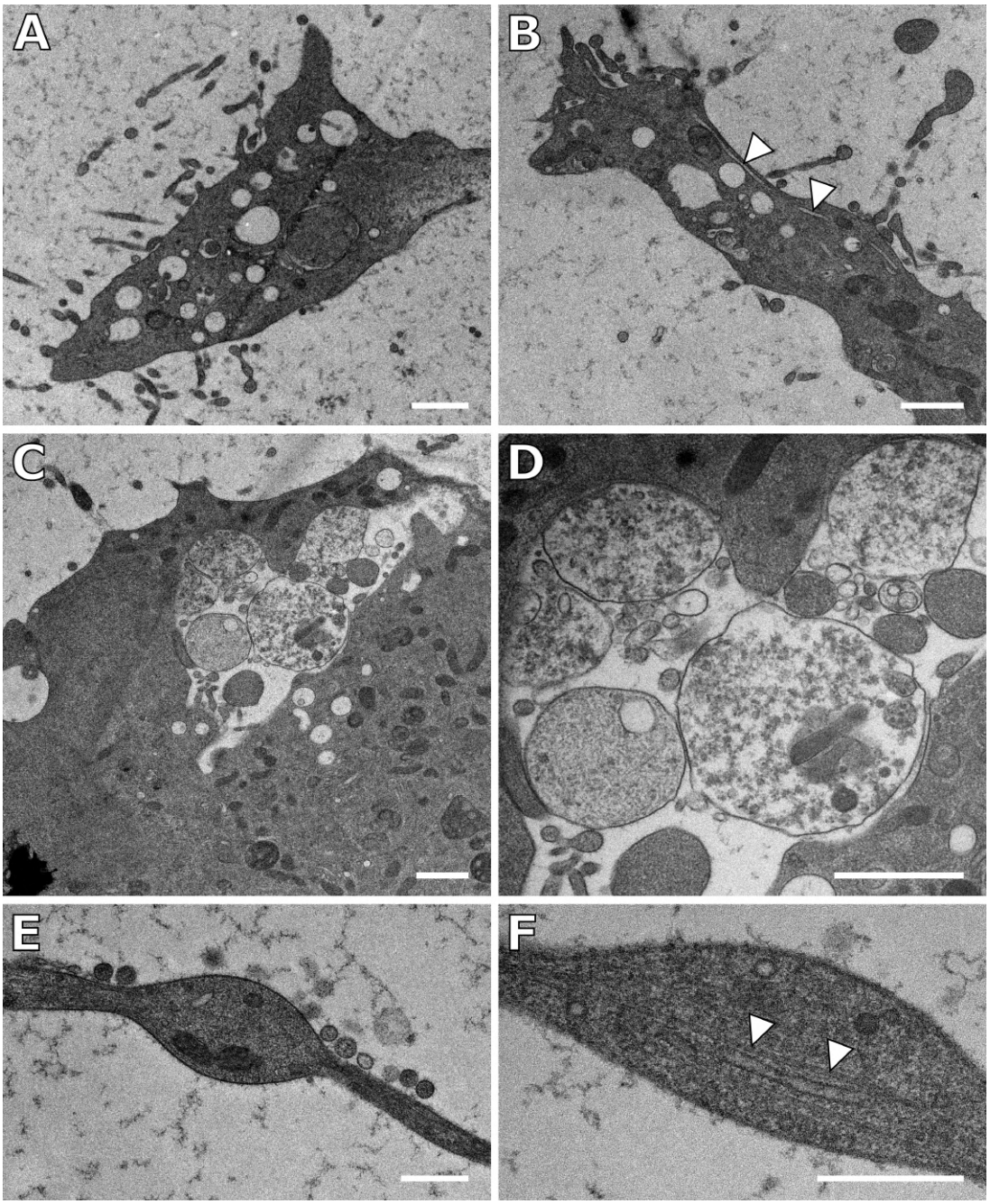

Figure 3.32.: **Transmission electron micrographs of primary mouse motor neurons processed by HPF/FS.** Primary motor neurons were cultured for six days on sapphire discs and then subjected to HPF/FS according to the morphology protocol, embedded in Epon resin and cut into ultrathin sections. TEM reveals near-native structure preservation. **A and B** Growth-cone-like structures. They show many fine protrusions. Arrowheads point to endoplasmic reticulum. Scale bars: 1 µm. **C and D** Cell body with large phagosome. Scale bars: 1 µm. **E and F** Varicosities of axons. Microtubules within are clearly visible (arrowheads). Scale bars: 500 nm.

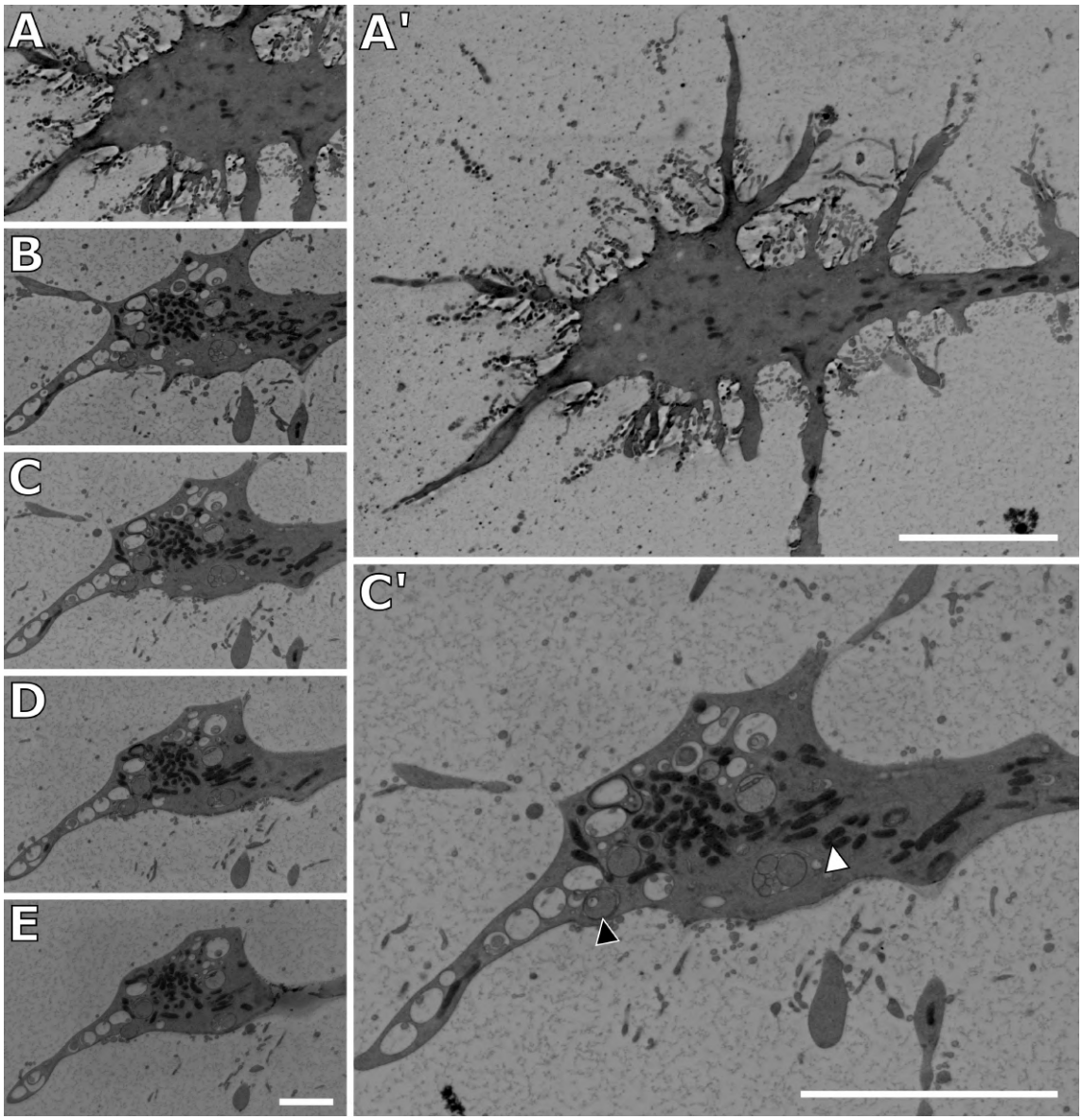

Figure 3.33.: **Consecutive sections through a growth cone reveal its ultrastructural morphology.** Growth cone of a cultured primary mouse motor neuron prepared according to the immuno protocol. **A - E** Consecutive 100 nm sections, beginning from the first one, i. e., the one closest to the sapphire disc on which it was cultured. **A', C'** More detailed views of **A** and **C**, respectively. **A'** shows the very fine protrusions typical for growth cones only present at the very first section, i. e., directly on top of the sapphire disc. **C'** Deeper in the tissue organelles like mitochondria (white arrowhead) and autophagosomes (black arrowhead) appear. For a high-magnification view of **C'** see supplemental Figure A.3 in the appendix. Scale bars: **A - E**: 2 µm, **A', C'**: 5 µm.

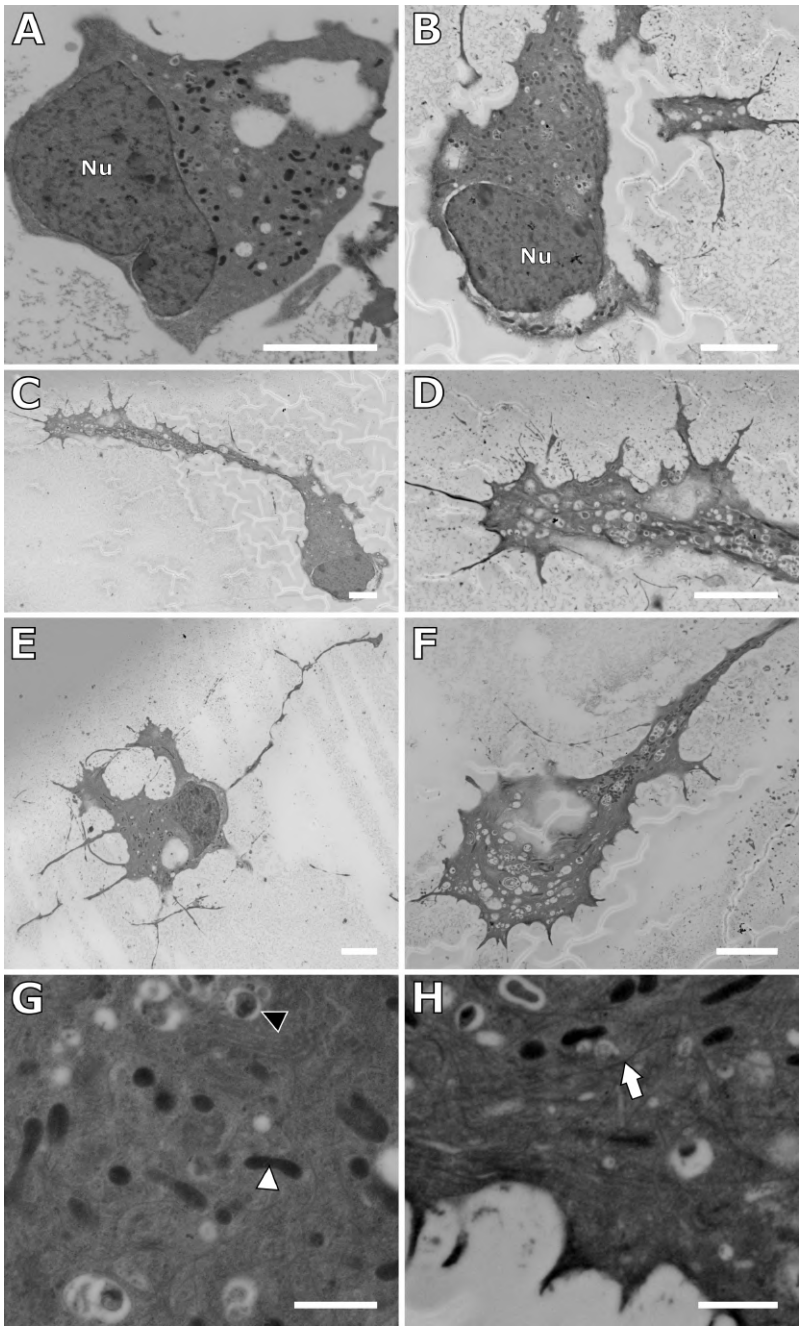

Figure 3.34.: **Scanning electron micrographs of primary mouse motor neurons expressing FUS(P525L) processed by HPF/FS.** Primary motor neurons were transducted with FUS(P525L) via lentivirus, cultured for six days on sapphire discs, and then subjected to HPF/FS according to the immuno protocol, embedded in LR White resin and cut into ultrathin sections. SEM reveals near-native structure preservation. **A and B** Cell bodies including nuclei (Nu). **C** Whole cell including growth cone. **D** Growth cone of **C** shown at higher magnification. **E** Whole cell including dendrites and two growth cones. **F** Further example of a growth cone. **G and H** Detailed view of the cytoplasm. Mitochondria (white arrowhead), phagosomes (black arrowhead), and microtubules (white arrow) are clearly visible. Scale bars: **A - F**: 5 µm, **G, H**: 1 µm.

a FUS(P525L) construct (see Figure 1.7). Again, Michael Skoruppa cultured the motor neurons on sapphire discs for six days and I processed them via HPF/FS. We stained 100 nm LR White sections against beta-Actin to reveal cellular regions of high motility, such as growth cones. Hoechst was used as a nuclear stain. The FUS constructs were stained via their HA-tags (cf. Figure 1.7) and an antibody against mouse FUS was used to stain for the native mouse FUS of the motor neurons. Figures 3.35 - 3.38 show a typical srAT result of four consecutive sections in detail, Figure 3.39 summarizes them. The Actin and Hoechst stains were used as intrinsic independent landmarks for correlation (cf. Figure 3.3). The native FUS was located almost exclusively in the nucleus, as expected [Dormann et al. 2010]. The HA-tag stain against the FUS constructs was only present in about half of the cells investigated. This signifies a transduction rate of about 50 % for the viral transduction. In those cells that showed HA-tag signal, the mutated FUS was located predominantly in the nucleus, but there were also many puncta in the cytoplasm, although not in axons or dendrites or growth cones. This result is consistent with our results in the worm, were FUS501 localization was similarly spread over nucleus and cell body, but not the processes (Figures 3.29 - 3.31). We also observed strong HA-tag stain in small round extracellular structures of about 1.5 µm in diameter (Figure 3.36). These structures were also positive for native FUS and beta-Actin. However, since they are too small for dead cells and too large to be exosomes, they remain enigmatic. Likely, these structures just represent random debris that unspecifically binds antibodies.

Overall, these results suggest that localization of mutated FUS works similarly well in mouse and worm. We showed how srAT can be used on primary motor neurons for future investigations involving protein localization in an ultrastructural context.

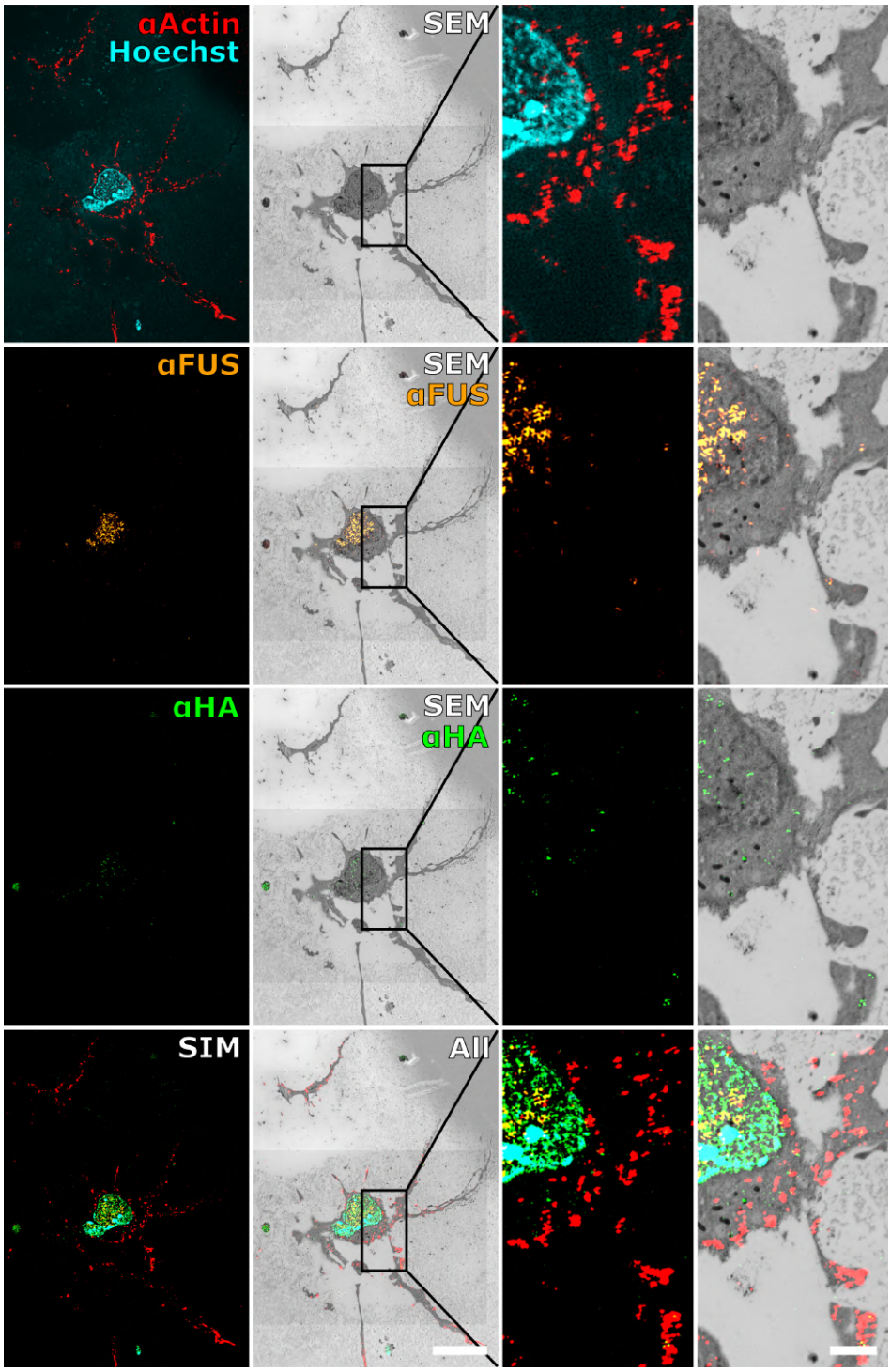

Figure 3.35.: **Localization of FUS proteins in cultured mouse primary motor neurons via srAT, section 1.** Native FUS (orange) is localized almost exclusively to the nucleus. FUS(P525L) (green) was transducted by lentivirus and is located in nucleus and cytoplasm. Beta-Actin (red) and Hoechst (cyan) stains were used for correlation. The two columns on the right show the indicated area at higher magnification. Scale bars: left columns: 10 µm, right columns: 2 µm.

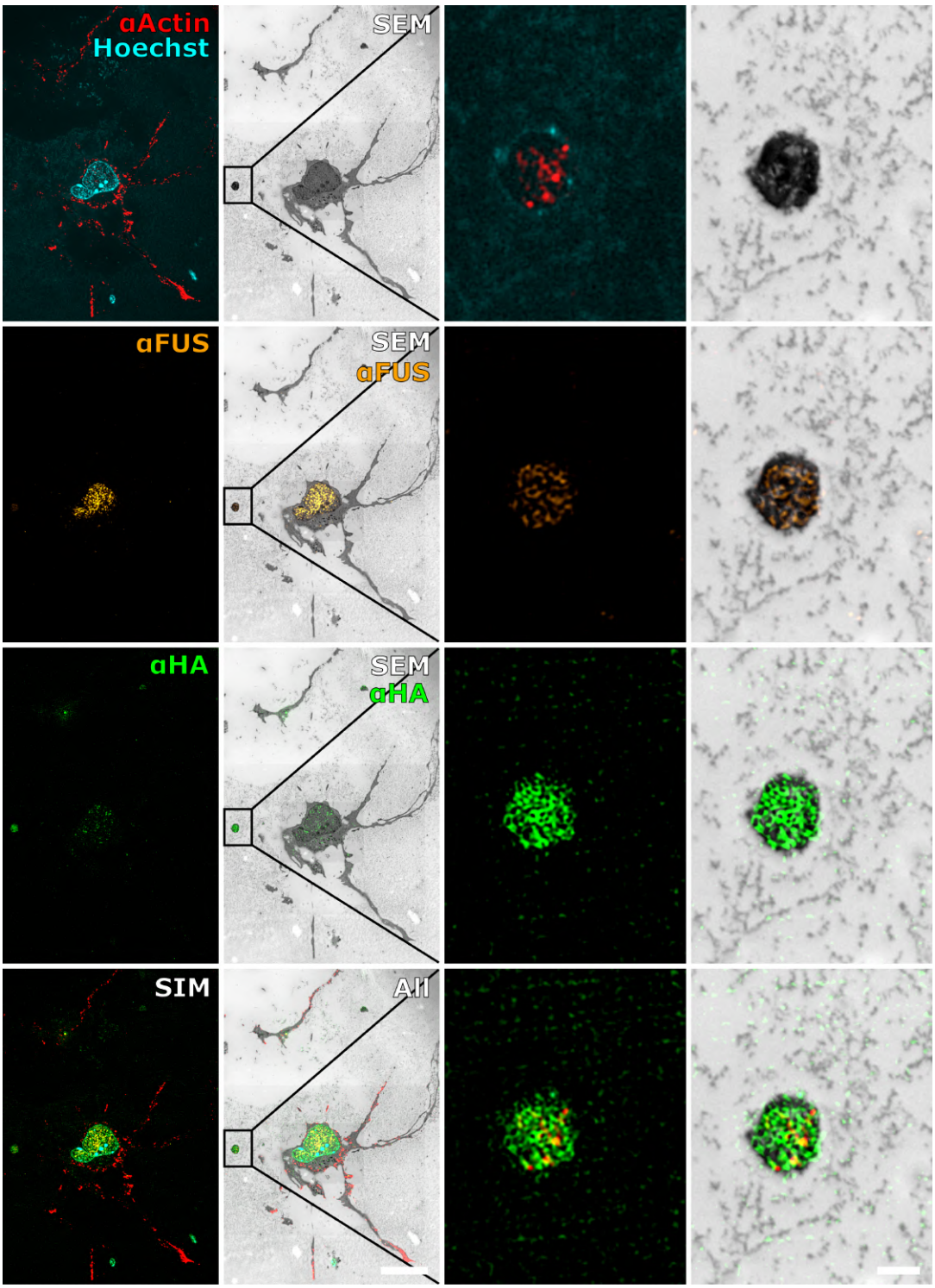

Figure 3.36.: **Localization of FUS proteins in cultured mouse primary motor neurons via srAT, section 2.** Native FUS (orange) is localized almost exclusively to the nucleus. FUS(P525L) (green) was transducted by lentivirus and is located in nucleus and cytoplasm. Beta-Actin (red) and Hoechst (cyan) stains were used for correlation. The two columns on the right show the indicated area at higher magnification. Scale bars: left columns: 10 µm, right columns: 1 µm.

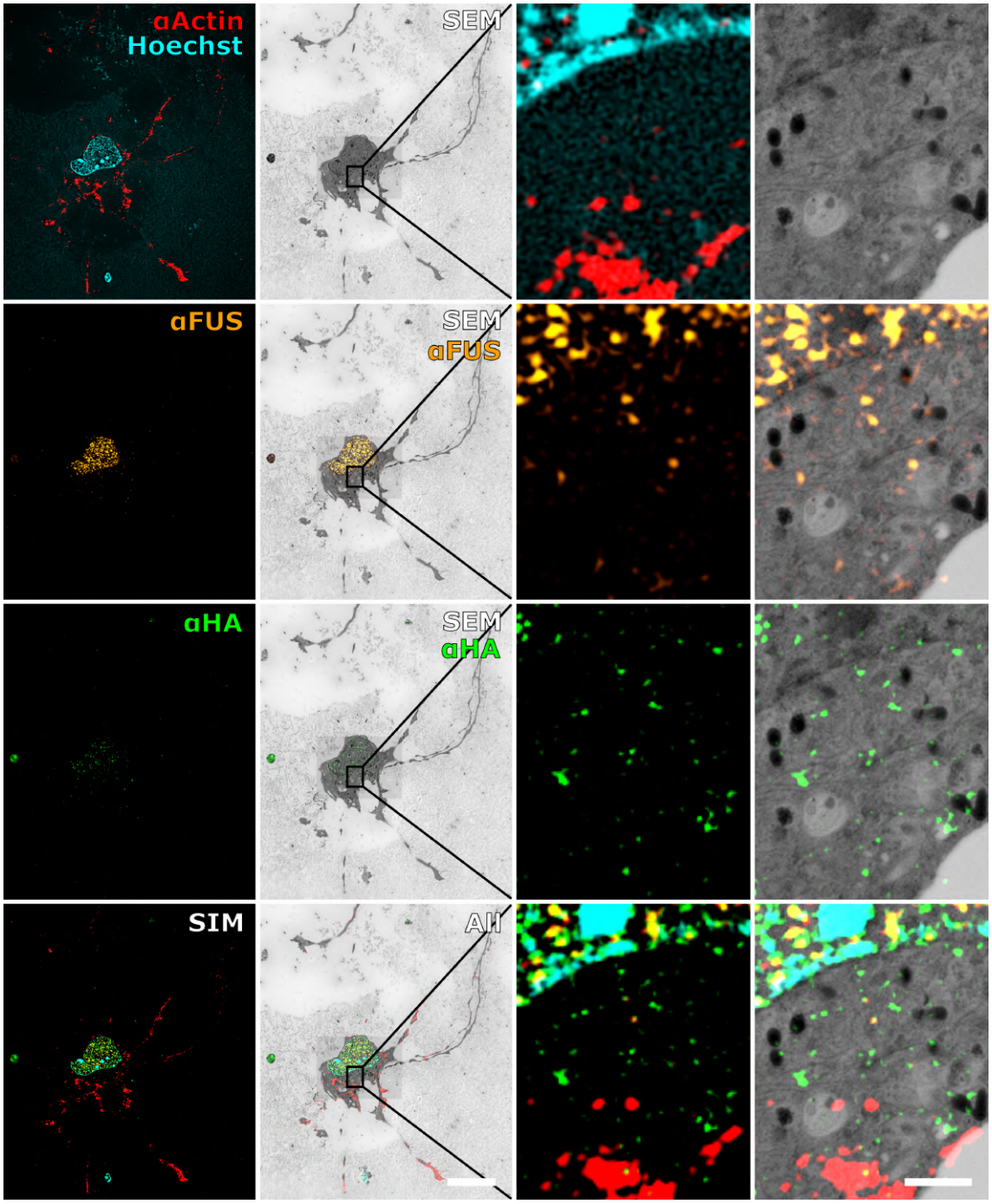

Figure 3.37.: **Localization of FUS proteins in cultured mouse primary motor neurons via srAT, section 3.** Native FUS (orange) is localized almost exclusively to the nucleus. FUS(P525L) (green) was transducted by lentivirus and is located in nucleus and cytoplasm. Beta-Actin (red) and Hoechst (cyan) stains were used for correlation. The two columns on the right show the indicated area at higher magnification. Scale bars: left columns: 10 µm, right columns: 1 µm.

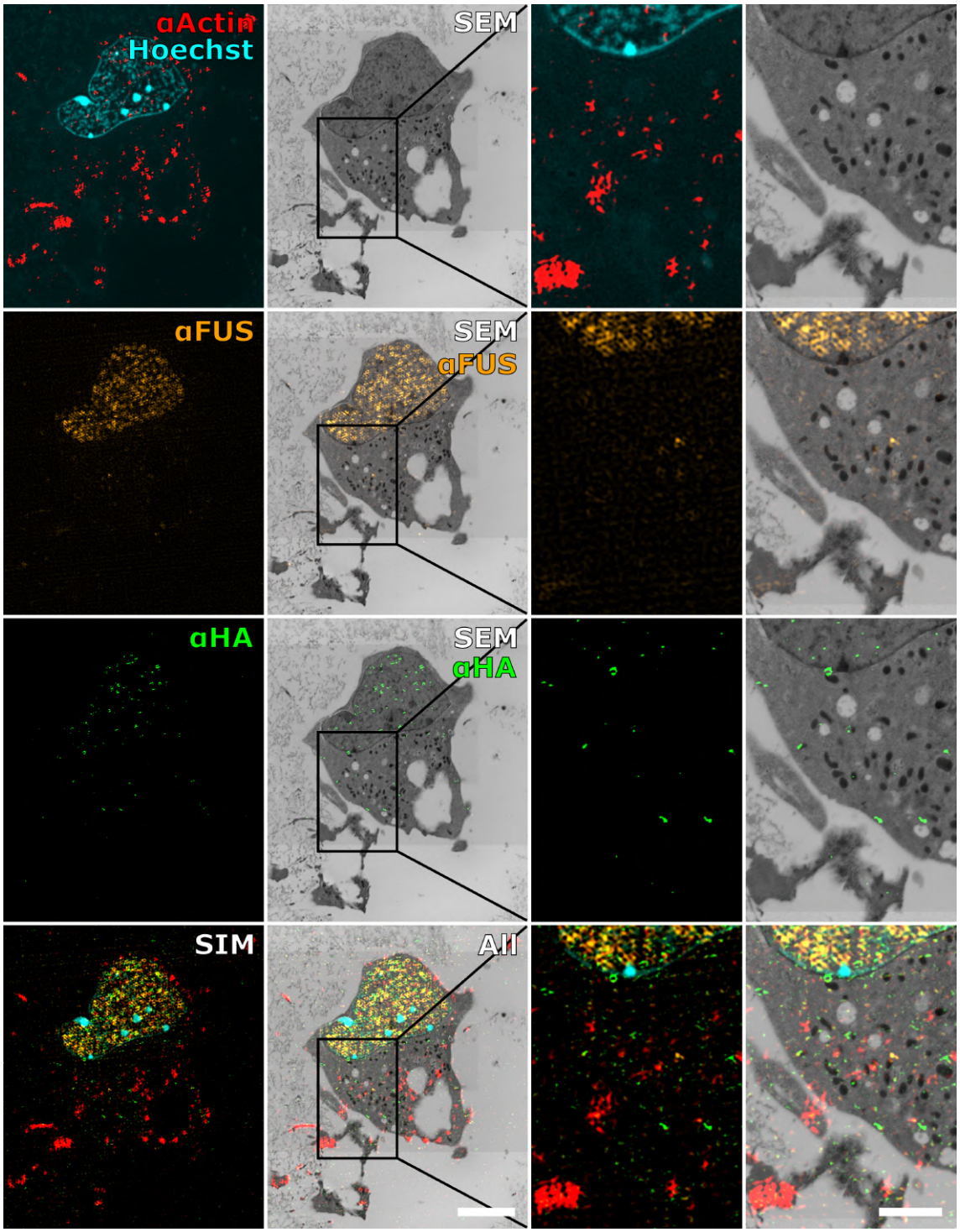

Figure 3.38.: **Localization of FUS proteins in cultured mouse primary motor neurons via srAT, section 4.** Native FUS (orange) is localized almost exclusively to the nucleus. FUS(P525L) (green) was transducted by lentivirus and is located in nucleus and cytoplasm. Beta-Actin (red) and Hoechst (cyan) stains were used for correlation. The two columns on the right show the indicated area at higher magnification. Scale bars: left columns: 5 µm, right columns: 2 µm.

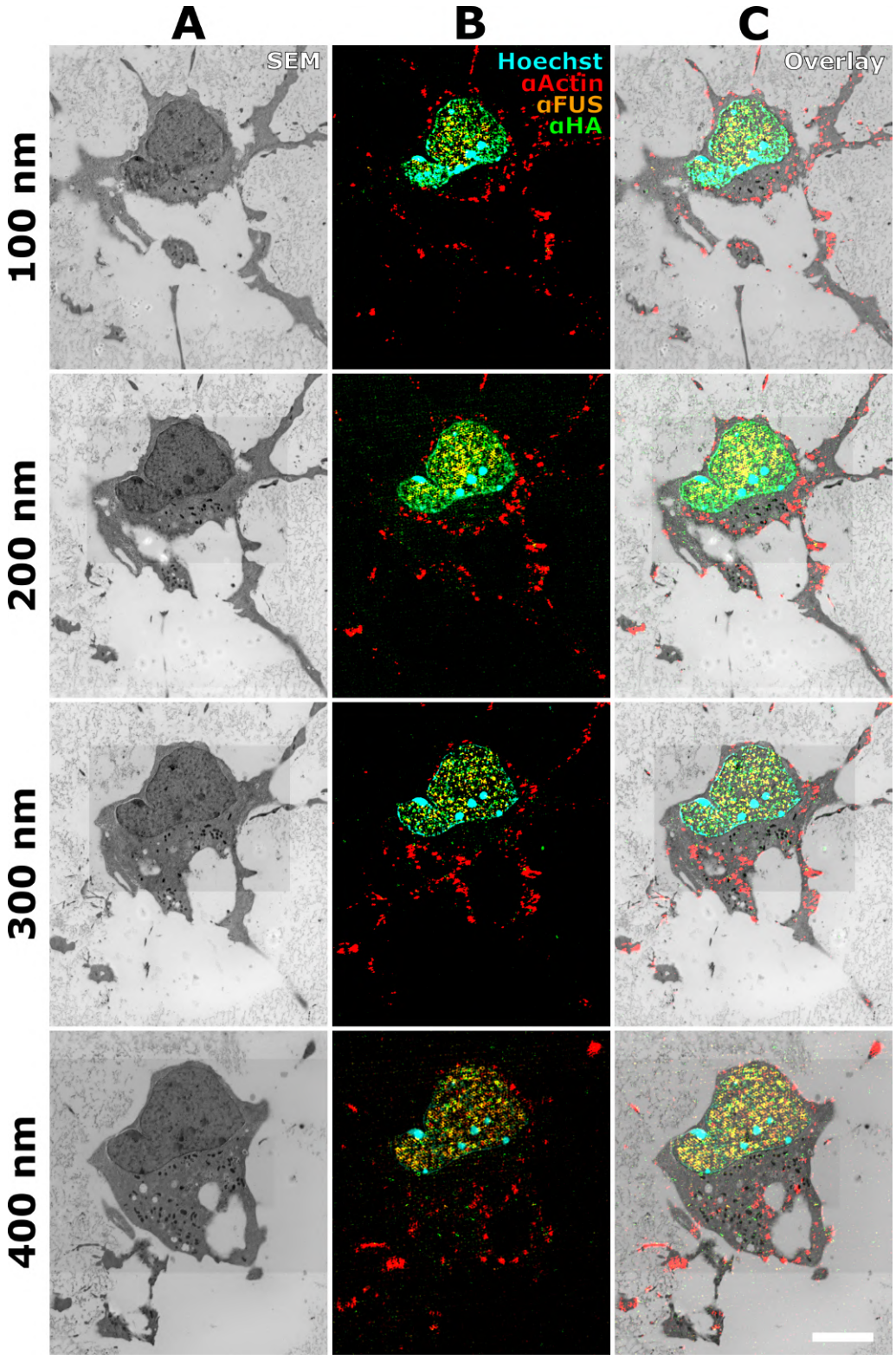

Figure 3.39.: **Localization of FUS proteins in cultured mouse primary motor neurons via srAT, series.** A summary of Figures 3.35 - 3.38. The cell body can be followed through four consecutive 100 nm sections. Scale bar: 5 µm.

4. Discussion

4.1. Re-mapping of the *C. elegans* connectome is feasible and useful

When Sydney Brenner and his colleagues published the "mind of a worm" [White et al. 1986], the first and only connectome of an entire adult organism, they were arguably ahead of their times. The great effort it took, and the lack of computer-assisted analysis and reconstruction, deterred follow-up studies to a large extent. Now, with new advanced imaging techniques and software at our disposal, the *C. elegans* connectome can finally be re-visited and amended.

In this thesis, I developed a method for mapping gap junctions with high accuracy and precision while retaining the molecular identity of the involved innexins. The annotation of the complete set of gap junctions at the *C. elegans* connectome seems to be a logical next step. This will update and improve the circuitry map and also offer valuable insights into the functions of gap junctions in general. I also co-developed a protocol to produce connectome data-sets for *C. elegans dauer* larvae. Understanding of the *dauer* nervous system might be instrumental for the development of new drug targets to combat parasitic nematodes, which are a serious socio-economic burden.

Connectomes are essential but, alone, are not sufficient for a comprehensive understanding of nervous systems. A better understanding of cell biology and synaptic function is needed, before this can be achieved. An accurate computer simulation of a worm's entire nervous system will be an important milestone towards that goal.

4.1.1. Mapping all gap junctions of the *C. elegans* nervous system including their molecular identities is now feasible

Electrical synapses formed by gap junctions are inarguably essential components of the nervous system and thus the connectome. White et al. [1986] included all gap junctions they could find in their "mind of a worm". To identify gap junctions they missed, I developed super-resolution array tomography (srAT) on the basis of array tomography [Micheva and Smith 2007]. I used srAT to map gap junctions containing a specific innexin at the *C. elegans* connectome [Markert et al. 2016] for the first time.

Compared to other 3D electron microscopy techniques like serial block-face scanning electron microscopy (SBF-SEM) and focused ion-beam scanning electron microscopy (FIB-SEM) [Peddie and Collinson 2014; Titze and Genoud 2016], srAT has a low throughput. Manually sectioned arrays need to be stained, imaged with two modalities, and resulting images have to be correlated. However, in return for time spent, srAT offers the retention of molecular identity. And although its throughput might be lower, srAT still makes it feasible to obtain a complete annotated data-set of the entire adult *C. elegans*, including all gap junctions and their molecular identities.

The *C. elegans* nervous system expresses 14 different innexins [Bhattacharya et al. 2019]. This is a large number to map, but seven innexins are especially widely expressed, in more than 40 neuron classes each [Bhattacharya et al. 2019]. Thus, mapping of these seven would likely reveal the vast majority of the gap junctions in the nervous system. Most of the others can be efficiently mapped by specifically targeting the neurons that express these only.

To attempt the mapping of the gap junctions with srAT, either specific antibodies against innexins or worm lines with specifically tagged innexins need to be created. Staining of the innexins would then be achieved directly or via targeting their tags. However, with srAT the number of innexins that can be stained simultaneously is limited to three, since SIM typically offers four channels and at least one of them needs to be reserved for correlation (cf. Figure 3.3). When targeting seven innexins, this means three different worms need to be stained, each with two or three innexins analyzed simultaneously. To reduce the effort, high pH treatment is used to elute antibodies for subsequent rounds of staining with different antibodies [Micheva and Smith 2007; Micheva et al. 2010b, a; Collman et al. 2015; Smith 2018]. Ultrastructure suffers with each elution treatment, but the result can still be used

[Collman et al. 2015]. This way, all three rounds of staining for seven innexins can be performed on a set of sections from a single worm. Furthermore, multi-spectral imaging and linear unmixing deconvolution methods can be used to better separate overlapping emission spectra of fluorophores [Dickinson et al. 2001]. In the future, a single round of imaging could produce sets with all seven innexins labeled if progress of technology enables reliable separation of 8 channels.

In the following, I will give an estimate for the time needed to complete data acquisition and correlation for one worm with the equipment I used here (see section "Materials and methods") and for one round of antibody staining.

Given that an adult worm is about one millimeter in length, this would result in 10,000 sections, if cut transversally at 100 nm thickness. In my experience, 100 nm sections offer the best compromise between axial resolution, reliability of ultramicrotomy results, and SEM contrast. These 10,000 sections need to be collected on glass slides. One hundred sections per slide can be processed and imaged conveniently. Thus, the whole worm would fit on about 100 microscope slides and obtaining these would take one or two weeks. It takes, approximately, a whole day of work to stain and image 50 sections with SIM. Assuming full dedication of a single person to the project and five days of work a week, SIM imaging can theoretically be completed in a little bit less than a year. The next steps, contrasting and carbon coating, can be performed on all 100 slides in a few days. SEM imaging typically takes a bit more time than SIM imaging, since multiple regions of interest have to be imaged at higher magnifications to be able to reconstruct the nervous system. A realistic average progress is 30 sections per day. Thus, SEM imaging would take about one and a half years. Assuming correlation of SIM and SEM images is performed entirely manually, I would estimate that the daily progress would amount to about 50 sections. This adds another year.

From these estimates, it would take a single skilled person about 3.5 years to complete data acquisition for a whole adult worm. This estimate assumes full-time dedication to the project and no major set-backs, so the actual time required is probably longer. However, it is still a feasible project, even when assuming a single person effort. A concerted effort involving multiple people would reduce the required time significantly. More importantly, there are many ways this workflow can potentially be sped up considerably.

Of the many ways to speed up srAT, I will focus on three specific points. First of all, ultramicrotomy can be done by an automated tape-collecting ultramicrotome (ATUM), where sections are automatically cut and collected on tape [Schalek et al. 2011; Hayworth et al. 2014]. It is conceivable to run this section tape through some sort of staining conveyor belt, where immunostainings and washes are automatically applied sequentially. Sections can then be imaged on tape, provided the tape itself does not exhibit autofluorescence. Second, the bottle necks of image acquisition and correlation can be addressed. Automated imaging software [Eliceiri et al. 2012] and multi-beam SEM [Keller et al. 2014] could speed up imaging considerably. Along these lines, SIM to SEM image correlation could potentially be automated by trained neural network algorithms. In fact, semi-automatic approaches already exist [Paul-Gilloteaux et al. 2017]. Such advances in the workflow could reduce the time needed to obtain a new srAT connectome data-set, each with at least three proteins of interest localized, to mere months. Mapping not only of all gap junctions, but also individual innexins in the *C. elegans* nervous system is thus feasible via srAT. Third and last, we may be able to automate a portion of the analysis. The very time-consuming tracing of neurons in the data-sets to identify specific gap junctions can hopefully be automated by neural network algorithms, similar to the correlation mentioned above. In fact, having many data-sets available will surely help with training the neural network algorithms.

This feat of mapping gap junctions would be very challenging using any other technique. Serial TEM requires an enormous amount of skill and time to section with delicate slotted grids. This may change, as automated image acquisition is beginning to emerge [Schorb et al. 2019]. SBF-SEM and FIB-SEM are techniques for acquisition of large volumes of data, but usually at lower magnification. Thus, chemical synapses can be mapped, but images lack resolution to map gap junctions with confidence. Also, these are destructive techniques, so regions of interest can be imaged only once. With srAT, regions of interest that were discovered during image analysis can be imaged at higher magnifications later. And, most importantly, it is generally not possible to obtain the molecular identity of proteins of interest with any of these techniques. Mapping of innexins as an important next step in *C. elegans* connectomics will thus only be readily achievable with srAT.

The srAT approach is by no means restricted to gap junction analysis. It has proven to be reliable and flexible; the technique has been used and adapted for many other models and applications [Markert et al. 2017]. In one study, we used

srAT to localize lipid rafts in methicillin-resistant *Staphylococcus aureus* (MRSA), a novel and promising drug target [García-Fernández et al. 2017]. Together with Martin Jahn, I adapted srAT for fluorescence *in situ* hybridization (FISH) to study uncultivatable symbiotic bacteria in marine sponges [Jahn et al. 2016] and even the interactions between these bacteria, their host, and bacteriophages [Jahn et al. 2019].

4.1.2. Studying the "innexome" of *C. elegans* will offer valuable insights into gap junction function

I have discussed how mapping of gap junctions is an important step for connectomics and how it can be achieved via srAT. However, since srAT also reveals the molecular identity of the involved innexins, such an analysis goes beyond the mere mapping of connectivity and allows for a functional analysis of gap junction types in *C. elegans* as well. It is remarkable that *C. elegans* – although it generally has a very reduced number of protein variants – possesses 25 different innexin genes [Simonsen et al. 2014], while humans only have 21 different connexin genes [Söhl and Willecke 2004]. This represents an innexin diversity that is indeed unmatched by any other model organism [Altun et al. 2009; Simonsen et al. 2014]. The innexins are not the only unusually large protein family in the worm. *C. elegans* has 61 proteins of the nicotinic acetylcholine receptor family, almost three times as many as mammals [Jones et al. 2007], and G-protein coupled receptors represent the largest gene family in *C. elegans* with more than 1,300 members [Vidal et al. 2018]. Thus, although very reduced in many ways, the worm is highly complex in others. It can be speculated that *C. elegans* is using these large gene families to achieve a functional complexity that mammals achieve by exploiting a multitude of splice variants and generally having many more specialized cells and cell types.

The impressive variety of innexins in *C. elegans* suggests the existence of a complex "innexome" that is utilized to manipulate and fine-tune gap junctions. If this is the case then the variety of gap junctions in the nervous system possibly represents a layer of complexity that compensates at least some of the functional complexity lost by reducing the number of neurons. This would help to explain how the worm can perform many complex behaviors despite deploying only 302 neurons to process and execute them. Studying gap junctions by taking the innexome into account will

therefore likely be one of the keys to a truly comprehensive understanding of the *C. elegans* nervous system.

Innexins are an essential component of the nervous system, and they are involved in nearly all aspects of *C. elegans* development [Simonsen et al. 2014]. This includes roles in oocyte maturation, fertilization, cell identity, innate immunity, and movement [Simonsen et al. 2014]. However, it is still unclear if innexins are post-translationally modified and if they have channel-independent functions. Also, we do not know which molecules are able to pass through innexin gap junctions and at what times [Simonsen et al. 2014]. Thus, studying innexins in *C. elegans* has a high potential for elucidating fundamental properties and functions of gap junctions. An excellent example of this is a very recent study by Bhattacharya et al. [2019]. They analyzed the plasticity on innexin expression in the *C. elegans* nervous system. They found that innexin expression patterns are highly plastic in a spatiotemporal manner. Innexin expression is altered by environmental stimuli and leads to modification of existing (electrical) synapses as well as *de novo* synapse formation. Their data suggests the existence of gap junction-specific conductances, depending on innexin compositions. They also demonstrated that these circuit modifications lead to behavioral plasticity. Bhattacharya et al. [2019] performed this analysis not only in adult worms but in all larval stages, including the *dauer* larva. When they compared non-*dauer* to *dauer* expression, it became apparent that there are widespread changes of neuron-type-specific innexin expression in *dauers*. For example, normal *dauer* locomotion was contingent upon the downregulation of the innexin UNC-7 in AVA interneurons.

Comprehension of the innexome will offer valuable insights into the roles of different innexins and the spectrum of their functions in the nervous system and beyond. Of note, Bhattacharya et al. [2019] investigated cell(type)-specific innexin expression, but did not take individual gap junctions into account. Mapping of the electrical synapses including their gap junction-specific innexin expression via srAT would be a milestone on the way to a truly complete "electrical connectome" [Bhattacharya et al. 2019].

4.1.3. Acquisition of the *dauer* larva connectome via FIB-SEM is feasible and might be instrumental for easing the socio-economic burden of nematode parasites

During this thesis, Anna Steyer and I acquired, to our knowledge, the first FIB-SEM data-sets of *C. elegans dauer* larvae and the first isotropic *C. elegans* FIB-SEM data-set of this quality, with an effective voxel size of 5 nm. To achieve this, I established a HPF protocol for *dauer* larvae building on previous work of Johannes Kattan (Master's thesis) and, together with Anna Steyer, an embedding protocol using minimal resin [Schieber et al. 2017].

The data-sets are a valuable resource for *dauer* ultrastructure. They can be used to perform a full volumetric reconstruction of the anterior sensory system, similar to Doroquez et al. [2014], who did this for the adult worm based on serial TEM data-sets and electron tomography. This work will be a valuable resource for comparisons of the anatomies of the sensory systems between *C. elegans* stages and across species. Secondly, the data-sets are currently used by my own colleagues for a reconstruction of the anterior connectome of the *dauer*, including the nerve ring. This work already offered valuable insights into connectome variability between individuals as well as between *dauer* and adult stages. Interestingly, some neurons show significant re-wiring in the *dauer* stage. Many affected neurons have functions in *dauer*-specific processes. Thus, there is evidence for a link between the connectome and behavior [Britz et al., personal communication].

Our achieved resolution for the FIB-SEM data-sets was sufficient for tracing synaptic circuitry and reconstructing the anterior sensory system. Even so, some ultrastructural features, such as systematic detection of clear-core synaptic vesicles or gap junctions, are beyond FIB-SEM resolution. However, FIB-SEM has only recently been applied to biological samples and technical advances are expected [Narayan and Subramaniam 2015]. Thanks to the minimal resin embedding technique [Schieber et al. 2017], preparation of the samples for FIB-SEM was relatively straightforward and readily reproducible. We did not have any issues with charging or contrast by using our standard sample preparation protocol, and contrasting was even throughout the sample. Thus, FIB-SEM is a powerful complementary technique to SBF-SEM, which requires special sample preparation and embedding procedures in order to avoid charging of the sample during imaging, although the charging issue now seems to have been largely resolved by introducing focal gas injection [Deerinck et al.

2018]. However, due to the small acquisition window of FIB-SEM, this technique is more suitable for smaller samples such as *C. elegans* larvae or parts of adults, like the nerve cords. For larger specimens, SBF-SEM remains probably the best choice.

The minimal resin protocol we established for FIB-SEM imaging of *dauer* worked well. The Durcupan resin used for this application is highly viscous, and we did not expect that we would be able to drain it from the worms very efficiently. However, dragging the worms out of the resin is very effective, and we were able to minimize resin, such that it is barely visible in micrographs. Even fine details of the cuticle surface could be discerned (cf. Figure 3.11). Thus, this protocol might be a serious alternative to classical SEM. With classic SEM preparations, specimens often shrink by substantial amounts, with up to 30 % reduction in diameter [Gusnard and Kirschner 1977; Boyde et al. 1981]. In contrast, minimal resin embedding is based on HPF/FS, which retains near-native preservation of biological samples and causes virtually no shrinkage. Our method enabled us to precisely target our regions of interest for FIB-SEM imaging.

The FIB-SEM imaging of roughly one forth of the *dauer* larva took about 10 days, without interruption. Thus, a whole larva can be imaged in mere weeks using current technology. This opens up the possibility to acquire high-quality data-sets for connectomics and other analyses of *C. elegans* larvae. This will be an invaluable resource for studying variability and developmental plasticity of connectomes in *C. elegans*. If automated annotation of the data-sets via trained algorithms can be achieved, obtaining a new connectome could become a matter of months or even weeks. Increasing sample size in connectomics is essential to get an idea of inter-individual variability. Also, functional studies using genetic mutants would be feasible and could potentially boost our understanding of the nervous system significantly.

The *dauer* larva is of special interest among the larval stages. It is analogous to the dispersal stages of many parasitic nematode species, although *C. elegans* is non-parasitic [Westheide and Rieger 2013]. Like *dauer*, these dispersal stages often do not feed and withstand harsh environmental conditions until they find a suitable host. It has already been shown that the anterior sensory systems of *C. elegans* and certain parasites are very similar [Bumbarger et al. 2007; Ragsdale et al. 2009; Bumbarger et al. 2009; Zhu et al. 2011]. Two studies compared infectious larval stages of parasites directly to *C. elegans dauers* and noted remarkable similarities [Ashton et al. 1995; Fine et al. 1997]. Furthermore, control of larval arrest and

exit is conserved between parasitic and free-living nematodes [Crook 2014]. These similarities suggest that *dauer* larvae represent a pre-adaption for the evolution of parasitism in nematodes [Crook 2014]. Research of *dauer* biology can therefore help with combating nematode parasites. *Dauer* entry, maintenance, and exit are potential points of attack, as well as *dauer*-specific features of the nervous system. For example, it has been reported that the usually non-neuronal innexin INX-6 is expressed in the AIB neurons of *dauer* larvae only, where it forms gap junctions and regulates locomotion in response to environmental stimuli [Bhattacharya et al. 2019]. Proteins like this might be prime candidates for targets for new nematicides. Also, *dauers* show specific behavior that helps them survive and spread. Understanding the mechanism of this behavior from the connectome might give us clues how to suppress it and thus inhibit the dispersal of parasites.

Indeed, many nematicides work on the nervous system. For example, levamisol is a potent cholinergic agonist [Lewis et al. 1980; Martin 1993; Rand 2007], piperazine is a GABA agonist [Martin 1993], avermectins, like ivermectin, irreversibly open glutamate-gated chloride channels [Campbell et al. 1983; Martin 1993; Wolstenholme and Rogers 2005], aldicarb is a cholinesterase inhibitor [Baron R L 1994], and pyrantel pamoate inhibits neuromuscular transmission [Jain et al. 2006]. These examples demonstrate that the nervous system offers good targets for the development of treatments. Many proteins are obviously sufficiently different from possible mammalian orthologues that side effects are manageable or virtually non-existent. It can be expected that more targets for new nematicides are to be discovered. I predict that the as of yet under-researched innexins will be key to many future nematicides. One study concerned with the mechanisms of ivermectin-resistance in *C. elegans* found that the innexins UNC-7 and UNC-9 contribute to ivermectin-sensitivity [Dent et al. 2000]. Of note, the authors show that UNC-7 and UNC-9 gap junctions contribute to ivermectin-sensitivity specifically by altering the connectivity, i. e., the connectome, of the worm.

4.1.4. For computer simulation of the worm's nervous system a comprehensive connectome is necessary but not sufficient

So far, the connectomics effort in *C. elegans* has not led to a comprehensive understanding of how connectivity informs behavior. This is in part due to the fact that the connectome alone cannot describe all interactions between neurons or make

sense of the nature of their connections [Bargmann and Marder 2013]. On the other hand, the connectome itself is not complete. The genome of *C. elegans* was instrumental as one of the backgrounds for comparison for the human genome [Venter et al. 2001]. For the human genome project, it was crucial to develop the methods and prove feasibility in principle with way smaller genomes before attempting the human one. With the connectome, this is even more so the case, since the increase in complexity spans many more orders of magnitude than with genomes. Before we understand the worm with its 302 neurons, how can we hope to understand the zebrafish brain with its about 100 million [Hinsch and Zupanc 2007] much less the human brain with its 86 billion [Azevedo et al. 2009] neurons? To make things even worse, vertebrate brains are highly plastic. Connections and cells die and are born all the time. That means, the connectome changes every minute or even second. Thus, *C. elegans* seems to be our only plausible chance of generating and also comprehending a connectome and its dynamics as of yet.

We will know that we achieved a meaningful description of the *C. elegans* nervous system once we can simulate it. Emulation of a freely behaving worm entirely *in silico* would mark a breakthrough in neuroscience. Such a simulation would also be an invaluable research tool [Karr et al. 2012]. Any systems neuroscience experiment can be simulated in the artificial worm first. The activity states of all neurons can be recorded at all times, during any behavior, in any simulated ablation experiment, and in any simulated genetic mutant or transgene worm. Even the dynamics of the nervous system down to its development from zygote to death could be implemented in the future. If we follow this path, *C. elegans* might well be the first animal that can be comprehensively simulated on a cellular level. Of course, along the way, anything we learn about *C. elegans* can potentially be transferred to more complex brains and organisms.

As alluded to earlier, connectomes will be necessary but not sufficient to reach a comprehensive understanding of the nervous system [Bargmann and Marder 2013]. Connectivity maps alone do not contain information about neuromodulation and specific properties of individual cells and synapses [Bargmann and Marder 2013]. A recent report found that behavior in *C. elegans* can even be controlled transgenerationally by neuronal small RNAs [Posner et al. 2019]. Also, I discussed the complexity of the innexome and how this complexity is utilized in the worm for expanding the functional capabilities of the nervous system. This discussion was focusing on gap junctions, the electrical synapses. However, classical chemical synapses are, of

course, also of high importance. They are complex cellular machineries with more than a hundred specific proteins involved that work together in an often tiny space of much less than one cubic micrometer. Because of these dimensions, electron tomography is the method of choice to study synaptic processes. And one way to elucidate the synaptic machinery is studying the functions of the involved proteins via forward genetics, i. e., screening for mutations with relevant phenotypes using time-efficient assays and analyzing the proteins discovered that way. In this thesis I analyzed the effects on the ultrastructure of one such protein, SAD-1, to further elucidate its role in the synapse.

4.2. A model for the molecular mechanisms of SAD-1 functions in synapses begins to emerge

SAD-1 has been first described almost 20 years ago [Crump et al. 2001] and many of its roles in the nervous system have been revealed via thorough genetic and biochemical studies [Crump et al. 2001; Hung et al. 2007; Kim et al. 2008, 2010]. Now, I was able to describe specific effects of lack of SAD-1 on the ultrastructure of the excitatory NMJ in *C. elegans*. I found an overall destabilization of axonal integrity that manifests in more irregularly shaped varicosities (Figure 3.20), misaligned microtubules (Figure 3.21), and nested synapses (Figures 3.18 and 3.19). Additionally, quantification of vesicles pointed to larger vesicle pools compared to controls, while the density of specifically the dense core vesicles (DCVs) was decreased. The median size of individual clear core vesicles (CCVs) was increased (Figure 3.22). These findings have to be considered within the context of what is already known about the roles of SAD-1 and existing models.

4.2.1. The effect of SAD-1 on size, shape, and position of vesicle clusters may be secondary to its effect on synaptic integrity

It has been well established that SAD-1 is involved in axonal identity regulation and synapse formation [Crump et al. 2001] and that it regulates these processes through distinct mechanisms [Hung et al. 2007]. *sad-1* is initially expressed in the

late embryo, when many synapses are first made, and expression continues throughout the whole nervous system into adulthood [Crump et al. 2001]. Kim et al. [2008] showed that SAD-1 activity is necessary in establishing neuronal polarity, but it is not required for its maintenance. Similarly, SAD-1 is also necessary for establishing synaptic organization, but when SAD-1 kinase activity is switched off, synapses remain intact. When SAD-1 was selectively switched on in later larval stages, synaptic organization could be re-established. Thus, SAD-1 activity shows distinct temporal requirements: It is strictly required during establishment of neuronal polarity, but its activity is not temporally restricted to the establishment phase in synaptic organization [Kim et al. 2008].

While *sad-1* is expressed in all motor neurons, Crump et al. [2001] and Hung et al. [2007] had to restrict their analysis of synaptic organization to the GABAergic inhibitory ones, because the synapses of cholinergic, excitatory motor neurons are greater in number and closer together than GABAergic synapses. It was thus necessary for analyses via fluorescence microscopy to limit analysis to GABAergic synapses to achieve single-synapse resolution. Since I analyzed NMJs with electron microscopy, I did not have this restriction and therefore focused on cholinergic synapses in my analysis. This is the first time these synapses have been analyzed with electron tomography.

It has been reported that lack of SAD-1 affects size, shape, and position of synaptic vesicle clusters [Crump et al. 2001]. The clusters appeared larger, more diffuse, and mislocalized to dendrites. My results are consistent with these findings but offer a more differentiated interpretation of some of these previous results.

Regarding vesicle pool size, clusters are not larger in my analysis, but more distant neighbors are closer together without overall pool density being affected (Figure 3.22). In my interpretation, in larger pools the probability of a given vesicle being isolated will be smaller. I also analyzed distances of CCVs to the active zone. In *sad-1* worms, these distances tended to be greater, but the difference was not quite statistically significant. Two factors probably influenced this result. First, my analysis took all vesicles into account, not only the ones at the periphery. Thus, the contribution of a sub-population of more distant vesicles to the median might have been too small to reach statistical significance. Of note, the plot of vesicle distances to active zones shows a small population of distant vesicles that is missing in controls (see Figure 3.22B). Second, I analyzed only tomograms of transverse sections of synapses that included active zones. This way, I only accounted for

pool size in two dimensions, i. e., the left-right and dorsal-ventral axes, but not in anterior-posterior (anterograde-retrograde) direction. However, since the nerve cords are tightly packed with axons, a spread of the vesicle pool will likely occur mostly in anterior-posterior directions where there is more space, i. e., vesicle pools reach further into the axon. Indeed, this has been previously observed [Crump et al. 2001]. Future analyses should include not only the active zone area but also the synaptic periphery to achieve a more accurate assessment of vesicle pool size in *sad-1* mutants.

The analysis of vesicle sizes revealed a small but statistically significant difference in CCV size. The median diameter of CCVs in *sad-1* was about 3.5 % smaller compared to controls. This result is unexpected and has not been reported previously. Because the difference is so small, significance was only achieved because many hundreds of vesicles had been analyzed with the help of automatic vesicle reconstruction and classification tools (see Results). Since these tools had been published only recently [Kaltdorf et al. 2017, 2018], this might be one of the reasons this phenotype has been overlooked so far. Now, this analysis bottle neck has been overcome. Another reason might be that I processed samples via HPF/FS and utilized electron tomography. Thus, near-native structure preservation and high image resolution in all three axial dimensions allow for a much more accurate analysis of vesicle sizes and subtle differences are more readily revealed.

The finding that vesicle pools appeared more diffuse in *sad-1* mutants was mostly supported by fluorescence microscopy data [Crump et al. 2001]. Puncta of vesicle markers were more spread out. This was interpreted as a consequence of the spread of vesicle pools. However, my results point to a second component of this phenotype. The spread of the vesicle pools might be caused, in part, by changes of synapse shapes. I found many protrusions and irregularly shaped synapses in *sad-1* worms (Figure 3.20). The nested synapses I observed (Figures 3.18 and 3.19) seem to represent extreme cases of this phenotype. These protrusions and even the nested synapses contain vesicles, so vesicle pools are more fragmented and thus might appear more diffuse in fluorescence microscopic analyses. Although Crump et al. [2001] had performed a TEM analysis of motor neuron synapses, they did not report such phenotypes and concluded that the overall structure of the axons was normal. This could be due to three reasons. First, they limited their analysis to GABAergic synapses, whereas I focused on cholinergic ones, and GABAergic synapses show less protrusions, possibly. Second, they analyzed 10 synapses in total. I recorded more

than 100 tilt series, which still represented only a subset of the total number of sections I looked at. I found three instances of nested synapses and analyzed two. Thus, Crump et al. [2001] might have missed them by chance. However, they did observe irregular branching in the sensory ASI neuron. Third, irregularly shaped synapses were probably masked by artifacts caused by classical chemical fixation. It is well-documented that this type of fixation causes membranes to loose shape and form protrusions [Rostaing et al. 2004]. Indeed, the electron micrographs of Crump et al. [2001] show irregularly shaped synapses for both, *sad-1* mutants and N2 controls. When *C. elegans* samples are fixed with HPF/FS, N2 synapses are more rounded and regular-shaped [Rostaing et al. 2004] (Figure 3.20). Morrison et al. [2018] recently performed TEM on *sad-1* motor neurons using HPF/FS, but they do not show any micrographs and do not comment on ultrastructural features other than the number of DCVs per synapse (see below).

4.2.2. SAD-1 function is probably linked to regulation of microtubules

What is the mechanism of SAD-1 function? Its physiological substrates are unknown. SAD-1 seems to be distantly related to the cell polarity kinase PAR-1 [Crump et al. 2001]. PAR-1 regulates the microtubule cytoskeleton [Labbé et al. 2003]. In mammals, two orthologs of SAD-1 exist, SAD-A and SAD-B. They have been shown to phosphorylate Tau [Kishi et al. 2005; Barnes et al. 2007], and Tau is a protein that is associated with microtubules. It is thought that SAD kinases regulate neuronal polarity in mammals by promoting microtubule dynamics during axon extension [Witte et al. 2008]. Indeed, *C. elegans* SAD-1 phosphorylates human Tau *in vitro* [Kim et al. 2010]. In my analysis, I discovered changes in microtubule positioning and orientation in *sad-1* synapses (Figure 3.21). These findings suggest that SAD-1 function might also be related to microtubule regulation. I hypothesize that the irregularly shaped varicosities I found in *sad-1* worms (Figure 3.20) are linked to misalignment of microtubules. Since my microtubule analysis is based on electron tomography and thus focused on relatively small volumes of the nerve cords, this observation has to remain qualitative. A more large-scale approach using (super-resolution) fluorescence microscopy may be suitable to examine and quantify overall deviations in microtubule layout.

Crump et al. [2001] speculated that SAD-1 affects trafficking of vesicles along microtubules, which could account for changes in vesicle pool morphology in *sad-1* worms. Subsequent studies have since corroborated this [Edwards et al. 2015; Morrison et al. 2018]. Interestingly, SAD-1 seems to affect the transport of synaptic vesicles, both CCVs and DCVs. Edwards et al. [2015] found that SAD-1 is involved in "trapping" CCVs at synapses. In a null-allele background, CCVs are mislocalized to distal synapse-free regions of the axon of the DA9 motor neuron.

This observation suggests that SAD-1 helps with release of CCV cargo from microtubules specifically at synapses. If CCVs are not released, then they are transported "too far" into distal regions. Morrison et al. [2018] investigated the transport of DCVs and made similar observations. SAD-1 was involved in transporting DCVs from somata to axons. Kymographs of labeled DCVs being transported *in vivo* revealed that SAD-1 promotes anterograde transport. Once DCVs reach the synapse, SAD-1 helps to inhibit transport in both directions. In a *sad-1* null-mutant, DCV density is increased in somata and reduced by about 50 % in synapses, as revealed by fluorescence microscopy. They also performed TEM on serial ultrathin sections of cholinergic motor neurons just to count individual DCVs. This analysis also suggested a reduction of DCVs in the *sad-1* null background, but since DCV numbers per synapse were highly variable, their result was not statistically significant [Morrison et al. 2018]. However, my analysis supports this result. Using electron tomography and automated vesicle classification, I was able to find a significant reduction of DCV density in cholinergic motor neurons (see Figure 3.22D). Together, these results make a strong case that SAD-1 influences vesicular transport along microtubules. It might do so via motor proteins (kinesins or dyneins), either influencing their hold on cargo or their hold on microtubules.

But if SAD-1 function is linked to microtubules, what could be its physiological substrate(s)? As mentioned earlier, it has been reported that SAD-1 phosphorylates human microtubule-binding protein Tau *in vitro* [Kim et al. 2010]. *C. elegans* possesses a single Tau orthologue, *ptl-1* [Goedert et al. 1996]. It is expressed mostly in mechanosensory neurons, with the exception of PVM [Goedert et al. 1996]. Knockout of *ptl-1* leads to reduced sensitivity to touch stimuli, probably due to specific interactions of PTL-1 with MEC-7 and MEC-12, the mechanoreceptor-specific Tubulins [Gordon et al. 2008]. Thus, PTL-1 seems to be involved mainly in mechanosensation, a role that has not been reported for SAD-1. Moreover, PTL-1 is broadly associated with microtubules, whereas SAD-1 is restricted to synapses [Crump et al.

2001; Hung et al. 2007] and the *ptl-1* mutant does not show neuronal polarity defects (Mei Zhen group, unpublished data). It is therefore unlikely that PTL-1 is the most relevant substrate of SAD-1 in motor neurons. However, weak *ptl-1* expression has been reported in at least some motor neurons [Gordon et al. 2008] and *ptl-1* knockout caused senescence phenotypes in GABAergic motor neurons. With age, neurons expressing fluorescent reporters showed branching and blebbing [Chew et al. 2013], which is consistent with reduced synaptic integrity observed in *sad-1* mutants. Furthermore, PTL-1 and SAD-1 share a dependence on tightly controlled expression levels. Variation from wild-type levels caused phenotypes in both mutants [Hung et al. 2007; Chew et al. 2013]. These findings may warrant further investigations into functional links between PTL-1 and SAD-1. For example, if SAD-1 and PTL-1 are linked via roles in neuron maintenance, *sad-1* worms could be tested for effects on longevity to reveal such a link. If the link exists, I would expect that longevity effects in a *ptl-1*; *sad-1* double mutant are not significantly increased compared to the single mutants.

SAD-1 may interact with microtubule-associated proteins other than PTL-1. However, there are currently no promising candidates in discussion (Mei Zhen and Wesley Hung, personal communication). It is crucial to discover the physiological substrate(s) of SAD-1 to elucidate the mechanisms of its functions. Substrates that are not directly related to microtubules should therefore be considered as well. One such candidate is discussed in the following section.

4.2.3. SAD-1 might provide a mechanistic link between neuronal activity and synapse development

It has been shown that SAD-1 is not dependent on vesicles for localization and that establishment of the active zones happens independent of SAD-1 [Crump et al. 2001]. However, SAD-1 localization is tightly linked to synapses and dependent on NAB-1 (Neurabin), SYD-1, and SYD-2 (Liprin-α) [Patel et al. 2006; Chia et al. 2012]. Crump et al. [2001] proposed that SAD-1 indirectly mediates an interaction between vesicle clusters and active zones by phosphorylation of downstream targets. Since SAD-1 seems to fulfill these two independent functions of promoting vesicle clustering and neuronal polarity, Crump et al. [2001] further hypothesized that it may help with linking axon-dendrite polarity to external signals that promote presynaptic development. These concepts are consistent with a model of SAD-1 function

involving TWK-40. This protein is a rectifying two-pore-domain potassium channel (K2P) [Mathie et al. 2010] and was found in a mutagenesis screen for suppressors of *sad-1* [Pekar 2013]. Interestingly, loss-of-function mutations of *twk-40* suppress the locomotion defect and synaptic morphology phenotype caused by *sad-1* mutation in *twk-40*; *sad-1* double mutants [Pekar 2013]. Loss-of-function mutation of *twk-40* alone has the opposite effect of *sad-1* mutation: The bending amplitude during locomotion is increased compared to wild-type controls and worms show exaggerated movements [Mei Zhen group, unpublished observations]. Additionally, TWK-40 and SAD-1 co-localize near synapses and electrophysiological analyses revealed that the resting membrane potential of TWK-40 mutants is changed [Mei Zhen group, unpublished data]. Taken together, these findings and observations can be combined into a model of SAD-1 as a regulator of TWK-40, such that loss of SAD-1 could cause a decreased neuronal excitability in neurons. Of note, a study in cultured hippocampal neurons in rats found a correlation between neurotransmitter release and SAD kinase expression [Inoue et al. 2006]. A decrease in excitability is then a likely cause of the synapse defects in *sad-1* worms (Figure 4.1). The increased vesicle pool size could be a compensatory effect of decreased excitability. SAD-1 influences transport of both CCVs and DCVs in similar ways (see above), yet the DCV pool is smaller in null-mutants, while the CCV pool is increased (see above and Figure 3.22D). DCVs are released via different mechanisms that do not rely on depolarization [Richmond and Broadie 2002; Jacob and Kaplan 2003; Salio et al. 2006; Hoover et al. 2014], so their number does not necessarily have to be compensated for when excitability of the synapse is decreased. Thus, excitability might explain this discrepancy between CCV and DCV pool sizes. It is conceivable that the irregularly shaped varicosities (Figure 3.20) are also a consequence of decreased excitability, although this phenotype is likely linked to microtubule misalignment as well. Future work would benefit from the consideration of how far SAD-1 represents a link between microtubule regulation and excitability.

Notably, the excitability model is consistent with the observation that proper function of SAD-1 is dose-dependent [Hung et al. 2007]. Too much or too little SAD-1 could affect resting membrane potential via TWK-40, with deleterious effects on neuron and synapse morphology. If this excitability model is correct, it would provide the first mechanistic link to explain how synapse development is regulated by neuronal activity.

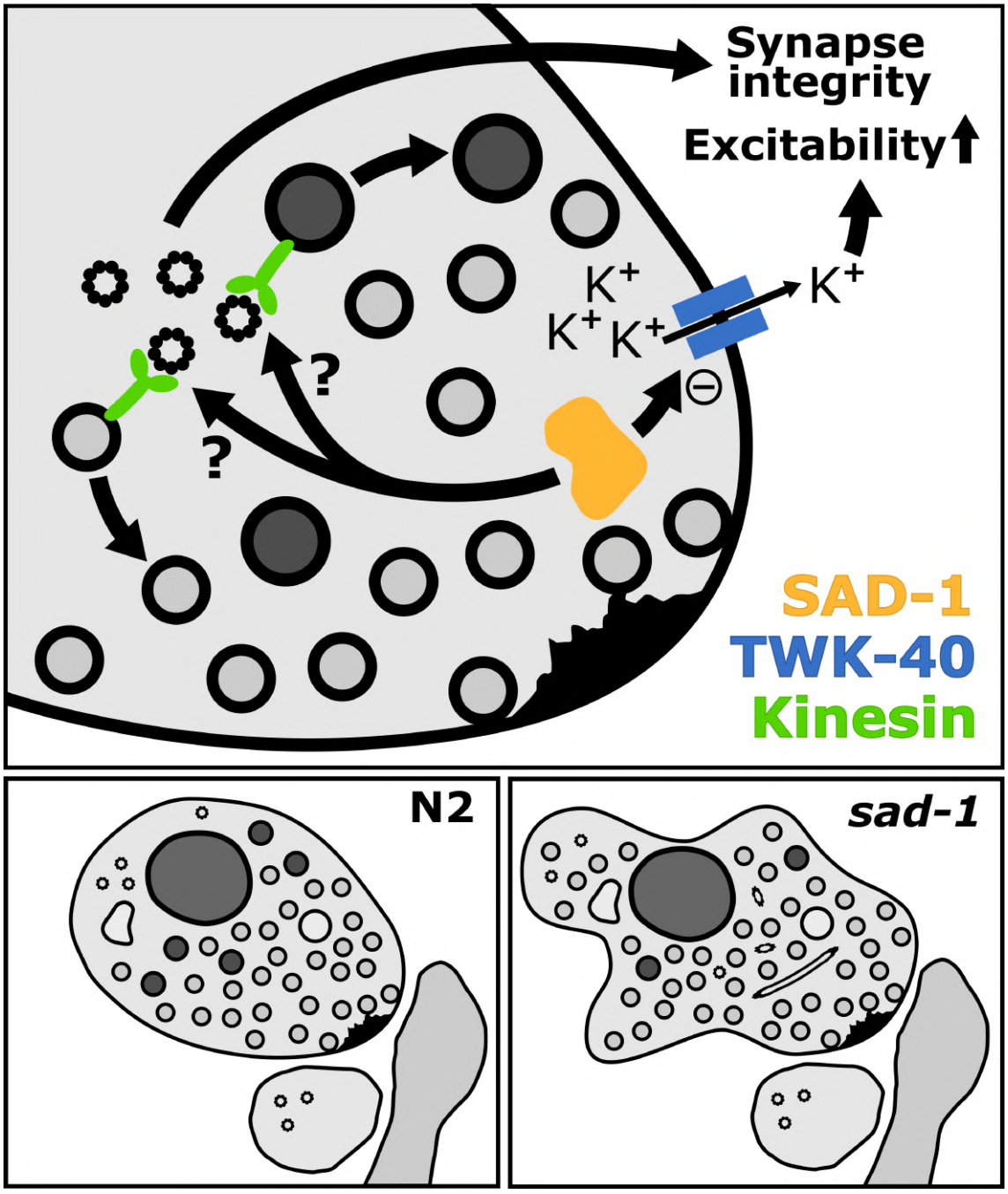

Figure 4.1.: **A model for the roles of SAD-1 at the synapse.** SAD-1 may negatively regulate the potassium leak channel TWK-40, which increases synaptic excitability and integrity. SAD-1 also affects microtubules and influences transport and trapping of synaptic vesicles, likely via a kinesin motor protein. Microtubule orientation might also contribute to synapse integrity by providing scaffolding and cellular transportation in general. Schematic synapses on the bottom show wild-type (N2) ultrastructural features (cf. Figure 1.5) and summarize phenotypes observed in *sad-1* worms: irregularly shaped varicosities, misaligned microtubules, decreased DCV pools, and increased and diffuse CCV pools.

To validate the excitability model of SAD-1 function, further studies are needed. One important study would be the analysis of synapses of *twk-40* mutants via electron microscopy to assess effects of these mutations on synaptic ultrastructure. For locomotion, *twk-40* reverses the *sad-1* phenotype and worms move with increased bending amplitude. Ultrastructural features could be similarly reversed, and if this were true, I would expect smaller vesicle pools and tight synaptic organization in *twk-40* mutants, along with perfectly aligned microtubules and evenly shaped varicosities. The *twk-40*; *sad-1* double mutant shows normal locomotion and synapse morphology, as judged by fluorescence microscopy [Pekar 2013]. Again, it will be insightful to investigate if *sad-1* phenotypes are also suppressed on an ultrastructural level. It has been shown that not all *sad-1* effects are restored in the double mutants; a propensity to move backward and defects in polarity remain [Pekar 2013]. Thus, an analysis via electron tomography might reveal subtle structural phenotypes that could offer insights into these other aspects of SAD-1 function.

As mentioned above, SAD-1 and TWK-40 co-localize near synapses. However, due to the extremely small size of synapses, a more precise localization was not possible via fluorescent reporters. However, srAT could be used to put both proteins in full ultrastructural context. It might be very insightful to map the precise locations of SAD-1 and TWK-40. Do they co-localize on this level? Is SAD-1 restricted to the membrane? How is the localization of SAD-1 affected by TWK-40 mutations and vice versa? Questions like these could be addressed with srAT and their answers should prove instrumental in reconstructing a detailed mechanistic model of SAD-1 function.

Furthermore, electrophysiological analysis of *sad-1* mutants could confirm the hypothesized decrease in excitability. In addition, recording of miniature synaptic currents could offer supporting evidence for the difference in CCVs sizes I found. Generally, larger vesicles contain more neurotransmitter, which results in larger miniature currents [Oleskevich et al. 1999].

4.2.4. Advanced electron microscopy techniques are crucial for elucidating mechanistic models of SAD-1 function

In conclusion, I provided ultrastructural insight into the effects of *sad-1* mutation. My results generally confirmed previous findings but allowed for a more differentiated interpretation and re-contextualization of previous results. I discussed mod-

els of SAD-1 function and suggested future experiments to test the validity of the excitability model of SAD-1 function. I thus showcased how advanced electron microscopy techniques like electron tomography and srAT are crucial for elucidation of functional mechanisms of synaptic proteins. Electron microscopy also makes it possible to analyze individual vesicles, which is generally impossible with other current imaging methods. The example of *sad-1* also demonstrates that careful analysis of individual proteins is necessary for a comprehensive understanding of nervous systems. Dynamic changes in excitability of neurons, which SAD-1 might be orchestrating, are not taken into account by connectomes, yet they are crucially involved in development and function of the nervous system.

Here, I used the loss-of-function mutation of a synaptic protein to elucidate proper synaptic function. However, there is an increasing number of disorders that affect the synapse, and they are consequently (re)classified as synaptopathies. Thus, studying the synapse is not only crucial for understanding the nervous system, but can also help with elucidating disease mechanisms. In turn, analysis and modeling of synaptopathies will help us to understand normal synaptic function.

4.3. Ultrastructural analysis of ALS models offers new mechanistic insights and provides tools for future research

Mutation of the Fused in Sarcoma (FUS) protein is one of the causes of amyotrophic lateral sclerosis (ALS). To elucidate the disease mechanisms, *C. elegans* has been established as an ALS model [Murakami et al. 2012, 2015]. With *C. elegans*, it was possible to address a long-standing question: Does mutated FUS cause ALS via dominant gain-of-function or loss-of-function effects [Sendtner 2011; Dormann and Haass 2011]? Worms expressing FUS mutation alleles exhibit dysfunction of motor neurons caused by a dominant gain-of-function mechanism [Murakami et al. 2012]. Furthermore, it was discovered with *C. elegans* that mutated FUS can form irreversible hydrogels that impair ribonucleoprotein (RNP) granule function. This provides a possible causative mechanism for degeneration of motor neurons [Murakami et al. 2015].

Because there is a compelling case for ALS to be classified as a synaptopathy [Fogarty 2019], an analysis of effects of mutated FUS on synapses is an important next step. For *C. elegans*, powerful tools to investigate the synapse on an ultrastructural level are well established. In this thesis, we utilized electron tomography and srAT to analyze presynaptic ultra-architecture of NMJs and FUS localization in the nerve cords in *C. elegans*. Additionally, we showcased how these methods can be applied to cultured mouse motor neurons. Overall, our results are consistent with previous findings and offer new insights.

4.3.1. Electron tomography reveals ultrastructural effects of FUS-expression in NMJ synapses of *C. elegans*

We analyzed synapses affected by mutated FUS on an ultrastructural level for the very first time in samples processed by HPF/FS. We found alterations in synaptic vesicles. In FUS501 worms, a population of unusually large vesicles appeared in presynapses of NMJs. Although the true nature of these large vesicles remains uncertain, I consider them to be most likely endosomes, for three reasons. First, their appearance and location is consistent with normal endosomes in *C. elegans* NMJs, i. e., they are roughly spherical and are located within the pool of synaptic vesicles. Their morphology is also consistent with the endosomes that Watanabe et al. [2013b] identified at the *C. elegans* NMJ. Second, they fail to form a population that is clearly distinct from normal endosomes within the FUS501 genotype and also compared to controls (see Figure 3.26A). Specifically, there is a continuous distribution of sizes, with only some reaching extreme diameters of more than 100 nm. It was not possible to separate "FUS501 vesicles" and presumably normal endosomes into two distinct groups, although sub-populations of endosomes might be present in all genotypes (see below). Third, in the absence of evidence suggesting otherwise, the endosome interpretation is the most parsimonious. I considered if these endosomes might in fact be autophagosomes, but this explanation is inconsistent with the morphology of autophagosomes in *C. elegans* [Meléndez et al. 2003]. Moreover, autophagosomes feature double membranes and our electron tomograms clearly show that the large endosomes have single membranes (see Figure 3.25). I also considered if they might be part of the endoplasmic reticulum (ER). While almost all of the structures in question appear to be spherical and thus not continuous with the ER, they could be vesicles derived from ER. However, the ER we saw in our tomograms was inconspicuous. It appeared as irregularly shaped tubes at the

synaptic periphery. The large vesicles appeared throughout the synapse, also close the active zone. Still, the ER model should be tested in future studies. It may be possible to stain against these vesicles with specific markers via srAT to consolidate their identity. For example, RAB-5 would be a marker for endosomes, and proteins of the EMC complex [Richard et al. 2013] could be used as ER markers. However, for the reasons stated above, I will consider the large vesicles to be endosomes for now.

We observed that some of these endosomes contain electron-dense filamentous aggregations. While I also found such filled endosomes in controls, they were significantly larger in FUS501 worms. However, when comparing diameters of clear endosomes, there were no significant differences (Figure 3.26). This suggests that there are two populations of endosomes present (clear and filled ones) in all genotypes, but only the endosomes of the filled population are larger on average in FUS501.

Since mutated FUS proteins are known to form aggregates [Murakami et al. 2015], we checked if endosomes contain FUS501 aggregates. FUS501 was not detected in the nerve cord processes using srAT but was detected in the motor neuron somata. Since the nerve cords contain the NMJs, this result suggests that FUS501 does not enter synapses in detectable amounts. This is consistent with studies using fluorescent markers [Murakami et al. 2012, 2015].

In Alzheimer's disease and Down syndrome, endosomes are enlarged as well [Cataldo et al. 2008; Colacurcio et al. 2018]. This is caused by acceleration of neuronal endocytosis. However, our vesicle analysis suggests a decrease in endocytosis (see below). Thus, these endosomes remain enigmatic for now.

The electron-dense filamentous aggregates within these endosomes remain enigmatic as well. It is unknown if these filaments are native structures or caused by FUS501 expression. They might just represent an aging phenotype, considering the worms used for our analyses were six days of age. Also, I cannot rule out the possibility that these structures are artifacts caused by HPF/FS. It is conceivable that soluble proteins within the endosome clump together upon freeze-substitution.

My analysis of synaptic vesicles showed that fewer vesicles are docked in FUS worms but those that are, are located closer to the active zone. These results indicate that docking is impaired. As a consequence, synaptic transmission and excitability should be reduced. Indeed, our collaborator Prof. Shangbang Gao showed via electrophysiological analysis that the frequency of miniature currents is significantly reduced

in worms expressing FUS501 but not amplitude (see Figure A.5 in the appendix). This is consistent with less spontaneous release events due to less docked vesicles. The observation that docked vesicles are closer to the active zone could represent a compensation mechanism. Maybe reduced synaptic transmission is countered with a stronger tethering of vesicles to calcium channels at the active zone. Whatever the case may be, a decrease in excitability and synaptic transmission offers a plausible cause for atrophy and degeneration of muscles [Kong et al. 2009; Ruiz et al. 2010].

In ALS, excitotoxicity is a topic of great concern with regards to neuron degeneration, as recently reviewed by Fogarty [2018]. It is thought that neurons are driven to decay by hyper-excitability. This seems to be the case for several forms of ALS [Fogarty 2018]. However, for FUS-mediated ALS it has been reported that motor neuron degeneration is preceded by hypo-excitability instead [Martínez-Silva et al. 2018]. This again emphasizes the high heterogeneity of ALS [Hardiman et al. 2017]. Indeed, our results support the hypo-excitability model and are thus consistent with mouse FUS models [Martínez-Silva et al. 2018].

I also quantified the distance of all vesicles to the center of the active zone. For both CCVs and DCVs these distances were significantly smaller in FUS worms compared to N2, with FUS501 and FUSwt being similar to each other, although the difference between these two was still significant. This indicates generally smaller vesicle pools in FUS worms.

The quantification of vesicle sizes showed that CCVs are of very similar diameter, but DCVs are significantly smaller in FUS501 compared to FUSwt and N2. As DCVs are produced and mature in the soma [Hoover et al. 2014], maybe a systemic negative impact of FUS501 on protein trafficking leads to smaller DCVs being transported more readily than larger ones. The DCV fraction of the vesicle pool is more than doubled in FUS501. It is also conceivable that DCV accumulate because their release is impaired in FUS501 worms. This might be linked to overall reduced synaptic activity. Release of DCVs is triggered by a small increase in intracellular calcium levels [Salio et al. 2006], and calcium levels are correlated with synaptic activity. Thus, a decrease in activity might impair DCV release. DCVs accumulated more than three-fold when a DCV-associated calcium sensor was mutated in *Drosophila* [Renden et al. 2001]. The *C. elegans* orthologue of this sensor, UNC-31, has been reported as essential for DCV release [Speese et al. 2007], and thus, a similar effect would be expected in the worm.

We used two worm lines as controls in all experiments, N2 and FUSwt. While N2 was important as wild-type reference, our results emphasize the importance of FUSwt as a second control. Wild-type human FUS clearly has effects on the worm and the ultrastructure of its nervous system. Of note, it has been reported previously that FUSwt worms show a small but significant decrease in motility compared to N2 [Murakami et al. 2012]. Even though this effect was much more pronounced in worms expressing mutated FUS alleles, some influence of FUSwt was to be expected. It will be difficult to clearly distinguish between effects of FUS proteins in *C. elegans* that are intrinsic and those that are connected to toxicity related to ALS. This is one of the disadvantages of the worm as an ALS model. Based on our results, it seems that the effects of FUSwt were perhaps underestimated because some become apparent only in analyses that include ultrastructural features.

4.3.2. srAT reveals the ultrastructural context of FUS localization

We observed clusters of FUS in the nucleus and cytoplasm with srAT (Figures 3.29 - 3.31). This confirms previous reports based on fluorescence microscopy [Murakami et al. 2012, 2015]. While srAT allowed us to localize FUS with high precision and accuracy, we did not find ultrastructural equivalents for the FUS accumulations. However, Murakami et al. [2015] show strong evidence that irreversible FUS hydrogels are associated with RNP granules. Such granules have been described via electron microscopy before [Biggiogera et al. 1997; Souquere et al. 2009; Jokhi et al. 2013], and thus, it should be possible in principle to visualize ultrastructural features of FUS aggregates or the RNP granules they attach to. This could be achieved by high magnification TEM imaging and/or adjustments in the sample preparation protocol. Maybe in this case classical protocols using aldehyde fixation at room temperature are more likely to reveal RNP granules, as previous studies used such protocols to describe RNP granule ultrastructure [Biggiogera et al. 1997; Souquere et al. 2009]. If FUS protein could be localized with srAT directly in or at RNP granules, this would strongly support the hypothesis that FUS toxicity is mediated via influencing RNP granules.

4.3.3. Electron tomography and srAT can be applied to cultured mouse motor neurons as powerful research tools

C. elegans is an excellent model for many basic questions in neurobiology. However, its relatively big evolutionary distance to humans limits its value as a model for many biomedical questions. Mouse models are more common for these questions, but also come with disadvantages. It is very challenging to access cellular processes *in vivo* in mice. Cultured cells carry their own disadvantages, but they are a good compromise. In FUS research, culturing primary motor neurons has led to important insights [Wang et al. 2013; Kamelgarn et al. 2016; Guerrero et al. 2016]). I showcased how HPF/FS preserves the ultrastructure of these neurons in a near-native state, which organelles can be observed with our protocols, and how srAT can be used to localize proteins in their ultrastructural context. I suggest future studies make use of these methods. Ultrastructural morphology offers unique insights and reveals phenotypes that are otherwise overlooked (cf. section 4.2).

4.3.4. A reduction of local protein translation might account for large endosomes and vesicle docking defects

Based on previous findings and our results, a model of the disease mechanism can be hypothesized. FUS has many functions related to DNA and RNA processing and maintenance [Ratti and Buratti 2016], and knock-out leads to perinatal death in mice [Hicks et al. 2000]. However, certain mutation alleles, like FUS501, cause degeneration of motor neurons via a dominant gain-of-function effect in *C. elegans* [Murakami et al. 2012]. Irreversible hydrogels formed by mutated FUS impair RNP granule function. This reduces the rate of new protein synthesis [Murakami et al. 2015]. This has a systemic effect on the neuron. However, the effect on axons and synapses is likely particularly detrimental, since it is known from mouse research that such intracellular compartments are heavily dependent on local translation regulation by RNP granules [Holt and Schuman 2013; Akbalik and Schuman 2014; Jung et al. 2014] and are also important in *C. elegans* [Yan et al. 2009]. Furthermore, the synaptic machinery consists of more than a hundred proteins that need to be regulated to ensure proper function [Südhof 2004]. It thus seems plausible to hypothesize that the defect in vesicle docking that I found is caused by a shortage of proteins essential to the docking process. Maybe the large endosomes are a consequence of a disturbance of vesicle recycling for similar reasons. Under physiological

conditions, vesicles are recycled via the ultrafast endocytosis pathway [Watanabe et al. 2013a, b]. After endocytosis, vesicles are regenerated in a clathrin-dependent manner [Watanabe et al. 2014]. Shortage of clathrin or other components of this pathway could cause an accumulation of endocytosed membrane represented by large endosomes. This hypothesis is supported by my result that median distance of vesicles to the active zone is reduced in FUS worms, which is consistent with a reduction of vesicle pool size.

If this model is correct, it would be expected to find synaptic defects also in other neurons that rely heavily on local translation, i. e., neurons with long processes. This is the case for the mechanosensory neurons for gentle touch, for example. If FUS constructs are expressed specifically in these neurons, reaction to touch should be impaired because FUS501 disrupts their excitability. FUSwt expressed as a control should not have the same impairment, although a small effect would not be unexpected (see above).

In summary, we have shown synaptic architecture changes in worms expressing mutated FUS, located FUS with srAT in its ultrastructural context in worms and cultured mouse motor neurons, and discussed a model for the cytotoxic effects of mutated FUS involving local translation. This work thus further substantiates *C. elegans* as an ALS disease model and showcases how advanced light and electron microscopy techniques can aid in the elucidation of ALS disease mechanisms.

4.4. Conclusions and outlook

Although understanding the nervous system is a goal far out of reach, I was able to make steps towards it. In this thesis, I focused on synapses of a very tractable model system, *C. elegans*. Synapses are key to the understanding of nervous systems. We need to know where they are, and we need to know how they function, i. e., signal, on a molecular level. The former is the domain of connectomics; the latter is the domain of molecular neurobiology. I advanced connectomics by establishing super-resolution array tomography as a means of mapping electrical synapses including their molecular identity, and I advanced it further by co-establishing focused ion-beam scanning electron microscopy as a method of obtaining larval connectomes, the *dauer* larva in particular. Thus, I contributed to the accuracy and completeness

of connectomes as well as increasing the number of connectome data-sets to add the aspects of development, variability, and plasticity to *C. elegans* connectomics.

I advanced molecular neurobiology by further elucidating the roles of a synaptic protein, a SAD kinase, in the complex synaptic machinery and by further elucidating the synaptopathic effects of a human disease protein, FUS. This was made possible to a large extent by analyzing the synaptic architecture on the nanometer scale. Thus, I contributed to the challenging task of understanding the molecular machineries of chemical synapses.

Both, connectomics and molecular neurobiology are essential for comprehension of the nervous system as a whole. The synthesis of both will be one of the most important tasks of future research on the path towards this goal. I firmly believe that *C. elegans* remains the best model for making swift progress in this field. With the new advanced imaging and image processing techniques at our disposal, the comprehension of the fundamental principles of nervous system function seems just within reach. The methods, practices, and understanding developed in the worm can then be applied and translated to other organisms. These insights will aid substantially in the comprehension of more complex brains.

References

Akbalik, G. and Schuman, E. M. (2014). mRNA, Live and Unmasked. Science *343*, 375–376.

Albert, P. S. and Riddle, D. L. (1983). Developmental alterations in sensory neuroanatomy of the *Caenorhabditis elegans* dauer larva. Journal of Comparative Neurology *219*, 461–481.

Albertson, D. G. and Thompson, J. N. (1976). The pharynx of *Caenorhabditis elegans*. Philosophical Transactions of the Royal Society of London. B, Biological Sciences *275*, 299–325.

Albrecht, U., Seulberger, H., Schwarz, H. and Risau, W. (1990). Correlation of blood-brain barrier function and HT7 protein distribution in chick brain circumventricular organs. Brain Research *535*, 49–61.

Altun, Z. F., Chen, B., Wang, Z.-W. and Hall, D. H. (2009). High resolution map of *Caenorhabditis elegans* gap junction proteins. Developmental Dynamics *238*, 1936–1950.

Andersson, M. K., Ståhlberg, A., Arvidsson, Y., Olofsson, A., Semb, H., Stenman, G., Nilsson, O. and Åman, P. (2008). The multifunctional FUS, EWS and TAF15 proto-oncoproteins show cell type-specific expression patterns and involvement in cell spreading and stress response. BMC Cell Biology *9*, 37.

Ashton, F. T., Bhopale, V. M., Fine, A. E. and Schad, G. A. (1995). Sensory neuroanatomy of a skin-penetrating nematode parasite: *Strongyloides stercoralis*. I. Amphidal neurons. Journal of Comparative Neurology *357*, 281–295.

Azevedo, F. A. C., Carvalho, L. R. B., Grinberg, L. T., Farfel, J. M., Ferretti, R. E. L., Leite, R. E. P., Filho, W. J., Lent, R. and Herculano-Houzel, S. (2009). Equal numbers of neuronal and nonneuronal cells make the human brain an isometrically scaled-up primate brain. Journal of Comparative Neurology *513*, 532–541.

Bargmann, C. I. and Marder, E. (2013). From the connectome to brain function. Nature Methods *10*, 483–490.

Bargmann, C. I. and Mori, I. (1997). Chemotaxis and Thermotaxis. In *C. elegans* II, (Riddle, D. L., Blumenthal, T., Meyer, B. J. and Priess, J. R., eds),. Cold Spring Harbor Laboratory Press Cold Spring Harbor (NY) 2nd edition.

Barnes, A. P., Lilley, B. N., Pan, Y. A., Plummer, L. J., Powell, A. W., Raines, A. N., Sanes, J. R. and Polleux, F. (2007). LKB1 and SAD Kinases Define a Pathway Required for the Polarization of Cortical Neurons. Cell *129*, 549–563.

Baron R L (1994). A carbamate insecticide: a case study of aldicarb. Environmental Health Perspectives *102*, 23–27.

Bentley, B., Branicky, R., Barnes, C. L., Chew, Y. L., Yemini, E., Bullmore, E. T., Vértes, P. E. and Schafer, W. R. (2016). The Multilayer Connectome of *Caenorhabditis elegans*. PLOS Computational Biology *12*, e1005283.

Betzig, E., Patterson, G. H., Sougrat, R., Lindwasser, O. W., Olenych, S., Bonifacino, J. S., Davidson, M. W., Lippincott-Schwartz, J. and Hess, H. F. (2006). Imaging Intracellular Fluorescent Proteins at Nanometer Resolution. Science *313*, 1642–1645.

Bhattacharya, A., Aghayeva, U., Berghoff, E. G. and Hobert, O. (2019). Plasticity of the Electrical Connectome of *C. elegans*. Cell *176*, 1174–1189.e16.

Biggiogera, M., Bottone, M. G. and Pellicciari, C. (1997). Nuclear ribonucleoprotein-containing structures undergo severe rearrangement during spontaneous thymocyte apoptosis. A morphological study by electron microscopy. Histochemistry and Cell Biology *107*, 331–336.

Boyde, A., Franc, F. and Maconnachie, E. (1981). Measurements of critical point shrinkage of glutaraldehyde fixed mouse liver. Scanning *4*, 69–82.

Brenner, S. (1974). The Genetics of *Caenorhabditis elegans*. Genetics *77*, 71–94.

Brose, N., O'Connor, V. and Skehel, P. (2010). Synaptopathy: dysfunction of synaptic function? Biochemical Society Transactions *38*, 443–444.

Bumbarger, D. J., Crum, J., Ellisman, M. H. and Baldwin, J. G. (2007). Three-dimensional fine structural reconstruction of the nose sensory structures of *Acrobeles complexus* compared to *Caenorhabditis elegans* (Nematoda: Rhabditida). Journal of Morphology *268*, 649–663.

Bumbarger, D. J., Wijeratne, S., Carter, C., Crum, J., Ellisman, M. H. and Baldwin, J. G. (2009). Three-dimensional reconstruction of the amphid sensilla in the microbial feeding nematode, *Acrobeles complexus* (nematoda: Rhabditida). Journal of Comparative Neurology *512*, 271–281.

Burnell, A. M., Houthoofd, K., O'Hanlon, K. and Vanfleteren, J. R. (2005). Alternate metabolism during the dauer stage of the nematode *Caenorhabditis elegans*. Experimental Gerontology *40*, 850–856.

Burr, A. H. (1985). The photomovment of *Caenorhabditis elegans*, a nematode which lacks ocelli. Proof that the response is to light, not radiant heating. Photochemistry and Photobiology *41*, 577–582.

Campbell, W. C., Fisher, M. H., Stapley, E. O., Albers-Schonberg, G. and Jacob, T. A. (1983). Ivermectin: a potent new antiparasitic agent. Science *221*, 823–828.

Cassada, R. C. and Russell, R. L. (1975). The dauerlarva, a post-embryonic developmental variant of the nematode *Caenorhabditis elegans*. Developmental Biology *46*, 326–342.

Cataldo, A. M., Mathews, P. M., Boiteau, A. B., Hassinger, L. C., Peterhoff, C. M., Jiang, Y., Mullaney, K., Neve, R. L., Gruenberg, J. and Nixon, R. A. (2008). Down Syndrome Fibroblast Model of Alzheimer-Related Endosome Pathology: Accelerated Endocytosis Promotes Late Endocytic Defects. The American Journal of Pathology *173*, 370–384.

Chalfie, M., Sulston, J. E., White, J. G., Southgate, E., Thomson, J. N. and Brenner, S. (1985). The neural circuit for touch sensitivity in *Caenorhabditis elegans*. Journal of Neuroscience *5*, 956–964.

Chalfie, M., Tu, Y., Euskirchen, G., Ward, W. W. and Prasher, D. C. (1994). Green fluorescent protein as a marker for gene expression. Science *263*, 802–805.

Chew, Y. L., Fan, X., Götz, J. and Nicholas, H. R. (2013). PTL-1 regulates neuronal integrity and lifespan in *C. elegans*. Journal of Cell Science *126*, 2079–2091.

Chia, P. H., Patel, M. R. and Shen, K. (2012). NAB-1 instructs synapse assembly by linking adhesion molecules and F-actin to active zone proteins. Nature Neuroscience *15*, 234–242.

Chou, S. M. (1992). Pathology: light microscopy of amyotrophic lateral sclerosis. Handbook of amyotrophic lateral sclerosis *6*, 133–181.

Colacurcio, D. J., Pensalfini, A., Jiang, Y. and Nixon, R. A. (2018). Dysfunction of Autophagy and Endosomal-Lysosomal Pathways: Roles in Pathogenesis of Down Syndrome and Alzheimer's Disease. Free radical biology & medicine *114*, 40–51.

Collman, F., Buchanan, J., Phend, K. D., Micheva, K. D., Weinberg, R. J. and Smith, S. J. (2015). Mapping Synapses by Conjugate Light-Electron Array Tomography. The Journal of Neuroscience *35*, 5792–5807.

Couteaux, R. and Pécot-Dechavassine, M. (1970). Synaptic vesicles and pouches at the level of "active zones" of the neuromuscular junction. Comptes Rendus Hebdomadaires Des Seances De l'Academie Des Sciences. Serie D: Sciences Naturelles *271*, 2346–2349.

Cox, G. N., Staprans, S. and Edgar, R. S. (1981). The cuticle of *Caenorhabditis elegans*: II. Stage-specific changes in ultrastructure and protein composition during postembryonic development. Developmental Biology *86*, 456–470.

Crook, M. (2014). The dauer hypothesis and the evolution of parasitism: 20 years on and still going strong. International Journal for Parasitology *44*, 1–8.

Crump, J. G., Zhen, M., Jin, Y. and Bargmann, C. I. (2001). The SAD-1 Kinase Regulates Presynaptic Vesicle Clustering and Axon Termination. Neuron *29*, 115–129.

de Chaumont, F., Dallongeville, S., Chenouard, N., Hervé, N., Pop, S., Provoost, T., Meas-Yedid, V., Pankajakshan, P., Lecomte, T., Le Montagner, Y., Lagache, T., Dufour, A. and Olivo-Marin, J.-C. (2012). Icy: an open bioimage informatics platform for extended reproducible research. Nature Methods *9*, 690–696.

Deerinck, T. J., Shone, T. M., Bushong, E. A., Ramachandra, R., Peltier, S. T. and Ellisman, M. H. (2018). High-performance serial block-face SEM of nonconductive biological samples enabled by focal gas injection-based charge compensation. Journal of Microscopy *270*, 142–149.

Denk, W. and Horstmann, H. (2004). Serial Block-Face Scanning Electron Microscopy to Reconstruct Three-Dimensional Tissue Nanostructure. PLoS Biol *2*, e329.

Dent, J. A., Smith, M. M., Vassilatis, D. K. and Avery, L. (2000). The genetics of ivermectin resistance in *Caenorhabditis elegans*. Proceedings of the National Academy of Sciences *97*, 2674–2679.

Dickinson, M., Bearman, G., Tille, S., Lansford, R. and Fraser, S. (2001). Multi-Spectral Imaging and Linear Unmixing Add a Whole New Dimension to Laser Scanning Fluorescence Microscopy. BioTechniques *31*, 1272–1278.

Dixon, S. J. and Roy, P. J. (2005). Muscle arm development in *Caenorhabditis elegans*. Development *132*, 3079–3092.

Dormann, D. and Haass, C. (2011). TDP-43 and FUS: a nuclear affair. Trends in Neurosciences *34*, 339–348.

Dormann, D., Rodde, R., Edbauer, D., Bentmann, E., Fischer, I., Hruscha, A., Than, M. E., Mackenzie, I. R. A., Capell, A., Schmid, B., Neumann, M. and Haass, C. (2010). ALS-associated fused in sarcoma (FUS) mutations disrupt Transportin-mediated nuclear import. The EMBO Journal *29*, 2841–2857.

Doroquez, D. B., Berciu, C., Anderson, J. R., Sengupta, P. and Nicastro, D. (2014). A high-resolution morphological and ultrastructural map of anterior sensory cilia and glia in *Caenorhabditis elegans*. eLife *3*, e01948.

Ebersold, H. R., Cordier, J.-L. and Lüthy, P. (1981). Bacterial mesosomes: Method dependent artifacts. Archives of Microbiology *130*, 19–22.

Edwards, S. L., Yorks, R. M., Morrison, L. M., Hoover, C. M. and Miller, K. G. (2015). Synapse-Assembly Proteins Maintain Synaptic Vesicle Cluster Stability and Regulate Synaptic Vesicle Transport in *Caenorhabditis elegans*. Genetics *201*, 91–116.

Eliceiri, K. W., Berthold, M. R., Goldberg, I. G., Ibáñez, L., Manjunath, B. S., Martone, M. E., Murphy, R. F., Peng, H., Plant, A. L., Roysam, B., Stuurman, N., Swedlow, J. R., Tomancak, P. and Carpenter, A. E. (2012). Biological imaging software tools. Nature Methods *9*, 697–710.

Emmons, S. W. (2015). The beginning of connectomics: a commentary on White et al. (1986) "The structure of the nervous system of the nematode *Caenorhabditis elegans*". Philosophical Transactions of the Royal Society B: Biological Sciences *370*, 20140309.

Erkut, C., Vasilj, A., Boland, S., Habermann, B., Shevchenko, A. and Kurzchalia, T. V. (2013). Molecular Strategies of the *Caenorhabditis elegans* Dauer Larva to Survive Extreme Desiccation. PLOS ONE *8*, e82473.

Fialka, I., Schwarz, H., Reichmann, E., Oft, M., Busslinger, M. and Beug, H. (1996). The estrogen-dependent c-JunER protein causes a reversible loss of mammary epithelial cell polarity involving a destabilization of adherens junctions. The Journal of Cell Biology *132*, 1115–1132.

Fine, A. E., Ashton, F. T., Bhopale, V. M. and Schad, G. A. (1997). Sensory neuroanatomy of a skin-penetrating nematode parasite *Strongyloides stercoralis*. II. labial and cephalic neurons. Journal of Comparative Neurology *389*, 212–223.

Fire, A., Xu, S., Montgomery, M. K., Kostas, S. A., Driver, S. E. and Mello, C. C. (1998). Potent and specific genetic interference by double-stranded RNA in *Caenorhabditis elegans*. Nature *391*, 806–811.

Fogarty, M. J. (2018). Driven to decay: Excitability and synaptic abnormalities in amyotrophic lateral sclerosis. Brain Research Bulletin *140*, 318–333.

Fogarty, M. J. (2019). Amyotrophic lateral sclerosis as a synaptopathy. Neural Regeneration Research *14*, 189–192.

Forero, D. A., Casadesus, G., Perry, G. and Arboleda, H. (2006). Synaptic dysfunction and oxidative stress in Alzheimer's disease: Emerging mechanisms. Journal of Cellular and Molecular Medicine *10*, 796–805.

Gan, Q. and Watanabe, S. (2018). Synaptic Vesicle Endocytosis in Different Model Systems. Frontiers in Cellular Neuroscience *12*.

García-Fernández, E., Koch, G., Wagner, R. M., Fekete, A., Stengel, S. T., Schneider, J., Mielich-Süss, B., Geibel, S., Markert, S. M., Stigloher, C. and Lopez, D. (2017). Membrane Microdomain Disassembly Inhibits MRSA Antibiotic Resistance. Cell *171*, 1354–1367.e20.

Gilula, N. B., Reeves, O. R. and Steinbach, A. (1972). Metabolic Coupling, Ionic Coupling and Cell Contacts. Nature *235*, 262–265.

Girard, L. R., Fiedler, T. J., Harris, T. W., Carvalho, F., Antoshechkin, I., Han, M., Sternberg, P. W., Stein, L. D. and Chalfie, M. (2007). WormBook: the online review of *Caenorhabditis elegans* biology. Nucleic Acids Research *35*, D472–D475.

Goedert, M., Baur, C. P., Ahringer, J., Jakes, R., Hasegawa, M., Spillantini, M. G., Smith, M. J. and Hill, F. (1996). PTL-1, a microtubule-associated protein with tau-like repeats from the nematode *Caenorhabditis elegans*. Journal of Cell Science *109*, 2661–2672.

Golden, J. W. and Riddle, D. L. (1984). The *Caenorhabditis elegans* dauer larva: Developmental effects of pheromone, food, and temperature. Developmental Biology *102*, 368–378.

Goodenough, D. A. and Paul, D. L. (2009). Gap Junctions. Cold Spring Harbor Perspectives in Biology *1*, a002576.

Gordon, P., Hingula, L., Krasny, M. L., Swienckowski, J. L., Pokrywka, N. J. and Raley-Susman, K. M. (2008). The invertebrate microtubule-associated protein PTL-1 functions in mechanosensation and development in *Caenorhabditis elegans*. Development Genes and Evolution *218*, 541–551.

Grencis, R. K. and Cooper, E. S. (1996). *Enterobius*, *Trichuris*, *Capillaria*, and hookworm including *Ancylostoma caninum*. Gastroenterology Clinics *25*, 579–597.

Guerrero, E. N., Wang, H., Mitra, J., Hegde, P. M., Stowell, S. E., Liachko, N. F., Kraemer, B. C., Garruto, R. M., Rao, K. S. and Hegde, M. L. (2016). TDP-43/FUS in motor neuron disease: Complexity and challenges. Progress in Neurobiology *145-146*, 78–97.

Gusnard, D. and Kirschner, R. H. (1977). Cell and organelle shrinkage during preparation for scanning electron microscopy: effects of fixation, dehydration and critical point drying. Journal of Microscopy *110*, 51–57.

Gustafsson, M. G. L. (2000). Surpassing the lateral resolution limit by a factor of two using structured illumination microscopy. Journal of Microscopy *198*, 82–87.

Hall, D. H. and Russell, R. L. (1991). The posterior nervous system of the nematode *Caenorhabditis elegans*: serial reconstruction of identified neurons and complete pattern of synaptic interactions. Journal of Neuroscience *11*, 1–22.

Haraguchi, C. M. and Yokota, S. (2002). Immunofluorescence technique for 100-nm-thick semithin sections of Epon-embedded tissues. Histochemistry and Cell Biology *117*, 81–85.

Hardiman, O., Al-Chalabi, A., Chio, A., Corr, E. M., Logroscino, G., Robberecht, W., Shaw, P. J., Simmons, Z. and van den Berg, L. H. (2017). Amyotrophic lateral sclerosis. Nature Reviews Disease Primers *3*, 17071.

Haueis, P. and Slaby, J. (2017). Connectomes as constitutively epistemic objects: Critical perspectives on modeling in current neuroanatomy. Progress in Brain Research *233*, 149–177.

Hayworth, K. J., Morgan, J. L., Schalek, R., Berger, D. R., Hildebrand, D. G. C. and Lichtman, J. W. (2014). Imaging ATUM ultrathin section libraries with WaferMapper: a multi-scale approach to EM reconstruction of neural circuits. Frontiers in Neural Circuits *8*.

Hayworth, K. J., Xu, C. S., Lu, Z., Knott, G. W., Fetter, R. D., Tapia, J. C., Lichtman, J. W. and Hess, H. F. (2015). Ultrastructurally smooth thick partitioning and volume stitching for large-scale connectomics. Nature Methods *12*, 319–322.

Hedgecock, E. M. and Russell, R. L. (1975). Normal and mutant thermotaxis in the nematode *Caenorhabditis elegans*. Proceedings of the National Academy of Sciences *72*, 4061–4065.

Heilemann, M., Linde, S., Schüttpelz, M., Kasper, R., Seefeldt, B., Mukherjee, A., Tinnefeld, P. and Sauer, M. (2008). Subdiffraction-Resolution Fluorescence Imaging with Conventional Fluorescent Probes. Angewandte Chemie International Edition *47*, 6172–6176.

Heiligenstein, X., Paul-Gilloteaux, P., Raposo, G. and Salamero, J. (2017). eC-CLEM: A multidimension, multimodel software to correlate intermodal images with a focus on light and electron microscopy. In Methods in Cell Biology, (Müller-Rxeichert, T. and Verkade, P., eds), vol. 140, of Correlative Light and Electron Microscopy III pp. 335–352. Academic Press.

Helmprobst, F., Frank, M. and Stigloher, C. (2015). Presynaptic architecture of the larval zebrafish neuromuscular junction. Journal of Comparative Neurology *523*, 1984–1997.

Helmstaedter, M., Briggman, K. L., Turaga, S. C., Jain, V., Seung, H. S. and Denk, W. (2013). Connectomic reconstruction of the inner plexiform layer in the mouse retina. Nature *500*, 168–174.

Herken, R., Fussek, M., Barth, S. and Götz, W. (1988). LR-White and LR-Gold resins for postembedding immunofluorescence staining of laminin in mouse kidney. The Histochemical Journal *20*, 427–432.

Hicks, G. G., Singh, N., Nashabi, A., Mai, S., Bozek, G., Klewes, L., Arapovic, D., White, E. K., Koury, M. J., Oltz, E. M., Kaer, L. V. and Ruley, H. E. (2000). Fus deficiency in mice results in defective B-lymphocyte development and activation, high levels of chromosomal instability and perinatal death. Nature Genetics *24*, 175.

Hinsch, K. and Zupanc, G. K. H. (2007). Generation and long-term persistence of new neurons in the adult zebrafish brain: A quantitative analysis. Neuroscience *146*, 679–696.

Holt, C. E. and Schuman, E. M. (2013). The Central Dogma Decentralized: New Perspectives on RNA Function and Local Translation in Neurons. Neuron *80*, 648–657.

Hoover, C. M., Edwards, S. L., Yu, S.-c., Kittelmann, M., Richmond, J. E., Eimer, S., Yorks, R. M. and Miller, K. G. (2014). A Novel CaM Kinase II Pathway Controls the Location of Neuropeptide Release from *Caenorhabditis elegans* Motor Neurons. Genetics *196*, 745–765.

Horisberger, M. (1981). Colloidal gold : a cytochemical marker for light and fluorescent microscopy and for transmission and scanning electron microscopy. Scanning electron microscopy *1*, 9–31.

Hotez, P. J., Brooker, S., Bethony, J. M., Bottazzi, M. E., Loukas, A. and Xiao, S. (2004). Hookworm Infection. New England Journal of Medicine *351*, 799–807.

Houthoofd, K., Braeckman, B. P., Lenaerts, I., Brys, K., De Vreese, A., Van Eygen, S. and Vanfleteren, J. R. (2002). Ageing is reversed, and metabolism is reset to young levels in recovering dauer larvae of *C. elegans*. Experimental Gerontology *37*, 1015–1021.

Humbel, B. M., Sibon, O. C., Stierhof, Y. D. and Schwarz, H. (1995). Ultra-small gold particles and silver enhancement as a detection system in immunolabeling and in situ hybridization experiments. The Journal of Histochemistry and Cytochemistry: Official Journal of the Histochemistry Society *43*, 735–737.

Hung, W., Hwang, C., Po, M. D. and Zhen, M. (2007). Neuronal polarity is regulated by a direct interaction between a scaffolding protein, Neurabin, and a presynaptic SAD-1 kinase in *Caenorhabditis elegans*. Development *134*, 237–249.

Inoue, E., Mochida, S., Takagi, H., Higa, S., Deguchi-Tawarada, M., Takao-Rikitsu, E., Inoue, M., Yao, I., Takeuchi, K., Kitajima, I., Setou, M., Ohtsuka, T. and Takai, Y. (2006). SAD: A Presynaptic Kinase Associated with Synaptic Vesicles and the Active Zone Cytomatrix that Regulates Neurotransmitter Release. Neuron *50*, 261–275.

Jacob, T. C. and Kaplan, J. M. (2003). The EGL-21 Carboxypeptidase E Facilitates Acetylcholine Release at *Caenorhabditis elegans* Neuromuscular Junctions. Journal of Neuroscience *23*, 2122–2130.

Jahn, M. T., Arkhipova, K., Markert, S. M., Stigloher, C., Lachnit, T., Pita, L., Kupczok, A., Ribes, M., Stengel, S. T., Rosenstiel, P., Dutilh, B. E. and Hentschel, U. (2019). A symbiont phage protein aids in eukaryote immune evasion. bioRxiv *1*, 608950.

Jahn, M. T., Markert, S. M., Ryu, T., Ravasi, T., Stigloher, C., Hentschel, U. and Moitinho-Silva, L. (2016). Shedding light on cell compartmentation in the candidate phylum Poribacteria by high resolution visualisation and transcriptional profiling. Scientific Reports *6*, 35860.

Jain, R., Jadon, N. and Radhapyari, K. (2006). Determination of antihelminthic drug pyrantel pamoate in bulk and pharmaceutical formulations using electro-analytical methods. Talanta *70*, 383–386.

Jarrell, T. A., Wang, Y., Bloniarz, A. E., Brittin, C. A., Xu, M., Thomson, J. N., Albertson, D. G., Hall, D. H. and Emmons, S. W. (2012). The Connectome of a Decision-Making Neural Network. Science *337*, 437–444.

Jokhi, V., Ashley, J., Nunnari, J., Noma, A., Ito, N., Wakabayashi-Ito, N., Moore, M. J. and Budnik, V. (2013). Torsin Mediates Primary Envelopment of Large Ribonucleoprotein Granules at the Nuclear Envelope. Cell Reports *3*, 988–995.

Jones, A. K., Davis, P., Hodgkin, J. and Sattelle, D. B. (2007). The nicotinic acetylcholine receptor gene family of the nematode *Caenorhabditis elegans*: an update on nomenclature. Invertebrate Neuroscience *7*, 129–131.

Jung, H., Gkogkas, C. G., Sonenberg, N. and Holt, C. E. (2014). Remote Control of Gene Function by Local Translation. Cell *157*, 26–40.

Kaltdorf, K. V., Schulze, K., Helmprobst, F., Kollmannsberger, P., Dandekar, T. and Stigloher, C. (2017). FIJI Macro 3D ART VeSElecT: 3D Automated Reconstruction Tool for Vesicle Structures of Electron Tomograms. PLOS Computational Biology *13*, e1005317.

Kaltdorf, K. V., Theiss, M., Markert, S. M., Zhen, M., Dandekar, T., Stigloher, C. and Kollmannsberger, P. (2018). Automated classification of synaptic vesicles in electron tomograms of *C. elegans* using machine learning. PLOS ONE *13*, e0205348.

Kamelgarn, M., Chen, J., Kuang, L., Arenas, A., Zhai, J., Zhu, H. and Gal, J. (2016). Proteomic analysis of FUS interacting proteins provides insights into FUS function and its role in ALS. Biochimica et Biophysica Acta (BBA) - Molecular Basis of Disease *1862*, 2004–2014.

Karr, J. R., Sanghvi, J. C., Macklin, D. N., Gutschow, M. V., Jacobs, J. M., Bolival, B., Assad-Garcia, N., Glass, J. I. and Covert, M. W. (2012). A Whole-Cell Computational Model Predicts Phenotype from Genotype. Cell *150*, 389–401.

Kasthuri, N., Hayworth, K. J., Berger, D. R., Schalek, R. L., Conchello, J. A., Knowles-Barley, S., Lee, D., VÃ¡zquez-Reina, A., Kaynig, V., Jones, T. R., Roberts, M., Morgan, J. L., Tapia, J. C., Seung, H. S., Roncal, W. G., Vogelstein, J. T., Burns, R., Sussman, D. L., Priebe, C. E., Pfister, H. and Lichtman, J. W. (2015). Saturated Reconstruction of a Volume of Neocortex. Cell *162*, 648–661.

Keller, A. L., Zeidler, D. and Kemen, T. (2014). High throughput data acquisition with a multi-beam SEM. In Scanning Microscopies 2014 vol. 9236, p. 92360B, International Society for Optics and Photonics.

Kenyon Cynthia (2011). The first long-lived mutants: discovery of the insulin/IGF-1 pathway for ageing. Philosophical Transactions of the Royal Society B: Biological Sciences *366*, 9–16.

Kim, J. S., Lilley, B. N., Zhang, C., Shokat, K. M., Sanes, J. R. and Zhen, M. (2008). A chemical-genetic strategy reveals distinct temporal requirements for SAD-1 kinase in neuronal polarization and synapse formation. Neural Development *3*, 23.

Kim, J. S. M., Hung, W., Narbonne, P., Roy, R. and Zhen, M. (2010). *C. elegans* STRADα and SAD cooperatively regulate neuronal polarity and synaptic organization. Development *137*, 93–102.

Kishi, M., Pan, Y. A., Crump, J. G. and Sanes, J. R. (2005). Mammalian SAD Kinases Are Required for Neuronal Polarization. Science *307*, 929–932.

Klassen, M. P. and Shen, K. (2007). Wnt Signaling Positions Neuromuscular Connectivity by Inhibiting Synapse Formation in *C. elegans*. Cell *130*, 704–716.

Knopp, S., Steinmann, P., Keiser, J. and Utzinger, J. (2012). Nematode Infections: Soil-Transmitted Helminths and Trichinella. Infectious Disease Clinics *26*, 341–358.

Kong, L., Wang, X., Choe, D. W., Polley, M., Burnett, B. G., Bosch-Marcé, M., Griffin, J. W., Rich, M. M. and Sumner, C. J. (2009). Impaired Synaptic Vesicle Release and Immaturity of Neuromuscular Junctions in Spinal Muscular Atrophy Mice. Journal of Neuroscience *29*, 842–851.

Kremer, J. R., Mastronarde, D. N. and McIntosh, J. R. (1996). Computer Visualization of Three-Dimensional Image Data Using IMOD. Journal of Structural Biology *116*, 71–76.

Kukulski, W., Schorb, M., Welsch, S., Picco, A., Kaksonen, M. and Briggs, J. A. G. (2011). Correlated fluorescence and 3D electron microscopy with high sensitivity and spatial precision. The Journal of Cell Biology *192*, 111–119.

Kurth, T., Schwarz, H., Schneider, S. and Hausen, P. (1996). Fine structural immunocytochemistry of catenins in amphibian and mammalian muscle. Cell and Tissue Research *286*, 1–12.

Kwiatkowski, T. J., Bosco, D. A., LeClerc, A. L., Tamrazian, E., Vanderburg, C. R., Russ, C., Davis, A., Gilchrist, J., Kasarskis, E. J., Munsat, T., Valdmanis, P., Rouleau, G. A., Hosler, B. A., Cortelli, P., Jong, P. J. d., Yoshinaga, Y., Haines, J. L., Pericak-Vance, M. A., Yan, J., Ticozzi, N., Siddique, T., McKenna-Yasek, D., Sapp, P. C., Horvitz, H. R., Landers, J. E. and Brown, R. H. (2009). Mutations in the FUS/TLS Gene on Chromosome 16 Cause Familial Amyotrophic Lateral Sclerosis. Science *323*, 1205–1208.

Labbé, J. C., Maddox, P. S., Salmon, E. D. and Goldstein, B. (2003). PAR proteins regulate microtubule dynamics at the cell cortex in *C. elegans*. Current biology: CB *13*, 707–714.

Lagier-Tourenne, C., Polymenidou, M. and Cleveland, D. W. (2010). TDP-43 and FUS/TLS: emerging roles in RNA processing and neurodegeneration. Human Molecular Genetics *19*, R46–R64.

Lewis, J. A. and Hodgkin, J. A. (1977). Specific neuroanatomical changes in chemosensory mutants of the nematode *Caenorhabditis elegans*. Journal of Comparative Neurology *172*, 489–510.

Lewis, J. A., Wu, C. H., Berg, H. and Levine, J. H. (1980). The genetics of levamisole resistance in the nematode *Caenorhabditis elegans*. Genetics *95*, 905–928.

Li, J.-Y., Plomann, M. and Brundin, P. (2003). Huntington's disease: a synaptopathy? Trends in Molecular Medicine *9*, 414–420.

Lichtman, J. W. and Sanes, J. R. (2008). Ome sweet ome: what can the genome tell us about the connectome? Current Opinion in Neurobiology *18*, 346–353.

Liu, L. X. and Weller, P. F. (1993). Strongyloidiasis and other intestinal nematode infections. Infectious disease clinics of North America *7*, 655–682.

López-Erauskin, J., Tadokoro, T., Baughn, M. W., Myers, B., McAlonis-Downes, M., Chillon-Marinas, C., Asiaban, J. N., Artates, J., Bui, A. T., Vetto, A. P., Lee, S. K., Le, A. V., Sun, Y., Jambeau, M., Boubaker, J., Swing, D., Qiu, J., Hicks, G. G., Ouyang, Z., Fu, X.-D., Tessarollo, L., Ling, S.-C., Parone, P. A., Shaw, C. E., Marsala, M., Lagier-Tourenne, C., Cleveland, D. W. and Da Cruz, S. (2018). ALS/FTD-Linked Mutation in FUS Suppresses Intra-axonal Protein Synthesis and Drives Disease Without Nuclear Loss-of-Function of FUS. Neuron *100*, 816–830.e7.

Löschberger, A., Franke, C., Krohne, G., Linde, S. v. d. and Sauer, M. (2014). Correlative super-resolution fluorescence and electron microscopy of the nuclear pore complex with molecular resolution. J Cell Sci *127*, 4351–4355.

Lucocq, J. (1994). Quantitation of gold labelling and antigens in immunolabelled ultrathin sections. Journal of Anatomy *184*, 1–13.

Lucocq, J. (2008). Chapter 4 Quantification of Structures and Gold Labeling in Transmission Electron Microscopy. In Methods in Cell Biology vol. 88, of Introduction to Electron Microscopy for Biologists pp. 59–82. Academic Press.

Lučić, V., Rigort, A. and Baumeister, W. (2013). Cryo-electron tomography: The challenge of doing structural biology in situ. J Cell Biol *202*, 407–419.

Markert, S. M., Bauer, V., Muenz, T. S., Jones, N. G., Helmprobst, F., Britz, S., Sauer, M., Rössler, W., Engstler, M. and Stigloher, C. (2017). 3D subcellular localization with superresolution array tomography on ultrathin sections of various species. In Methods in Cell Biology, (Müller-Reichert, T. and Verkade, P., eds), vol. 140, of Correlative Light and Electron Microscopy III pp. 21–47. Academic Press.

Markert, S. M., Britz, S., Proppert, S., Lang, M., Witvliet, D., Mulcahy, B., Sauer, M., Zhen, M., Bessereau, J.-L. and Stigloher, C. (2016). Filling the gap: adding super-resolution to array tomography for correlated ultrastructural and molecular identification of electrical synapses at the *C. elegans* connectome. Neurophotonics *3*, 041802–041802.

Martin, R. J. (1993). Neuromuscular transmission in nematode parasites and antinematodal drug action. Pharmacology & Therapeutics *58*, 13–50.

Martínez-Silva, M. d. L., Imhoff-Manuel, R. D., Sharma, A., Heckman, C., Shneider, N. A., Roselli, F., Zytnicki, D. and Manuel, M. (2018). Hypoexcitability precedes denervation in the large fast-contracting motor units in two unrelated mouse models of ALS. eLife *7*, e30955.

Mastronarde, D. N. (2005). Automated electron microscope tomography using robust prediction of specimen movements. Journal of Structural Biology *152*, 36–51.

Mathie, A., Al-Moubarak, E. and Veale, E. L. (2010). Gating of two pore domain potassium channels. Journal of Physiology *588*, 3149–56.

Meléndez, A., Tallóczy, Z., Seaman, M., Eskelinen, E.-L., Hall, D. H. and Levine, B. (2003). Autophagy Genes Are Essential for Dauer Development and Life-Span Extension in *C. elegans*. Science *301*, 1387–1391.

Michael, D. J., Cai, H., Xiong, W., Ouyang, J. and Chow, R. H. (2006). Mechanisms of peptide hormone secretion. Trends in Endocrinology & Metabolism *17*, 408–415.

Micheva, K. D., Busse, B., Weiler, N. C., O'Rourke, N. and Smith, S. J. (2010a). Single-Synapse Analysis of a Diverse Synapse Population: Proteomic Imaging Methods and Markers. Neuron *68*, 639–653.

Micheva, K. D., O'Rourke, N., Busse, B. and Smith, S. J. (2010b). Array Tomography: Production of Arrays. Cold Spring Harbor Protocols *2010*, pdb.prot5524.

Micheva, K. D. and Smith, S. J. (2007). Array tomography. Neuron *55*, 25–36.

Moor, H. (1987). Theory and Practice of High Pressure Freezing. In Cryotechniques in Biological Electron Microscopy, (Steinbrecht, R. A. and Zierold, K., eds), pp. 175–191. Springer Berlin Heidelberg Berlin, Heidelberg.

Mori, I. (1999). Genetics of Chemotaxis and Thermotaxis in the Nematode *Caenorhabditis elegans*. Annual Review of Genetics *33*, 399–422.

Morrison, L. M., Edwards, S. L., Manning, L., Stec, N., Richmond, J. E. and Miller, K. G. (2018). Sentryn and SAD Kinase Link the Guided Transport and Capture of Dense Core Vesicles in *Caenorhabditis elegans*. Genetics *210*, 925–946.

Murakami, T., Qamar, S., Lin, J. Q., Schierle, G. S. K., Rees, E., Miyashita, A., Costa, A. R., Dodd, R. B., Chan, F. T. S., Michel, C. H., Kronenberg-Versteeg, D., Li, Y., Yang, S.-P., Wakutani, Y., Meadows, W., Ferry, R. R., Dong, L., Tartaglia, G. G., Favrin, G., Lin, W.-L., Dickson, D. W., Zhen, M., Ron, D., Schmitt-Ulms, G., Fraser, P. E., Shneider, N. A., Holt, C., Vendruscolo, M., Kaminski, C. F. and St George-Hyslop, P. (2015). ALS/FTD Mutation-Induced Phase Transition of FUS Liquid Droplets and Reversible Hydrogels into Irreversible Hydrogels Impairs RNP Granule Function. Neuron *88*, 678–690.

Murakami, T., Yang, S.-P., Xie, L., Kawano, T., Fu, D., Mukai, A., Bohm, C., Chen, F., Robertson, J., Suzuki, H., Tartaglia, G. G., Vendruscolo, M., Schierle, K., S, G., Chan, F. T. S., Moloney, A., Crowther, D., Kaminski, C. F., Zhen, M. and St George-Hyslop, P. (2012). ALS mutations in FUS cause neuronal dysfunction and death in Caenorhabditis elegans by a dominant gain-of-function mechanism. Human Molecular Genetics *21*, 1–9.

Narayan, K. and Subramaniam, S. (2015). Focused ion beams in biology. Nature Methods *12*, 1021–1031.

Nisman, R., Dellaire, G., Ren, Y., Li, R. and Bazett-Jones, D. P. (2004). Application of Quantum Dots as Probes for Correlative Fluorescence, Conventional, and Energy-filtered Transmission Electron Microscopy. Journal of Histochemistry & Cytochemistry *52*, 13–18.

Njus, D., Kelley, P. M. and Harnadek, G. J. (1986). Bioenergetics of secretory vesicles. Biochimica et Biophysica Acta (BBA) - Reviews on Bioenergetics *853*, 237–265.

O'Hagan, R. and Chalfie, M. (2005). Mechanosensation in *Caenorhabditis elegans*. In International Review of Neurobiology vol. 69, of The Neurobiology of C. elegans pp. 169–203. Academic Press.

Ojeda, J. L., Ros, M. A. and Icardo, J. M. (1989). A technique for fluorescence microscopy in semithin sections. Stain Technology *64*, 243–248.

Oleskevich, S., Alvarez, F. J. and Walmsley, B. (1999). Glycinergic Miniature Synaptic Currents and Receptor Cluster Sizes Differ Between Spinal Cord Interneurons. Journal of Neurophysiology *82*, 312–319.

Patel, M. R., Lehrman, E. K., Poon, V. Y., Crump, J. G., Zhen, M., Bargmann, C. I. and Shen, K. (2006). Hierarchical assembly of presynaptic components in defined *C. elegans* synapses. Nature Neuroscience *9*, 1488.

Paul-Gilloteaux, P., Heiligenstein, X., Belle, M., Domart, M.-C., Larijani, B., Collinson, L., Raposo, G. and Salamero, J. (2017). eC-CLEM: flexible multidimensional registration software for correlative microscopies. Nature Methods *14*, 102–103.

Peddie, C. J. and Collinson, L. M. (2014). Exploring the third dimension: Volume electron microscopy comes of age. Micron *61*, 9–19.

Pekar, T. (2013). The Role of SAD-1 Kinase in Caenorhabditis elegans Neuronal Circuit Development and Function. PhD thesis, University of Toronto.

Pham-Gia, T. and Hung, T. L. (2001). The mean and median absolute deviations. Mathematical and Computer Modelling *34*, 921–936.

Phelan, P., Bacon, J. P., Davies, J. A., Stebbings, L. A., Todman, M. G., Avery, L., Baines, R. A., Barnes, T. M., Ford, C., Hekimi, S., Lee, R., Shaw, J. E., Starich, T. A., Curtin, K. D., Sun, Y.-A. and Wyman, R. J. (1998). Innexins: a family of invertebrate gap-junction proteins. Trends in genetics : TIG *14*, 348–349.

Posner, R., Toker, I. A., Antonova, O., Star, E., Anava, S., Azmon, E., Hendricks, M., Bracha, S., Gingold, H. and Rechavi, O. (2019). Neuronal Small RNAs Control Behavior Transgenerationally. Cell *0*.

R Core Team (2019). R: A Language and Environment for Statistical Computing. R Foundation for Statistical Computing Vienna, Austria.

Ragsdale, E. J., Ngo, P. T., Crum, J., Ellisman, M. H. and Baldwin, J. G. (2009). Comparative, three-dimensional anterior sensory reconstruction of *Aphelenchus avenae* (nematoda: Tylenchomorpha). Journal of Comparative Neurology *517*, 616–632.

Ramirez-Suarez, N. J., Belalcazar, H. M., Salazar, C. J., Beyaz, B., Raja, B., Nguyen, K. C. Q., Celestrin, K., Fredens, J., Færgeman, N. J., Hall, D. H. and Bülow, H. E. (2019). Axon-Dependent Patterning and Maintenance of Somatosensory Dendritic Arbors. Developmental Cell *48*, 229–244.e4.

Rand, J. B. (2007). Acetylcholine. WormBook: The Online Review of *C. elegans* Biology *1*, 1–21.

Ratti, A. and Buratti, E. (2016). Physiological functions and pathobiology of TDP-43 and FUS/TLS proteins. Journal of Neurochemistry *138*, 95–111.

Renden, R., Berwin, B., Davis, W., Ann, K., Chin, C.-T., Kreber, R., Ganetzky, B., Martin, T. F. J. and Broadie, K. (2001). *Drosophila* CAPS Is an Essential Gene that Regulates Dense-Core Vesicle Release and Synaptic Vesicle Fusion. Neuron *31*, 421–437.

Reynolds, E. S. (1963). The use of lead citrate at high pH as an electron-opaque stain in electron microscopy. The Journal of Cell Biology *17*, 208–212.

Richard, M., Boulin, T., Robert, V. J. P., Richmond, J. E. and Bessereau, J.-L. (2013). Biosynthesis of ionotropic acetylcholine receptors requires the evolutionarily conserved ER membrane complex. Proceedings of the National Academy of Sciences *110*, E1055–E1063.

Richmond, J. E. and Broadie, K. S. (2002). The synaptic vesicle cycle: exocytosis and endocytosis in *Drosophila* and *C. elegans*. Current Opinion in Neurobiology *12*, 499–507.

Rostaing, P., Real, E., Siksou, L., Lechaire, J.-P., Boudier, T., Boeckers, T. M., Gertler, F., Gundelfinger, E. D., Triller, A. and Marty, S. (2006). Analysis of synaptic ultrastructure without fixative using high-pressure freezing and tomography. European Journal of Neuroscience *24*, 3463–3474.

Rostaing, P., Weimer, R. M., Jorgensen, E. M., Triller, A. and Bessereau, J.-L. (2004). Preservation of Immunoreactivity and Fine Structure of Adult *C. elegans* Tissues Using High-pressure Freezing. Journal of Histochemistry & Cytochemistry *52*, 1–12.

Ruiz, R., Casañas, J. J., Torres-Benito, L., Cano, R. and Tabares, L. (2010). Altered Intracellular Ca^{2+} Homeostasis in Nerve Terminals of Severe Spinal Muscular Atrophy Mice. Journal of Neuroscience *30*, 849–857.

Russell, S. J. and Kahn, C. R. (2007). Endocrine regulation of ageing. Nature Reviews Molecular Cell Biology *8*, 681–691.

Salio, C., Lossi, L., Ferrini, F. and Merighi, A. (2006). Neuropeptides as synaptic transmitters. Cell and Tissue Research *326*, 583–598.

Sawin, E. R., Ranganathan, R. and Horvitz, H. R. (2000). *C. elegans* Locomotory Rate Is Modulated by the Environment through a Dopaminergic Pathway and by Experience through a Serotonergic Pathway. Neuron *26*, 619–631.

Schafer, W. R. (2018). The Worm Connectome: Back to the Future. Trends in Neurosciences *41*, 763–765.

Schalek, R., Kasthuri, N., Hayworth, K., Berger, D., Tapia, J., Morgan, J., Turaga, S., Fagerholm, E., Seung, H. and Lichtman, J. (2011). Development of High-Throughput, High-Resolution 3D Reconstruction of Large-Volume Biological Tissue Using Automated Tape Collection Ultramicrotomy and Scanning Electron Microscopy. Microscopy and Microanalysis *17*, 966–967.

Schieber, N. L., Machado, P., Markert, S. M., Stigloher, C., Schwab, Y. and Steyer, A. M. (2017). Minimal resin embedding of multicellular specimens for targeted FIB-SEM imaging. In Methods in Cell Biology, (Müller-Reichert, T. and Verkade, P., eds), vol. 140, of Correlative Light and Electron Microscopy III pp. 69–83. Academic Press.

Schindelin, J., Arganda-Carreras, I., Frise, E., Kaynig, V., Longair, M., Pietzsch, T., Preibisch, S., Rueden, C., Saalfeld, S., Schmid, B., Tinevez, J.-Y., White, D. J., Hartenstein, V., Eliceiri, K., Tomancak, P. and Cardona, A. (2012). Fiji: an open-source platform for biological-image analysis. Nature Methods *9*, 676–682.

Schmitt, A., Hasan, A., Gruber, O. and Falkai, P. (2011). Schizophrenia as a disorder of disconnectivity. European Archives of Psychiatry and Clinical Neuroscience *261*, 150.

Schorb, M., Haberbosch, I., Hagen, W. J. H., Schwab, Y. and Mastronarde, D. N. (2019). Software tools for automated transmission electron microscopy. Nature Methods *16*, 471.

Schwarz, H. and Humbel, B. (2014). Correlative Light and Electron Microscopy Using Immunolabeled Sections. In Electron Microscopy, (Kuo, J., ed.), number 1117 in Methods in Molecular Biology pp. 559–592. Humana Press.

Sendtner, M. (2011). TDP-43: multiple targets, multiple disease mechanisms? Nature Neuroscience *14*, 403–405.

Simonsen, K. T., Moerman, D. G. and Naus, C. C. (2014). Gap junctions in *C. elegans*. Frontiers in Physiology *5*.

Singh, S., Singh, B. and Singh, A. P. (2015). Nematodes: A Threat to Sustainability of Agriculture. Procedia Environmental Sciences *29*, 215–216.

Smith, S. J. (2018). Q&A: Array tomography. BMC Biology *16*, 98.

Söhl, G., Maxeiner, S. and Willecke, K. (2005). Expression and functions of neuronal gap junctions. Nature Reviews Neuroscience *6*, 191–200.

Söhl, G. and Willecke, K. (2004). Gap junctions and the connexin protein family. Cardiovascular Research *62*, 228–232.

Souquere, S., Mollet, S., Kress, M., Dautry, F., Pierron, G. and Weil, D. (2009). Unravelling the ultrastructure of stress granules and associated P-bodies in human cells. Journal of Cell Science *122*, 3619–3626.

Speese, S., Petrie, M., Schuske, K., Ailion, M., Ann, K., Iwasaki, K., Jorgensen, E. M. and Martin, T. F. J. (2007). UNC-31 (CAPS) Is Required for Dense-Core Vesicle But Not Synaptic Vesicle Exocytosis in *Caenorhabditis elegans*. Journal of Neuroscience *27*, 6150–6162.

Sporns, O., Tononi, G. and Kötter, R. (2005). The Human Connectome: A Structural Description of the Human Brain. PLoS Computational Biology *1*.

Starich, T. A., Xu, J., Skerrett, I. M., Nicholson, B. J. and Shaw, J. E. (2009). Interactions between innexins UNC-7 and UNC-9 mediate electrical synapse specificity in the *Caenorhabditis elegans* locomotory nervous system. Neural Development *4*, 16.

Stierhof, Y. D. and Schwarz, H. (1989). Labeling properties of sucrose-infiltrated cryosections. Scanning microscopy. Supplement *3*, 35–46.

Stierhof, Y.-D., Schwarz, H., Villiger, W. and Kellenberger, E. (1991). Yield of immunolabel compared to resin sections and thawed cryosections. Colloidal gold: principles, methods, and applications *3*, 87–115.

Stiernagle, T. (2006). Maintenance of *C. elegans*. WormBook: The Online Review of *C. elegans* Biology , 1–11.

Stigloher, C., Zhan, H., Zhen, M., Richmond, J. and Bessereau, J.-L. (2011). The presynaptic dense projection of the Caenorhabiditis elegans cholinergic neuromuscular junction localizes synaptic vesicles at the active zone through SYD-2/liprin and UNC-10/RIM-dependent interactions. The Journal of neuroscience *31*, 4388–4396.

Stretton, A. O. (1976). Anatomy and development of the somatic musculature of the nematode *Ascaris*. Journal of Experimental Biology *64*, 773–788.

Südhof, T. C. (2004). The Synaptic Vesicle Cycle. Annual Review of Neuroscience *27*, 509–547.

Südhof, T. C. (2012). The Presynaptic Active Zone. Neuron *75*, 11–25.

Südhof, T. C. (2013). Neurotransmitter Release: The Last Millisecond in the Life of a Synaptic Vesicle. Neuron *80*, 675–690.

Sulston, J. E. and Horvitz, H. R. (1977). Post-embryonic cell lineages of the nematode, *Caenorhabditis elegans*. Developmental Biology *56*, 110–156.

Suzuki, T., Fujikura, K., Higashiyama, T. and Takata, K. (1997). DNA Staining for Fluorescence and Laser Confocal Microscopy. Journal of Histochemistry & Cytochemistry *45*, 49–53.

Takamori, S., Holt, M., Stenius, K., Lemke, E. A., Grønborg, M., Riedel, D., Urlaub, H., Schenck, S., Brügger, B., Ringler, P., Müller, S. A., Rammner, B., Gräter, F., Hub, J. S., De Groot, B. L., Mieskes, G., Moriyama, Y., Klingauf, J., Grubmüller, H., Heuser, J., Wieland, F. and Jahn, R. (2006). Molecular Anatomy of a Trafficking Organelle. Cell *127*, 831–846.

Taylor, M. J., Hoerauf, A. and Bockarie, M. (2010). Lymphatic filariasis and onchocerciasis. The Lancet *376*, 1175–1185.

Titze, B. and Genoud, C. (2016). Volume scanning electron microscopy for imaging biological ultrastructure. Biology of the Cell *108*, 307–323.

Tobin, D. M. and Bargmann, C. I. (2004). Invertebrate nociception: Behaviors, neurons and molecules. Journal of Neurobiology *61*, 161–174.

van de Linde, S., Löschberger, A., Klein, T., Heidbreder, M., Wolter, S., Heilemann, M. and Sauer, M. (2011). Direct stochastic optical reconstruction microscopy with standard fluorescent probes. Nature Protocols *6*, 991–1009.

van Essen, D. C., Smith, S. M., Barch, D. M., Behrens, T. E. J., Yacoub, E. and Ugurbil, K. (2013). The WU-Minn Human Connectome Project: An overview. NeuroImage *80*, 62–79.

Vance, C., Rogelj, B., Hortobágyi, T., Vos, K. J. D., Nishimura, A. L., Sreedharan, J., Hu, X., Smith, B., Ruddy, D., Wright, P., Ganesalingam, J., Williams, K. L., Tripathi, V., Al-Saraj, S., Al-Chalabi, A., Leigh, P. N., Blair, I. P., Nicholson, G., Belleroche, J. d., Gallo, J.-M., Miller, C. C. and Shaw, C. E. (2009). Mutations in

FUS, an RNA Processing Protein, Cause Familial Amyotrophic Lateral Sclerosis Type 6. Science *323*, 1208–1211.

Varshney, L. R., Chen, B. L., Paniagua, E., Hall, D. H. and Chklovskii, D. B. (2011). Structural Properties of the *Caenorhabditis elegans* Neuronal Network. PLOS Computational Biology *7*, e1001066.

Venter, J. C., Adams, M. D., Myers, E. W., Li, P. W., Mural, R. J., Sutton, G. G., Smith, H. O., Yandell, M., Evans, C. A., Holt, R. A., Gocayne, J. D., Amanatides, P., Ballew, R. M., Huson, D. H., Wortman, J. R., Zhang, Q., Kodira, C. D., Zheng, X. H., Chen, L., Skupski, M., Subramanian, G., Thomas, P. D., Zhang, J., Miklos, G. L. G., Nelson, C., Broder, S., Clark, A. G., Nadeau, J., McKusick, V. A., Zinder, N., Levine, A. J., Roberts, R. J., Simon, M., Slayman, C., Hunkapiller, M., Bolanos, R., Delcher, A., Dew, I., Fasulo, D., Flanigan, M., Florea, L., Halpern, A., Hannenhalli, S., Kravitz, S., Levy, S., Mobarry, C., Reinert, K., Remington, K., Abu-Threideh, J., Beasley, E., Biddick, K., Bonazzi, V., Brandon, R., Cargill, M., Chandramouliswaran, I., Charlab, R., Chaturvedi, K., Deng, Z., Francesco, V. D., Dunn, P., Eilbeck, K., Evangelista, C., Gabrielian, A. E., Gan, W., Ge, W., Gong, F., Gu, Z., Guan, P., Heiman, T. J., Higgins, M. E., Ji, R.-R., Ke, Z., Ketchum, K. A., Lai, Z., Lei, Y., Li, Z., Li, J., Liang, Y., Lin, X., Lu, F., Merkulov, G. V., Milshina, N., Moore, H. M., Naik, A. K., Narayan, V. A., Neelam, B., Nusskern, D., Rusch, D. B., Salzberg, S., Shao, W., Shue, B., Sun, J., Wang, Z. Y., Wang, A., Wang, X., Wang, J., Wei, M.-H., Wides, R., Xiao, C., Yan, C., Yao, A., Ye, J., Zhan, M., Zhang, W., Zhang, H., Zhao, Q., Zheng, L., Zhong, F., Zhong, W., Zhu, S. C., Zhao, S., Gilbert, D., Haynes, C., Heiner, C., Hladun, S., Hostin, D., Houck, J., Howland, T., Ibegwam, C., Johnson, J., Kalush, F., Kline, L., Koduru, S., Love, A., Mann, F., May, D., McCawley, S., McIntosh, T., McMullen, I., Moy, M., Moy, L., Murphy, B., Nelson, K., Pfannkoch, C., Pratts, E., Puri, V., Qureshi, H., Reardon, M., Rodriguez, R., Rogers, Y.-H., Romblad, D., Ruhfel, B., Scott, R., Sitter, C., Smallwood, M., Stewart, E., Strong, R., Suh, E., Thomas, R., Tint, N. N., Tse, S., Vech, C., Wang, G., Wetter, J., Williams, S., Williams, M., Windsor, S., Winn-Deen, E., Wolfe, K., Zaveri, J., Zaveri, K., Abril, J. F., Guigó, R., Campbell, M. J., Sjolander, K. V., Karlak, B., Kejariwal, A., Mi, H., Lazareva, B., Hatton, T., Narechania, A., Diemer, K., Muruganujan, A., Guo, N., Sato, S., Bafna, V., Istrail, S., Lippert, R., Schwartz, R., Walenz, B., Yooseph, S., Allen, D., Basu, A., Baxendale, J., Blick, L., Caminha, M., Carnes-Stine, J., Caulk, P., Chiang, Y.-H., Coyne, M., Dahlke, C., Mays, A. D., Dombroski, M., Donnelly, M., Ely, D., Esparham, S., Fosler, C., Gire, H., Glanowski, S., Glasser, K., Glodek, A., Gorokhov, M., Graham, K., Gropman, B., Harris, M., Heil, J., Henderson, S., Hoover, J., Jennings, D., Jordan, C., Jordan, J., Kasha, J., Kagan, L., Kraft, C., Levitsky, A., Lewis, M., Liu, X., Lopez, J., Ma, D., Majoros, W., McDaniel, J., Murphy, S., Newman, M., Nguyen, T., Nguyen, N., Nodell, M., Pan, S., Peck, J., Peterson, M., Rowe, W., Sanders, R., Scott, J., Simpson, M., Smith, T., Sprague, A., Stockwell, T., Turner, R., Venter, E., Wang, M., Wen,

M., Wu, D., Wu, M., Xia, A., Zandieh, A. and Zhu, X. (2001). The Sequence of the Human Genome. Science *291*, 1304–1351.

Vidal, B., Aghayeva, U., Sun, H., Wang, C., Glenwinkel, L., Bayer, E. A. and Hobert, O. (2018). An atlas of *Caenorhabditis elegans* chemoreceptor expression. PLOS Biology *16*, e2004218.

Vidal-Gadea, A., Ward, K., Beron, C., Ghorashian, N., Gokce, S., Russell, J., Truong, N., Parikh, A., Gadea, O., Ben-Yakar, A. and Pierce-Shimomura, J. (2015). Magnetosensitive neurons mediate geomagnetic orientation in *Caenorhabditis elegans*. eLife *4*, e07493.

Waller, P. J. (1997). Nematode parasite control of livestock in the tropics/subtropics: the need for novel approaches. International Journal for Parasitology *27*, 1193–1201.

Wang, W.-Y., Pan, L., Su, S. C., Quinn, E. J., Sasaki, M., Jimenez, J. C., Mackenzie, I. R. A., Huang, E. J. and Tsai, L.-H. (2013). Interaction of FUS and HDAC1 regulates DNA damage response and repair in neurons. Nature Neuroscience *16*, 1383–1391.

Watanabe, S., Liu, Q., Davis, M. W., Hollopeter, G., Thomas, N., Jorgensen, N. B. and Jorgensen, E. M. (2013a). Ultrafast endocytosis at *Caenorhabditis elegans* neuromuscular junctions. eLife *2013*, e00723.

Watanabe, S., Rost, B. R., Camacho-Pérez, M., Davis, M. W., Söhl-Kielczynski, B., Rosenmund, C. and Jorgensen, E. M. (2013b). Ultrafast endocytosis at mouse hippocampal synapses. Nature *504*, 242–247.

Watanabe, S., Trimbuch, T., Camacho-Pérez, M., Rost, B. R., Brokowski, B., Söhl-Kielczynski, B., Felies, A., Davis, M. W., Rosenmund, C. and Jorgensen, E. M. (2014). Clathrin regenerates synaptic vesicles from endosomes. Nature *515*, 228–233.

Weimer, R. (2006). Preservation of *C. elegans* Tissue Via High-Pressure Freezing and Freeze-Substitution for Ultrastructural Analysis and Immunocytochemistry. In C. elegans, (Strange, K., ed.), number 351 in Methods in Molecular Biology pp. 203–221. Humana Press.

Weimer, R. M., Richmond, J. E., Davis, W. S., Hadwiger, G., Nonet, M. L. and Jorgensen, E. M. (2003). Defects in synaptic vesicle docking in *unc-18* mutants. Nature Neuroscience *6*, 1023.

Westheide, W. and Rieger, G., eds (2013). Spezielle Zoologie. Teil 1: Einzeller und Wirbellose Tiere. 3 edition, Springer Spektrum.

White, J. G., Southgate, E., Thomson, J. N. and Brenner, S. (1976). The structure of the ventral nerve cord of *Caenorhabditis elegans*. Philosophical Transactions of the Royal Society of London. B, Biological Sciences *275*, 327–348.

White, J. G., Southgate, E., Thomson, J. N. and Brenner, S. (1986). The Structure of the Nervous System of the Nematode *Caenorhabditis elegans*. Philosophical Transactions of the Royal Society of London B: Biological Sciences *314*, 1–340.

Wiese, S., Herrmann, T., Drepper, C., Jablonka, S., Funk, N., Klausmeyer, A., Rogers, M.-L., Rush, R. and Sendtner, M. (2010). Isolation and enrichment of embryonic mouse motoneurons from the lumbar spinal cord of individual mouse embryos. Nature Protocols *5*, 31–38.

Witte, H., Neukirchen, D. and Bradke, F. (2008). Microtubule stabilization specifies initial neuronal polarization. The Journal of Cell Biology *180*, 619–632.

Wolstenholme, A. J. and Rogers, A. T. (2005). Glutamate-gated chloride channels and the mode of action of the avermectin/milbemycin anthelmintics. Parasitology *131*, S85–S95.

Won, H., Mah, W. and Kim, E. (2013). Autism spectrum disorder causes, mechanisms, and treatments: focus on neuronal synapses. Frontiers in Molecular Neuroscience *6*.

Wright, K. A. (1979). *Trichinella spiralis*: An Intracellular Parasite in the Intestinal Phase. The Journal of Parasitology *65*, 441–445.

Yan, D., Wu, Z., Chisholm, A. D. and Jin, Y. (2009). The DLK-1 Kinase Promotes mRNA Stability and Local Translation in *C. elegans* Synapses and Axon Regeneration. Cell *138*, 1005–1018.

Yeh, E., Kawano, T., Ng, S., Fetter, R., Hung, W., Wang, Y. and Zhen, M. (2009). *Caenorhabditis elegans* Innexins Regulate Active Zone Differentiation. The Journal of Neuroscience *29*, 5207–5217.

Yemini, E., Jucikas, T., Grundy, L. J., Brown, A. E. X. and Schafer, W. R. (2013). A database of *Caenorhabditis elegans* behavioral phenotypes. Nature Methods *10*, 877–879.

Zhang, Z.-Q. (2013). Animal biodiversity: An update of classification and diversity in 2013. In : Zhang, Z.-Q. (Ed.) Animal Biodiversity: An Outline of Higher-level Classification and Survey of Taxonomic Richness (Addenda 2013). Zootaxa *3703*, 5–11.

Zhu, H., Li, J., Nolan, T. J., Schad, G. A. and Lok, J. B. (2011). Sensory neuroanatomy of *Parastrongyloides trichosuri*, a nematode parasite of mammals: Amphidial neurons of the first-stage larva. Journal of Comparative Neurology *519*, 2493–2507.

A. Appendix

A.1. List of contents on the supplemental DVD

The supplemental DVD contains the following:

1. A PDF file of this thesis with all figures in very high resolution
2. A PDF file of this thesis with all figures in normal resolution
3. Quantification raw data as excel files
4. The R scripts that have been used for quantification and plotting of data

A.2. Supplemental figures

Figure A.1 expands on Figure 3.30 by including the fluorescence channels acquired by SIM separately. Figure A.2 similarly expands on Figure 3.31 by including the aligned SIM channels separately.

Figure A.3 offers a detailed view of Figure 3.33C'.

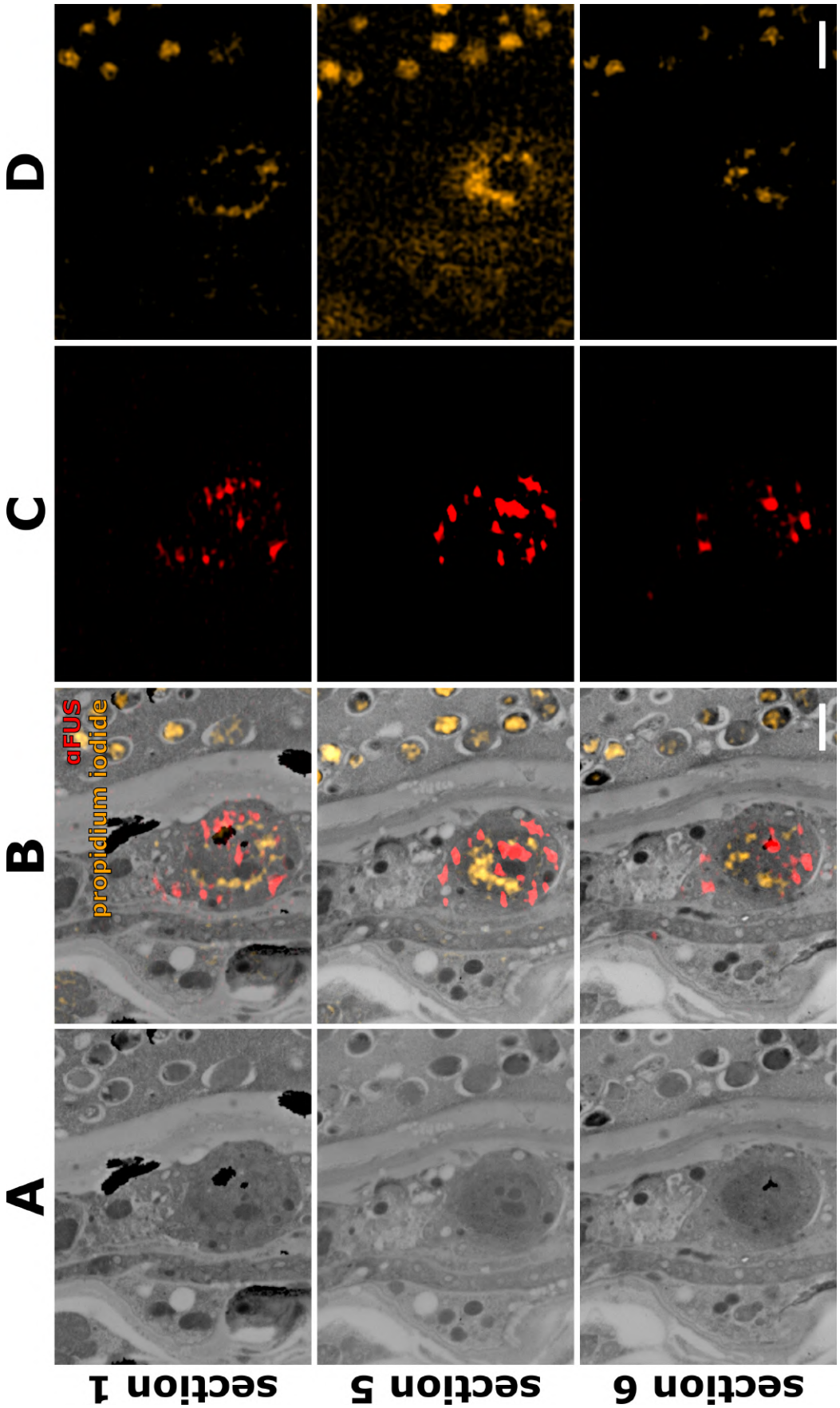

Figure A.1.: **Supplemental Figure related to Figure 3.30.** SIM channels are shown separately.

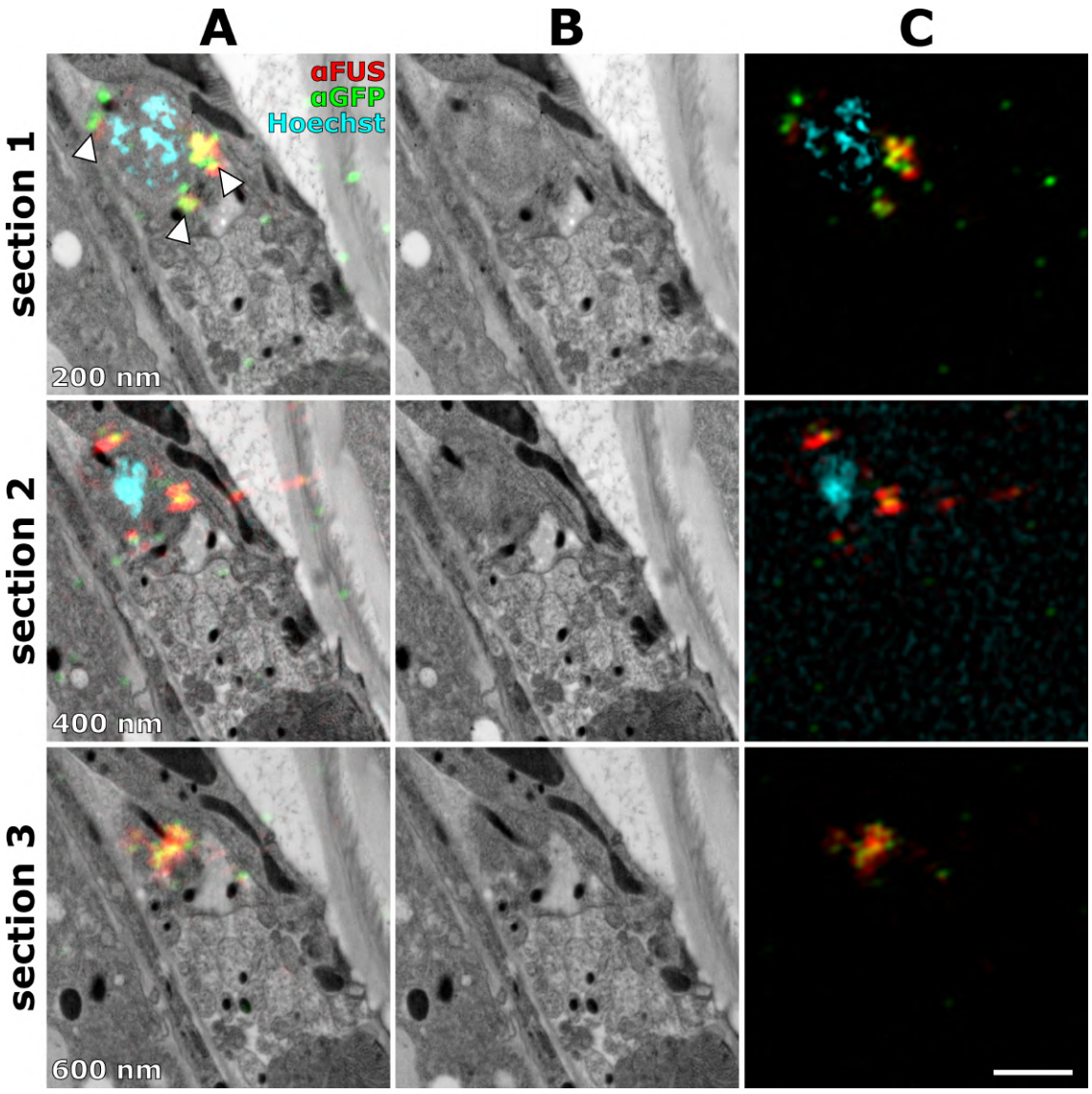

Figure A.2.: **Supplemental Figure related to Figure 3.31.** Aligned SIM channels are shown separately.

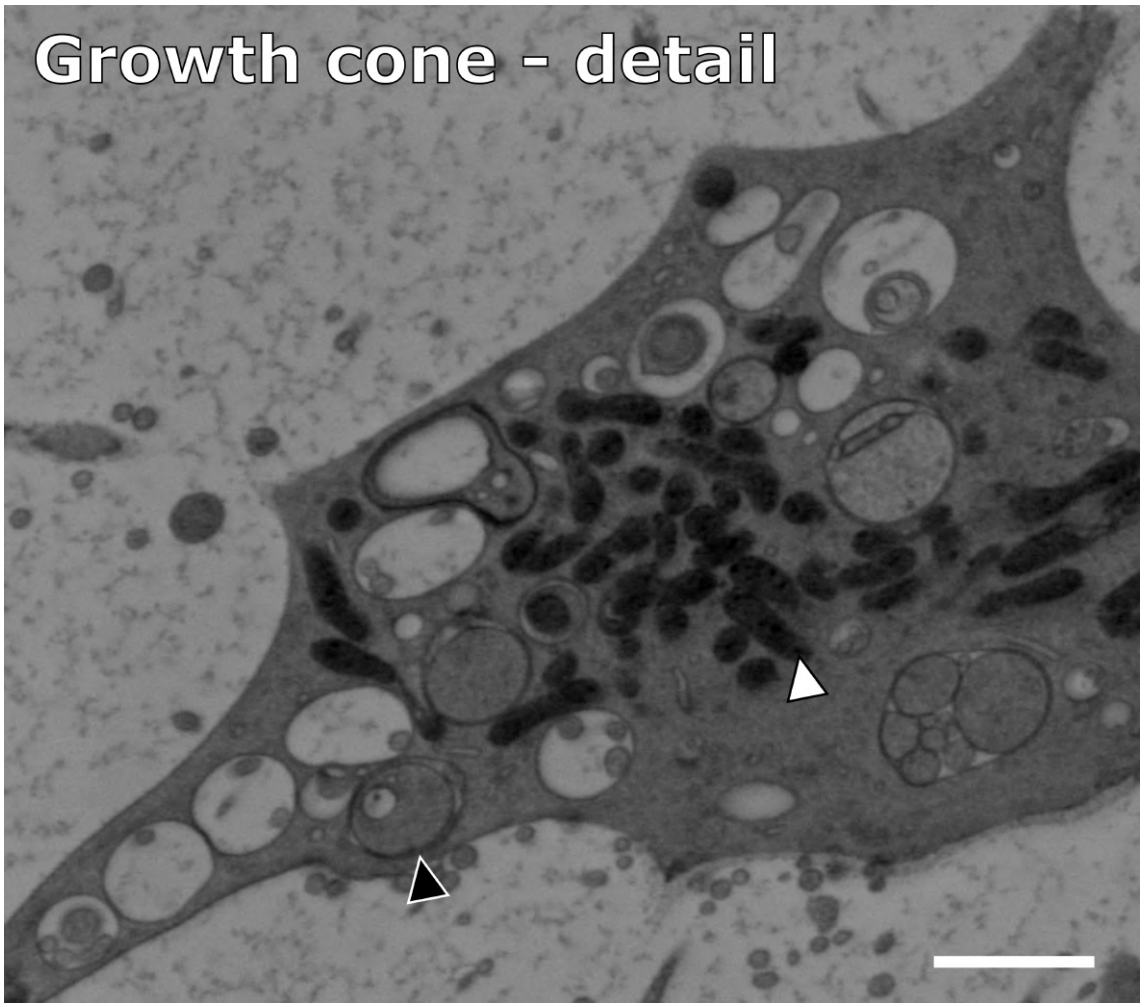

Figure A.3.: **Supplemental Figure related to Figure 3.33.** Higher magnification view of Figure 3.33C'. Black arrowhead points to an autophagosome. Double membrane is readily visible. White arrowhead points to mitochondria. Scale bar: 1 µm.

A.3. "Best practice" for acquisition of tilt series with serial EM

In the course of the thesis work, different settings and approaches for imaging with the serial EM software on the JEM-2100 TEM (JEOL) were used. In the end, a best practice approach was reached that is time efficient without compromising quality. It is described in the following.

I used the live acquisition mode of the EMmenu camera software and chose a region of interest and determined the desired magnification. The defocus was neutralized pressing the "standard focus" button. Focus was adjusted by wobbling without changing the defocus value but by moving the goniometer up or down. I adjusted the beam such that the camera had at least 10,000 counts per second of acquisition. Then, serialEM was started. I adjusted the values for the acquisition modes. For "Record" I set binning to two, the exposure time to one second, and the drift to at least one second. If the image was blurry due to shift, I increased that value until the shift was not visible anymore. For "Trial" and "Focus" I set binning to 4, the exposure time to 0.5 seconds and the shift to 0. This results in blurry images due to shift, but I came to realize that this does not affect tilt series quality at all. However, setting these values to 0 saves a lot of acquisition time. When this was set up, I started the tilt series in the software and usually used tilt angles from 60° to -60 °. The beam shift should be rather low, around 2 µm, to avoid detrimental misalignment of the beam during acquisition. This does not apply to low magnifications, however. If imaging at 8000× or lower, the beam shift should be set to about 10 µm. This usually ensures that the whole tilt series is executed without the need for resetting the beam shift at all, which results in a very smooth tilt series. At higher magnifications, though, the opposite was the case. Additionally, I skip refining the eucentricity. I never had a tilt series where this step was necessary. The defocus I just set to 0, independent of current focus. With this I usually get perfect auto-focusing at every angle. Finally, I started the tilt series. A tilt series at a magnification of 30,000× took about 45 min with these settings.

A.4. Structured illumination microcopy of FUS501 and FUSwt expression *in vivo*

Figure A.4 shows micrographs of FUS501 and FUSwt expression in living L3 larvae. They were imaged to confirm that they show the expected expression pattern. The results were consistent with the literature [Murakami et al. 2012, 2015] and thus I used these worm strains for experiments. FUWwt seemed restricted to the nuclei of neurons and FUS501 was distributed more diffusely, while also forming small, bright puncta which are presumably identical in nature with the aggregates I found with srAT (see Figures 3.29, 3.30, 3.31).

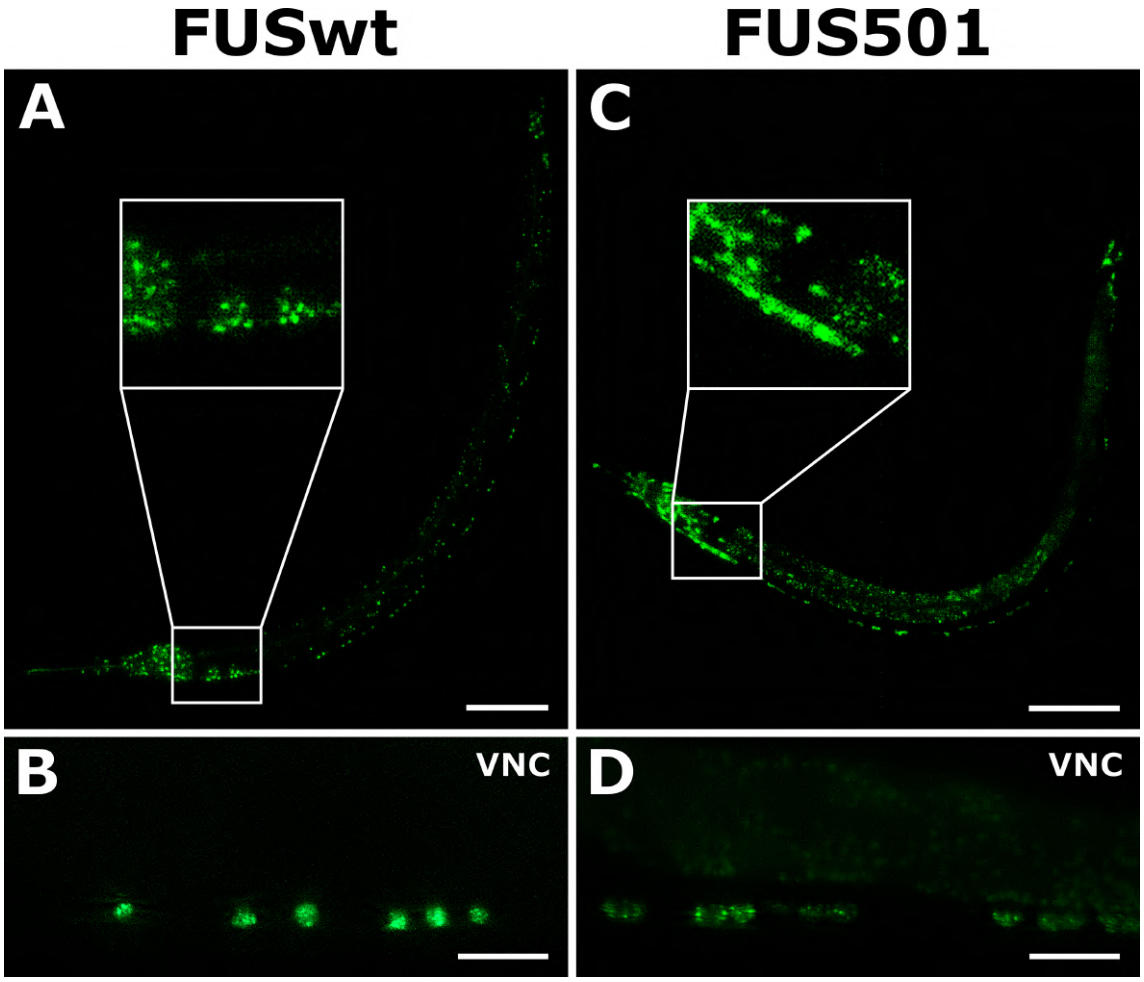

Figure A.4.: **Structured illumination micrographs of FUS501 and FUSwt expression in living worms.** FUS501 and FUSwt were imaged in living L3 larvae via their GFP-tags. Shown are maximum intensity projections of z-stacks. **A** Overview of FUSwt expression in the whole larva. Scale bar: 50 µm. **B** FUSwt expression in the ventral nerve cord (VNC). Scale bar: 10 µm. Note how FUSwt is located in distinct circular patterns, presumably within nuclei. **C** Overview of FUS501 expression in the whole larva. Scale bar: 50 µm. **D** FUS501 expression in the ventral nerve cord (VNC). Scale bar: 10 µm. Note how FUS501 is distributed more diffusely and forms small puncta, presumably aggregates.

A.5. Electrophysiological data of FUS501 worms and controls

Our collaborator Prof. Shangbang Gao[18] obtained electrophysiological data of FUS worms (Figure A.5). They show that mini excitatory synaptic currents recorded at the ventral nerve cord have a significantly reduced frequency in FUS501 worms compared to FUSwt and N2 worms. The amplitudes showed no significant differences. This points to a reduced probability of vesicle fusion in FUS501 worms.

[18]Key Laboratory of Molecular Biophysics of the Ministry of Education, College of Life Science and Technology, Huazhong University of Science and Technology, Wuhan, China

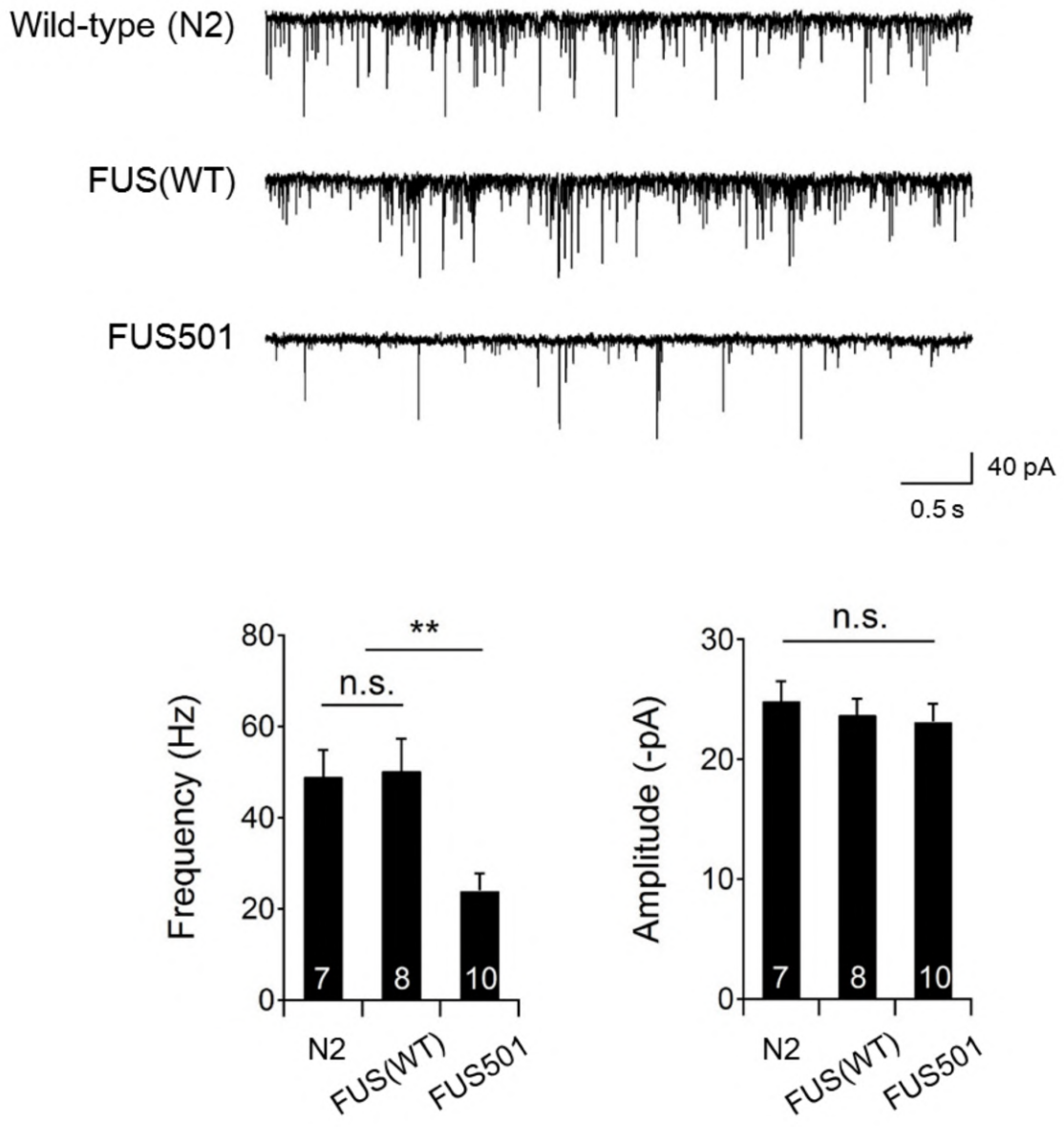

Figure A.5.: **Frequency of mini excitatory synaptic currents is reduced in FUS501 worms, but not amplitude.** Unpublished data of Shangbang Gao. Used with permission.

Acknowledgments

Sebastians Rezept für eine leckere Promotion

Für den Grundteig eine große Menge Würmer anziehen und unter Rühren frische Betreuung zugeben, bis eine geschmeidige Konsistenz erreicht ist. Würmer gibt es überall, aber bei der Betreuung auf gute Qualität achten. Sie sollte eine gute Mischung aus Mentorschaft, offenen Ohren und Freiräumen sein. Ich nehme immer nur die von Christian, das ist die beste, die ich finden konnte. Der Teig wird unter hohem Druck schockgefrostet und bei -90 °C inkubiert und nur schrittweise erwärmt. Den Teig dann in Harz einbetten und aushärten lassen. Mit einem extrem scharfen Messer in ultrafeine Scheiben schneiden.

Die ultrafeinen Scheiben, einen Sack Zeit, einen gehäuften Esslöffel Hirnschmalz und einen ordentlichen Schuss Durchhaltevermögen sorgfältig vermischen und an einem warmen Ort gehen lassen. Der Ort ist dabei entscheidend. Es sollte sehr gutes Arbeitsklima herrschen, damit die Promotion nicht sauer oder bitter wird. Ich empfehle die Zentrale Abteilung für Mikroskopie. Alle Menschen dort sind immer hilfsbereit und freundlich und halten zusammen. Dadurch wird die Promotion besonders locker. Ganz viel Lachen und Humor verleihen ihr zudem eine ausgezeichnete Saftigkeit. Eine Prise von Georgs Weisheit hier und da sorgt für eine feine Würze, die die Promotion nochmal deutlich aufwertet.

Glücklicherweise konnte ich als Backtriebmittel Studienstiftung auftreiben. Dadurch entfalten sich die Aromen ganz besonders gut, was eine enorme Bereicherung darstellt, und die Promotion geht schön auf, ohne wieder zusammenzufallen. Überdosierung ausgeschlossen.

Gebacken wird bei 200 kV Ohneluft im Rotationsverfahren oder bei 5 kV Oberhitze auf einem Array-Blech. Bei letzterem Verfahren kann man noch vorher großzügig mit Laserlicht bestreichen und alles in Uranylacetat und Bleicitrat marinieren. Vor dem Backen mit etwas Kohle ablöschen.

Für die feine süße Note die Promotion mit einer Glasur aus Freundschaft überziehen. Die besten Erfahrungen habe ich hier mit der von Nika gemacht. Es entsteht eine schöne, glänzende Schicht, die auch unter schwierigen Bedingungen nie verläuft.

Guten Appetit!

DIESES Kochbuch ist voll mit köstlichen Rezepten, natürlich fast alle mit Würmern. So ein Kochbuch zu schreiben war gar nicht so einfach und hat ganz schön lange gedauert. Aber am Ende ist es doch ganz gut geworden, finde ich, aber ich hatte ja auch viel Hilfe.

Zum Beispiel von **Philip**, der mir am Ende noch sehr dabei geholfen hat, die Maßangaben alle richtig zu berechnen und darzustellen. Außerdem hat er sich bereit erklärt, für mein Kochbuch eine wirklich ausführliche Rezension zu schreiben. Daher wird er auch einer der ersten sein, der ein Exemplar bekommt.

Christian, unser Küchenchef, schreibt auch eine Rezension und erhält ein Vorab-Exemplar. Aber er kennt das Buch sowieso schon ziemlich genau, denn er hat mir von allen am meisten geholfen, dass dieses Buch gut wird. Immer hatte er noch eine gute Idee parat, wie ich die Zutaten und Arbeitsabläufe noch besser beschreiben kann und er hat auch ein sachkundiges Auge auf die Produktfotos geworfen, ob sie denn auch appetitanregend sind.

Ohne ihn gäbe es dieses Buch sowieso nicht. Er hat mich gefördert und immer an mich geglaubt und mir das Schreiben dieses Buches anvertraut. Und er hat mich damals den Würmern vorgestellt. Ein Schicksalhafte Begegnung. Christian hat aus einem Küchenjungen einen Koch gemacht. Ohne ein einziges strenges Wort. Das soll ihm mal einer nachmachen.

Ich hatte auch viel Hilfe von **Georg**. Er war immer da und hat bereitwillig geholfen, wo er nur konnte. Selbst schon seit vielen Jahren in der Branche, macht ihm so schnell keiner was vor in Sachen Flambieren, Marinieren, Gratinieren oder Vögel-Inspizieren. Dieses Buch hatte er in seiner Rohfassung gelesen und mir wertvolles Feedback gegeben.

Extrem wertvoll war auch die Hilfe von **Andy** und **Rashi**. Sie haben beide schon einmal so ein Kochbuch geschrieben und konnten mir daher gute Ratschläge und Ermutigungen geben. Außerdem haben sie mein Buch gelesen und trotz der knappen Zeit sehr sorgfältig auf den Fachjargon überprüft, denn sie haben den beide sozusagen nativ mit der Muttermilch aufgesogen und wissen genau, wie man in der Branche gut formuliert. Beide haben so viel Mühe in dieses Buch investiert, dass ich ein schlechtes Gewissen habe. Ich muss mir überlegen, wie ich wieder etwas zurückgeben kann.

Ohne **Nika** wäre dieses Buch wohl auch ganz anders geworden. Nicht nur hat sie dafür gesorgt, dass ich beim Schreiben nicht verdurste/verhungere/durchdrehe, sie hat auch tatkräftig und fleißig mitgeholfen. Manchmal muss man eben die Erbsen einzeln abwiegen und das hätte mich viel Zeit gekostet, wenn Nika das nicht gemacht hätte. Und man konnte mit ihr wirklich über alles reden. Egal ob über Religion oder Politik oder so heikle Themen wie das Verschütten von Kürbissuppe beim Trampolinspringen, es war immer lustiger, wenn sie in der Nähe war.

Es war schwer, sich bei so vielen unterschiedlichen und komplexen Rezepten den nötigen Sachverstand anzueignen. Glücklicherweise hatte ich auch hier viel Hilfe. **Daniel Witvliet** ist in manchen Wurm-Zubereitungsarten viel erfahrener als ich und hat mir immer gerne und schnell geholfen, wenn ich eine Frage hatte. **Mei Zhen** hat mir nicht nur mit gutem Rat geholfen, sie hat mir auch erlaubt, ein paar ihrer besten Rezepte für dieses Buch zu adaptieren und aufzunehmen. Und ihre Würmer für besonders leckere Gerichte hat sie mir auch immer geschickt.

Bei ein paar Rezepten habe ich mich aus dem Fenster gelehnt, denn sie enthielten gar keine Würmer! Gut, dass **Mehri** und **Heinz** mir hier helfen konnten, sie trotzdem gut zu beschreiben. Heinz hat mir außerdem sehr damit geholfen, vergrabene Schätze an Rezepten in ganz alten Kochbüchern aufzutreiben und hat dafür sogar seine Schreibtischschublade ausgeleert. Man muss nicht immer den Brei neu erfinden, oft stehen in alten Kochbüchern die besten Tricks!

Für ein Kapitel meines Kochbuchs mit speziellen Würmern mit Sahne-Apfelsine-Dattelsoße (SAD) war auch die Hilfe von **Wesley Hung** sehr wertvoll. Wesley hatte derlei Würmer schon vor Jahren so in der Art zubereitet und konnte mir daher viele Tipps und Tricks verraten. Viele davon findet man noch gar nicht in Kochbüchern, es waren echte Geheimtipps.

Ein Kapitel war besonders ambitioniert, da wollte ich Fenchel-Urgetreide-Suppe (FUS) zubereiten. Gut, dass ich dieses Kapitel nicht alleine ausarbeiten musste. **Michael** hat hier mit mir zusammen daran gearbeitet. So konnten wir neben der Variante der Suppe mit Würmern auch eine ohne Würmer (für Allergiker) kreieren. Deren Gelingen ist praktisch ausschließlich Michaels Verdienst. Auch sonst hat er sich richtig ins Zeug gelegt für unsere Rezepte und unermüdlich Geschmackstests durchgeführt, um die verschiedenen Nuancen herauszuarbeiten. Dafür saß er oft viele Stunden vor einem Ofen fest, entweder dem Ohneluft Rotationsgarer oder dem Array-Grill. Es hat immer viel Spaß gemacht, mit ihm zusammenzuarbeiten und er hat auch immer sofort geholfen, wenn er irgendwie konnte. Ich bin auch sehr froh, dass **Professor Sendtner** und **Mei** dieses, wie gesagt doch etwas ambitionierte, Vorhaben unterstützt und auch wertvolle Kommentare zum Kochbuch beigesteuert haben.

Ein paar **Sebastians** müssen natürlich auch noch erwähnt werden. So hat der Britz-Sebastian mir beim Schreiben gern ein bisschen den Rücken freigehalten und seine Hilfe bei allem immer bereitwillig angeboten. Für das Kochbuch war seine Mitarbeit instrumental. Zusammen haben wir die richtige Methode entwickelt, saisonal-regionalen Avocado-Tofu (srAT) richtig zu grillen. Das ist eine essentielle Beilage für viele Wurmgerichte. Er wird nun meinen Kochlöffel erben und ich wünsche ihm viel Glück und Erfolg bei seinem eigenen Kochbuch! Mögen die Würmer ihm wohlgesonnen wuseln. Der Schleemilch-Sebastian hat mir mit geistiger Stärke und Weisheit beigestanden und auch nie mit seiner Expertise in schwierigen Backformeln gegeizt.

Die guten Kolleginnen in der Küche muss ich ganz besonders erwähnen:

Brigitte, stets eine Ruhepol, hat sich immer bemüht anderen zu helfen. Sie war es, die mir mit sehr viel Geduld und Sorgfalt beigebracht hat, wie man so einen Wurmbraten nach dem Backen richtig mit dem Diamantmesser tranchiert. Auf dieser exzellenten Basis konnte ich meine Fertigkeiten mit dem Messer über die Jahre gut ausbauen. Und das war entscheidend für das Gelingen dieses Kochbuchs!

Claudia in der Küche zu haben, war auch immer ein Glück. Sehr erfahren, war sie schwer aus der Ruhe zu bringen. Wenn mal die Milch übergekocht ist, blieb sie ganz cool. Man konnte sie auch zu allen möglichen Rezepten befragen. Bei fast jedem Problem konnte sie helfen.

Daniela war eine echte Freundin. Immer gut gelaunt hat sie jeden Spaß mitgemacht. Immer, wenn man mal Hilfe gebrauchen konnte, war sie die erste, die „hier!“ schreit. Dabei war ihr keine Herausforderung zu groß. Selbst wenn man die waghalsigsten neuen Soßen ausprobiert hat, oder die Würmer mal ganz anders als sonst gratinieren wollte, sie war dabei. Und immer wenn's mal wieder länger gedauert hat, brachte sie einen Kuchen mit. Bei allem, was mit Schokolade zu tun hatte, war sie unsere Expertin.

Gaby kenne ich noch nicht so lange, aber ich finde, sie passt perfekt in unsere Keller-Familie.

Elisabeth hat uns schönerweise häufig in der Küche besucht. Sie war oft damit beschäftigt, Trypanmisu (oder so ähnlich) zuzubereiten, aber immer, wenn man sie getroffen hat, ging einem das Herz auf und der Himmel wurde ein bisschen heller.

Auch wenn ich gegen Ende in einen ruhigeren und kühleren Teil der Küche umgezogen bin, so war die Zeit hinten im Esszimmer/Büro/Froschraum/Plauderecke doch immer schön. Das lag an **Anne** und **Frederik** und **Corinna** (die Experten für Froschrezepte) und **Laura**, die immer da waren, und Nika eigentlich auch, und es war ein harmonisches Miteinander. Das ist alles andere als selbstverständlich. Und gut versorgt wurden wir da hinten auch immer. **Marie-Christine**, Küchenchefin *par excellence*, brachte oft erlesene Spezialitäten aus aller Welt mit, um unsere Gaumen zu schulen. Und Witz und Humor brachte sie auch immer ganz viel mit!

Bei so einem Unterfangen wie dem Schreiben eines Kochbuchs fällt natürlich auch immer ganz viel Papierkram an, der mit Kochen gar nichts zu tun hat. Zum Beispiel Abrechnungen für Fortbildungsreisen zu anderen Küchen. Eigentlich ist sowas ja immer unangenehm und nervig. In meinem Fall hat es fast schon Spaß gemacht. **Margot** hat sich darum nämlich immer sofort und sorgfältig und zuverlässig gekümmert, mit einer Menschlichkeit, die alles andere als selbstverständlich ist.

Sehr froh war ich auch über unsere Freunde von der EMBL (Europäische Meisterschule für Baguette und Lasagne). Besonders über **Anna** (sie hat die EMBL inzwischen verlassen) und **Yannick**. Nicht nur gab es regen Austausch zwischen unseren Küchen, sie haben mich sogar einen ihrer Hightech-Öfen benutzen lassen. Damit konnte ich Wurmlasagne machen wie noch nie zuvor. Mit unfassbar vielen, hauchfeinen Schichten. Und einer leckeren Platin-Kruste. Das heißt, eigentlich habe

ich mal wieder nur den fertig gewürzten und marinierten Wurm mitgebracht und Anna hatte die ganze Arbeit. Aber bei schwierigen Gerichten sollte man die Profis ranlassen. Wenn ich mir heute die Videos davon anschaue, läuft mir immer noch das Wasser im Munde zusammen. Das Rezept findet sich natürlich prominent hier im Kochbuch (siehe unter „Flambiert in Bordeauxwein – super-edle Mehrschichtlarve," FIB-SEM).

Und **Yannick** muss ich nochmal besonders erwähnen, weil er mich immer unterstützt hat. Das hat mir mehr bedeutet, als er wahrscheinlich ahnt. Ohne seine Hilfe wäre ich zum Beispiel bestimmt nie in den lebensverändernden Sommer-Kochkurs in Woods Hole reingekommen. Da habe ich wirklich noch viel über das Kochen und Backen dazugelernt und auch Freunde für's Leben gefunden.

Mit **Martin** zusammen habe ich immer sehr gerne Meeresfrüchte eingemacht und verarbeitet. Auch nachdem er nach Kiel gegangen war, weil da die Muscheln nun einmal frischer sind, hat er mir immer mal wieder einen Link zu einem neuen Rezept-Trend geschickt. Davon haben es auch ein paar in mein Kochbuch geschafft.

Ein paar mal habe ich mich, ganz verwegen, auch an einen delikaten Sturmeintopf rangetraut. Aber dafür braucht man nun wirklich viel Erfahrung. **Sven** war aber immer da. Eigentlich habe ich nur die Würmer in den Topf geworfen und mariniert. Daraus hat er dann den Eintopf gekocht (mit Laser!) und dann auch schön auf dem Teller angerichtet. Immer wieder lecker und lässt die Gäste staunen.

Alex hat mich die ganze Zeit hindurch begleitet. Er hat alles abgekriegt. Alles. In der letzten Phase, als ich nur noch zum Schlafen nach Hause kam, hat er sich kein einziges Mal beschwert. Kein einziges. Und hat mir noch jeden Tag tolles Essen gebracht. Fast immer selbst gekocht! Zwar ohne Würmer (er hat einen anderen Stil als ich), aber dafür auch immer lecker. Ich habe wirklich unfassbares Glück, so einen jungen, gutaussehenden Privatkoch für's Leben gefunden zu haben.

Und wer ist von allen am meisten Schuld? Natürlich **Mami**. Sie hat in mir die Lust am Kochen und Backen geweckt, schon seit ich ganz klein war. Dass ich dieses Kochbuch überhaupt in Angriff nehme, dazu wäre es ohne sie wohl nie gekommen. Denn man braucht schließlich jemanden, der an einen glaubt, und der einen fördert. Und natürlich ist sie auch heute noch immer da, wenn ich sie brauche. Genau wie meine Schwestern **Kathinky** und **Caro**. Und auch **Rico**. Mit starker Familienbande ist das Leben besser gewürzt, knuspriger und, vor allem, herzhafter.

Und, zu guter Letzt, hatte ich natürlich ganz, ganz viel Hilfe von den Stars dieses Kochbuchs, den **Würmern**. Damals, an jenem schicksalhaften Tag, als ich sie das erste Mal gesehen habe, war es Liebe auf den ersten Blick. Und sie haben mich nie im Stich gelassen. Sie haben bereitwillig alles hingenommen, was ich mit ihnen angestellt habe und dabei ihre gute Laune und Eleganz nicht verloren. Sie haben mir immer Gesellschaft geleistet, wenn ich mal spät nachts im Labor war und haben mir zugehört, wenn ich Frust hatte. Ich hoffe, dass sie stolz sind auf dieses Kochbuch, das ihnen gewidmet ist.

Sebastian's recipe for a delicious PhD

FOR the basic batter cultivate a large amount of worms and add fresh supervision while stirring until a smooth consistency is reached. Worms can be found everywhere, but make sure to get good quality supervision. It should contain a perfect mixture of mentor-ship, open doors, and freedom. I always use the one from Christian. This is the best I could find. The dough is flash-frozen under high pressure, incubated at -90 °C, and then warmed up stepwise. Embed the dough in resin and let cure. Cut in ultrathin slices with an extremely sharp knife.

Thoroughly mix the ultrathin slices, a sack of time, a heaped tablespoon of brain-wrecking, and a generous shot of grit and let it rise in a warm place. The location is of utmost importance. The working atmosphere should be excellent or the PhD might turn sour or bitter. I recommend the Imaging Core Facility. All the people there are always helpful and kind and stick together. This makes the PhD especially fluffy. A ton of laughter and humor bestow an exquisite juiciness. A pinch of Georg's wisdom here and there provides sophisticated seasoning that adds great value to the PhD.

Fortunately, I could get my hands on Studienstiftung leavening agent. This helps the aroma to unfold, an enormous enrichment, and the PhD rises beautifully without collapsing at the end. Overdosing impossible.

Bake airless at 200 kV while rotating or on a 5 kV grill on an array baking sheet. When choosing the latter method, you can slather it with laser light and marinate everything in uranyl acetate and lead citrate. Quench with a little bit of carbon before baking.

For a delicate sweet touch, cover the PhD with a glaze of friendship. I achieved the best results with the one from Nika. You will get a beautiful, glossy coating that is completely stable even in harsh conditions.

Enjoy!

THIS cookbook is filled with luscious recipes and of course most of them contain worms. To write such a cookbook was not at all easy and took a really long time. But in the end, it turned out pretty good, I think. But then I had a lot of help too.

For example from **Philip**, who helped me a lot in the end with calculating the measurements correctly and depicting them. Moreover, he agreed to write an elaborate review for my cookbook. That is the reason he will be one of the first to get a copy of the book.

Christian, our head chef, is also going to write a review and gets a copy in advance. But he is quite familiar with this book already, because he helped me more than anyone to make this book into something worthwhile. He always had another idea how to describe the ingredients and procedures in an even better way and he also judged the product photos with the eye of an expert. To make sure they are mouth-watering.

But without him, this book wouldn't exist anyway. He supported me and always believed in me and entrusted me with writing this book. And he is the one who first introduced me to the worms, back in the day. What a fateful encounter that was. Christian made a cook out of a scullion, without a single stern word. I'd like to see anyone beat that.

I also had a lot of help from **Georg**. He was always there and happy to help, no matter what. Since he is in the business for many years himself, no-one can easily match him when it comes to frying, marinating, grilling, or bird watching. He has read this book in its raw version and gave me valuable feedback.

Extremely valuable help I got also from **Andy** and **Rashi**. They both had written such a cookbook before and thus could give me good advice and encouragement. Moreover, they read my book with utmost diligence on really short notice and checked it for language. They both know the appropriate kitchen jargon, because they got it natively from their mothers, so to speak. Thus, they knew exactly how to polish a sentence. The effort they invested in this book was so great that I have a guilty conscience. I will have to think about how to give something back.

Without **Nika** this book would have been different, no doubt. Not only did she take care that I don't die of thirst/hunger/madness, she also directly helped me without hesitation. Sometimes it is necessary to weigh every pea individually and that would have cost me a lot of time indeed if Nika hadn't done it. And you could talk to her about anything. It didn't matter if was about religion, politics, or such grave topics as spilling pumpkin soup while jumping on a trampoline, it was always more fun when she was around.

It was challenging to acquire the necessary expertise for so many diverse and complex recipes. Fortunately, I had a lot of help there too. **Daniel Witvliet** has much more experience in certain ways of cooking a worm than I do and he was always quick and happy to help when I had a question. **Mei Zhen** did not only help with good

advice, she also let me adapt and include some of her most exciting recipes for this book. And she also often sent me her special worms for extra-delicious dishes.

For some recipes, I went out on a limb because they didn't even contain worms! Luckily, **Mehri** and **Heinz** were able and willing to help me describing these appropriately anyway. Furthermore, Heinz had helped me a lot to dig up treasures of recipes from ancient cookbooks and he even emptied out his desk drawer for that. You don't always have to re-invent the dough, old cookbooks often contain the best tricks!

For one chapter of my cookbook concerning Szechuan avocado dumplings (SAD) as a special worm dish, the help of **Wesley Hung** was invaluable. Wesley had already cooked this dish years ago and thus he could teach me a lot about it. Many of his hints and tricks cannot even be found in cookbooks yet, they were true insider tips.

One chapter was particularly ambitious. I tried to make fried udon salad (FUS). Luckily, I didn't have to manage this chapter on my own. **Michael** and I worked on it together. Thus we could create not only the salad including worms, but also a worm-free version (for people with allergies). Practically all the credit for the success of the latter goes to Michael. And besides that he really gave it his all to make our recipes work. He tirelessly performed taste tests to work out the nuances. That's why he spent a lot of time in front of ovens, either our airless rotational oven or the array grill. It was great fun working with him and he was always there to help if he was at all able to. I am also very glad that **Professor Sendtner** and **Mei** supported this, as I said, very ambitious enterprise and also contributed to the cookbook with valuable comments.

And of of course a few **Sebastians** have to get mentions as well. The Britz-Sebastian took some loads off of me during the writing phase and he always offered to help in any way. His contribution to the cookbook was truly instrumental. Together, we developed a method to grill seasonal regional avocado tofu (srAT) in just the right way. This is an essential side in many worm dishes. He will inherit my pots and pans and I wish him success and good fortune for his own cookbook! May the worms wiggle well for him. The Schleemilch-Sebastian supported me with spiritual strength and wisdom and never held back his expertise in complicated baking formulas.

A very honorable mention of course also for my dear colleagues in the kitchen:

Brigitte, ever the haven of tranquility, was always there to help people. She is the one who taught me, with a lot of patience and diligence, how to properly carve a worm roast after baking with the diamond knife. Over the years, I could easily build my knife skills on this excellent basis. And this was crucial for the success of this cookbook indeed!

We were also lucky to have **Claudia** in the kitchen. Very experienced, she was hard to unsettle. If the milk happened to boil over, for example, she totally kept her cool.

And you could ask her about all kinds of recipes. She was able to help with almost any problem.

Daniela was a true friend. Always in a good mood she was up for anything. Any time someone needed help, she was there first. And no challenge was to big for her. Even when trying the most audacious new sauces or when someone wanted to barbecue the worms in an entirely new way, she was in. And when the evenings got late, she brought cake. For anything chocolate-related she was our expert.

Gaby I don't know for a very long time yet, but I can tell that she fits perfectly in our basement family.

It was nice that **Elisabeth** often visited us down in the kitchen. She was often busy with preparing trypanmisu (or something like that), but every time you talked to her, you were cheered up and the sky seemed to turn a bit brighter.

Even though I moved into a more cool and quiet corner of our kitchen at the end, I always enjoyed the time back in our dining room/office/frog room/chatting corner. That was because of **Anne** and **Frederik** and **Corinna** (team frog dishes) and **Laura**, who were there, and Nika too, most of the time. It was always a place of harmony and concord. This is far from granted. And we were also taken care of pretty nicely back there. **Marie-Christine**, *chef cuisinière par excellence*, supplied us with selected delights from all over the world to sophisticate our palates. And she also supplied us with wit and humor *en masse*!

When you undertake something like writing a cookbook there is always going to be a lot of paperwork required. Paperwork that has nothing to do with cooking. For example, administration and accounting for travel to vocational training at other kitchens. Usually, this is unpleasant and annoying. In my case, however, it was almost fun! **Margot** took care of all that. Swiftly and diligently and reliably, with a level of cordiality that went above and beyond.

My heart also goes out to our friends at the EMBL (European Masterschool for Baguette and Lasagna). Especially to **Anna** (she since left the EMBL) and **Yannick**. Not only was there fruitful exchange between our kitchens, they even let me use one of their high-tech ovens. Thus I was able to prepare worm lasagna like never before. With a mind-boggling number of extremely thin layers. Plus, a delicious platinum crust on top. That is, actually I just brought a seasoned and marinated worm and Anna did all the work. But you should leave the challenging dishes to the experts. My mouth still waters when I watch the video of this lasagna. The recipe is of course prominently featured in this cookbook (search under "Flambéed in Bordeaux-wine – sophisticated exquisite multilayer-larva," FIB-SEM).

And I want to mention **Yannick** specifically, because he always supported me. That meant more to me than he probably realizes. Without his help, I would never have been able to secure a place in that life-changing summer cooking class in Woods Hole, for example. I really learned a lot of new things about cooking and baking there and also found friends for life.

I very much enjoyed making and processing sea food preserves with **Martin**. Even after he went to Kiel, because, let's face it, the shrimp is just more fresh there, he regularly sent me links to new cooking trends. A few of those made it in this book.

On a few occasions I got very bold and dared to prepare delicate storm hotpot. But for this sort of thing a lot of experience is required. But **Sven** was there for me. I actually just threw the worms in the pot and marinated them. Then Sven was the one who cooked it into a stew (with a laser!) and beautifully arranged it on the plate. Delicious every time and the guests are amazed.

Alex was at my side the whole time. He got everything dumped on him. Everything. In the final phase, when I only came home to sleep, he didn't complain. Not one single time. Instead, he brought me amazing food every day. Almost all of it he had made himself, of course. Although it never contained worms (his style is very different from mine), it was delicious every time. I am incredibly blessed to have found such a young and handsome private chef for life.

And who gets the most credit? Well, **Mami** of course. She is the one who instilled a delight for cooking and baking in me, from a very young age. Without her, it's unthinkable that I even would have taken up this task to work on a cookbook in the first place. After all, you need someone who believes in you, who supports you. And of course she is still always there for me when I need her. Just as my sisters, **Caro** and **Kathinky**. And **Rico** too. With strong family ties, life is just better seasoned, more crispy, and, most of all, heartier.

And last but certainly not least, I had a lot of help from the stars of this cookbook, the **worms**. On that fateful day a few years ago, when I first met them, it was love on first sight. And they never let me down. They took everything I did to them with elegance and a smile. They kept me company on lonely nights in the lab and they listened when I voiced my frustrations. I hope they are proud of this cookbook that is dedicated to them.

Eidesstattliche Erklärung nach §7 Abs. 2 Satz 3, 4, 5 der Promotionsordnung der Fakultät für Biologie

Eidesstattliche Erklärung

Hiermit erkläre ich an Eides statt, die Dissertation: „**Vertiefung des Verständnisses synaptischer Architektur von der einzelnen Synapse bis zum Netzwerk mit modernsten bildgebenden Verfahren**," eigenständig, d. h. insbesondere selbständig und ohne Hilfe eines kommerziellen Promotionsberaters, angefertigt und keine anderen, als die von mir angegebenen Quellen und Hilfsmittel verwendet zu haben.

Ich erkläre außerdem, dass die Dissertation weder in gleicher noch in ähnlicher Form bereits in einem anderen Prüfungsverfahren vorgelegen hat.

Weiterhin erkläre ich, dass bei allen Abbildungen und Texten bei denen die Verwertungsrechte (Copyright) nicht bei mir liegen, diese von den Rechtsinhabern eingeholt wurden und die Textstellen bzw. Abbildungen entsprechend den rechtlichen Vorgaben gekennzeichnet sind sowie bei Abbbildungen, die dem Internet entnommen wurden, der entsprechende Hypertextlink angegeben wurde.

Affidavit

I hereby declare that my thesis entitled: "**Enriching the understanding of synaptic architecture from single synapses to networks with advanced imaging techniques**" is the result of my own work. I did not receive any help or support from commercial consultants. All sources and/or materials applied are listed and specified in the thesis.

Furthermore, I verify that the thesis has not been submitted as part of another examination process neither in identical nor in similar form.

Besides I declare that if I do not hold the copyright for figures and paragraphs, I obtained it from the rights holder and that paragraphs and figures have been marked according to law or for figures taken from the internet the hyperlink has been added accordingly.

Würzburg, den 24. Juni 2019

Sebastian Matthias Markert

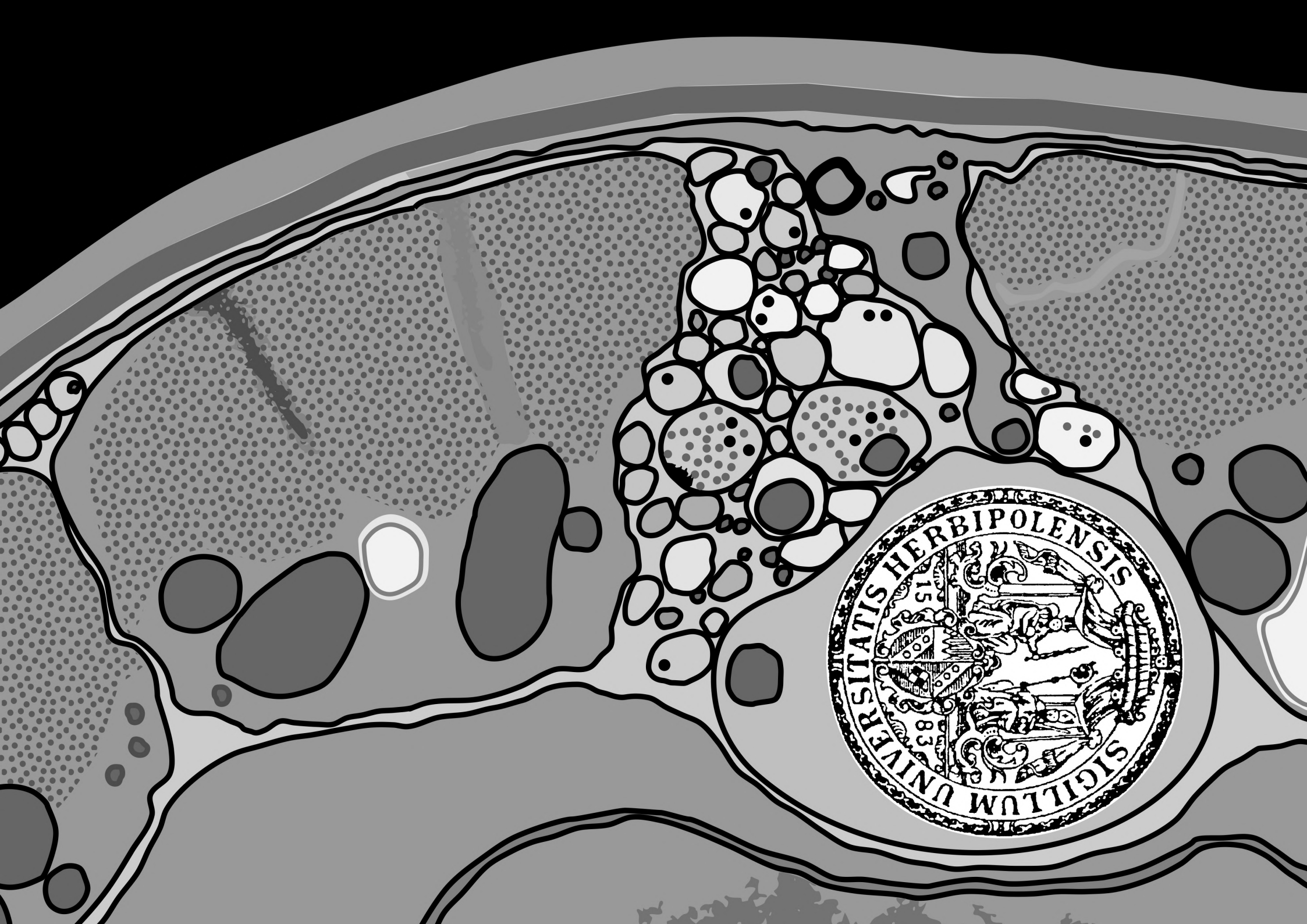
SIGILLUM UNIVERSITATIS HERBIPOLENSIS
15
83